IN-SPAN SPLICING FOR CONTINUOUS PRESTRESSED CONCRETE GIRDER BRIDGES

A Dissertation

by

REZA BAIE

Submitted to the Office of Graduate and Professional Studies of
Texas A&M University
in partial fulfillment of the requirements for the degree of

DOCTOR OF PHILOSOPHY

Chair of Committee,	John B. Mander
Co-Chair of Committee,	Mary Beth D. Hueste
Committee Members,	Peter B. Keating
	Mohammed E. Haque
Head of Department,	Robin Autenrieth

May 2017

Major Subject: Civil Engineering

ABSTRACT

When bridge spans exceed 45 m it is necessary to have modular construction methods to effectively join the segments in-span and form a continuous structure with substantially longer span lengths. In-span splicing of prestressed concrete girders to extend span length of bridges have been effectively used in several recent bridge construction projects. However, the extent and limitation of such a construction approach, as well as associated analysis and design challenges have not been systematically explored.

Concepts of deflection balancing and load balancing were considered to provide a platform for design of slab-on-in-span spliced prestressed concrete girder bridges. Three methods of construction were investigated that benefit from in-span splices: shored, partially shored, and heavy-lift construction. Design procedures and construction sequences were compared and contrasted, and discussed in detail. A prototype bridge geometry was designed for all three methods of construction approaches, and the results compared and conclusions drawn.

From the prototype design, an experimental test specimen was abstracted and an experimental testing investigation described. Three test setups were adapted to investigate the performance of each of the three splices, in three different load combinations. Results were presented for the full-scale laboratory tests on each splice regions under service load through to failure.

Based on the results of the experimental investigation, diagonal cracks in the splice regions of prestressed concrete girder bridges may adversely affect the flexural behavior of the splices and reduce their post-cracked ultimate strength and deformability. A generalized moment-curvature approach was developed along a diagonal crack plane to directly account for the effects of flexure-shear interaction. A formulation was provided to calculate the nominal capacity of such sections incorporating the interacting effects of flexure and shear.

A Compatibility Strut-and-Tie Modeling (C-STM) was introduced as an effective alternative method of structural analysis for when members were subjected to high moment demands coupled with high shear intensity. The C-STM approach was advanced to model the behavior of slab-on-spliced prestressed concrete girder bridges where shear-flexure interaction may influence system performance particularly near regions that are spliced. The efficacy of the approach was demonstrated by modeling the experimental performance of the test specimen.

DEDICATION

To my wife, my parents and my sister.

ACKNOWLEDGEMENTS

I would like to thank my committee chair, Dr. Mander, and committee co-chair, Dr. Hueste, for their invaluable guidance and support throughout the course of my study and research. This work would have not been possible without their insightful knowledge, vision, and advice. I am deeply grateful for Dr. Hueste, Dr. Mander, Texas Transportation Institute, and the Zachry Department of Civil Engineering for their financial support during my course of study as a PhD student.

I am grateful to Dr. Haque, for his insightful comments and serving on my advisory committee. I wish to sincerely thank Dr. Keating for serving on my advisory committee as well as providing space and expertise as the director of the High-Bay Structural and Material Testing Laboratory. I am also thankful to Matthew Potter and Ramiro Vanoye-Trevino for assisting me during the experimental testing. I would also like to acknowledge and thank my great colleagues, Anagha Parkar, Akshay Parchure, Tevfik Terzioglu and Dongqi Jiang.

My utmost gratitude goes to my father, Mr. Janali Baei, my mother, Ms. Fatemeh Pourpashang, my wife, Ms. Dena Rezaei and my sister, Miss Sara Baei. I would have never made it through this journey without their sincere support and selfless sacrifices.

CONTRIBUTORS AND FUNDING SOURCES

This work was supported by a dissertation committee consisting of Professor John Mander as advisor, Dr. Mary Beth Hueste as co-advisor, and Dr. Peter Keating of the Department of Civil Engineering and Dr. Mohammed Haque of the Department of Construction Science.

Part of literature review (Chapter 2), design concept study (Chapter 3 and Appendix A), and design and construction of experimental test specimen was in collaboration with Anagha Parkar and Akshay Parchure, Master of Science students of Department of Civil Engineering. Michelle Prouty and Tristan Sarremejane, Master of Science students of Department of Civil Engineering assisted with construction of test specimen and material testing (Appendix B). Dr. Peter Keating and staff of High Bay Material and Structural Testing of Department of Civil Engineering provided expertise and space for experimental program.

This research was partially funded by Texas Department of Transportation under Project Number 6651. Texas Transportation Institute of Texas A&M University provided space, utility and coordination to facilitate the research.

Contents of this research are solely the responsibility of the author and do not necessarily represent the official views of the Texas Department of Transportation.

TABLE OF CONTENTS

Page

LIST OF FIGURES

Page

LIST OF TABLES

Page

1 INTRODUCTION

1.1 BACKGROUND AND MOTIVATION

As urban areas become increasingly congested, topographical and environmental issues demand the extension of bridge spans with minimal traffic interference and construction time. Modular construction methods need to be considered wherever possible so that individual bridge segments may be pre-fabricated and hauled to the construction site. Among different design options, precast prestressed concrete girder bridges have been widely used as an economical modular construction method. However, the girders have been mostly designed for simply supported spans. Therefore, the hauling limitation for length, height, and weight of individual segments impose an upper bound in the range of 45 to 50 m depending on the nature of the roads between the precasting plant and bridge construction site. A height limitation of 3 m is common due to vertical curves on roadways, especially at railway crossings and a weight limitation generally of 900 kN, but not more than 1000 kN. Weight limitations are based on axial arrangements of the transporting equipment, as well as crane capacity limitations.

Since the first use of prestressed concrete girder bridges in the 1950s, they have been widely used for short to medium span lengths nationwide. Many studies have been carried out over the past decades to propose methods that will lead to extending the span length of prestressed concrete girder bridges. Most of these methods suggest modifications on design methods, improving material properties, changing the shape and size of girder sections, and splicing the girders over the pier to provide continuity.

While each of the aforementioned methods have contributed in improving the design and performance of the bridges over time, the effect on increasing the span length has been only marginal due to the weight and length limitations. On the other hand, an in-span splicing technique may be used to effectively double the span length of concrete girder bridges to about 90 m.

For in-span splicing, individual girder segments are pretensioned and cast at a precasting plant and then transported to the construction site. Then by splicing them— either before or after erection— longer segments can be achieved. Additional benefits of this method of construction include: reducing the girder lines, minimizing the structure depth, avoiding placement of piers in waterways, improving aesthetics, improving seismic resistance due to continuity, reduction of long term maintenance and increased durability. Together, these attributes lead to an economical and competitive solution as compared to other bridge alternatives, particularly bridges with steel superstructures.

Although splicing girders may provide versatile design options with competitive project costs, spliced girder bridges have not become as popular as other types of bridges. According to NCHRP 517 Report (Castrodale and White 2004), over 250 bridges had used this technique to extend the span length nationwide, yet most of them are localized in certain states such as Colorado, New York, Massachusetts, Oregon, Washington and Florida.

The lack of field data and experimental assessment on performance of in-span splices, has also made designers hesitant to adopt the in-span splicing technique to lengthen spans. Additionally, as the design of such bridges is tightly related to the

sequence of construction and construction loads, a lack of a standard design procedure and an optimum construction sequence through which the effect of construction loads on final prestressing layout is minimized, limits the applicability of this type of bridge with in-span splices.

1.2 NEW CONTRIBUTIONS AND SIGNIFICANCE

The expected contributions of this research to the body of knowledge are as follows:

1. Even though there are several projects using in-span splicing, lack of standardized design and construction procedures have limited spliced girder bridges. Minimalistic details are developed which can be considered the starting point for standardization. A deflection balancing concept rather than the load balancing approach is discussed and formulated herein.
2. There is limited experimental information on the expected performance of in-span splices. A full size specimen abstracted from a designed prototype bridge is constructed and then tested to failure. The specimen includes three in-span splices that facilitate the performance assessment of the splice connections in different combinations of positive moment, negative moment and shear, for service limit states through ultimate strength.
3. Due to narrow webs and the existence of PT ducts in the web, high inelastic shear deformation is possible. It is expected that the shear-flexure interaction will affect the capacity of the splice regions. An enhanced moment-curvature analysis is proposed to provide an integrated analysis tool that includes the effect of diagonal cracks and shear in the flexural behavior of such bridges.

4. Compatibility strut-and-tie modeling (CSTM) is further developed to model the behavior of spliced prestressed concrete girder bridges. Loads are applied through displacement control which allows the model to capture the post-peak behavior of the structure. CSTM is adopted to model a test specimen in both positive and negative bending and the results are validated by experimental data.

1.3 WHAT THEN IS PARTICULARLY NEW IN THIS DISSERTATION?

Limited previous work has been done to assess the performance of in-span splices; in particular there is a general lack of experimental data. Numerous design examples suggest the success of this method of construction; however lack of experimental information to validate the performance of splices beyond the service limit raises questions regarding failure modes and means to improve performance, if necessary.

While no other thorough studies have assessed the performance of in-span splices, the proposed experimental study provides detailed information on splice behavior and the entire structure for different load combinations during construction, service and strength limit states. More robust splice detailing can be proposed through the study of performance of the splices beyond the service limits. Recommendations are made through observing the behavior modes so that unwanted brittle failure may be avoided.

Shear-flexure interaction may affect the post-cracking performance of splice regions. While several studies have been conducted to predict the shear capacity of prestressed concrete sections, they are mostly focused on regions where shear is the predominant state of failure. On the other hand, to capture the effect of diagonal cracks with moment curvature analysis, finer mesh is required and beam elements are not able to

effectively model such behavior. This results in more computation time and cost. In this research an integrated moment-curvature analysis tool is proposed where the effects of shear-flexure interaction are considered in the post-cracked behavior of prestressed concrete sections.

Compatibility strut-and-tie modeling (CSTM) is well developed in the past decade to capture the behavior of reinforced concrete. However, limited studies have expanded the approach for prestressed concrete members. In this study, CSTM is further developed to model the performance of slab-on-spliced prestressed concrete girder bridges and results are validated through experimental data for both positive and negative bending.

1.4 ORGANIZATION OF THE DISSERTATION

Following this introductory chapter, the organization of the dissertation follows:

Chapter 2 provides a literature review that discusses the relevant existing literature categorized as history of design and construction of continuous prestressed concrete bridges, previous studies on performance of spliced concrete girders, and the shear-flexure interaction modeling of prestressed bulb tee concrete sections.

Chapter 3 develops bridge designs based on different construction methods and construction sequences. It discusses associated issues for each type of construction and develops a standard procedure in accordance with the AASHTO LRFD Bridge Design Specifications (AASHTO 2014) for each type of construction. The concept of deflection balancing is introduced and considered for design cases. Then a prototype bridge is designed considering relevant AASHTO articles for each type of construction and the results for each case are compared.

Chapter 4 describes the experimental investigation of a full-scale specimen and presents observations of the performance of the specimen during the test, along with the experimental results generated from the data analysis of collected data.

Chapter 5 introduces the effect of flexure-shear interaction on behavior of spliced prestressed concrete girder bridges. This chapter provides an analytical and numerical approach to incorporate the coupling effects of shear and flexure through a generalized moment-curvature analysis. The concept of compression shift is introduced in the chapter and recommendations for design of splices are proposed.

Chapter 6 provides an advanced analysis approach using compatibility strut-and-tie modeling (CSTM) to simulate the behavior of spliced prestressed concrete bridges. CSTM is adopted to model the behavior of a test specimen for both positive and negative bending and results are validated by experimental data.

Chapter 7 presents the general findings and recommendations regarding design, construction issues, and splice detailing and proposes recommendations for improved constructability and performance of a spliced precast girder bridge structure. The outcome of the study is presented and compared to previous studies. The advantages and disadvantages of this design approach are discussed and recommendations for future studies are given.

In addition to the abovementioned chapters, following the references, four appendices are presented. Appendix A provides a detailed design example of the prototype bridge using in-span splicing. Appendix B provides information regarding specimen design, abstraction and construction, along with the instrumentation plan. Appendix C

presents the derivation for deflection balancing. Appendix D provides the derivation for geometry proportion of C-STM modeling.

2 LITERATURE REVIEW

2.1 INTRODUCTION AND SCOPE

This section presents the literature review of the earlier work relevant to this study. First, an extensive review of state-of-practice on spliced concrete girder bridges is presented, followed by previous studies on performance of such bridges. The history of in-span spliced concrete bridges is illustrated along with various proposed methods of design and construction. Then, previous studies on analysis tools of such type of bridges are presented, categorized as either flexural or shear-flexure interaction behavior modes for prestressed concrete sections. Finally, research questions arising from this previous work are given and discussed.

2.2 STATE-OF-PRACTICE ON SPLICED CONCRETE GIRDER BRIDGES

2.2.1 Preliminary Remarks

Splicing techniques for bridge girders have been used for several decades. Splices may be generally categorized as either on-pier splices or in-span splices. On-pier splices have been used in various projects to provide continuous spans and thereby increase span lengths, but have limitations in markedly expanding short span structures into long span bridges. To increase span lengths by a considerable degree, it is necessary to use some form of in-span splices so that the span length can exceed the maximum precast unit length. This section discusses both on-pier and in-span spliced used in past practice and also developed through research.

2.2.2 On-Pier Splicing Techniques in Practice

Ficenec et al. (1993) described two bridges adopting on-pier splicing for continuity in Nebraska. The pedestrian/bike overpass bridge was comprised of 5 spans of 27-27-38-27-27 m and the main viaduct bridge consisted of six exterior spans of 26 m long, and 35 m long interior spans. For both bridges, Nebraska Type 4-A sections with 1.4 m or 1.3 m depth were selected. The proposed design of continuous prestressed concrete with on-pier splicing was selected as the winning bid, with an estimate cost lower than the steel plate girder option. Pretensioning strands were coupled and tensioned over the pier to provide continuity. Straight and harped pretensioning was used for individual segments. The design option was the most economical bid, yet the span length was limited to 38.1 m.

NCHRP Report 519 (Miller et al., 2004) presents the results of research on different connections of simple span precast concrete girders for continuity. Through this study the authors surveyed numerous past projects and gathered information to investigate the type of negative and positive moment connection at the support, the age at which the continuity is established, construction sequence, and design techniques. The connection details included: (i) extended prestressing strands; (ii) extended strands with the girder ends embedded into diaphragm; (iii) extended strands with girder ends embedded into the diaphragm with horizontal bars placed through the web of the girder; (iv) extended mild steel bars; (v) extended bar with the girder ends embedded into the diaphragm; and (vi) extended bars with the girder ends embedded into the diaphragm with additional stirrups near the bottom of the girder.

All the specimens were detailed for 1.2 M_{cr} (cracking moment of the composite section) and all achieved the design cracking moment. However, the details with embedded girders in the diaphragm and horizontal bars or additional stirrups showed higher ductility. They also concluded that even though the thermal loading did not reduce the flexural capacity of the connections, repeated thermal effects could create serviceability issues over time.

2.2.3 In-span Splicing Techniques in Practice

In-span splicing has been used for both single span and multi-span bridges. When the in-span splicing technique is used for a multi-span bridge, there are mainly two different construction methods that can be adopted: shored and partially shored construction. For shored construction, shore towers or piers are provided at all connections to support the individual segments for self-weight and construction loads. For partially shored construction, the shore towers are removed from the main span to provide a versatile design option for cases where environmental, topological or transportation concerns do not allow having shore towers in main span.

Post-tensioning is an essential part of design for in-span splices, as due to lack of pretensioning and individual post-tensioning, such sections may have a low flexural capacity. Splices can be post-tensioning either locally —often called a “stitched splice”, or continuously —known as continuity PT. In this section, a selection of previous projects for different types of post-tensioning and types of construction is presented.

Caroland et al. (1992) presented the design of Shelby Creek Bridge with a total length of 305 m in eastern Kentucky. The winning bid proposed using spliced prestressed

concrete I-girders with a span configuration of 49-66-66-66-49 m, while the alternative bid with a steel delta frame was estimated to cost $2 million more than the concrete alternative. Seven girder lines, using 2590 mm deep prismatic sections spaced 3.8 m apart supported the 216 mm thick and 26 m wide deck slab. Each girder line was comprised of nine equal length segments of 33 m long. Individual segments were pretensioned for self-weight. Drop-in segments were post-tensioned before erection on the construction site. For this partially shored bridge construction, the drop-in segments were held and supported by on-pier segments through Cazaly hangers, while the temporary bottom pretensioning of on-pier segments was being released. CIP closures and in-span splices were poured and locally stressed. Fig. 2.1 depicts the prestressing layout, locally post-tensioned splices, and prestressing of the pier cap.

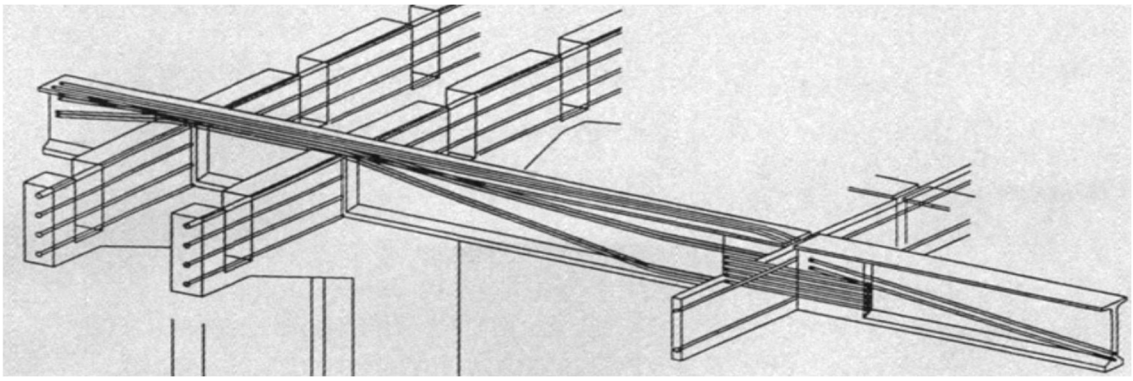

(a) Prestressing layout of girders, pier cap, and splices

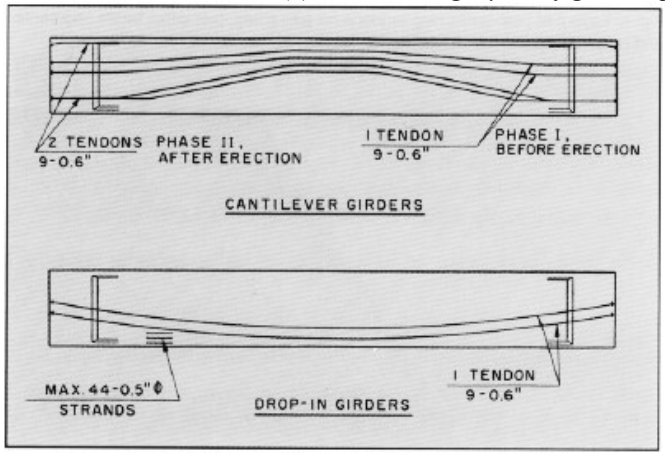

(b) Prestressing layout of the girders

(c) Cazaly Hanger System

Fig. 2.1 Prestressing layout of girder segments, splices and pier cap for Shelby Creek Bridge (Caroland et al. 1992).

* 1 ft =0.3048 m, 1 in. = 25.4 mm

Jenssen and Spaans (1994) presented the design and construction of the Highland View Bridge in Florida. The span configuration of the bridge was 59-76-59 m and partially shored construction was adopted. Haunched sections were used for on-pier segments, where the depth of the section varied from 1930 mm at the ends to 2590 mm at the center, as shown in Fig. 2.2 Drop-in segments were supported by cantilevered on-pier segments, using a temporary strong back. The drop-in segments were 43.3 m long and the length of on-pier segments was 32.3 m. Five AASHTO Type VI girder lines spacing at 2.9 m carried the weight of the superstructure and live loads.

Mumber et al. (2003) presented the design of the Ocean City-Longport Bridge in New Jersey. Due to maintenance issues, the steel bridge option was ruled out and preference was given to a prestressed concrete design option. Deep water and environmental issues restricted the use of shore towers; therefore, an unshored construction was adopted for the design of the 180 m long bridge with span configuration of 56-68-56 m. Modified AASHTO Type VI I-girders with 2290 mm depth was selected for the design. A tie-down system was considered that provided a temporary moment connection between the pier cap and pier girders that transferred the unbalanced moment to the pier. After erection of the end segments, the moments were balanced and the temporary tie town was removed. Fig. 2.3 presents the details of the temporary tie down.

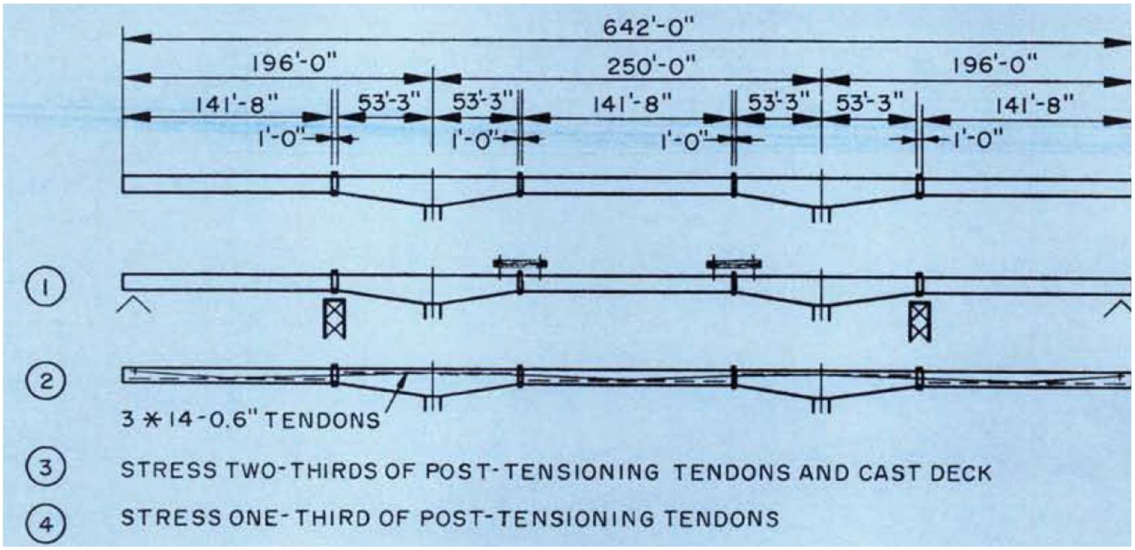

(a) Side elevation of the bridge

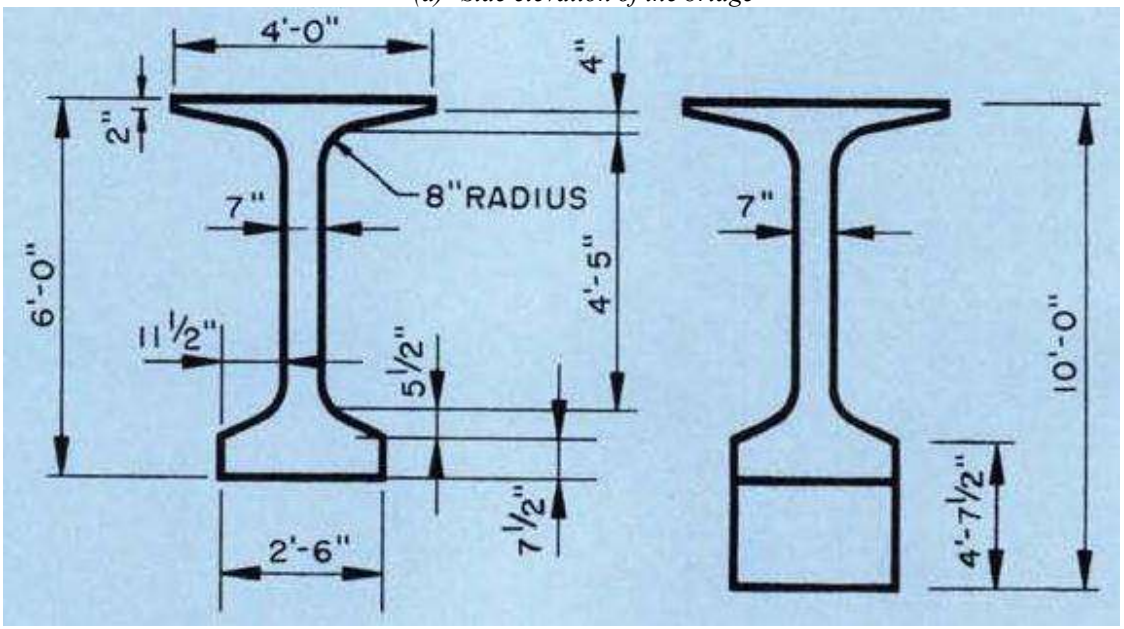

(b) Cross section of the haunched and standard section.

Fig. 2.2 Side elevation and cross section of Highland View Bridge in Florida (Jenssen and Spaans, 1994).

* 1 ft =0.3048 m, 1 in. = 25.4 mm

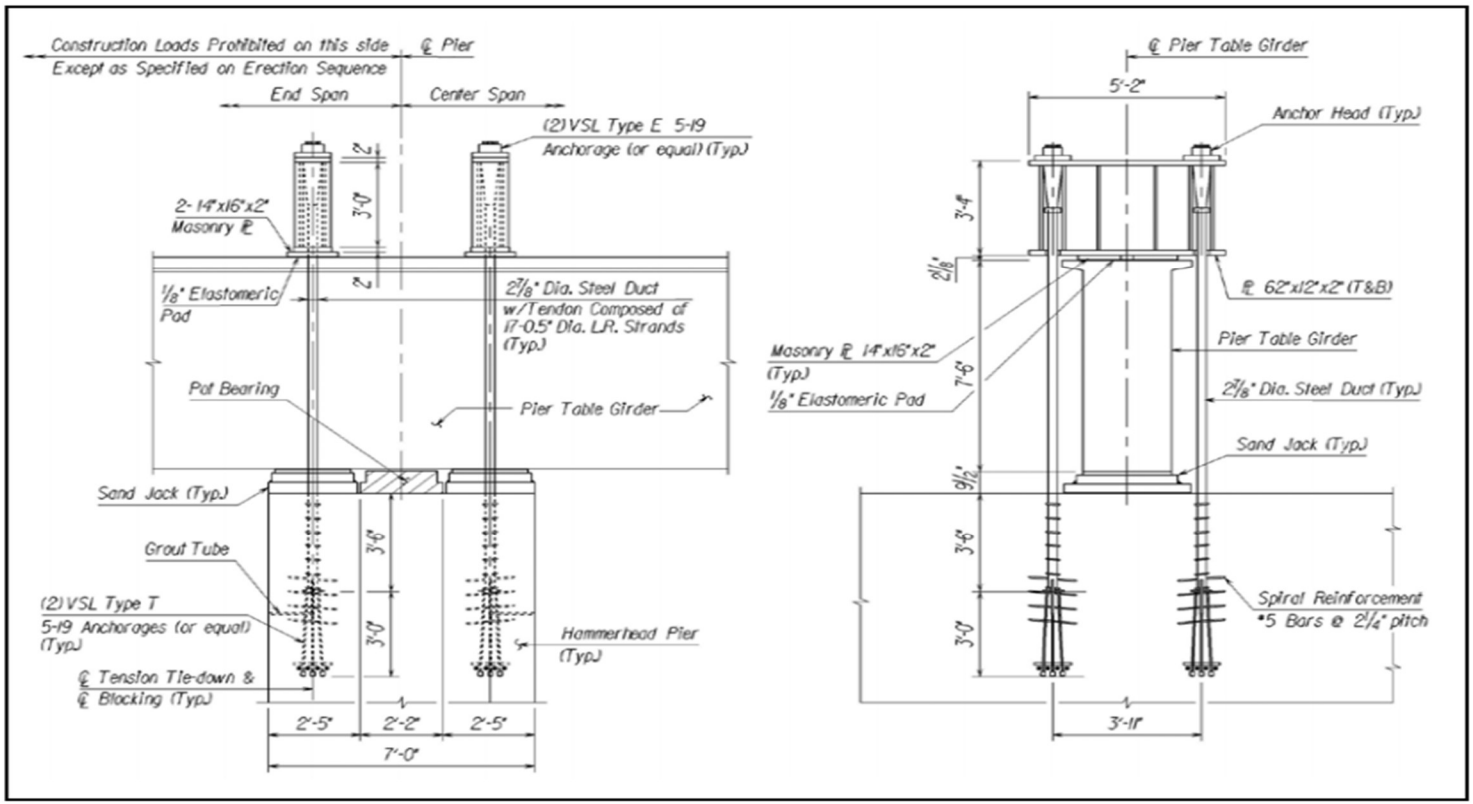

Fig. 2.3 Detail of the temporary moment connection for Ocean City-Longport Bridge (Mumber et al., 2003).
* 1 ft =0.3048 m, 1 in. = 25.4 mm

Fitzgerald and Stelmack (1996) presented the design of the Main Street Viaduct in Pueblo, Colorado. The 246 m long bridge crossed over twelve railroad tracks, the Arkansas River and its dike, and a city street. The bridge was comprised of eight girder lines spaced at 3.7 m, and five spans ranging from 27 m to 53 m long. Haunched sections were used with varying depth from 1830 mm to 2440 mm. A partially shored construction was adopted where shore towers were provided at the back spans. Strongbacks were provided on top of the girder to transfer the weight of the drop-in segment to on-pier segments. Fig. 2.4 presents photos of the bridge construction.

Endicott (1996) and Nicholls and Prussack (1997) described the design of the Rock Cut Bridge crossing over the Kettle River in Washington State. For this single span bridge, three equally long segments of 19.2 m where spliced in the third points to compose the 58 m long span bridge. Four girder lines were spaced at 1.9 m and 2260 mm deep decked sections were used to avoid casting the deck at the construction site. A launching truss was used to push the post-tensioned superstructure across the span and a crane placed the girder line in their specific locations.

Nikzad et al. (2006) presented the design and construction of Old 99 Riverside Bridge in Washington. The bride consisted of eight girder lines and five spans ranging from 46 m to 55 m. In the proposed method of construction, pretensioned precast segments in shorter lengths were fabricated and transported near construction site. Then, segments of each span was spliced on the ground, and post-tensioned. Then, each span was erected on piers and after completion of all five spans, the concrete slab was poured. Eventually continuity post-tensioning was stressed along the entire length of the bridge to provide

additional capacity and to enhance the bending capacity of the over-pier splice. Fig. 2.5 presents the details of the construction sequence for this bridge.

The recent design and construction of the Sylvan Avenue Bridge across the Trinity River near Dallas represented a current state-of-the-practice example of spliced girder construction in the state of Texas. This bridge had 23 spans and utilizes pretensioned simply supported girders, as well as continuous and post-tensioned girder construction with in-span splices. There were three post-tensioned portions among the 23 spans that were each composed of three continuous spans as shown in Fig. 2.6.

Most of the spans used a new Tx82 prestressed concrete section shape. However, in order to create the 76 m span river crossing, it was necessary to use haunched girders as shown in Fig. 2.6 (b), because shore towers could not be used for the main span.

The haunch-modified girders were cast on soffits in order to create the centerline haunch. In contrast with TxDOT standard shapes where the girders customarily have a 178 mm wide web, the Tx82 modified girder had 254 mm wide web, primarily to accommodate the PT ducts. Fig. 2.6 (c) and (d) show some steps of the construction process in the photographic record. Fig. 2.6 (a) shows placement of the central drop-in girder in Span 11. In order to provide girder stability during construction, it was necessary to provide a shore-tower beneath the splices within the back spans.

(a) Shoring towers provided in the back-span in partially shored construction

(b) Haunched segments are used for on-pier segments

Fig. 2.4 Construction of Main Street Viaduct in Pueblo, Colorado (Fitzgerald and Stelmack, 1996)

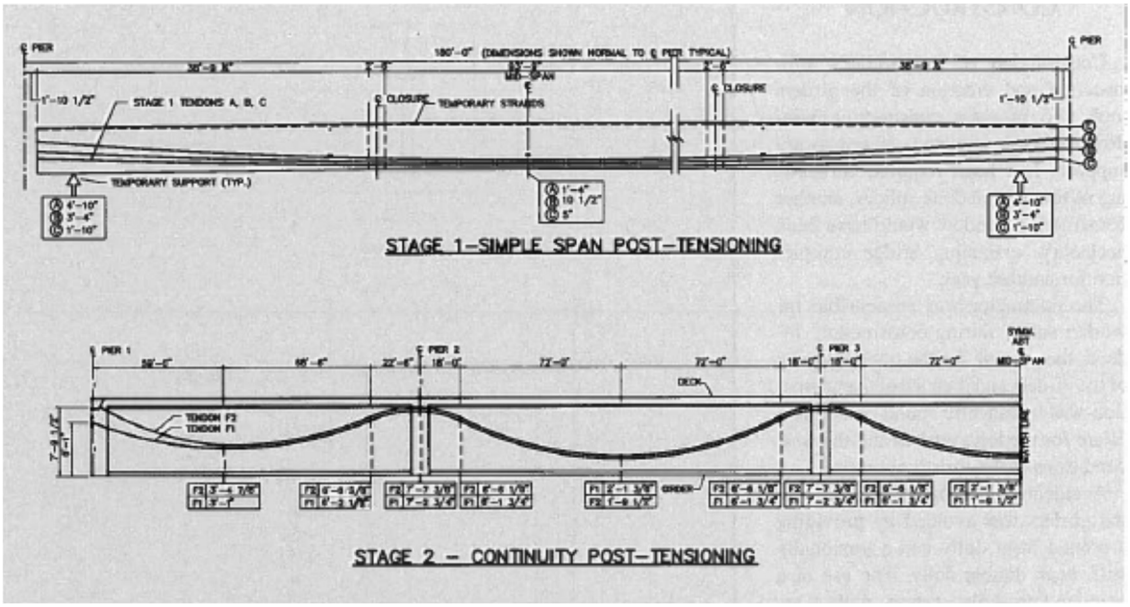

(a) Different Stages of PT: Stage 1 on simple span; Stage 2 as continuity PT

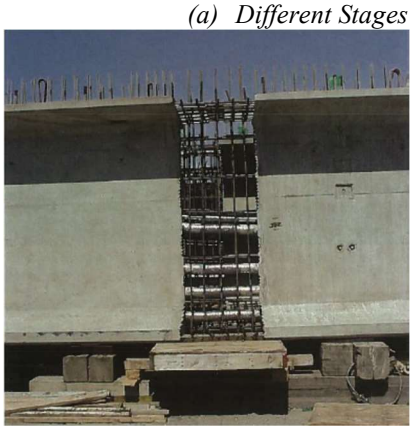

(b) In-span splice

(c) Erection of entire span

Fig. 2.5 Post-tensioning and construction details of Old 99 Riverside Bridge (Nikzad et al., 2006).

* 1 ft =0.3048 m, 1 in. = 25.4 mm

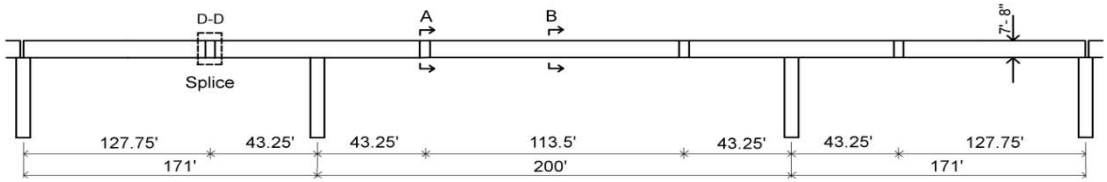

(a) Elevation for Spans 6 to 8 and 16 to 18.

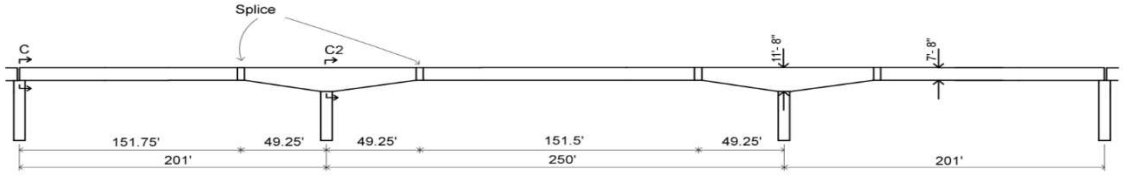

(b) Elevation for Spans 10 to 12.

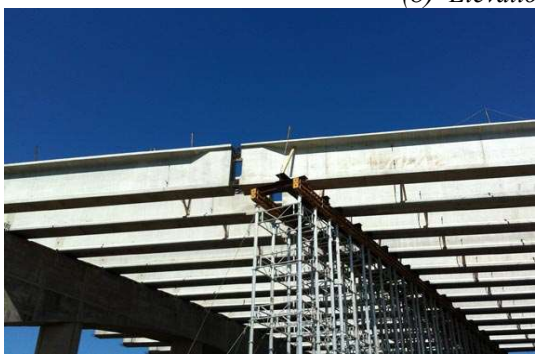

(c) In-span splices in the back span on shoring towers

(d) Erection of drop-in segments

Fig. 2.6 Geometry and construction details of Sylvan Avenue Bridge in Dallas, Texas (Webber 2014).

* 1 ft =0.3048 m, 1 in. = 25.4 mm

2.3 STATE-OF-THE-ART ON SPLICED CONCRETE GIRDER BRIDGES

2.3.1 Preliminary Remarks

Numerous studies have been performed by previous researchers to assess the performance of splices in concrete girder bridges, as well as splice detailing, design procedures and recommendations. Most of the previous research is focused on the performance assessment of on-pier splices and extensive experimental data has been gathered. However, until recently, no comprehensive experimental study had been conducted on the performance of in-span splices, and most of the design recommendations were proposed by practitioners. In this section, previous numerical and experimental studies and recommendations on the performance and design of on-pier splices and in-span splices are presented.

2.3.2 Studies on Performance of On-Pier Splices

Kaar et al. (1960) investigated the performance of a connection detail for on-pier splices. In this non-prestressed detail, the deck reinforcement was made continuous over the pier to improve the performance of the splice for negative bending. A continuous diaphragm was considered over the pier to provide lateral stability and enhanced capacity over the pier. Reinforcement was primarily provided in the top of the section and the deck to resist the common negative bending over the pier.

Mattock and Kaar (1960) extended the study by providing additional reinforcement to enhance the capacity of the on-pier splice for positive bending resulting from creep, shrinkage, and thermal loads. Two connection details with positive bending capacity were proposed and tested: fillet welding the projecting ends of the reinforcement

bars to a structural steel angle; and bending the projecting ends of the reinforcement to form right angle hooks. They conducted an experimental study on a half-scale specimen with two spans for both static and dynamic loading. The experimental results for negative bending supported the findings of Kaar et al. (1960). The experimental performance suggested that the proposed connection can withstand the cyclic design loads for an indefinite number of applications. Comparison of the performance of the two proposed details showed that the welded detail performed better for the service limit state as well as ultimate strength, given that welding is done with careful attention.

Bishop (1962) proposed a bolted steel plate connection where steel plates were placed in the top and bottom flange spanning over the end of both adjacent girders, and then bolted from top to bottom to provide continuity for both positive and negative bending. For construction, to balance the moment of the self-weight, the abutment end of the girders was raised and the connection was bolted on the pier end. By lowering the abutment ends on the bearings, a bending moment was created that balanced the dead weight of the segments. While this innovative method provides partial load balancing for the dead loads, it is difficult to construct and due to limited space, the bottom plate welding became troublesome. It also changes the loading condition from a simply supported beam to a balanced cantilever beam, which required additional reinforcement in the on-pier splice to provide essential capacity.

NCHRP Report 322 (Oesterle et al., 1989) presented the results of an experimental study on the effect of the creep and shrinkage on the continuous prestressed concrete bridges with on-pier splices. This comprehensive study provided a state-of-the-art report

of previous studies as well as DOT inputs, and experimentally considered the effects of the long-term and short-term behavior of on-pier splices. Experimental results suggested that pre-compression is required to avoid cracking in on-pier splices, due to the combined effect of long term creep and shrinkage as well as gradient temperature.

Mirmiran et al. (2001b) carried out a study on the positive bending cracking of on-pier spliced concrete girder bridges. The research considered the simple-span prestressed bridges that were made continuous over piers for continuity under live loads. The researchers recommended "a minimum amount of positive moment reinforcement equivalent to 1.2*Mcr*" should be used to limit the crack width in the diaphragm and to avoid significant loss of continuity, where *Mcr* is the cracking moment of the diaphragm section. Researchers suggested that both bent embedded bars and bent strands detail can successfully provide the required capacity. While bent strands were easier to construct due to their flexibility, they were found to fail by gradual pullout of the strands at each cycle of loading. On the other hand, the bent bars were difficult to construct and caused congestion in the connection region, however they improved the connection capacity. Researchers found that additional stirrups in the connection did not increase the connection capacity, but they improved the ductility of the section.

Sun (2004) investigated a threaded rod system that was originally proposed at the University of Nebraska. Two continuity details were investigated: using high strength threaded bars crossing the connection, and using high strength bars in line and welding the transverse bars to longitudinal straps to form a steel box, as shown in Fig. 2.7 (a) and (b). The proposed connection detail would be placed prior to casting the deck, hence

locking in a permanent negative moment to prevent cracking in the bottom flange due to the effect of secondary temperature moments. It also intended to limit the deflection of the bridge, as the superstructure would act like a continuous beam for the weight of the deck.

Newhouse et al. (2005) conducted research on continuity on-pier splices for precast concrete I-girder sections. Three continuity details were tested: the first two consisted of a full continuity diaphragm with a cast-in-place deck, and the third one had only the deck slab continuous over the pier. For the first test, the pretensioning strands were extended in the connection region and bent 90 degrees. The second continuity detail with full diaphragm included #6 180 degree bent bars extended in the connection region for a non-contact reinforcement splice. Results of the experimental program suggested that the continuity detail with the #6 bent bars was slightly stiffer with smaller cracks opened up at the interface of the wet splice under static and dynamic loads. They also concluded that the effect of thermal gradient and secondary thermal moment was more critical than the effect of creep and shrinkage. They proposed to design the girder segments as simply supported beams for dead load and live load, and as a continuous beam for ultimate strength. Fig. 2.7 (c) and (d) shows the tested splice details for Test 1 and 2, respectively.

Dimmerling et al. (2005) presented the results of NCHRP Project 12-53 on different types of on-pier splice connections. The research focused on different proposed details for positive and negative bending to make simple-span concrete girder bridges continuous for live loads. Fig. 2.8 presents the details of six types of connections that were studied and tested experimentally. Three loading regimes were considered for each specimen: cyclic loading in service limits; loading to cracking moment; and a maximum

1,000,000 cycles of loading between $M_{cr} + M_{LL+}$ and $M_{cr} - M_{LL-}$; where M_{cr} is the cracking moment of the section, and M_{LL} and M_{LL-} are the live load bending demand in positive and negative bending, respectively.

2.3.3 Studies on Performance of In-Span Splices

Abdel-Karim and Tadros (1992) provided a state-of-practice on previous use of in-span splices. They reviewed several previous designs and pointed out the issues regarding design and construction. They mentioned that the standard I-girder sections were modified to eliminate the end block regions and provide a special end diaphragm. The study proposed that the splicing technique provided a good option for acceptable curved alignment. The study also noted that use of haunched sections over the piers, would enhance the negative bending capacity of this regions, while providing a higher vertical clearance for the traffic under the bridge.

Ronald (2001) presented the use of in-span splices coupled with post-tensioning in construction of bridges in Florida that reached span length of 97.5 m. Multi-stages post-tensioning was used to provide continuity through the splices and the deck. He provided details of using two stages of PT: the first stage would be applied on girder segments to make a continuous beam for the weight of the deck; and the second stage were applied after casting the deck to provide residual compressive stress in the deck and avoid cracking. Ronald discussed that by using multiple stage PT, the spacing between girder lines would increase. Therefore, the cost of post-tensioning could be compensated by fewer girder lines, as well as removal of piers, due to longer spans.

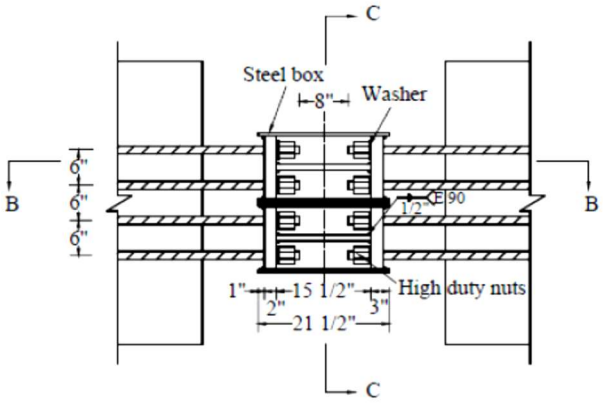

(a) Plan view of steel box connection with threaded bars (Sun, 2004)

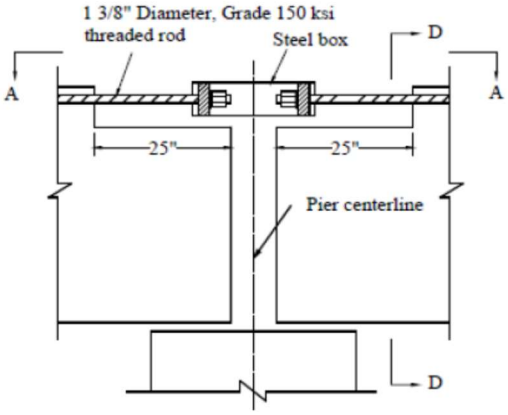

(b) Side elevation of steel box connection with threaded bars (Sun, 2004)

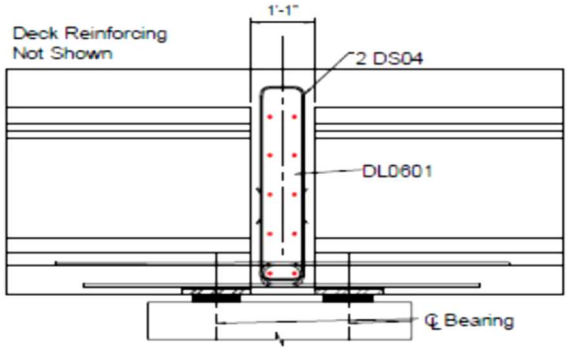

(c) Extended strands in connection with 90-degree bend (Newhouse et al., 2005)

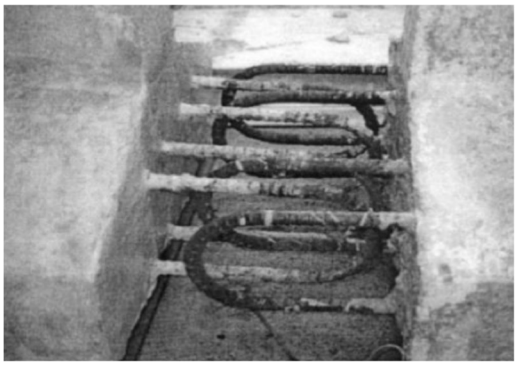

(d) #6 bend bars extended in connection (Newhouse et al., 2005)

Fig. 2.7 Different proposed connection details for on-pier splicing.

* 1 ft =0.3048 m, 1 in. = 25.4 mm

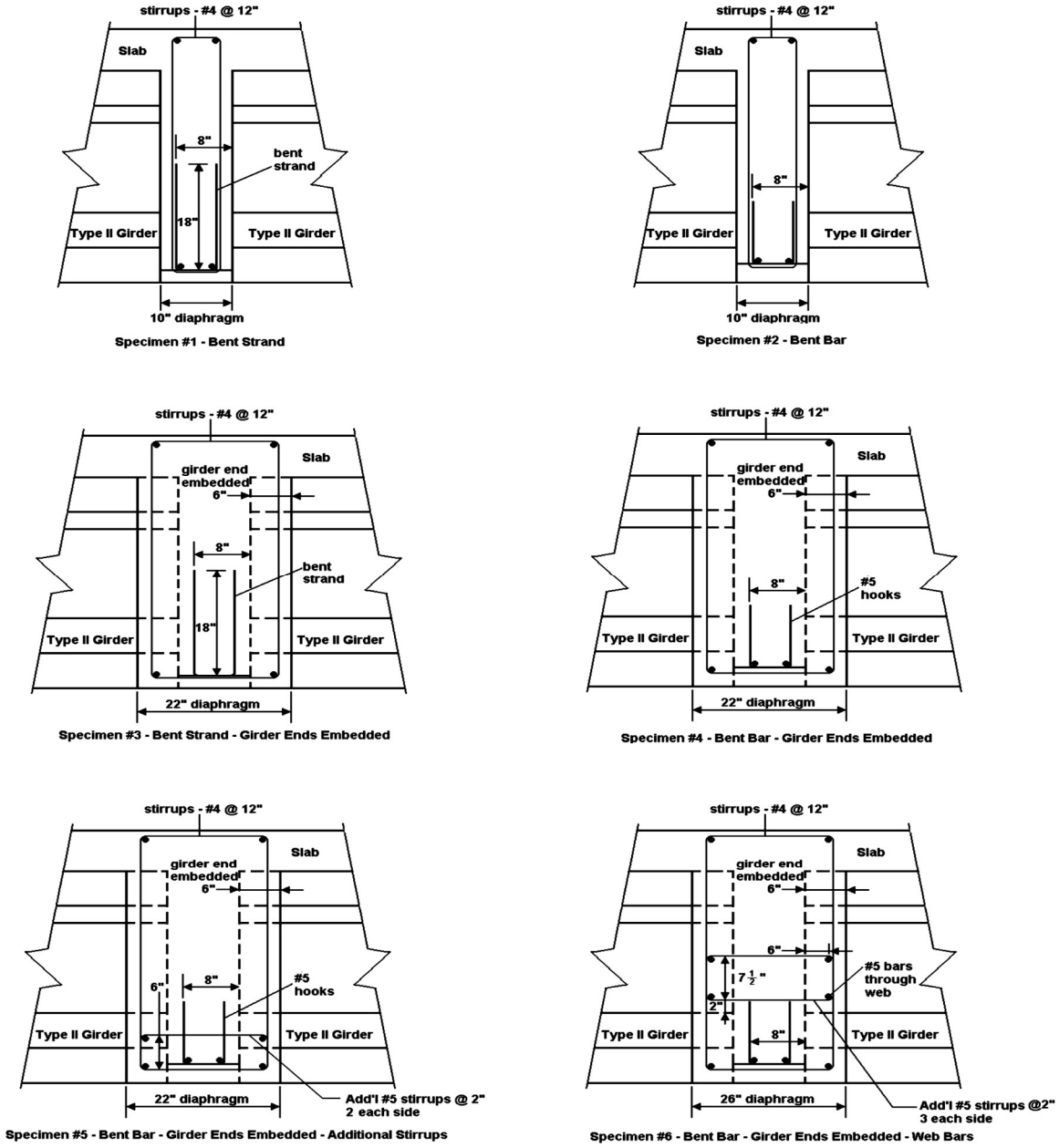

Fig. 2.8 Six different connection details for on-pier splicing (Dimmerling et al., 2005).

* 1 ft =0.3048 m, 1 in. = 25.4 mm

Tadros and Sun (2003) developed a design to reach a span length of 91.4 m using in-span splicing and partially shored construction. They mentioned that critical demands occurred at pier segments; hence either a deeper section should be used along the length of the bridge, or haunched segments should be provided for over pier segments. Instead of having a single haunched segment, Tadros and Sun proposed using a haunch block (as shown in Fig. 2.9) to minimize the fabrication costs, as well as maintaining the weight of each segment within acceptable limits. Based on their study, for a three span continuous bridge, a span configuration of $0.8L - L - 0.8L$ was proposed as the most efficient configurations. They suggested that the optimal dimensions for the haunch block were $0.5L$ long, and $0.9h$ high; where L was the main span length and h was the height of the prismatic section.

Through the research investigation described in NCHRP Report 517 (Castrodale and White 2004), standard details and design examples for long-span continuous precast, prestressed concrete bridge girders were presented. From the results of the trial designs, changes and enhancements to the AASHTO code were also proposed. Castrodale and White (2004) also confirmed that precast, prestressed concrete bridge girders are rarely used for spans exceeding 48.8 m due to material limitations, hauling size and weight limitations, and lack of design aids for the design of long span prestressed concrete girders. Castrodale and White (2004) identified around 250 proven, spliced, precast, prestressed concrete girder bridges built around the nation but the experience and information on these job specific projects was not available widely for use on similar proposed bridge projects.

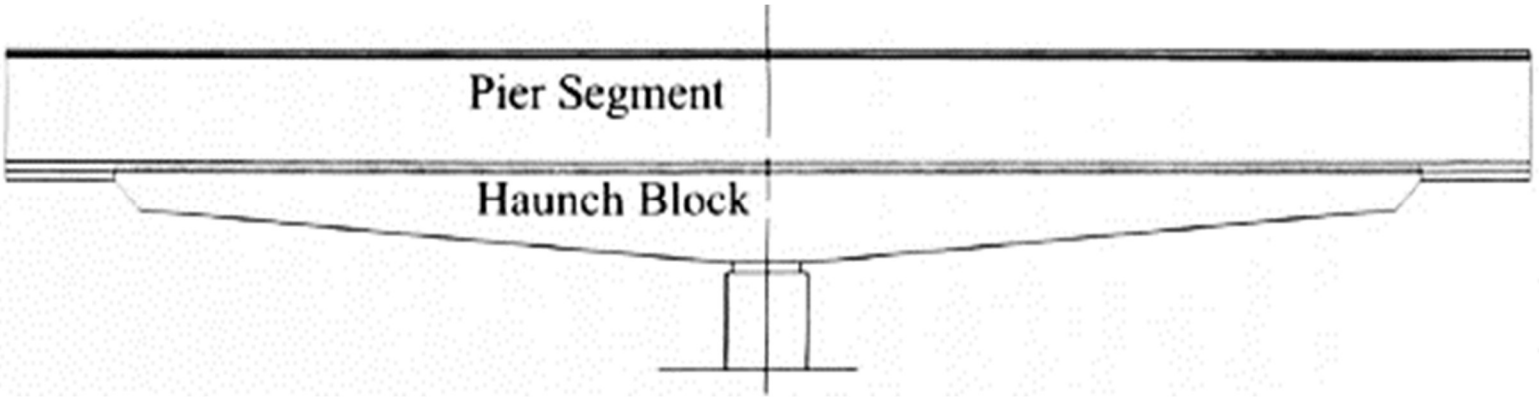

Fig. 2.9 Use of Haunch Block for over-pier segment (Tadros and Sun, 2003)

The NCHRP 517 report provided the needed documentation on all the known technologies for extending the span lengths of the prestressed concrete girders to 91.3 m. From the assessment of all these methodologies, this study concluded that the splicing of precast, prestressed concrete girders has the potential to significantly increase the span lengths without the need to change the section to more expensive segmental box girder alternatives.

Castrodale and White (2004) identified the use of splicing with multiple means and locations within the span, and provided a list of similarities and differences between spliced girder construction and segmental bridge construction. NCHRP Report 517 summarized both material-related options and design enhancements for extending the span lengths. The material-related options included:

- High strength concrete.
- Specified density concrete.
- Increased strand size.
- Increased strand strength.
- Decks of composite materials.

The alternatives for design enhancements included:

- Modifying standard girder sections.
- Creating new standard girder sections.
- Modifying strand pattern or utilization.
- Enhancing structural systems.

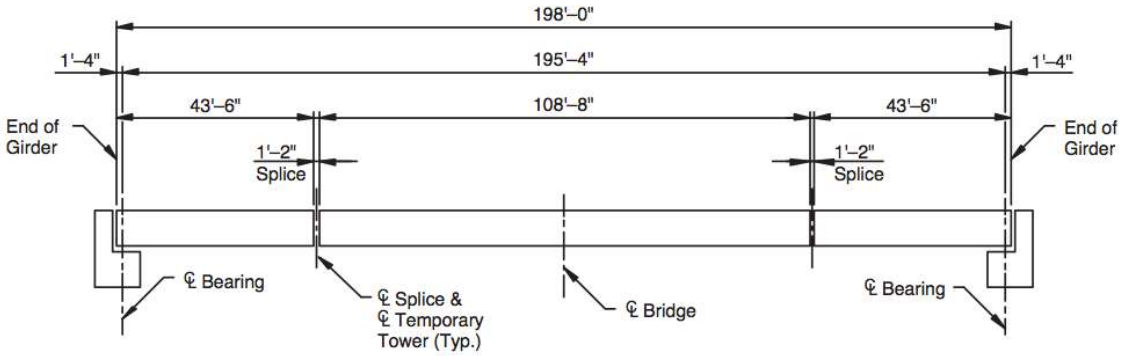

(a) Simply supported bridge with two in-span splices.

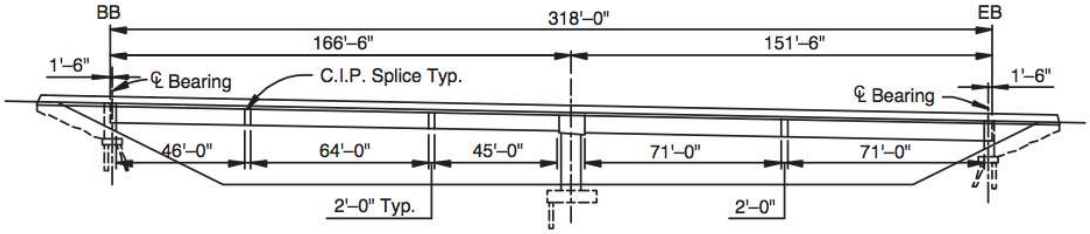

(b) Two-span continuous bridge with one splice within each span.

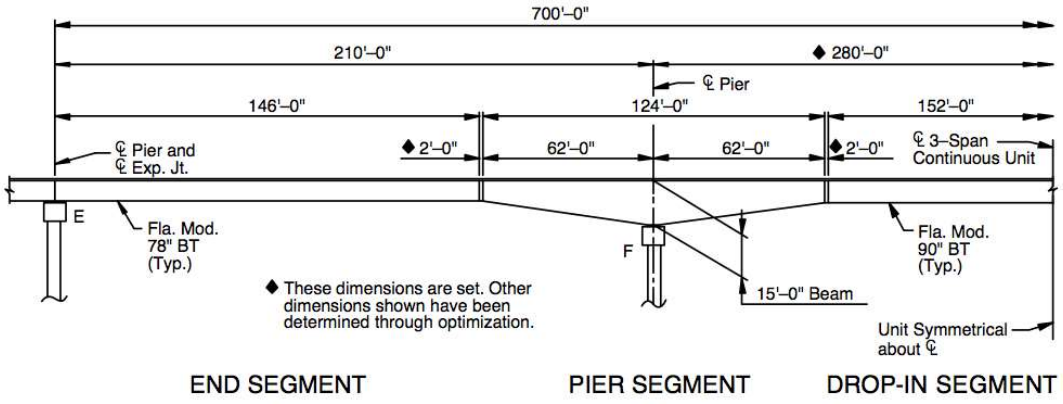

(c) Three-span continuous bridge with two splices within the central span and one splice in each of the side spans.

Fig. 2.10 Design examples from NCHRP Report 517 (Castrodale and White 2004).

* 1 ft =0.3048 m, 1 in. = 25.4 mm

The multiple design examples presented in NCHRP Report 517 provide guidance for comparing the potential alternatives to extend span lengths. The three examples present how to design a single span spliced PCI BT-96 Girder, a two-span spliced U-Beam Girder, and a continuous three-span girder. The three examples have in-span splices. Fig. 2.10 presents the three examples.

Hueste et al. (2011) studied the construction feasibility of continuous prestressed concrete girder bridges through two focus group meetings consisting of: (1) precasters that are responsible for casting the girder units and transporting them to the construction site, and (2) general bridge contractors that are concerned with the erection, splicing, and PT of the girder components, as well as the construction of the remainder of the bridge including the deck and substructure. In addition, members of the TxDOT project monitoring committee attended the meetings. The main findings from the focus group meetings are provided below. More details of the focus group results, as well as conducted preliminary bridge designs are presented in the FHWA 0-6651-1 Report by Hueste et al. (2011). Findings from the precasters are:

- In general, all the precasting plants are well equipped to handle fabricating a variety of over-pier, end, and drop-in segments.
- Increasing the span length results in an increase in the weight of precast elements. Precautions should be taken so that the weight does not exceed 890 kN considering transportation limits.
- The desirable limits for I-girder segments is length around 42.7 m, weight around 890 kN, and depth around 3 m. For the U-girder shapes, the precasters

recommended limiting the segment length to 40 m considering weight limits for transportation.

- The recommended maximum span length for a spliced girder bridge is around 80 m, considering the stability issues of long-span drop-in segments and deep haunched over-pier segments.
- Use of a constant standard girder section depth for over-pier segments is preferred over the haunched girders to avoid issues related to high initial cost of fabrication, stability issues during transportation, and lifting weight issues onsite.
- There are no concerns with widening the webs to resolve the issue of maximum shear demand at the supports. The webs can be widened by increasing the space between the forms, which will result in widened top and bottom flanges of the girder section. It is a one-time cost to purchase a new soffit. Standardizing the precast elements will help reduce the overall cost.
- Fabricating end segments with thickened ends is not an issue. The length of an end block is typically 3–4.5 m.
- Of the four different types of splice connections discussed (ranging from fully reinforced/non-prestressed to fully prestressed with PT), the precasters preferred partially prestressed spliced connection details.
- Some discussion was held about using longer precast panels over the supports with longitudinal prestressing. The precasters indicated that this should be no problem. Findings from the contractors are:

- The proposed bridge system provides another alternative to steel girder bridges, especially in coastal areas where corrosion of steel bridges is an issue.
- Experienced contractors prefer to limit the span range for the continuous spliced girders to approximately ± 76 m to 82 m.
- Unshored construction (no shore towers) is preferred because it saves significant time during construction and reduces the construction costs. Often the required footprint is not available to place shore towers.
- Using fewer girders increases cost competitiveness of bridges.
- The contractors suggested that keeping the girder weights as low as possible and adopting repetitive girder details aid in better pricing by the precasters.
- Contractors prefer the constant web depth option for the haunched girders because it is easy to fabricate and has more stability.
- Contractors noted that the option of two separate girder segments spliced over the pier provides flexibility of splicing the girder segments within the span on the ground before lifting them into place on site. This is a preferred option because no temporary shoring is required on site. However, issues related to the weight of the whole assembly and the size of the equipment in lifting and placing the spliced girder segments are anticipated.
- The main issue noted during erection of the girders is the lateral stability of the girder segments due to wind.
- The partially prestressed connection detail was the most preferred with respect to on-site construction due to its relative constructability.

- Contractors prefer having two design options for bid: one with a standard precast concrete girder shape and one with a steel plate girder.
- The quality control process is more complex for the proposed bridge system.
- Sequencing of the CIP concrete and PT operations are needed up front.
- Contractors look at both schedule and economy to determine the best option.

Additional findings from the designer/owner (TxDOT) are:

- TxDOT engineers noted that this bridge type would compete well with shorter span segmental bridges. They also indicated that they are not using steel girder bridges along the coast, and the proposed bridge type would not compete with just steel girder bridges.
- It would be useful to consider various design options using life-cycle cost analysis. TxDOT is just now starting to use life-cycle cost analysis. Traditionally, initial cost has been used to evaluate design options.
- TxDOT engineers preferred solutions where the fascia girder did not possess a widened end at the drop-in splice location. This sentiment was to preserve the clean lines of the side elevation of the bridge deck. However, this presents a significant challenge, with the resulting narrow web solution it is not possible to terminate and anchor the PT; the PT must run continuously through the splice. One option is retain the same profile as the girder only for the outside face of the fascia girder. The inside face of the fascia girder, along with both faces of the interior girders, could be widened at the ends adjacent to the splices to accommodate the PT anchorage.

Alawneh (2013) suggested a spliced girder system as a replacement for traditionally curved bridges. In the proposed system, shorter straight segments were precast and spliced with an angle to simulate a horizontal curve with a 60 m radius. Two specimens were constructed: one with I-girder segments and one adopting tub girder segments. Two splices were used to reach a test span of 183 m. One of the splices matched the girder cross section, while the other splice was cast as a thickened section, adopting the thickness of the bottom flange for the thickness of the web. A single point load was applied at midspan. Flexural failure occurred in the midspan away from the splice zones.

Moore et al. (2014), in a recent companion study sponsored by TxDOT, compared the shear behavior of post-tensioned girders for steel ducts and plastic ducts. Through 11 tests with different duct materials and diameters and different web widths, the effect of duct material and duct diameter-to-web width ratio was investigated. They concluded that all the specimens failed due to localized crushing of the web concrete at the level of the PT ducts and duct material had little effect on the shear resistance of the web. On the other hand, the duct diameter-to-web width ratio played a significant role in the shear resistance of the web. The shear stress at ultimate changed from $0.2\ f'_c$ for the lowest duct diameter-to-web width ratio of 0.33 to $0.16\ f'_c$ for the ratio of 0.44.

Williams et al. (2015), as a follow up on the previous study, presented their study through Report FHWA 0-6652-2. In this research, they provided the results of a survey with a focus on duct material, shear interface detail, longitudinal reinforcement detailing, and length of splice. The report includes the results of an experimental program on shear behavior of in-span splices. Use of plastic ducts and a 230 mm web provided a critical

shear section in the web that violated the allowable limits of 0.4 in the AASHTO LRFD Specifications for the duct diameter-to-web width ratio. For this case, the ratio was 0.44, which was 10 percent higher than the AASHTO limit.

Williams et al. (2015) tested two specimens under the same loading setup. Concrete strength and prestressing levels were the same for both specimens. The major difference between the two specimens was the amount of longitudinal interface reinforcement at the splice connections. Specimen 1 included 14-#4 straight bars in the flanges passing through the splice region and 6-#3 straight bars passing through the web. In Specimen 2, 8-#6 straight bars passed through the bottom flange, 8-#5 bars were considered for the top flange, and the same 6-#3 bars were passed through the web. Specimen 2, with the higher amount of longitudinal reinforcement, showed about 5 percent more loading capacity and 20 percent more deflection before failure.

Based on the experimental data, Williams et al. (2015) proposed modifications to the AASHTO LRFD Specifications for the general shear design procedure. In the modifications, they included an additional strength reduction factor to account for the reduction in the shear resistance due to the presence of PT ducts.

2.4 MOMENT-CURVATURE ANALYSIS OF PRESTRESSED CONCRETE BEAMS

Burns (1964) presented the moment-curvature relationships for beam sections with both mild steel and prestressing strands. His proposed method was based on changing the strain in the top fiber, and changing the level of neutral axis to reach equilibrium. For post-cracking moment, the compression force was determined by area integration of the stress-

strain diagram. The results of the proposed method were verified by the experimental data from a study conducted at the University of Illinois.

While the proposed method by Burns (1964) provided an elegant method of analysis for prestressed concrete sections, it did not consider the capacity of the concrete in tension. Also, as the proposed method did not use the fiber method of analysis, it was not easy to modify for irregular or more detailed cross sections. Also, the material property assignment was not quite feasible for a composite section with different material properties. He did not consider the initial curvature in the analysis and the resulting graphs started at the origin, rather than with a shift due to initial prestressing effects. Also, experimental results suggested that the proposed method does not accurately capture the post-cracking behavior of the sections for higher levels of prestressing.

Shushkewich (1990) developed an analytical approach to formulate the moment-curvature relationships for the common beam shapes under both axial and prestress loads. Analysis was conducted in two phases for both cracked and uncracked sections. Material properties and section properties were generalized for different practical shapes such as I-beams, T-beams, inverted T-beams, rectangular, box, and channel section. Stresses and strains were formulated based on the position of the neutral axis and the effect of axial load and prestress loads were considered in the sections. This paper proposed a valuable relationship for the flexural analysis of these specific types of cross sections. However, due to its point-wise formulation, it lacked a numerical approach to calculate the continuous graph of moment-curvature behavior. The approach also did not include the capacity of the concrete in tension. Long and complicated formulas were proposed to

determine the section properties of cracked concrete. However, by considering the initial curvature of the beam due to prestressing, the proposed method provided a rational relationship for prestressed and partially prestressed beams.

Rodrigues-Gutierrez and Aristizabal-Ochoa (2001) presented an interactive moment-force-curvature analysis for reinforced and prestressed concrete beams under biaxial bending and axial loads. Their study was the completion of their previous work by considering tension stiffening, creep and shrinkage effects. They proposed a unique approach to calculate the compression and tension force in concrete. Unlike other common approach, where fiber elements parallel to the neutral axis are considered to calculate the force in concrete, the proposed approach considered trapezoidal elements perpendicular to neutral axis. Gauss's integral method was used to calculate the effective concrete force in each of the trapezoids. After formulating the equilibrium in terms of numerical calculations, they developed a flowchart to carry out the analysis. The proposed model was verified with previously conducted experimental data.

While the research proposed by Rodrigues-Gutierrez and Aristizabal-Ochoa (2001) presented an elegant method of flexural analysis, it did not count for multiple stages of prestressing. The presented diagrams in the paper did not count for the initial curvature of prestressing. The proposed trapezoidal element method was quite innovative, but encounters computation difficulties for more irregular cross-sections. The accurate modeling of material including the non-brittle tension failure of concrete makes the model more refined.

Oehlers et al. (2011) presented a study on the effect of partial interaction of concrete and reinforcement on flexural behavior of reinforced concrete beams. Oehlers et al. discussed that the conventional moment-curvature analysis relied on the full bond of concrete and reinforcement, which enabled the researchers to develop three-dimensional behavior of the beams based on two-dimensional moment-curvature analysis. The paper provided a systematic literature review on previous studies of related components of moment-curvature analysis, including empirical models for hinge length and moment of inertia, discrete crack rotation, deformation of RC beams, strain profiles, tension stiffening, hinges and energy absorption, and moment redistribution. In this research, they studied the bond-slip behavior for different types of rebar and provided graphs of strain profile for variation of bar diameter. While this insightful study provided valuable understandings of different parameters contributing to flexural behavior, its applicability was limited to reinforced concrete.

Pirayeh Gar et al. (2012) presented a study where the effects of tension stiffening were included in the moment-curvature analysis of prestressed concrete beams. After presenting a closed-form solution for moment-curvature behavior of prestressed concrete members, they formulated the tension stiffening effect in prestressed concrete. A parametric study was carried out to investigate the effects of prestressing ratio on moment-curvature behavior and neutral axis location. They conclude that for fully prestressed concrete the effect of tension stiffening on flexural behavior of the beams at the service limit states is negligible. However, they suggest that as the level of prestressing decreases the effect of tension stiffening becomes more pronounced.

2.5 SHEAR-FLEXURE INTERACTION: EFFECT OF DIAGONAL CRACKS

Rosenblueth (1965) criticized the traditional moment-curvature analysis for not being able to capture the descending branches in the generalized force-deformation behavior of the concrete beams. He discussed that crushing of concrete in compression is not necessarily a material failure mechanism, but rather a structural instability which leads to lower flexural capacity. He proposed a moment-rotation approach to study the post-cracking behavior of beams in the hinge regions, by introducing the "contaminated" region" which is affected by yielding of material, as well as diagonal cracks. The proposed model did not consider the contribution of concrete in tension. Even though the paper mentions the effect of diagonal 45° cracks in formation of the hinge zone, it does not consider the effect of shear-flexure interaction in the flexural behavior of the beam.

Russo et al. (1991) studied the effect of shear-flexure interaction by investigating the ratio of the flexural capacity of the reinforced concrete beams under both shear and flexure and beams under pure flexure (M_u/M_{ft}). The research proposed that the ratio of M_u/M_{ft} depends mainly on the shear span (a/d) and the longitudinal reinforcement ratio (ρ). By referring to a previous experimental study by Kani (1966), they developed a 3-D diagram relating the moment ratio to reinforcement ratio and the shear span. The concept of "valley of diagonal failure" was introduced that illustrated the situation where for a specific combination of shear span and reinforcement ratio, the moment ratio (M_u/M_{ft}) reduced from 1 to a lowest of 0.6. The effect of shear span was studied as the indicator of which shear transfer mechanism governs: the beam action or the arch action. Based on their plastic theory solution (lower bound solution), they proposed that for a shear span

between 1 to 7, the moment ratio could possibly be lower than 1, depending on the reinforcement ratio. The study proposed a valuable ratio to take into account the effects of shear-flexure interaction.

Recupero et al. (2003 and 2005) presented a thorough study on shear-flexure interaction of reinforced and prestressed concrete beams. They divided the height of the section in three separate layers: top flange and top portion of the web that carries the compression, central section of the web that resists shear by having a diagonal compression stress field, and the bottom flange and lower part of the web that is in tension. Based on the proposed model, the equilibrium equations were set and formulated. The interaction diagrams were created for different transverse reinforcement ratios as a function of longitudinal reinforcement and the angle of prestressing tendons. The results of the proposed method were verified by experimental data and the model was used to design a prestressed concrete bridge. While the proposed method effectively modelled the interaction of shear and flexure, it did not account for the interaction of the shear carried by the concrete and transverse reinforcement. Also, the model did not consider the effect of diagonal cracks and the fact that at ultimate, the concrete does not carry shear between cracks.

Cladera et al. (2015) extended their study on shear-flexure interaction of rectangular reinforced concrete sections to account for the effect of flanges for I-shaped and T-shaped beams. They noticed that as the flange width increases, the shear capacity of the section increases up to 25%. They deduced that in contrary to design code provisions, compression concrete does contribute to the shear strength of the beams. Based

on their study, in reinforced concrete beams subjected to both shear and flexure, the main zone of failure includes a vertical flexural crack in the tension zone, accompanied by primary and secondary diagonal cracks in the web area. According to their observation, cracking and damage concentrated around the critical shear crack, which is the diagonal crack that merges with the main flexural crack. As shown in Fig. 2.11, the shear capacity was divided in four components of compression chord, aggregate interlock, dowel effect of longitudinal reinforcement, and the transverse reinforcement contribution. Each component was empirically formulated, so that the aggregate interlock effect decreases as crack widths grow.

While the proposed model by Cladera et al. (2015) was an original study on the cases where the shear-flexure interaction leads to a compression failure in the top flange, rather than a strut failure or other types of shear failure, it strongly depended on the experimental observations and empirical equations. The proposed model did not consider the tension capacity of the concrete, but it effectively considered the effect of widened cracks in reduction of aggregate interlock. The proposed model gives a good insight for analysis of the thin webbed concrete beams for reinforced concrete, but does not include the effects of prestressing axial loads.

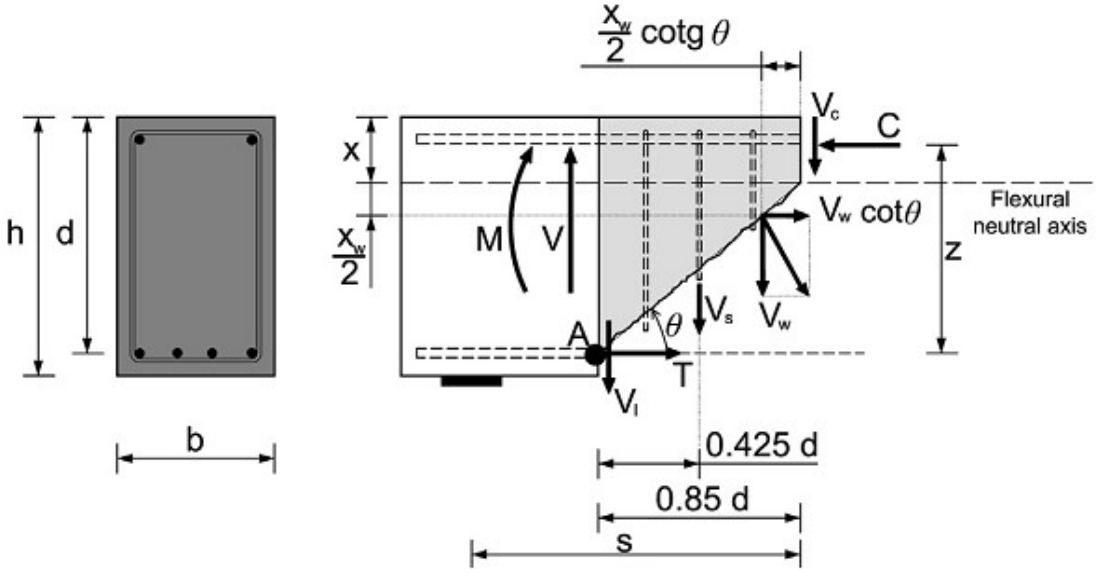

(a) Shear components on the critical shear crack

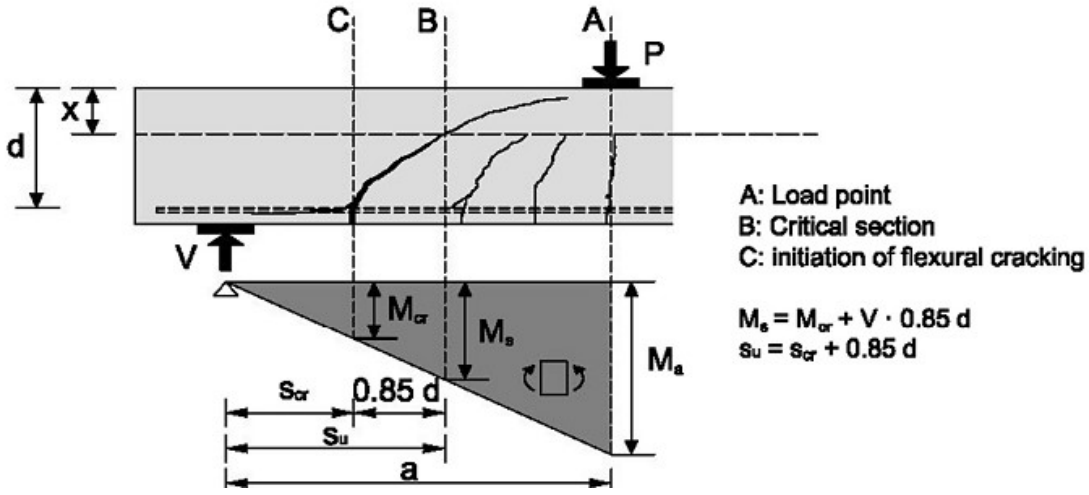

(a) Scheme of shear-flexure cracks and critical section

Fig. 2.11 Shear-flexure interaction and modeling of shear transfer mechanism (Cladera et al., 2015).

2.6 STRUT AND TIE MODELING OF CONCRETE BEAMS

2.6.1 Plastic Truss Modeling

Ritter (1899) and Morsch (1901) developed a truss model to independently incorporate the effect of transverse reinforcement in shear resistance of reinforced concrete. They proposed that diagonal cracks in a reinforced concrete beam form in 45° angles, and assumed that no shear is transferred perpendicular to this crack. Based on this assumption, they proposed an equivalent truss for concrete beams, where concrete carried the compression in the compression chord and struts, while reinforcement provided capacity in the tension chords and vertical ties.

Marti (1985) proposed that strut-and-tie modeling (STM) can be effective in capturing the behavior of D-regions. They defined D-regions (disturbed regions) in locations with a discontinuity in geometry and material or regions in proximity of applied concentrated loads. Schlaich et al. (1987) defined two general D-regions and B-regions (Bernoulli regions or Beam regions) and recommended a strut-and-tie modeling for design and analysis of D-regions where uncracked elastic properties of concrete were adopted for the truss model.

Sritharan and Ingham (2003) developed a force transfer method (FTM) for analysis and behavior assessment of bridge joints subjected to seismic forces. While they used the same principles as STM, they specifically developed the model for seismic behavior of the joints and incorporated the effect of post-tensioning.

Collins et al. (2008) conducted a research using a large database of many previous experiments on shear behavior of concrete beams in North America, Based on the results,

they proposed that the current ACI provisions could be unconservative for deep beams or higher reinforcement ratios. This research showed that use of STM without considering compatibility and other interdependent failure mechanisms (such as shear-flexure interaction, anchorage, and bond), could lead to unsafe designs.

2.6.2 Compatibility Truss Modeling

Paulay (1971a) studied the shear-flexure interaction, different shear resistance mechanisms, deformation characteristics, and elastic stiffness of thin web beams. He proposed a variable angle truss model incorporating the truss action, arch action, flexural rotation, and beam elongation. The proposed truss action was composed of concrete compression members and reinforcement as tension ties and tension chord. The arch action would transfer the shear in deep beams through a single concrete truss directing from the point of applied load to the support. In the proposed model, the flexural rotation pertained to the rotation of the member due to strains in reinforcement, and the beam elongation referred to the total elongation of the reinforcement. The proposed method took into account the compatibility of strains through considering the four abovementioned components.

Kim and Mander (1999; 2000a; 2000b; 2005; 2007) through an extensive study proposed a comprehensive compatibility-based truss model to analyze the shear-flexure interaction of D-regions and derived as analytic solution for deformation of cracked elastic concrete elements. They proposed both constant and variable angle truss models, where the former was applicable for analysis of B-regions and the latter was proposed for analysis of D-regions. Cyclic Inelastic Strut-Tie (CIST) modeling was proposed as an

analytical tool for modeling the shear-flexure interaction of reinforced concrete using a general-purposed inelastic computer software.

To et al. (2001) developed a nonlinear strut-and-tie computational tool to assess the behavior of rectangular reinforced concrete beam with transverse hoops subjected to monolithic loading. This research was further extended to model the behavior of circular columns (To et al 2002). The proposed model was verified through large-scale experimental data and a portal frame experiment. The proposed model was further developed to incorporate the effect of cyclic loading (To et al. 2003).

Zhu et al. (2003) developed a compatibility-based STM to predict the width of diagonal cracks at re-entrant corners of structures, such as dapped ends of bridge girders and ledges of inverted T bent caps. The proposed model adopted a stiffness based approach and modeled the flexural and shear behavior of inverted T bent caps thorough two separate sub-trusses. The researchers illustrated how displacement compatibility could be used to combine the sub-trusses and capture the overall behavior of the structure.

Scott et al. (2012a; 2012b) formulated a compatibility strut and tie model to provide nonlinear force-deformation behavior for reinforced concrete beams. Following the proposed model by Kim and Mander (1999; 2005; 2007) they considered a variable angle truss model. The researchers proposed modifications to the effective concrete modulus of elasticity compression chord to adjust for stress distribution in the compression chords as well as the actual beam depth compared to the truss model. The stress-strain constitutive model of concrete was modified accordingly to capture the inelastic deformation of the beam for the uncracked section, cracked elastic and cracked plastic

spectrum. They also developed an arch action model and proposed methods to proportion the concrete for truss action and arch action. The proposed method was then implemented for analysis of a reinforced concrete bent cap and the results were validated by experimental data.

Karthik et al. (2016) proposed a displacement-based compatibility STM to capture the behavior of reinforced concrete structures subjected to monolithic and cyclic loading. They proposed methods to analyze the structure in displacement control and produce the ductile behavior of the structures. The proposed method was implemented in modeling of a bridge bent cap and the results were verified by the experimental data.

Karthik (2015) investigated the structural performance of bridge elements subjected to ASR and DEF deterioration. He proposed a coupled Compatibility STM (CSTM) through which the truss action and arch actions were modeled separately and the overall behavior of the element was assessed through displacement compatibility. The proposed method was applied to several structural elements and the results were verified by experimental data.

2.7 RESEARCH QUESTION ARISING

Based on the literature review on design and construction of continuous prestressed concrete girder bridges, the following research questions arise:

Question 1: *Given that the standard slab-on-I-girder bridges are one of the most economical options in Texas and US, is it possible to adopt a splicing method*

to effectively double the span length of existing prestressed concrete girder bridges and reach span lengths of up to 90 m?

Precast concrete girder bridges have been widely designed for short to medium spans as an economical, aesthetic, reliable solution with potential for rapid construction. Previous designs and studies suggest that they have the potential to become a competent economical solution for bridges spanning from 45 to 90 m. There are 250 bridges that have adopted in-span splicing technique to achieve longer spans, but since the design and construction procedures are not widely available to engineers, this art has been localized in certain states. Also, construction issues and optimum construction sequences have not been fully covered in previous studies.

Standardization of design on construction of this class of bridge can be the starting point of popularizing it. This research will review and implement a consistent load-balancing approach for continuous bridge girder design. An outline of some construction sequences and issues will be given.

Question 2: *How do the splice and the structure perform under normal service loads? And what is the performance of the structure and more specifically the splices, if they were overloaded to failure?*

Extensive previous studies have assessed the performance of on-pier splices. But there remains a lack of experimental investigations on the service and ultimate performance of the in-span splices. In order to make this type of bridge construction more accepted, a comprehensive experimental investigation is required to demonstrate and evaluate the performance of splices for different load combinations. In this research, a full scale 21.6

m long super-assemblage specimen is tested to failure. The specimen is an abstraction from a prototype bridge design of a continuous three span bridge with overall span lengths of 58-73-58 m. Three splices were located in the specimen which facilitated the assessment of splice performance for different combinations of positive and negative moments and shear.

Question 3: *Given that in-span splices are generally located in the regions with minimal flexural demands, the shear demands at splice locations remain high. Therefore, how would the interaction of shear and flexure in splice regions be affected by the post-cracking performance of in-span splices?*

Due to lower flexural capacity compared to precast girder segments, splices are general placed in locations with minimal flexural demands. But such regions with reduced flexural demand such as the inflection points for dead load, are still required to carry substantial live load moments and high shear arising from both dead and live loads. Considering lower flexural capacity of splices, the flexure may remain potentially the critical state for the splice regions. On the other hand, narrow-webbed sections are prone to cracking if the structure is overloaded under high applied shear force, particularly near the strength limit state. The combination of these two conditions would rise another potential critical state where shear-flexure interaction can affect the post-cracking performance of splices.

Question 4: *Given that due to the narrow web of I-girder sections, and the existence of post-tensioning ducts within the web, high inelastic shear deformations are*

possible: How well can existing flexural and shear methods of analysis predict the performance of a spliced girder bridge?

Conventional methods of deflection analysis are usually based on Euler-Bernoulli flexural deflection and do not consider shear deformation of structures. While more accurate analyses may consider Timoshenko beam deflection theory, it too is unable to precisely predict the deflection of locally loaded (disturbed) zones.

On the other hand, many researchers have proposed methods to study the shear capacity of the prestressed concrete members, where shear is the predominant state of failure. Considering low flexural capacity of the in-span spices, it is expected that an interaction of shear and flexure create a new critical state where the effect of diagonal cracks and vertical cracks merge and create a complex inclined critical section. While strut-and-tie modeling or finite element analysis can accurately model this behavior, they require advanced analytical capabilities that are time consuming to implement, especially in a design office setting.

In this research, a generalized moment-curvature analysis is proposed to capture the flexural behavior of a composite section with multiple stages of prestressing and construction loads. Then, this method is modified through re-formulation of equilibrium to capture the effect of shear-flexure interaction as a single integrated analysis tool.

Question 5: *Considering that splice regions are prone to diagonal cracks, how would the design demands of this regions and the adjacent girder sections be affected?*

As the diagonal crack emerges in the web area, it can shift the compression side of the critical section to the adjacent girder section. This phenomenon that is called compression

shift will reduce the capacity and ductility of the splice and the adjacent sections. To compensate for this capacity reduction, the design demands of such regions must be increased.

3 COMPARATIVE DESIGNS FOR IN-SPAN SPLICED LONG SPAN PRESTRESSED CONCRETE GIRDER BRIDGES

3.1 CHAPTER REVIEW

In-span splicing of prestressed concrete girders to extend the span length of bridges have been effectively used in several recent bridge construction projects. However, the extent and limitation of such a construction approach has not been systematically explored. While the most effective approach for long span girder construction use draped parabolic prestressing tendons, which in turn balance the dead loads, successive application of prestressing at different stages of modular construction can potentially lead to locked-in deflections if not properly dealt with by design. This chapter revisits bridge design that uses in-span splicing and construction approaches to provide a more in-depth understanding of design options and construction approaches for spliced prestressed concrete girder bridges. The concept of "deflection balancing" is introduced and the associated near optimum prestress design is formulated. Three methods of construction are investigated that benefit from in-span splices: shored, partially shored, and span-by-span (heavy-lift) construction. Design procedures and optimal construction sequences are compared and contrasted, and discussed in detail. A prototype bridge geometry is designed for all three methods of construction, and the results compared and conclusions drawn.

3.2 INTRODUCTION

As urban areas become increasingly congested, topological and environmental issues demand the extension of bridge spans with minimal traffic interference and construction

time. Therefore, modular construction methods need to be considered wherever possible so that individual bridge segments may be pre-fabricated and hauled to the construction site.

Among different design options, precast prestressed concrete girder bridges have been widely used as an economical solution for modular construction. Historically, precast girder bridges have been mostly designed as simply supported spans. A height limitation of 3 m is common due to vertical curves on roadways, especially at railway crossings. The weight of individual units is generally limited to 900 kN, but may be increased under exceptional circumstances to about 1000 kN. Weight limitations are based on axle arrangements of the transporting equipment, crane capacity limitations, and the limitations of existing bridge capacity on the chosen transportation route. Therefore, the hauling limitation for length, height, and weight of individual segments impose an upper bound in the range of 45 to 50 m depending on the nature of the roads between the precasting plant and the bridge construction site.

Since the first use of prestressed concrete girder bridges in the 1950s, they have been widely used for short to medium span lengths up to 50 m nationwide. During recent decades, several investigations have been conducted to propose methods to extend the span length capability of prestressed concrete girder bridges. Most of these methods suggest modifying the design approaches, improving material properties, changing the shape and size of girder sections, and splicing the girders over the pier to provide continuity (Bishop, 1962, Miller et al., 2004, Newhouse et al., 2005, Tadros, 2007, and Sun, 2004).

While each of the aforementioned methods have contributed to improvement of the design and performance of these bridges over time, the effect on increasing the span length has been marginal due to the weight and length limitations on the individual precast segments. On the other hand, an in-span splicing technique may be used to effectively double the span length of concrete girder bridges to about 90 m (Hueste, et al., 2011).

To obtain optimum vehicle ride quality of post-tensioned continuous spliced girder bridges, individual girder segments must (ideally) be straight prior to splicing to avoid locked-in deflections, upon application of post-tensioning. Overall, for prestressed concrete girders, there should be co-equal dual aims:

(1) to balance the loads so that under self-weight, there is a uniaxial state of stress in the continuous deck-girder system. This essentially negates the possibility of ongoing creep displacements;

(2) to minimize deflections under self-weight so that the best possible ride quality can be provided.

The concept of load balancing is not new; it was first championed by T.Y. Lin in his seminal text book (Lin, 1955) for both simply supported and continuous (indeterminate) structures. Generally, load balancing is best achieved by using draped post-tensioned (PT) prestress. However, it is often neither expedient nor economical to use PT for individual girders. Pretensioning is generally the economic solution for precast portions of a structure. If not properly managed by design, permanent deflection can be "locked in" during construction. For example, it is well known that constant eccentric pretensioned prestress can provide substantial upward camber to a beam. This needs to be

dealt with by providing a variable thickness haunch height beneath the topping slab to level the deck system. In this chapter, it is demonstrated how straight and harped pretensioned prestress systems may be designed to minimize the deflection under girder self-weight. This is particularly important for continuous bridges where in-span splices are adopted.

By implementing in-span splices, the individual precast girder segments can be effectively spliced to each other and form a longer span. However, design, analysis, and performance of in-span spliced precast prestressed concrete girder bridges are dependent on the method and sequence of construction (Hueste et al., 2016). Historically, there has been two broadly different construction methods adopted to extend the span length of a concrete girder bridge by using in-span splices: (i) shored construction; and (ii) unshored (or partially shored) construction.

For shored construction, temporary shore towers are provided to support each of the individual segments and to seat the formwork for the in-span splices. Lin et al. (1968), Abdol-Karim and Tadros (1995), and Fitzgerald and Stelmack (1996) have presented some practical examples of shored construction. Shored construction is associated with a simpler design and leading to more dependable construction practice. However, the versatility of shored construction is limited to those projects were the terrain and transportation constraints allow for placement of shore towers for all spans.

To provide a more versatile option, where wide rivers and valleys exist, or congested traffic areas do not permit disturbance in the main long span region, partially shored construction is often used as it eliminates the shore towers within the main span.

While this method of construction can be more cost-effective by decreasing the number of shore towers, it may require the use of haunched sections over the pier. Such a structural modification can substantially increase the project cost. Jenssen and Spaans (1992), Roland (2001), and Caroland et al. (1992) have provided details of construction aspects for partially shored constructed bridges.

As effective as the in-span splicing technique may be in providing a variety of construction methods, few examples of this class of extended span bridge exist. NCHRP 517 Report (Castrodale and White, 2004) provided a list of all bridges that have adopted in-span splices in prestressed concrete girder bridges. A review of the location of such bridges reveals that application of this technique has been localized in certain states, such as Florida, Washington, and Colorado, as a lack of infrastructure, fabrication equipment, and standard design procedures restrain the applicability for this class of continuous long-span girder bridge construction.

This chapter first introduces the concept of deflection minimization for precast beam portions that may be components of a longer structure. It then goes on to illustrate some of the issues that may affect the design by presenting the results of three contrasting methods to construct continuous long span slab-on-spliced prestressed girder bridges that are designed for (i) shored construction; (ii) partially shored construction; and (iii) unshored span-by-span heavy-lift construction of spliced girders. The concept of in-span splicing is revisited and three possible construction methods are introduced. Then, the design procedure for each type of construction is illustrated along with design and analysis recommendations. An optimum construction sequence is proposed for each of the three

methods of construction to minimize the effect of construction loads on the final layout of prestressing. Finally, a prototype bridge is designed for the three methods of construction and the results of prestressed solutions are compared with one another.

3.3 DEFLECTION BALANCING THROUGH PRETENSIONING

While for a simply supported beam, load balancing of self-weight with parabolically draped post-tensioned tendons can theoretically perfectly balance loads and negate self-weight deflections. This dual objective is not achievable with either straight or harped pretensioned strands. Harped pretensioning may partially balance the dead load as well as deflection, but generally, a design using pretensioned prestress aims to ensure stresses are maintained within allowable limits; deflections are disregarded by design, but are dealt with during construction. Pretensioned girders generally results in an upward camber, which are later dealt with by using variable depth haunches to form the deck slab. For simply supported bridges, this is not really a critical issue, as over time creep may reduce the upward camber.

For slab-on-spliced prestressed girder bridges, a mixture of both pretensioned and PT prestressing systems are used in any given design. Pretensioning is applied to individual girders to ensure sufficient strength exists for transportation and erection. Then, after casting the splices, PT is applied to provide continuity as well as strength through the cast-in-place splices. Given that for continuous bridges, PT is applied after casting the splices, if individual segments have excessive unbalanced deflections, they inevitably lead to “locked-in” deflection upon application of PT. Such locked-in deflections due to

construction may marginally reduce over time but will generally lead to ride quality problems.

Furthermore, when the individual segments are spliced in the construction sites, means of continuity, such as post-tensioning ducts, shear transfer hangers, top and bottom reinforcement, etc. need to be aligned properly to avoid construction issues. If individual girders have unbalanced deflection—generally upward camber or non-square girder ends— alignment difficulties arise, both with deck slab and PT ducts.

Therefore, when building a complex bridge system over multiple phases, load balancing alone is not sufficient as a design objective; a second and perhaps higher objective is needed: to balance deflections as well as practicable through all stages of construction.

For pretensioning design of a prestressed post-tensioned concrete girder bridge, two main goals are considered with regard to deflection balancing: (i) zero slope at member ends and (ii) minimal deflections throughout the member. The former ensures feasible splicing and alignment at the ends of adjacent girders; the latter aims to minimize the locked-in deflections as well as better ride quality. While both can be equally important, with eccentric pretensioning only one goal can be fully achieved.

Table 3.1 summarizes the applicability of deflection balancing for different design goals and type of pretensioning. A general relation between force and c.g.s eccentricity of the pretensioned prestress strands is defined as:

$$Fe_0 = \gamma_0 wL^2 = \gamma_0 WL \tag{3.1}$$

$$Fe_c = \gamma_c wL^2 = \gamma_c WL \tag{3.2}$$

in which F = effective prestressing force after losses; e_0 = c.g.s eccentricity at beam ends; e_c = eccentricity of c.g.s within the central span region of the beam; γ_0 = deflection balancing coefficient at the ends of the beam; γ_c = deflection balancing coefficient at mid-span of the beam; w = weight per unit load to be balanced; and $W = wL$ = total span dead weight, where L = span length.

For harped pretensioning, it can be derived that $\alpha = 0.3536$ gives the optimal solution regarding minimizing the required force to balance the self-weight (see derivation in Appendix A.3). If three equal-length units are used ($\alpha = 0.3333$), results close to the optimum solution ($\alpha = 0.3536$) may be achieved. Thus, $\alpha = 0.3333$ is used as a basis for comparative analysis for contrasting prestress layouts.

Fig. 3.1 presents the optimized solution for:

(1) *Eccentric prestress*: This is the most common form of pretensioning as it has the least costly manufacturing infrastructure.

(2) *Harped prestressed*: Harping has the effect of partially balancing loads and avoids debonding of eccentric strands.

(3) *Mixed solutions:* using both eccentric and harped prestress.

Fig. 3.1 shows the effect of different prestress solutions for deflection balancing of a simply supported beam. The three different approaches are shown in Fig. 3.1. (a), (b) and (c).

The bending moment diagrams for the prestressed solutions are presented in Fig. 3.1 (d). These are compared with the parabolic black curve representing the dead load moment diagram such that the mid-span moment is $M_D = WL/8$. Thus, the results

presented in Fig. 3.1 (d) are normalized to the maximum dead load moment (M_D) and the horizontal axis is normalized to the length of the beam (L) such that $X = xL$. The deformation profiles for the contrasting prestressing approaches for the simply supported beam under dead load alone are presented in Fig. 3.1 (e). The vertical axis is normalized to the deflection of a fixed-fixed supported beam ($WL^3/384EI$) and the horizontal axis is normalized to the length of the beam (L).

Table 3.1. Deflection balancing coefficient for eccentric and harped pretensioning

Pretensioning Type	**Main Goal**	γ_0	γ_c
Eccentric	Square Ends	0.08333 (1/12)	0.08333 (1/12)
Eccentric	Deflection Minimizing	0.01010 (1/9.9)	0.1010 (1/9.9)
Harped	Moment Balancing	0	0.125 (1/8)
Harped	Deflection Minimizing	0	0.122 (1/8.18)
Mixed	Square Ends/ Zero Mid-Span Deflection	0.00833 (1/120)	0.1125

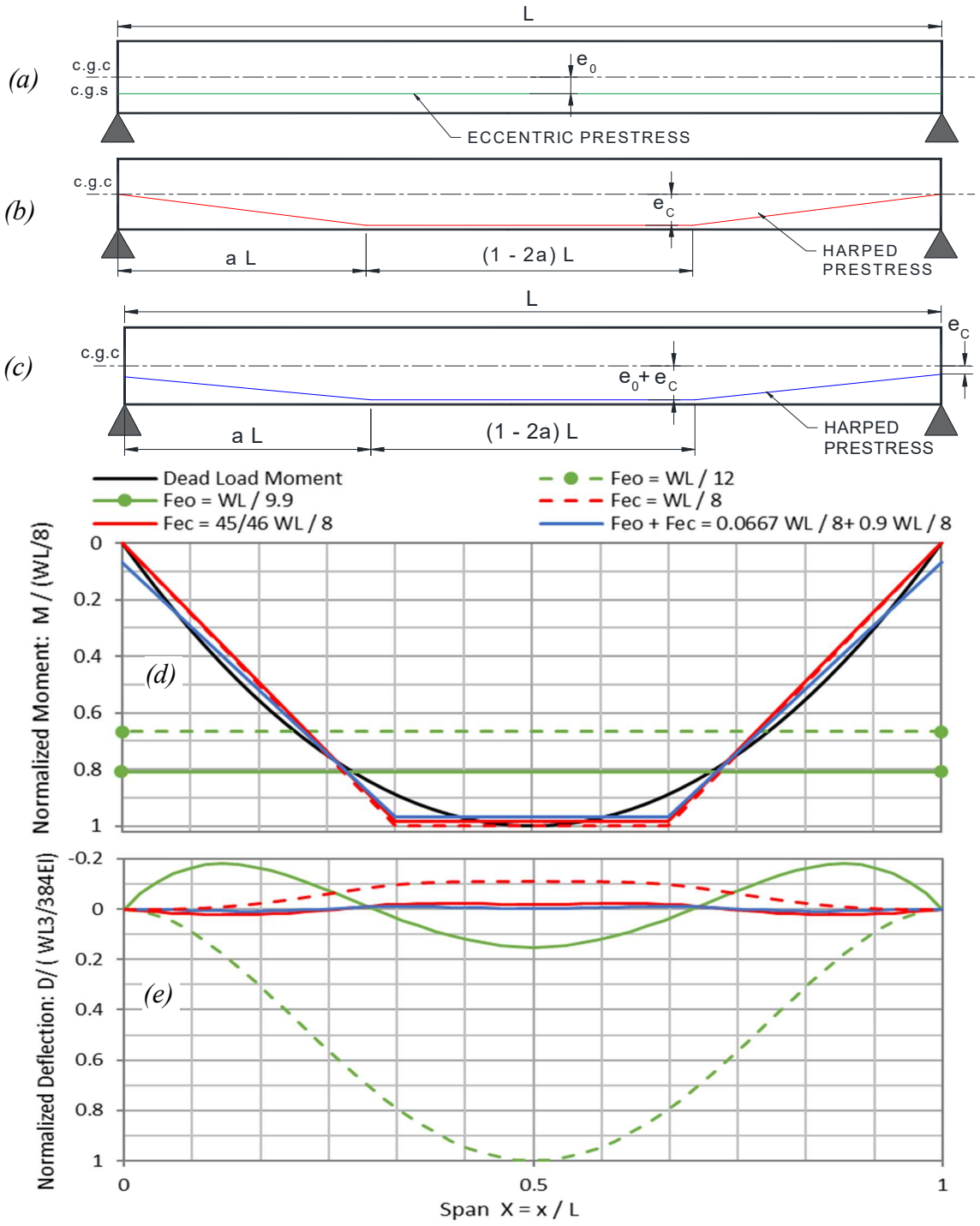

Fig. 3.1. Optimized pretensioning effects on load and deflection balancing using (a) eccentric prestress; (b) harped prestress (with concentric end condition; (c) mixed solution that uses end eccentricity (e_0) and mid-region harped eccentricity (e_c) (total mid-span eccentricity = $e_0 + e_c$); (d) resulting bending moment diagrams under dead load; and (e) deflection profiles under combined prestress and dead load.

3.3.1 Eccentric Prestress Solutions

The dashed green lines in Fig. 3.1 (d) and (e) respectively represent the normalized bending moment and normalized deflection of a simply supported beam when the eccentric prestress solution is adopted to provide square ends by adjusting the eccentricity to create fixing moment of a continuous beam: $Fe_c = WL/12$ ($\gamma_0 = 0.0833$). This solution provides zero slope at the unit ends (leading to square ends that are ideal for joining segments) but at the same time a substantial deflection remains, as only 80% of the deflection under self-weight is negated. This solution is adopted herein as the "reference" for comparison between different prestressing solutions.

The solid green lines in Fig. 3.1 (d) and (e) represent the eccentric solution when the deflections are minimized, as shown in Fig. 3.1 (b), and derived in Appendix A.3. For this solution, the eccentricity is set to $Fe_c = WL/9.9$ ($\gamma_0 = 0.1010$) and the resulting deflection is 18% of the reference. This solution provides best possible result in regard with deflection balancing, when an eccentric-only prestress solution is used.

3.3.2 Harped Prestress Solutions

In Fig. 3.1 (d) and (e) the dashed red lines represent the harped-only solution where the harped prestress is merely designed for balancing the mid-span moment ($Fe_c = WL/8, \gamma_c = 0.125$). This solution results in an upward camber along the entire length of the beam with the maximum deflection equal to 11% of the reference case (eccentric solution with square ends).

The solid red lines in Fig. 3.1 (d) and (e) represent the harped prestressing solution where the deflection is minimized. For this case, the central eccentricity is set to $Fe_c =$

$WL/8.18, \gamma_c = 0.122$. It is evident that this solution can significantly reduce the maximum deflection maximum to 3% of the reference case. Note that this harped solution is a marked improvement where the maximum deflection is reduced some 83% of the best eccentric-only prestress. Due to small deflections, the ends are also quite close to square, leading to an effective method of deflection balancing, using a harped-only solution.

3.3.3 Mixed Prestress Solutions

For the design of modular precast bridge span segments, it may be difficult to use either pure eccentric or true harped solutions. Therefore, it may be inevitable that some form of mixed solution is necessary. Fig. 3.1 (c) shows the prestress layout of a harped solution with some end eccentricity. Given that for this solution, two variables may be adjusted (γ_0 and γ_c), many viable mixed solutions are possible.

The blue lines in Fig. 3.1 (d) and (e) represent the optimal mixed prestress solution. The prestressing is optimized to provide square ends as well as zero mid-span deflection by setting $Fe_0 = WL/120 (\gamma_0 = 0.0083)$ and $Fe_c = 0.9WL/8$ ($\gamma_c = 0.1125$) as derived in Appendix A.3. As shown in Fig. 3.1 (e), the maximum deflection of mixed solution is only 2% of the reference solution where eccentric prestress is designed for square segment ends. The layout of deflection essentially suggests an essentially pare deflection balancing using pretensioning alone. This solution may be adopted as the best pretensioned alternative of using the draped parabolic PT solution.

3.4 METHODS OF CONSTRUCTION

3.4.1 Scope

Figure 3.2 presents three methods of construction: shored, partially shored and heavy-lift construction. These Methods are discussed for slab-on-spliced prestressed concrete girder bridges and the design and performance objective are compared and contrasted. While the first two methods have been successfully adopted by past practice to reach span lengths up to 90 m, the heavy-lift construction is not as popular for concrete girder bridges and in rare cases, the concept is used for single span bridges. A few examples of span-by-span construction are presented by Nicholls and Prussack (1997) and Nikzad et al. (2006), where two in-span splices were considered at third points of the bridge to construct a longer span.

3.4.2 Shored Construction

Fig. 3.2 (a) depicts a general form of shored construction for in-span spliced concrete girder bridges. In this method of construction, the shore towers are placed at the location of the in-span splices and individual girder segments are supported at their ends over the temporary towers. The existence of shore towers reduces the construction load demands, particularly for the on-pier segments. Therefore, prismatic sections generally suffice for this method of construction.

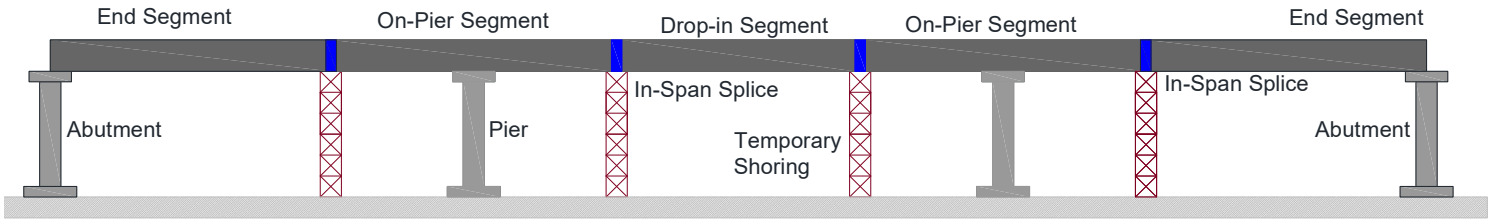

(a) Shored Construction

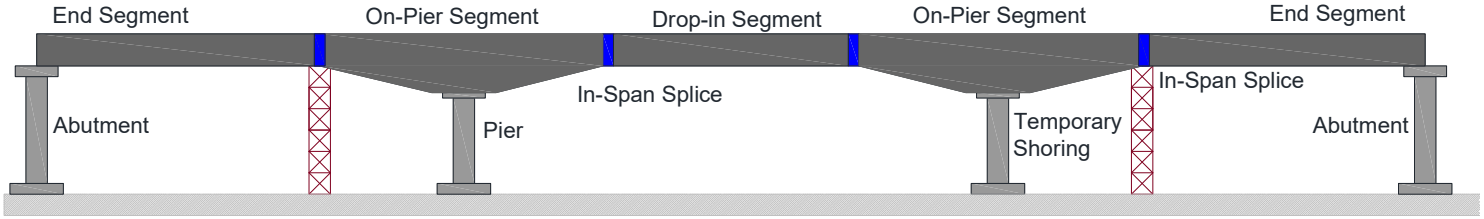

(b) Partially Shored Construction

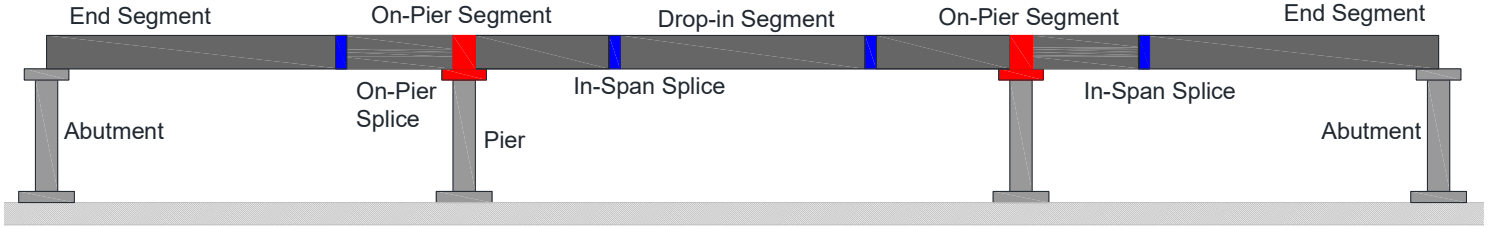

(c) Span-by-span (heavy Lift) Construction

Fig 3.2. Different methods of girder erection for continuous slab-on-I-girder prestressed concrete bridges requiring in-span splicing

In the shored method of construction, the individual girder segments are pretensioned at the precast plant. Stage I PT may be applied to the individual segments either at the precast plant or at the construction site. Following the placement of the girder on the shore towers, the splices are cast, then the Stage II PT is placed within the ducts and lightly tensioned for further construction safety/strength but not fully stressed.

The Stage II PT is fully stressed after all the girder segments are erected and splices and the concrete deck cast. In this way, the maximum amount of prestress is able to be applied to the deck slab, thereby improving its longevity particularly in the negative moment regions over the supports. Fig. 3.3 presents the construction sequence and typical I-shaped cross-sections associated with shored construction. Fig. 3.3 (a) to (g) illustrates the proposed optimum construction sequence for this type of construction. Fig. 3.3 (h) and (i) depicts an example of the precast girder cross section and composite girder and deck section for shored construction using a modified Tx70 girder section. It is shown that sections are mainly prismatic, and the eccentricity of the draped Stage II PT varies along the length of the beam with the lowest point at mid-span and the highest point over the interior piers, as expected for load balancing.

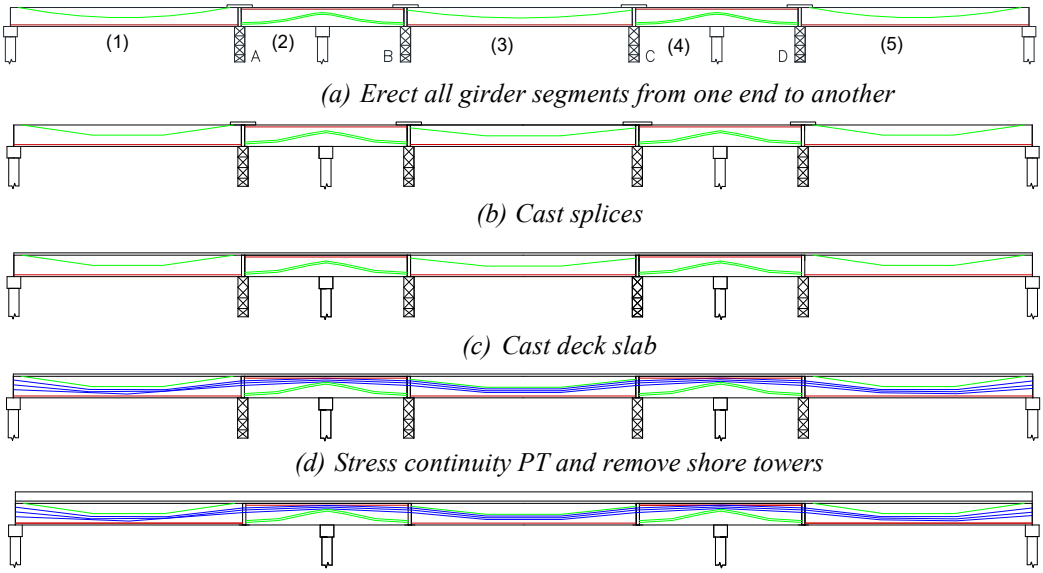

(a) Erect all girder segments from one end to another

(b) Cast splices

(c) Cast deck slab

(d) Stress continuity PT and remove shore towers

(e) Cast barriers and open bridge to traffic

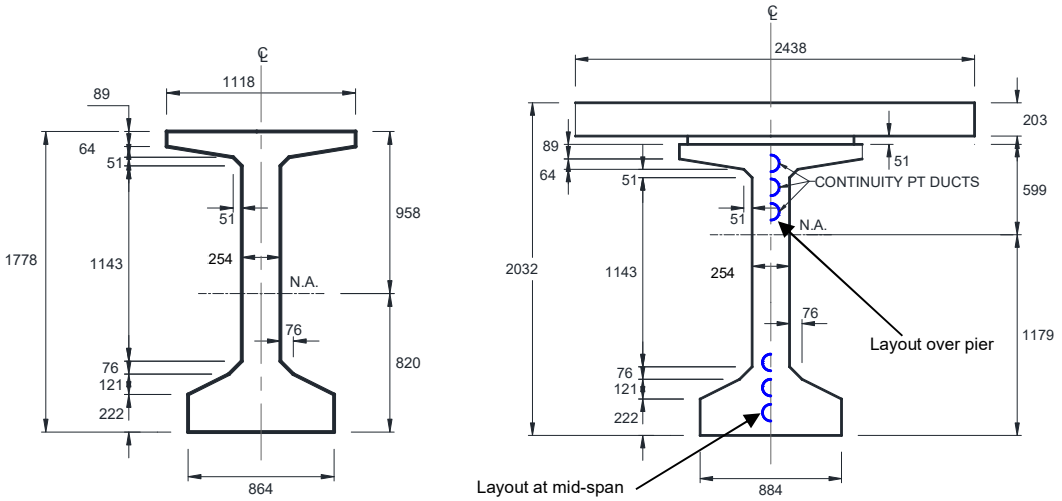

(f) Modified Tx70 *(g) Modified Tx70 Composite*

Fig 3.3. Shored construction sequence.

The load balancing approach is effectively applied for this method to ensure a load balanced superstructure, where the deflection is also successfully balanced. The main steps of such a design approach are summarized here. A detailed design example with associated AASHTO LRFD Bridge Design Specifications is provided in Appendix A.

1- Design pretensioning and Stage I PT to balance the dead weight of the girders. Pretensioning may be designed for transportation, to make sure all sections are tension-free. Some of the strands may be debonded at the ends to avoid overstressing of these sections.

   a. Calculate the PT force to balance the self-weight of the girders:

$$F = \frac{W_g L_g}{8 e_c} \tag{3.3}$$

   where W_g is the self-weight of the precast concrete girders; L_g is the length of each precast segment; and e_c is the central drape of the Stage I PT tendons. The maximum drape is restricted by the space needed for the Stage II PT tendons; two or three ducts with a center to center distance of 150 mm for Stage II PT gives a proper estimate for the available drape for Stage I PT.

2- Design the Stage II PT by assuming that the drape in the main span is equal to the overall height of the superstructure:

$$F = \frac{w_{d+si} {L_2}^2}{8H} \tag{3.4}$$

where $H = e_{c2} =$ height of the superstructure including girder, haunch, and the deck slab; L_2 =length of the main span; and w_{d+si}= uniform load due to deck

weight plus the superimposed dead load. Having the same force for all spans, the maximum drape of the back-span may be calculated using:

$$\frac{e_{c1}}{e_{c2}} = \left(\frac{L_1}{L_2}\right)^2 \tag{3.5}$$

where e_{c1} = tendon drape in back span (1); e_{c2} = tendon drape in main span (2); L_1 = length of back span; and L_2 = length of main span.

3- Check stresses for critical locations, namely, location of maximum positive moment of each span, at the splices, and over the piers. For higher span-to-depth ratios, compression may become critical in the bottom flange of the pier section, or at top flange of the mid-span. For such cases, supplemental compression reinforcement is recommended to increase the ductility.

4- Calculate the flexural demand for the strength limit state, and check the abovementioned sections to ensure they have sufficient nominal moment capacity.

5- Check that the deflection of the superstructure due to live load is within the allowable limits. Most of the deflection due to dead load is balanced by post-tensioning. If the deflection due to dead load is greater than allowed values, increase the force of Stage I PT or Stage II PT up to 15% and return to step 1b or 2.

6- Design shear based on the AASHTO LRFD Design Specifications. If the shear strength is not satisfied, use a deeper section, or widen the section. return to 1.

7- Design the splice detail for flexural and shear demands. Check the shear transfer capacity of the interface between the CIP splice and the adjacent precast girders.

Provide sufficient mild steel (or local pretressing) in the top flange of the splices, as these sections are prone to cracking when the deck concrete is being cast.

Based on the proposed design and the case studies by Parchure (2013), compression in the bottom flange of the girder is one of the critical states that needs to be addressed. In this case, the supplemental compression reinforcement can enhance the compression capacity of the bottom flange.

Shored construction provides the most reliable and easy-to-construct design option, as sufficient supports are provided during the construction. In addition, using the standard girder sections keeps the fabrication of the segments at the lowest possible cost. However, the fabrication, transportation and material cost of the shore towers may offset such economies if the falsework is not readily available to the contractor. This method of construction is restricted to the projects where the condition of the construction site allows the use of shore towers for all spans.

3.4.3 Partially Shored Construction

Fig. 3.2 (b) presents the general form of partially shored construction. The main difference between this method and shored construction is the elimination of the shore towers within the main span regions. This method is suitable for those cases where topological, environmental or transportation concerns do not allow use of shore towers in the main span.

In this method of construction, the end segments are first erected over the abutment and the shore towers in back-span to provide a counterweight for the drop-in segments in the main span region. Then, the on-pier segments are erected over the piers and the shore

towers in the back span and are connected to end segments with strongbacks, or tied down to foundation for stability upon erection of drop-in segments. Finally, the drop-in segments are placed and supported at the end of the cantilevered on-pier segments with strongbacks or Cazaly hangers (Caroland, et al., 1992). The detailed optimum sequence of construction and a typical cross section for the partially shored construction is presented in Fig. 3.4. Fig. 3.4 (a) to (g) depicts the sequence of construction. Fig. 3.4 (h) and (i) depict the typical cross section showing that generally haunched sections are used for pier segments. Similar to shred construction, the use of continuous beam design leads to a draped PT tendon profile where the eccentricity of the PT ducts is lowest at mid-span and highest the over interior piers.

In partially shored construction, the pretensioning strands are designed to carry the self-weight of the segments. In addition to that, the pretensioning of the on-pier segment is designed to carry half of the weight of the drop-in segment. Stage I PT is applied as continuity PT after all the segments are erected and the splices are cast. Stage II PT is stressed after the deck is cast to balance the dead weight of the deck and superimposed dead loads.

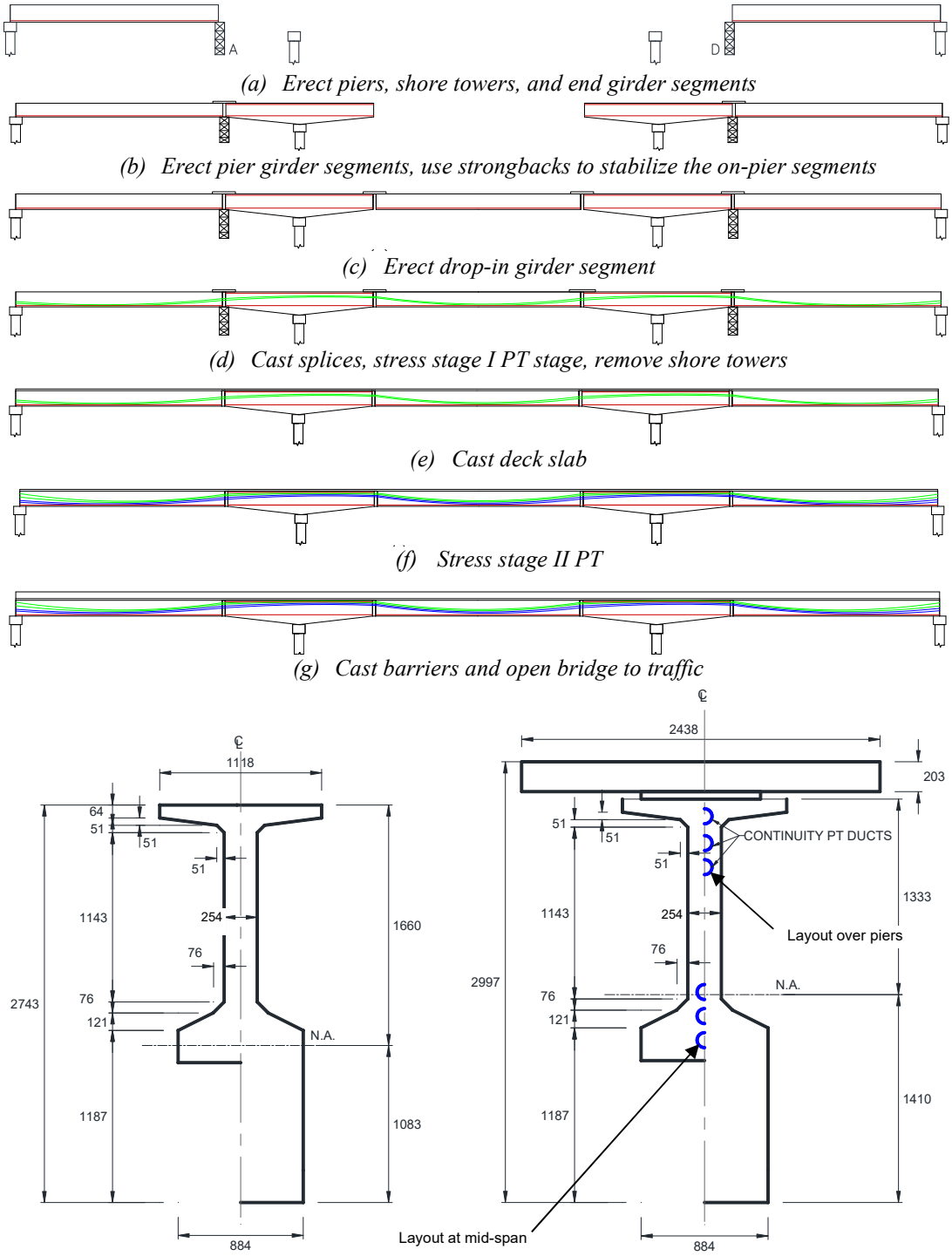

Fig 3.4. Sequence of construction with shore towers in back-span only.

The load balancing approach can be effectively used to create a constant state of compressive stress in the sections. However, care must be taken in the control of the deflections: given that only pretensioning is applied to individual girders, it must be designed to minimize deflections as discussed in previous section. The main steps of the design for partially shored construction are outlined as follows:

1- Design pretensioning to maintain a tension-free state at all sections of the precast girders. Pretensioning may be designed for anticipated loads during transportation, to make sure all sections are tension-free. Pretensioning of the on-pier segment must be designed for the self-weight and half of the weight of the drop-in segment.

2- Design Stage I PT for load balancing of the girders under girder self-weight. The PT force may be calculated based on a preliminary assumption of e = height of the superstructure:

$$F = \frac{W_g L_2}{8H} \tag{3.6}$$

where H =height of the superstructure from soffit of girder to top of the deck; L_2 =length of the main span; and W_g= weight of the prismatic girder segments. Having the same force for all spans, the maximum drape of the back-span may be calculated using Eq. (3.5).

3- Design Stage II PT to balance the dead weight of the deck and superimposed dead loads. Eq. (3.4) and (3.5) can be used to design the force and drape of the Stage II PT.

4- Check stresses for critical locations, namely, at the maximum positive moment location of each span, at each splice, and over piers where negative moment is maximum.

5- Calculate flexural demand for the strength limit state, and check the abovementioned sections to confirm that there is sufficient nominal capacity.

6- Check the deflections of the superstructure for dead loads. If deflection due to dead load is greater than allowed values per AASHTO specifications, increase the force Stage I PT or Stage II PT up to 15% and return to 2 or 3.

7- Design shear based on AASHTO specifications. If V_c is not satisfied, consider using a deeper section, or widen the section to allow a thicker web and return to step 1.

8- Design the splice detail for flexural and shear demands. Consider the maximum demands of the sections within a radius of H from the splice, where H is the height of the section.

As the flexural demands are quite high for the on-pier segments, both top and bottom pretensioning is typically required to enhance the flexural capacity of this segment. However, since the bottom flange of the on-pier segment carries significant compressive stresses when the live load is applied, the bottom pretensioning may adversely affect the performance and capacity of such sections. Therefore, it is suggested to use unbonded threadbars in the bottom flange and release them before casting the splices and running the Stage I PT. After the bars are released, the duct may be filled with grout and the threadbars will serve as compression reinforcement in the bottom flange.

In partially shored construction, the flexural demand on the pier segment are quite high and for cases. This leads to adopting haunched on-pier segments. Therefore, the cost of the fabrication for this type of construction may be somewhat more than that of shored construction. However, removal of half of the shore tower provides a better option for certain construction sites and makes this type of construction generally more economical. That said, the design, fabrication, and construction for this method is more complicated and requires a greater level of expertise.

3.4.4 Span-by-Span (Heavy Lift) Construction

Fig. 3.2 (c) shows the general form of heavy lift construction. In this method of construction, all of the shore towers are eliminated. The individual segments for each span are spliced on the ground close to the construction site and the superstructure is erected span-by-span. On-pier splices are then used to provide continuity throughout the entire length of the superstructure.

Because one of the concerns of practitioners is the possibility of deck replacement, one stage of PT is designed as external harped PT, which can be cut and replaced upon the requirement of the deck replacement. However, because additional individual segments are required in this approach, which eventually produce locked-in stresses and deflection, and as individual spans are simply supported for half of the construction process, deflections may become more critical in this method of construction. Therefore, a combined deflection balancing and load balancing approach is proposed for the prestressed design used in this construction method.

While heavy lift construction provides versatile options for the design and construction sequence, the proposed optimum sequence is illustrated in Fig. 3.5 (a) to (g). A major difference in the construction steps of this class of structure is casting and stitching of the on-pier segment. It is highly recommended to stitch the on-pier splices before casting the deck, as it effectively reduces the deflection of the superstructure. Associated design steps for the proposed construction sequence are outlined here to provide a satisfactory prestressing layout for both service and strength limit states:

1- Design top and bottom pretensioning based on deflection balancing summarized in Table 3.1.

2- Design the Stage I PT for the main span to balance deflection. Do not consider the deflection produced by the end moments, as that will be balanced later by the pier moments. Either external harped tendons or internal draped tendons may be used, although harped PT may provide more versatility for design. Design the required stiches for the on-pier splice to cancel the effect of end moments of the girders. Design the Stage II PT to balance the load of the attributed deck concrete + super imposed dead loads using Eq. (3.4) and (3.5).

3- Check stressed for critical locations, namely, middle of each span, splices, and over piers. For higher span to depth ratios, compression may become critical at bottom flange of pier section, or at top flange of mid-span. For such cases, supplemental compression reinforcement is recommended to increase the ductility.

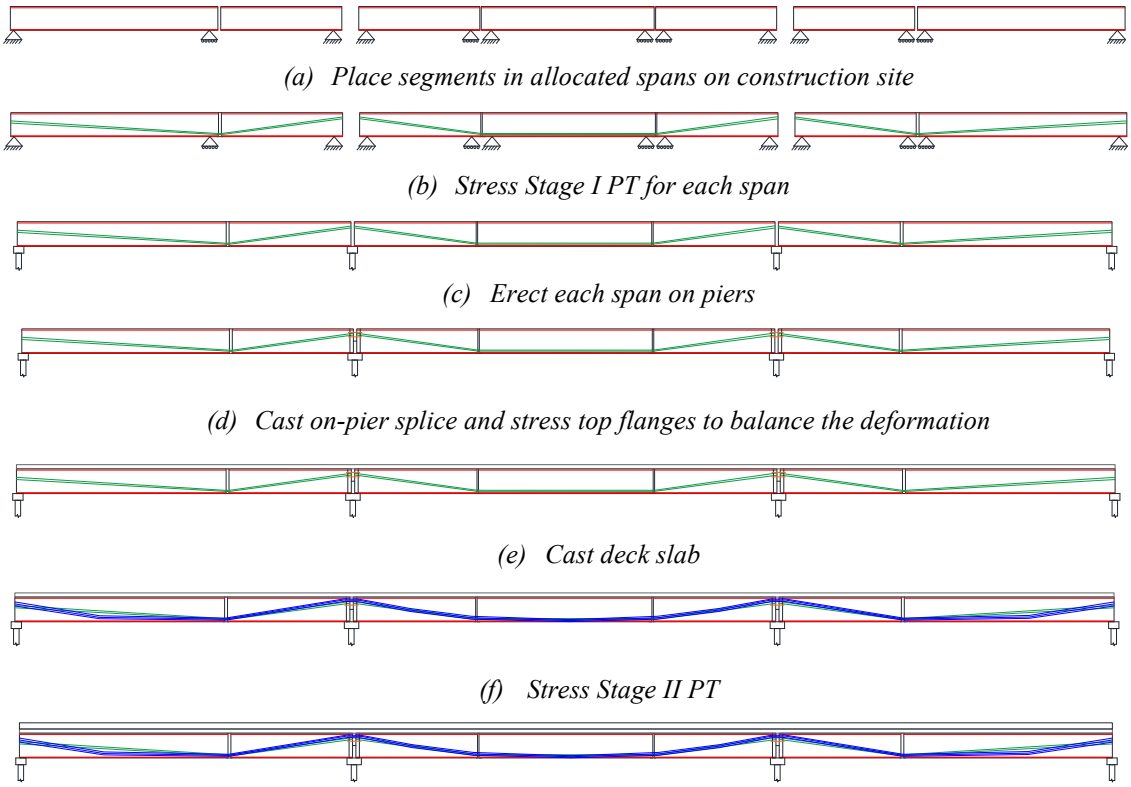

(a) Place segments in allocated spans on construction site

(b) Stress Stage I PT for each span

(c) Erect each span on piers

(d) Cast on-pier splice and stress top flanges to balance the deformation

(e) Cast deck slab

(f) Stress Stage II PT

(g) Cast barriers and open bridge to traffic

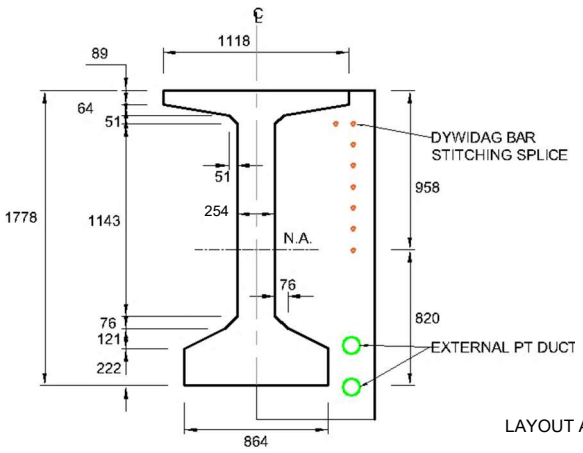

(h) Modified Tx70

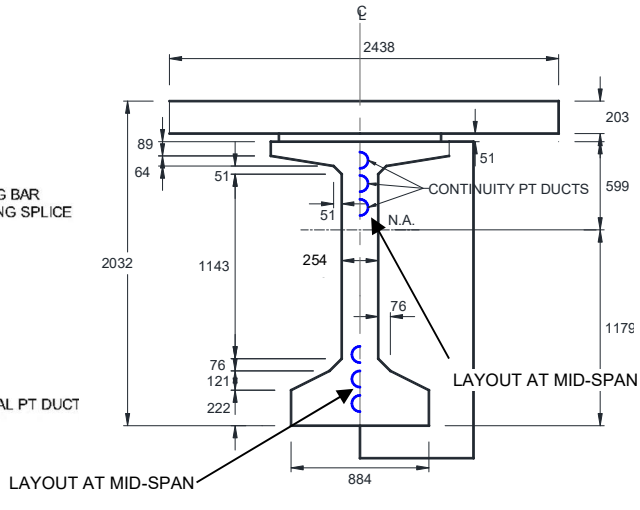

(i) Modified Tx70 Composite

Fig 3.5. Sequence of construction without shore towers (heavy lift construction).

4- Design shear based on AASHTO recommendation. If V_c is not satisfied, consider using a deeper section, or widen the section, therefore return to 1.

5- For splice design, consider the maximum demand of the sections within the radius of the depth of the section to count for the effect of compression shift.

The applied pier-moment to balance the deflection as well as the negative moments due to live load will create a substantial compressive stress in the bottom flange of the pier section. As shown in Fig. 3.5 (h) and (i), to avoid overstressing the bottom flange, a constant diaphragm is advised to run over the bent cap and provide higher compression capacity in the bottom flange of the on-pier splice.

The heavy lift construction provides an economical solution as it eliminates the requirement of the shore towers. However, it requires proper site conditions to allow for making the prestressing lines adjacent to the construction site. Also, when using harped PT, anchorages and thickened ends are required more frequently which adds to the cost of fabrication.

3.4.5 General Design and Construction Considerations

In-span splicing provides versatile design and construction options for concrete girder bridges. Three methods of construction are presented in previous sections with specific design guidance related to each method. In addition, some general considerations must be taken into account for design of in-span spliced prestressed concrete girder bridges, as outlined here:

1- For design of pretensioning and Stage I PT, two approaches can be used. In the first approach the layout of strands are designed for zero moment at the end of individual segments by adjusting the elevation of the strands so that the center of gravity of concrete ($c.g.s.$) of pretensioning plus Stage I PT at the end matches the center of gravity of steel ($c.g.c.$) of the girder section. If draped post-tensioning is used, this method provides practically zero deflection along the entire length of the segment as well as square ends.

2- As pretensioning and Stage I PT are not present in the splice regions, the splices have substantially lower flexural capacity as compared to precast girder segments. Therefore, it is strongly recommended to locate the in-span splices at the points with low flexural demands, namely close to the contraflexure points of the dead loads.

3.5 DESIGN CASE STUDY FOR THREE TYPES OF CONSTRUCTION

3.5.1 Prototype Bridge Geometry and Girder Cross Section

Fig. 3.6 presents the geometry of the prototype bridge. The elevation view shown in Fig. 3.6 (a) represents the prototype three-span continuous prestressed concrete bridge. In consultation with a TxDOT panel of engineers, precasters and contractors, the following parameters were selected for the prototype design:

- A three-span configuration using 58.5-74-58.5 m. The ratio of end span to center span length is 0.8.
- Based on transportation limitations, the length of the drop-in and end girder segments is 42.7 m, while that of on-pier segment is 30.5 m.

- Length of splice connections is 0.6 m.

Fig. 3.6 (a) shows the bridge cross-section at mid-span. The bridge has a total width of 14 m and a total roadway width of 13.5 m. The bridge superstructure consists of six modified Tx70 girders spaced 2.4 m center-to-center, with a 0.9 m overhang on each side, designed to act compositely with a 203 mm thick CIP concrete deck. The asphalt wearing surface thickness is 51 mm. TxDOT standard T501 type rails are considered in the design. Three design lanes are assumed for the purpose of design in accordance with the AASHTO LRFD Specifications (AASHTO 2014) and TxDOT Bridge Design Manual.

A modified Tx70 girder has been considered for the design. The web width of the standard Tx70 girder is increased to 254 mm to allow the placement of the PT ducts and comply with AASHTO revisions on minimum thickness to duct diameter ratio. The widened web width results in an increase in the width of the top flange to 1120 mm and of the bottom flange to 860 mm. However, for heavy lift construction, the width of the web is increased to 254 mm to enhance the shear capacity of the section, and the thickness of the top flange is increased by 50 mm to accommodate the top pretensioning and threadbars. The area of the 50 mm haunch is not considered in the calculation of the section properties and is only included in dead weight calculations.

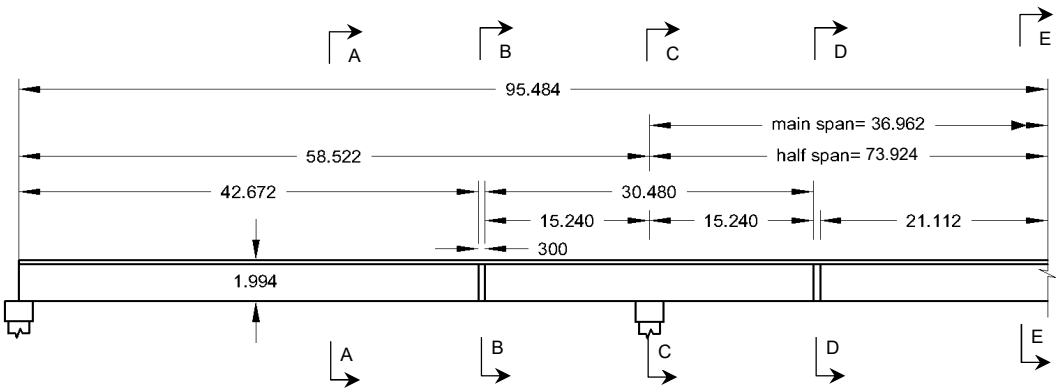

(a) Elevation of half-bridge and the location of the abstracted specimen

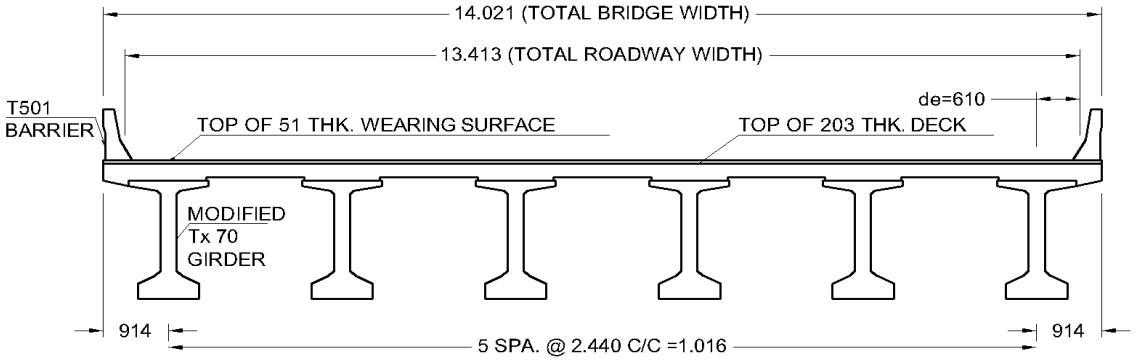

(b) Typical bridge deck cross section

Fig 3.6. Geometry and side elevation of prototype bridge with span configuration of 58.5-73.9-58.5 m (190-240-190 ft).

For shored and partially shored construction, two on-pier segments (30.5 m long), two end segments (42.7 m long), and one drop-in segment (42.7 m long) were used to comprise the 190 m bridge. However, unlike shored construction, the on-pier segments were designed as a 2.7 m maximum depth of haunched section.

For heavy lift construction, the back spans included a 21.3 m and a 36.6 m long prismatic segments, while the main span was comprised of two 21.3 m long segments and a 30.5 m long prismatic segment. For the sake of comparison with shored and partially shored construction, the 21.3 m long segments are called on-pier segments, while the 36.6 m long and 30.5 m long segments are called end segments and drop-in segments, respectively.

Table 3.2 provides the composite and non-composite uncracked elastic section properties for the prismatic and haunched modified Tx70 girder cross-section.

3.5.2 Design Assumptions and Parameters

Table 3.3 summarizes the design parameters selected for the prototype bridge. Material parameters such as concrete strength are defined based on standard practices that are followed by TxDOT throughout the state of Texas. A relative humidity of 65 percent is assumed based on the average value in Texas as specified in AASHTO LRFD Specifications (AASHTO 2014) Article 5.4.2.3. Additional parameters that describe the prestressing steel and mild steel are based on the AASHTO LRFD Specifications (AASHTO 2014). Appendix A provides detailed design procedure along with associated provisions from AASHTO LRFD Bridge Design Specifications.

Table 3.2. Section properties for modified Tx70 girders for continuous design.

Section Property	254 mm web	Composite 254 mm web	Haunched over Pier	Composite Haunched
Depth of N.A. from top of Girder, y_{top} (mm)	958	599	1660	1333
Depth of N.A. from bottom of Girder, y_{bot} (mm)	820	1179	1083	1410
Area, A (m^2)	0.713	1.04	1.55	1.89
Moment of Inertia, I_x (m^4)	0.286	0.536	1.003	1.920
Section Modulus, S_x^{top}, m^3	0.299	0.895	0.604	1.440
Section Modulus, S_x^{top}, m^3	0.349	0.455	0.926	1.362

Table 3.3. Design parameters.

Parameter		**Selected Value**
Concrete Strength at Service for Deck Slab, f'_c		28 MPa
Precast Concrete Strength at Release, f'_{ci}		45 MPa
Precast Concrete Strength at Service, f'_c		60 MPa
Coefficient of Thermal Expansion of Concrete		$6x10^{-5}$/° C
Relative Humidity		65%
Mild Steel	Yield Strength, f_y	410 MPa
	Modulus of Elasticity, E_s	200 GPa
Prestressing Steel (Low Relaxation)	Strand Diameter	15 mm
	Ultimate Tensile Strength, f_{pu}	1860 MPa
	Yield Strength, f_{py}	$0.9\,f_{pu}$
	Stress Limit at Transfer, f_{pi}	$f_{pi} \geq 0.75\,f_{pu}$
	Stress Limit at Service, f_{pe}	$f_{pe} \geq 0.8\,f_{py}$
	Modulus of Elasticity, E_p	196 GPa
	Coefficient of Friction, μ	0.25
	Wobble Coefficient	0.00065/m

The following assumptions are made for the prototype bridge design, based on FHWA 0-6651-1 report (Hueste et al. 2012):

1. Stage I and Stage II PT tendons are stressed from both the ends to minimize friction losses and to provide symmetry of stresses in the girders.
2. The PT tendons are encased in a 100 mm diameter metal duct. A maximum of 19-15 mm diameter strands can be encased in a 100 mm diameter duct. All the PT tendons are located in a single vertical plane.
3. For the design under consideration, the entire deck is cast in a single operation.
4. A CIP reinforced concrete deck of 200 mm thickness is used. A 50 mm thick haunch is assumed between the girders and the deck to accommodate construction tolerances and variation in camber.
5. A 50 mm thick asphalt wearing surface is assumed and its weight is applied as superimposed dead load.
6. The weights of the deck forms, strongbacks, temporary diaphragms, and other temporary components are minor and neglected in the design.
7. Permanent intermediate diaphragms are not considered in the design for shored and partially shored construction. Temporary intermediate diaphragms can be provided at critical locations, such as splice connections and piers for lateral stability of the girder, until the deck slab attains composite action.
8. The composite section properties are based on the transformed effective width of the composite deck slab considering the specific modulus of elasticity for the girder and deck, respectively.

9. The sign convention for the design considers tension as positive and compression as negative.

3.5.3 Pretensioning Design

Table 3.4 presents the pretensioning design for the girder segments for each of the construction methods. For pretensioning the girder segments, 15 mm diameter Grade 270 low relaxation strands with an ultimate tensile strength (f_{pu}) of 1860 MPa are considered. The initial stress in the pretensioning strands at transfer (f_{pi}) is taken as 0.75 f_{pu}, which is 1396 MPa. The force at transfer is calculated after taking the losses into account. Prestress losses of 20 percent are initially assumed in the pretensioned strands and then are further refined using AASHTO provisions.

Table 3.4. Summary of pretensioning design (0.6 in. dia. strands).

Construction Method	Strand Location	End Segment	On-Pier Segment	Drop-in Segment
Shored	Top flange	-	26	-
	Bottom flange	32	4 32 mm dia. Dywidag bars	24
Partially Shored	Top flange	-	24	-
	Bottom flange	24	20	24
Heavy Lift	Top flange	4	4	4
	Bottom flange	26	16	18

As Table 3.4 indicates, while the amount of pretensioning is comparable for shored and partially shored construction, less pretensioning is applied in heavy lift construction as only minimum amount is required for self-weight and handling. As mentioned before in heavy lift construction section, higher post-tensioning is required to balance the deflection of the bridge. Therefore, it is important to provide minimum pretensioning for this type of construction to avoid over-stressing the sections when both stages of PT are applied.

3.5.4 Stage I Post-Tensioning Design

For post-tensioning of the girder, 15 mm diameter low relaxation strands with f_{pu} of 1860 MPa are considered. The jacking force is assumed to be 0.70 f_{pu}, which is 1303 MPa. The force at transfer is calculated after taking the short-term losses into account. Prestress losses of 15 percent are assumed for the Stage I PT and then is refined using AASHTO provisions.

Table 3.5 presents the Stage I PT design for the girder segments. For shored and partially shored construction, the Stage I PT is internally draped and it is designed to balance the self-weight of the girder. For shored construction, Stage I PT is applied on individual girders, while for partially shored construction, continuous PT runs through the entire length of the bridge.

For heavy lift construction, the Stage I PT is designed to partially balance the deflection of each span. Both internal and external PT can be adopted for this stage of PT. In this design, higher amounts of PT are required for the first stage, the Stage I PT is

designed as external harped tendons. Harp points are located at the in-span splice locations and have thickened webs to provide sufficient capacity.

As predicted, the amount Stage I PT is markedly higher than that of shored and partially shored construction. The main reason is that for this type of construction, each span acts as a simply supported beam, hence the deflection is significantly higher and the required prestressing to balance that is essentially more than what is needed in the other types of construction.

3.5.5 Stage II Post-Tensioning Design

Table 3.6 shows the details for Stage II PT. Stage II PT was designed to act continuously to balance the deck and superimposed dead load and to be carried out on construction site. Internal draped tendons are considered for shored and partially shored construction. For heavy lift construction, both internal draped or external harped tendons are acceptable. For this case, because the Stage I PT was designed with external tendons, the Stage II PT was designed using internal draped tendons.

For Stage II PT, 15 mm dia. low relaxation strands with an f_{pu} of 1860 MPa are considered. The jacking force in the PT tendons was assumed to be 0.70 f_{pu}, which is 1303 MPa. The force at transfer is calculated after considering the losses. Prestress losses of 15 percent were assumed for the Stage II PT.

For heavy lift construction, in addition to Stage II PT, Dywidag bars are used to stitch the on-pier splice. It is recommended to stitch the on-pier splices before casting the deck concrete to provide continuity throughout the superstructure and limit the deflections

due to casting the deck. Eq. (6) can be used to calculate the required stitching force to balance the deflection of the superstructure.

Table 3.5. Stage I post-tensioning design.

Construction Method	End Segment (Back Span)	On-pier Segment	Drop-in Segment (Main Span)
Shored	19 (1 internal duct)	38 (2 internal ducts)	19 (1 internal duct)
Partially Shored	32 (2 internal ducts)	32 (2 internal ducts)	32 (2 internal ducts)
Heavy Lift	56 (4 external ducts)	-	60 (4 external ducts)

Table 3.6. Stage II post-tensioning design (internal tendons).

Construction Method	Drop-in Segment (Back Span	On-pier Segment	End Segment (Main Span)
Shored	57 (3 ducts)	57 (3 ducts)	57 (3 ducts)
Partially Shored	30 (2 ducts)	30 (2 ducts)	30 (2 ducts)
Heavy Lift	45 (3 ducts)	45 (3 ducts)	45 (3 ducts)

For the design case at hand, the required force for the on-pier stitching is 3530 kN, which requires 8-32 mm diameter Dywidag bars (Ggrade 150, 1034 MPa) in the top flange of the section. If only a thickened web is considered for over-pier splices, the maximum compressive stress of the section will be close to 11 MPa. Considering that the weight of the deck, Stage II PT, and the live loads significantly increases the negative bending demands of the pier segments, it is recommended to construct the on-pier splices as a constant diaphragm to avoid overstressing the bottom flange at the on-pier splices.

3.5.6 Splice Details

Splices are located at the dead load point of contraflexure ($\alpha = 0.74$ for back-span and $\alpha = 0.21$ for main span) in the prototype bridge to minimize the load demands at the splice. The length of the splice connection should be kept as small as practicable as there is no initial prestress in this region and a minimal amount of mild steel reinforcement is provided. However, the splice length should be large enough to accommodate splicing of the continuity PT tendon ducts and allow for proper vibration of the CIP concrete for the splice. The width of the splice connection is 610 mm based on recommendations in Hueste et al. (2016).

Fig. 3.7 presents a partially prestressed splice connection detail with minimal reinforcement. Mild steel reinforcement is provided in addition to continuity PT through the splice connection. The mild steel reinforcement consists of 180° bent hooked bars anchored into the adjacent girder flanges and extending into the joint. The mild steel bent bars are designed for the maximum factored design loads. The combination of PT and mild steel is expected to provide better durability and performance. Vertical reinforcement

is provided to strengthen the splice connection for shear. The integrity of the splice connection largely depends on the shear transfer mechanism at the interface of the precast girder and closure pour. This shear transfer mechanism is mainly provided by the compressive force provided by the continuous PT, the lapped 180° bent hooked bars in the connection, and a single shear key. Based on AASHTO LRFD Bridge Design Specifications (AASHTO 2014), an intentionally roughened surface is assumed for the end of the adjacent girders to enhance the shear transfer capacity of the interfaces.

3.5.7 Stress Check

Given that construction sequence and associates stresses play an important role in design of in-span spliced prestressed concrete girder bridges, it is necessary that stresses be checked in the critical regions to ensure a safe and durable design. Critical sections are shown in Fig. 3.6 (a) representing: maximum positive moment in back span (Section A-A), in-span splice in back span (Section B-B), maximum negative moment over pier (Section C-C), in-span splice in main span (Section D-D), and maximum positive moment in main span (Section E-E).

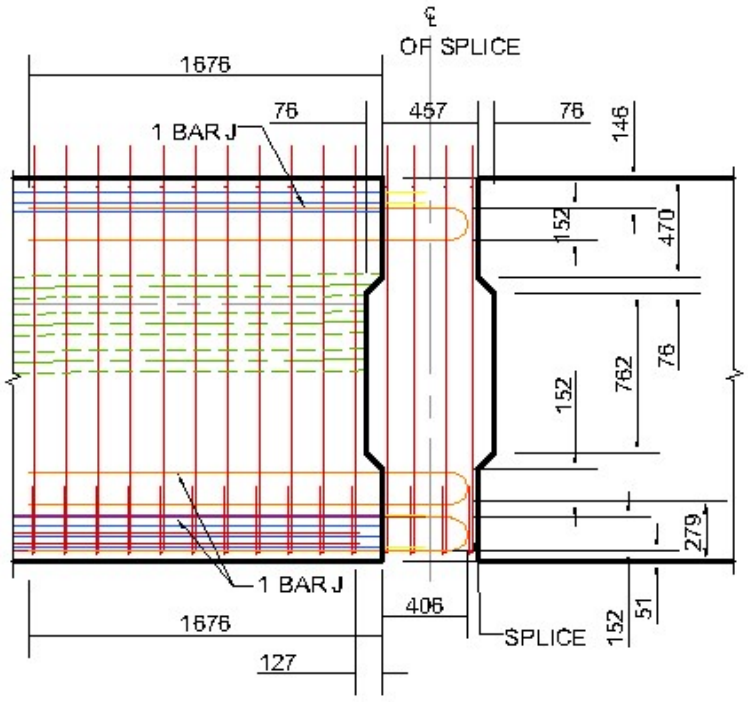

(a) Side elevation

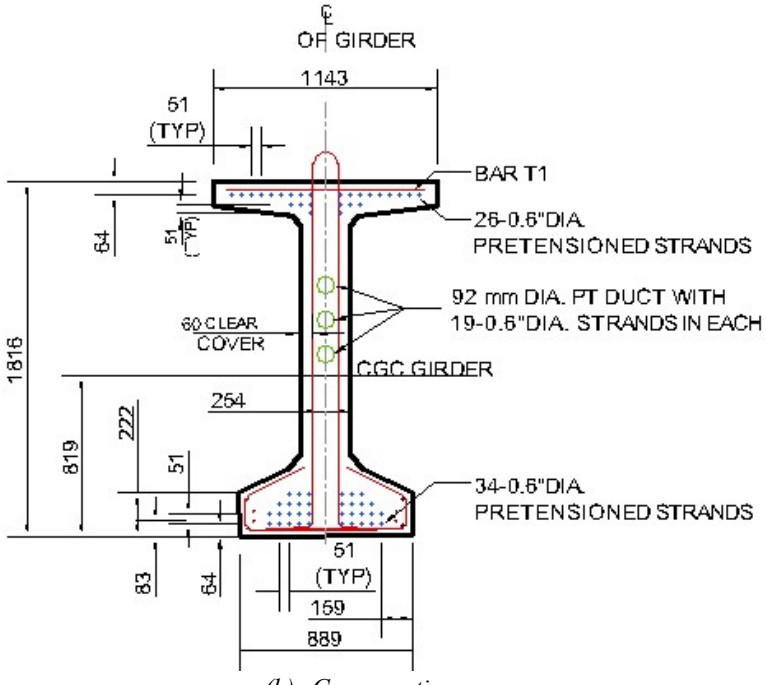

(b) Cross section

Fig 3.7. In-span splice detailing as tested in Chapter 4.

Table 3.7 summarizes the stress in the critical section at three main stage of construction as well as service limit state: (i) after pretensioning before long-term prestress losses; (ii) after casting the deck; (iii) after stressing post-tensioning and including long-term prestress losses; and (iv) at service limit states. Allowable stresses are adopted from AASHTO LRFD Bridge Design Specifications. The values in bold represent the situations where the allowable stresses are exceeded. For case (a) and (b), the stress exceeds in top flange of in-span splices, upon casting the deck slab. Given that in-span splices are located over shore towers, it is expected that they relatively significant negative moment upon casting the deck slab, therefore, the top flanges of such splices are prone to cracking. Mild steel must be provided in top flange of in-span splices to control the cracking, until the continuity post-tensioning is applied and the section is pre-compressed. For case (c) in Table 3.7, bottom flange of precast segment is overstressed in the bottom flange over the pier. Given that precast segments are pre-compressed through both pretensioning and post-tensioning, their reserved capacity in compression is limited. Additionally, relatively small area of bottom flange (compared to top flange plus deck slab) causes these regions to be potentially prone to high compressive stresses in regions with high negative moment demands, namely over piers. It is necessary that additional mild steel be provided in bottom flange of precast girders in high negative demand regions to enhance the capacity as well as ductility of these sections.

Table 3.7. Stress in critical sections during construction and service limit state.

Loading	Component	Location	Section					Limit	
			A-A (End Segment)	B-B (Splice Exterior)	C-C (Pier)	D-D (Splice exterior)	E-E (Drop-in Segment)	Compression (Service I)	Tension (Service III)
Step I (Before Loss)	Girder	Top	-11.56	-	-16.78	-	-11.10	-26.39	3.80
		Bot	-15.43	-	-16.89	-	-11.72		
Step II (Before Loss)	Girder	Top	-17.37	**7.72**	-18.88	**5.64**	-15.13	-26.39	3.80
		Bot	-10.34	-6.77	-15.05	-4.94	-8.20		
Step III (After Loss)	Girder	Top	-23.38	-3.90	-17.69	-4.54	-22.94	-26.39	3.80
		Bot	-19.31	-9.58	-28.79	-10.40	-14.75		
	Deck	Top	-3.03	-8.33	-3.73	-7.08	-4.52	-12.42	2.62
		Bot	-3.66	-7.67	-4.19	-6.72	-4.79		
Step IV - Service (After Loss)	Girder	Top	-30.30	-8.27	-11.25	-7.38	-30.23	-35.16	3.80
		Bot	-6.51	-1.50	**-40.70**	-3.32	-1.25		
	Deck	Top	-9.07	-12.15	1.90	-9.55	-10.89	-12.42	2.62
		Bot	-8.23	-10.56	0.06	-8.59	-9.60		

Fig. 3.8 presents an example of variation of stress block in the splice region in back-span. The first row in each case shows the effect of each stage of loading and the second row represent the accumulative stress block at the end of each stage of construction and live load. Appendix A presents the stress block of all critical section during construction and at the service limit state.

Table 3.8 compares the state of stress in the critical sections (at in-span splice, at mid-span of main span for maximum positive moment, and at pier for maximum negative moment) after application of all dead loads and stressing all PT and prestress losses for each of the three methods of construction. For shored construction, only one stage of PT is stressed after casting the splices, while for partially shored construction and span-by-span construction, both stages of PT are stressed after casting the in-span splices. Therefore, as the results in Table 3.8 reveal, the average compressive stress in the in-span splice regions is slightly lower than that for other two methods of construction.

Table. 3.8. Stress in critical section after dead load and prestress losses

Construction Type	Location	At Splice	At Mid-Span	At Pier
Shored Construction	Deck	-8.33	-4.52	-3.73
	Top Flange	-3.90	-22.94	-17.69
	Bottom Flange	-9.58	-14.75	-28.79
Partially Shored Construction	Deck	-3.63	-0.94	-3.91
	Top Flange	-11.69	-16.10	-7.97
	Bottom Flange	-8.94	-17.95	-9.82
Span-by-Span Construction	Deck	-2.27	-7.16	-1.53
	Top Flange	-13.54	-20.15	-17.17
	Bottom Flange	-25.51	-28.61	-22.46

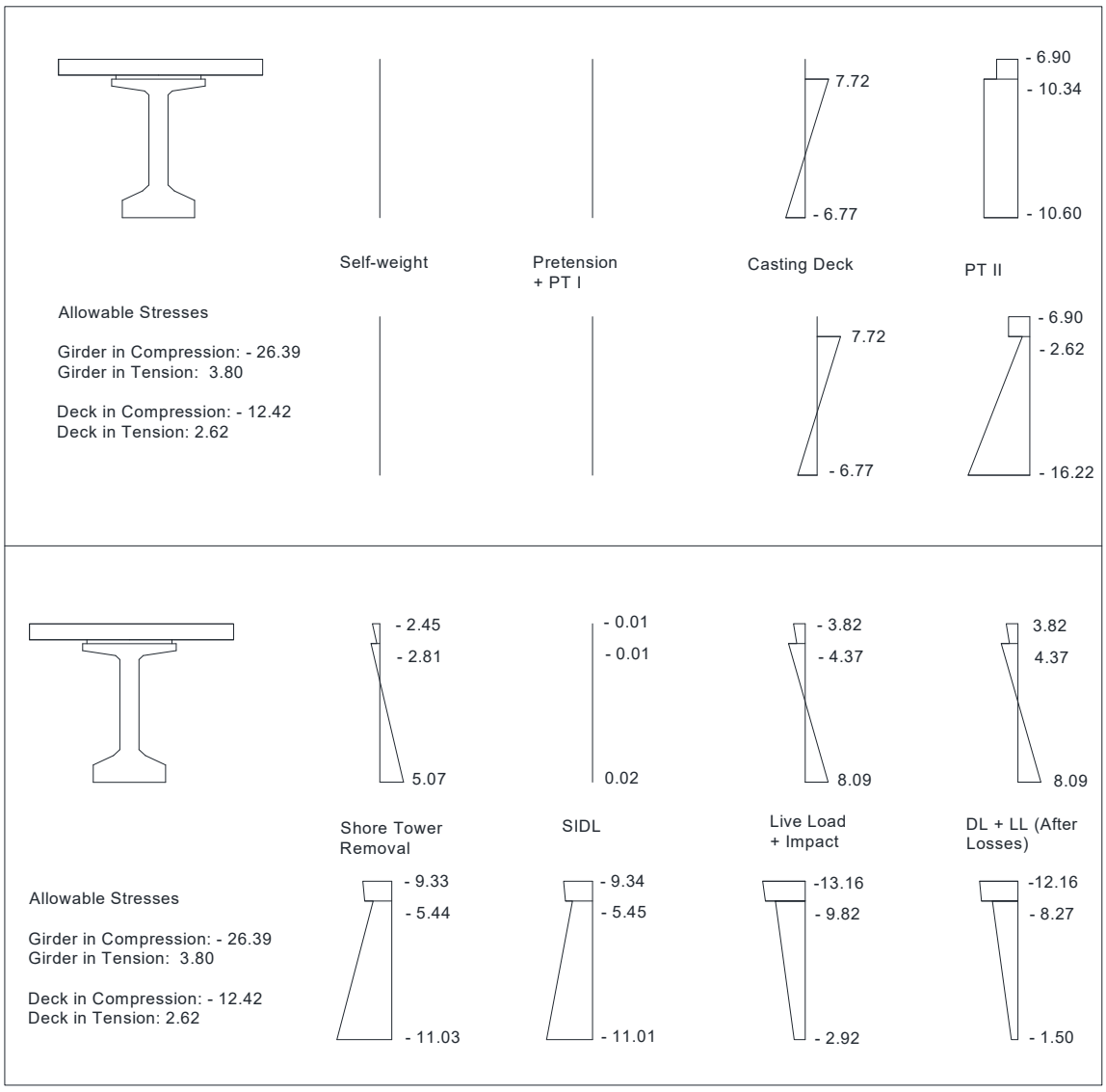

Fig. 3.8. Stress blocks for in-span splice (Section B-B in Fig. 3.6) during construction and service limit state.

3.6 DEFLECTION CHECKS

Fig. 3.9 presents the deflection profile of half of the prototype bridge during construction and after application of all dead load and prestressing for each of the three methods of construction. The solid blue line represents the deflection profile after casting the deck, and the solid red line represent the deflection profile upon stressing second stage of PT and after all losses are taken place.

For shored construction (Fig. 3.9 a), the Stage I PT is applied on individual girders and balances the deflection of individual segments. Also, since the deck is cast while girders are supported by shore towers, the deflection is significantly reduced. The Stage II PT is applied while shore towers are still in place and balances the dead weight of the deck. But, since the Stage II PT is applied on the composite section, the deflection due to weight of the girder is not completely balanced and some residual deflections remain.

For partially shored construction (Fig. 3.9 b), the Stage I PT is applied after casting the in-span splices on a continuous structure. Therefore, the "locked-in" deflections due to self-weight of individual girders and pretensioning is not perfectly balanced. However, the locked-in deflections are greatly reduced by implementing the deflection balancing through eccentric prestressing ($Fe_c = WL/9.9$, $\gamma_0 = 0.1010$). Since upon stressing the Stage I PT the shore towers are removed, deflection under the weight of the deck is significantly higher than that for shored construction. Given that the Stage II PT is designed to balance the dead load of the deck, it applied an equal amount of upward load, but given that the Stage II PT is applied on a composite section, it fails to completely balance the deflection.

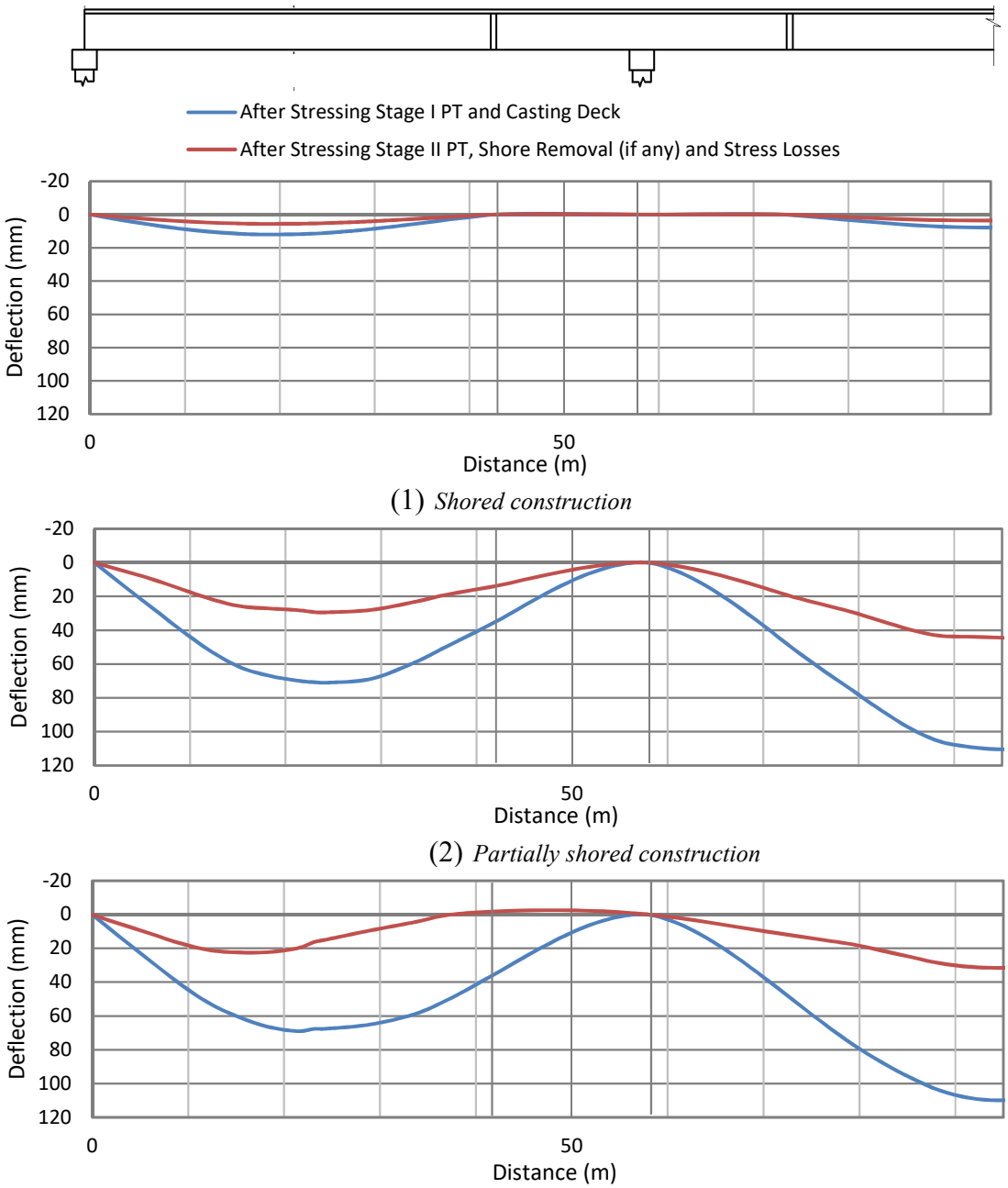

Fig. 3.9. Deflection profile after casting the deck and stressing PT for each of the three methods of construction.

For span-by-span construction, both stages of PT are applied after casting the in-span splices, therefore, some "locked-in" deflections remain in the individual segments. However, this deflection is minimized using a deflection balancing approach through eccentric prestressing by minimizing the deflections ($Fe_c = WL/9.9,\ \gamma_0 = 0.1010$). Given that no shore towers are used in this method of construction, the structure undergoes large amounts of deflections upon casting the deck slab concrete. However, if harped post-tensioning is used, the deflections may be significantly reduced upon stressing the tendons.

A comparison between final deflection profiles of each method of construction reveals that shored construction may significantly balance the deflection due to existence of shoring towers during casting the deck slab concrete. For all three methods of construction, given that Stage II PT is applied on a composite section, the deflection due to weight of deck slab may not be fully balanced, if the Stage II PT is designed for load balancing. The best approach to mitigate the final deflection is slightly over balancing the self-weight of girders through the Stage I PT, so that some upward camber exists in the superstructure prior to casting the deck.

3.7 CONCLUSIONS AND REMARKS

This chapter revisited the concept of the in-span splicing technique. Deflection balancing approach was introduced to minimize the deflection of the precast girder segments by pretensioning alone. Then, three different construction methods that adopt in-span splicing of precast concrete girder segments were discussed in detail to provide a general understanding of the versatility spliced precast girder bridge design. Design steps pertaining to each construction method were outlined. Based on the proposed design steps

a prototype bridge was designed for all three construction methods (shored, partially shored, and heavy lift) and the results of the prestressing design were compared for each of the construction methods. Based on the results and details of each construction method, the following remarks and conclusions are drawn:

1. If post-tensioning is not applied to individual precast segments, unbalanced deflection may lead to misalignment at splice regions and "locked-in" deflections upon stressing the continuity PT.
2. Deflection balancing technique by using pretension-only solutions can effectively reduce the locked-in deflection of individual precast segments. Deflection minimization may be done using eccentric-only prestress, harped-only prestress, and a mixed solution of both eccentric and harped prestress.
3. Harped pretensioning is more effective than eccentric-only prestress solution in balancing the deflection of the precast segments. But, a mixed solution of eccentric prestress and harped prestress solution can effectively balance the deflection of the precast segments under self-weight.
4. The in-span splicing technique can be effectively used to increase the span length of prestressed concrete girder bridges.
5. In-span splicing allows versatile design options and construction methods, which can effectively create bridges with span lengths from 45 m to 90 m. Proposed construction methods include: shored construction, partially shored construction, and heavy lift construction.

6. The shored construction method provides a reliable and safe option for cases where shore towers are allowed in the main span of the bridge. Because of lower construction demands, all segments can be designed as prismatic sections which leads to minimal fabrication cost. However, the existence of shore towers in all spans makes this type of construction less cost-effective at the site.
7. The partially shored construction method offers a versatile solution for situations where topological, environmental, and transportation concerns does not allow for having the shore towers in the main span. As the construction demands increase in this type of construction, generally haunched sections are required for the on-pier segments, which adds to the cost of fabrication. Nevertheless, the removal of half of the shore towers makes this type of construction very economical.
8. The heavy lift construction method is proposed as an innovative method of construction for continuous precast concrete bridges, where all of the shore towers are effectively removed from the construction process and construction costs are reduced. However, applicability of this type of construction is restricted to the projects where a proper construction site allows for creating a PT stressing line on the ground to prestress each of the spans. Also, additional costs of prestressing, thickened portions, and constant diaphragm reduces the cost-effectiveness of this type of construction.
9. Stressing the last stage of PT after casting the deck concrete can greatly enhance the capacity, long-term maintenance, and durability of the superstructure. It also

balances a portion of the deflections that is generated by the weight of the deck and the super imposed dead loads.

10. Practitioners have expressed their concerns regarding stressing of the deck concrete, as it makes the deck replacement more difficult. Part of the concern pertains to overstressing the girder. In order to address this concern, one of the two stages of PT can be applied as external harped PT tendons. These tendons can be released and replaced upon requirement of the deck replacement.
11. While the design procedure and stressing sequence of the prestress in each of the three construction methods varies, the total amount of prestressing for each method is quite comparable. Yet, heavy lift construction marginally requires higher levels of prestressing and construction demands.
12. Different splice details have been proposed that can apply for each of the construction methods. However, it is recommended that supplemental compression mild steel be added to the bottom flange of sections within the negative bending regions to enhance the ductility and performance of the bridge at strength limit states.
13. If the Stage II PT is applied after casting the deck slab concrete, the load balancing approach would not completely balance the deflection of the bridge under the weight of the deck. In this case, shored construction has proved to be most effective in controlling the maximum deflection.

4 INVESTIGATING THE EXPERIMENTAL PERFORMANCE OF IN-SPAN SPLICES

4.1 CHAPTER SUMMARY

When bridge spans exceed 45 m it is necessary to have modular construction methods to effectively join the segments in-span and form a continuous structure with substantially longer span lengths. An economical solution is experimentally investigated through which the existing Texas-shape precast prestressed bulb I-girder sections are adapted and field-spliced. By using not more than two in-span field-splice joints per span, the span length may be doubled to 90 m. In this paper, in-span splicing solutions are investigated for shored construction. From a prototype design, an experimental test specimen is abstracted and an experimental testing investigation described. Results are presented for the full-scale laboratory tests on two splice regions under service load through to failure. The cast-in-place splice is a minimalist partially-prestressed design where standard post-tensioned ducts pass through the connection and only minimal mild steel is added; the normal girder pretensioned tendons are absent within the splice as they terminate at the ends of each adjacent precast segment. The test results show that satisfactory performance is obtained meeting all service and strength requirements. However, if such splices are not located in zones of modest moment demand—such as when a splice is located at or near a pier support in a high negative moment zone—improved reinforcing details are recommended that provide additional section ductility to remove the propensity for a brittle compression failure mode.

4.2 BACKGROUND AND SCOPE

The most common form of construction for bridges with spans ranging from 12 m to 45 m is a simply supported system consisting of a reinforced concrete slab on pretensioned prestressed concrete girders. The practical upper limit of the system is governed by a 45 m length and 100 tonne pay load restriction for precast bulb I-girder units to permit road transportation from the casting plant to the construction site. In Texas, the cost of such simply supported bridge system is very competitive against all alternatives. If longer spans are to be used, alternatives tend to be based on regional construction customs. No matter what alternative form of construction is used, be it single-cell concrete box girders, multi-cell steel box girders, or steel plate girders, the unit cost jumps markedly—generally more than doubling. Adopting wet-splice connections enables the general form of the prestressed concrete I-girder bridges to be extended from 45 m to 90 m using the same casting forms for the precast units. In this way, the low unit cost of the system remains very competitive for longer spans.

In-span splicing has been proposed as a promising method for extending the span length of concrete girder bridges. According the NCHRP 517 Report (Castrodale and White, 2004), designers have implemented in-span splices in more than 200 bridges in the US to reach spans up to 100 m. In-span splicing has been used for both single span (Endicott 1996) and multi-span bridges (Jenssen and Spaans 1994, Fitzgerald and Stelmack 1996, Nikzad et al. 2006, Caroland et al. 1992).

Previous studies have assessed the performance of the in-span spliced bridges through analytical or numerical analysis (Abdel-Karim and Tadros 1992, Roland 2001,

Tadros and Sun 2003). However, until recently, a lack of experimental data and a standard design procedure have limited the application of this technique to certain states.

Hueste et al. (2011, 2016) developed standard procedures for the design of in-span spliced concrete girder bridges and conducted a full-scale experimental study on the performance of splices. This chapter focuses on the results of the experimental study to shed light on the performance of the specimen and splices in terms of applied positive and negative moments, as well as shear intensity.

The first section of this chapter describes the geometry of a prototype bridge, from which an experimental test specimen is abstracted. Next, visual experimental observations at key performance points arising from the applied loading of the specimen are presented along with force-deformation behavior as well as the strain and stress profiles. Finally, qualitative recommendations based on visual observations and data analysis results are given.

4.3 PROTOTYPE BRIDGE DESIGN AND CONSTRUCTION

Fig. 4.1 presents the prototype three-span continuous spliced precast, prestressed concrete bridge system that was used as the basis of this research. The design followed the recently revised provisions for spliced precast girders in the AASHTO LRFD Bridge Design Specifications (2014). As shown in Fig. 4.1 (a) and (b), the continuous three-span prototype consists of 58 m, 73 m, and 58 m (190-240-190 ft) spans; each composed of 42.7 m (140 ft) units in the positive moment regions and 30.5 m (100 ft) long units in the negative moment regions that are continuous over the two piers. Modified Tx70 prismatic girders [1780 mm (70 in.) deep] were used for each girder segment. To accommodate

grouted post-tensioning ducts, it was necessary to increase the standard Tx70 178 mm (7 in.) web to 254 mm (10 in.). This wider web width also helps provide increased shear capacity that is essential for the longer spans. Also, the thickness of top flange was increased by 38 mm (section depth increased to 1818 mm) to accommodate the top pretensioning strands.

The bridge was designed to support a standard 200 mm (8 in.) thick reinforced concrete deck. In accordance with the AASHTO LRFD Bridge Design Specifications (2014) the bridge was designed for a total of three HL-93 design live load traffic lanes. A T501 traffic barrier was also adopted as presented in the standard drawings of the TxDOT Bridge Design Manual (2010). A non-structural wearing surface of 50 mm (2 in.) thick was assumed. The spacing and overhang configuration considered for this Tx70 girder bridge results in optimum distribution of dead load and live load to the interior and exterior girders. Therefore, the same design requirements were adopted for all girders.

Design parameters for the prototype bridge were based on standard practice used by TxDOT. The specified compressive strength of the self-consolidating concrete used for the precast prestressed concrete girders was f'_c = 60 MPa (8.5 ksi) and at release f'_{ci} = 45 MPa (6.5 ksi). For the cast-in-place (CIP) deck, TxDOT Class S conventional concrete with f'_c = 30 MPa (4 ksi) was specified. For the pretensioned and post-tensioned (PT) concrete, the prestressing steel consisted of 15 mm (0.6 in.) diameter low relaxation strands with an ultimate tensile strength of 1860 MPa (270 ksi).

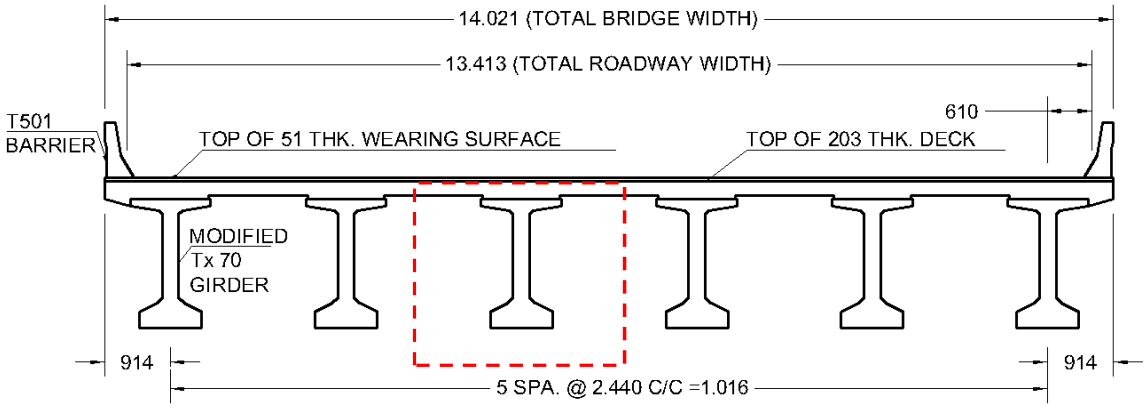

(a) Bridge deck cross section

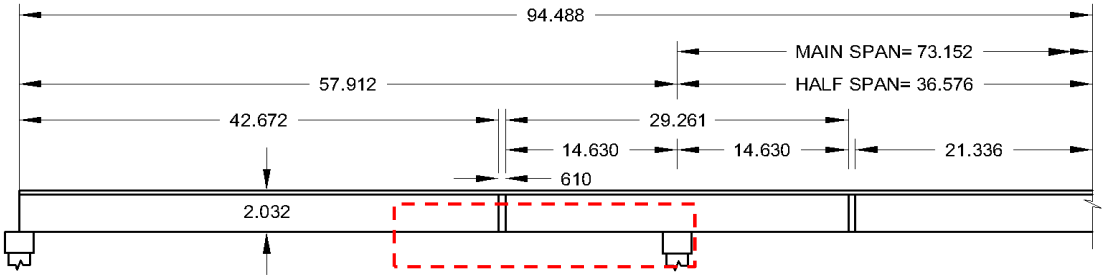

(b) Elevation of half-bridge and the location of the abstracted specimen

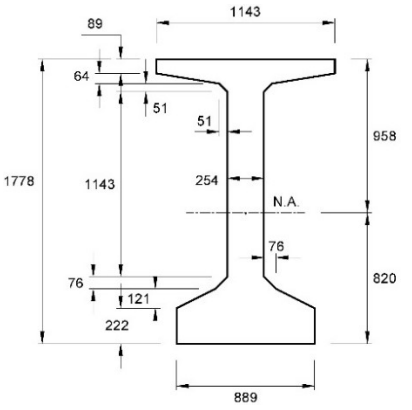

(c) Modified Tx70

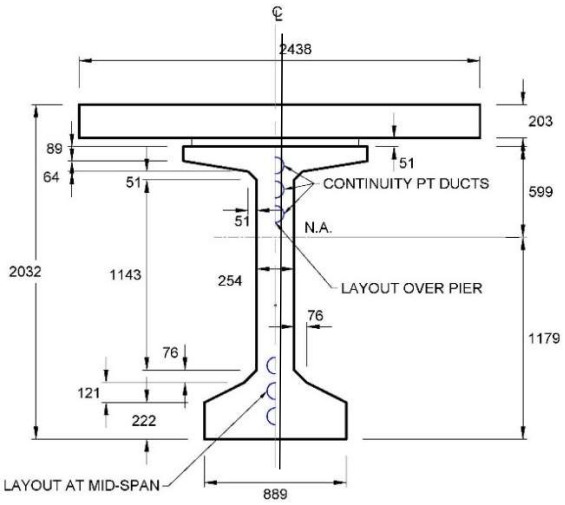

(d) Topped girder

Fig. 4.1 Prototype continuous three-span slab on prestressed concrete I-girder bridge.

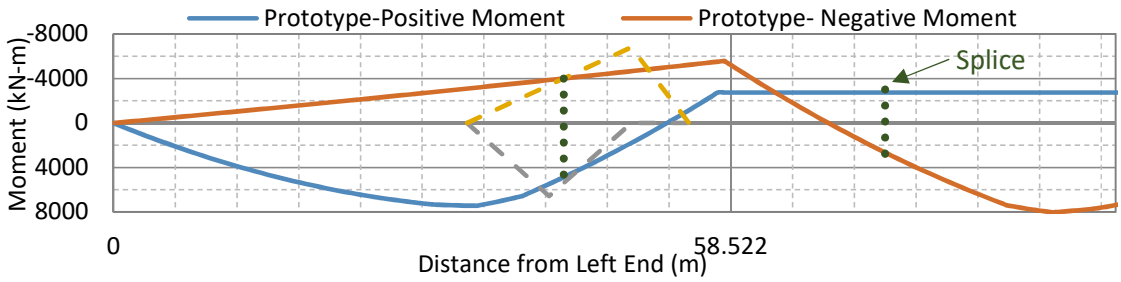

(a) Comparison of specimen and prototype demands over half length of prototype bridge

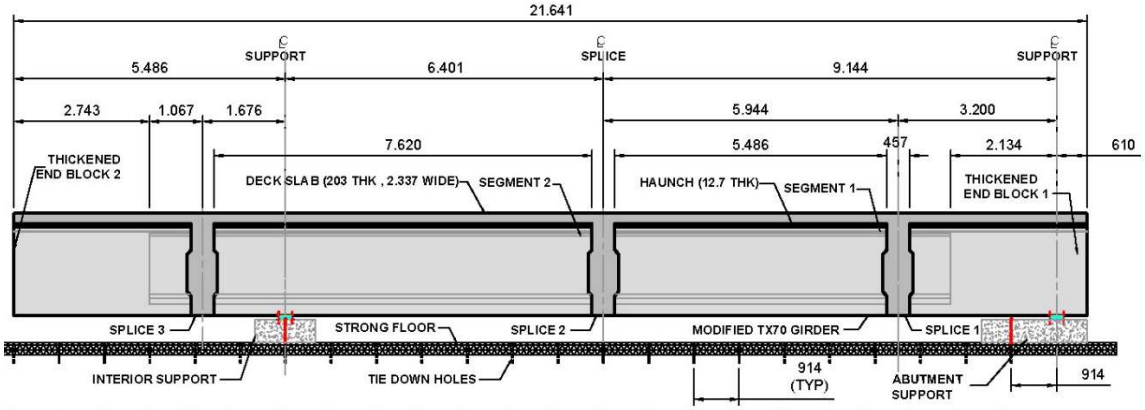

(b) Side elevation of the specimen with three splices (dimensions are in m)

Fig. 4.2 Specimen geometry and demand comparison.

In order to adequately design a continuous spliced girder bridge of this type, it is essential to conceive how the bridge construction should proceed. As discussed in Chapter 3, while the construction sequence may vary from bridge to bridge based on bridge location and crossing type (river versus highway overpass) and contractor preferences, three broad options may be used: (i) unshored construction, which is generally necessary for water crossings; (ii) shored construction, which may be more amenable for overpasses; and (iii) heavy lift construction, which allows to span between two piers without shoring towers. The latter was used herein as this method permits a final stage of PT where compression can be applied to the deck concrete. This helps avoid cracking in the deck, specifically in negative moment regions, thereby extending the life of the deck and hence the bridge.

The prototype continuous spliced prestressed concrete bridge was designed to satisfy allowable stresses during fabrication, construction, and during normal service conditions. This aim was to essentially eliminate the possibility of cracking through all stages of construction and service. Final ultimate limit state strength checks were made. Another key aim in the design was to balance dead load, as closely as practicable, during all stages of construction. This aim is twofold: (i) it ensures that the segments, when spliced, remain straight and properly aligned through the splice connections; and (ii) it ensures that following the casting of the deck and application of all PT, and when time-dependent losses are essentially complete, the bridge has no net deflection and is under a state of constant uniaxial compressive prestress. To achieve both sub-aims of this objective it is therefore necessary to apply the load-balancing PT in two stages: Stage I PT

is to balance only the girders in their spliced continuous form; and Stage II PT is to balance the additional applied dead load from the deck (plus superimposed dead load) that is placed once Stage I PT is complete. In this way, some compressive stress is applied to the deck slab, which is necessary particularly in the negative moment regions over the pier supports. Table 4.1 summarizes the pre- and post-tensioning details giving the number of strands and the resulting number of PT tendons.

4.4 EXPERIMENTAL STUDY: SPECIMEN ABSTRACTION

Fig. 4.2 (a) presents the bending moment diagrams (the solid lines) for the critical cases under live load plus impact (LL+I). The location of the splices are shown by the vertical dotted lines for which it is demonstrated that the maximum moment demands range from -4000 to 5000 kN-m. As it is not feasible to apply pretension prestress to the splice region, a minimalist partially prestressed concrete solution was designed whereby the continuity PT provided most (~90%) of the flexural strength, with some supplementary capacity being provided by several top and bottom mild steel U-bars that formed a non-contact splice within the splice region. The splice was detailed to use 190 mm slump 60 MPa (8.5 ksi) concrete. The standard web width of 254 mm was used through the splice.

Fig. 4.2 (b) presents the full-scale experimental specimen that was designed to incorporate three splice regions to investigate the in-service and ultimate limit state performance under applied loads. Due to length limitations of the test laboratory strong-floor, the specimen was conceived to capture the essence of the moment field in the prototype as well as other possible adverse scenarios. Fig. 4.2 (b) shows the side elevation

of the specimen and the three splices numbered 1 to 3 from the right. The three splices may be considered as follows:

Splice 1: This splice is under moderate moment and very high shear similar to about the 10 m location shown in Fig. 4.1 (b).

Splice 2: This splice was the main subject of this research, and is based on the demands at the 42 m point of Fig. 4.1 (b). When the specimen was loaded near Splice 2, the positive and negative moment demands were captured as shown by the dashed lines in Fig. 4.2 (a).

Splice 3: This splice was considered where a similar bridge to the prototype would be predominantly under negative moments at the 58.5 m position as shown in Fig. 4.2 (b).

Table 4.1 Prestressing summary

Description	End Segment	On-Pier Segment	Drop-in Segment
Pretensioning 15 mm Strands	32	26	24
Stage I PT Strands (Tendons)	19 (1)	38 (2)	19 (1)
Stage II PT Strands (Tendons)	57 (3)	57 (3)	57 (3)

Fig. 4.3 presents reinforcing and PT details of the partially prestressed Splice 2. Mild steel reinforcement was provided in addition to continuity PT running through the connection. The mild steel reinforcement consisted of 180-degree bent hooked U-bars

anchored into the adjacent girder flanges and extended into the splice region. The mild steel bent bars were designed for the maximum factored design loads. While the combination of PT and mild steel would normally be expected to provide better durability and performance, the mild steel in this detail was minimized to identify any potential adverse performance effects. The integrity of the splice connection largely depends on the shear transfer mechanism at the interface of the precast girder and the splice. This shear transfer mechanism was mainly provided by the lapped 180-degree bent hooked U-bars in the connection and roughened edges of the precast girder at the interface. Normal shear provisions were used to design the transverse hoops in the splice region.

A high slump conventional concrete with Type III Portland cement, f'_c = 60 MPa (8.5 ksi), and maximum aggregate size of 19 mm (0.75 in.) was adopted for the splice connections. Table 4.2 and 4.3 present the measured fresh and mechanical properties of the concrete for precast girder segments, splice connections, and deck slab. Detailed concrete mixture information and mechanical properties are reported by Hueste et al. (2016).

4.5 EXPERIMENTAL PERFORMANCE

4.5.1 Behavior in Splice 2 Region Under Positive Moment

Fig. 4.4 presents the experimental setup and results at failure when the loads were applied near Splice 2. As depicted in Fig. 4.4 (a), two point loads were applied and each actuator was calibrated to increase the load at a rate of 4 kN/s. The main aim of this test setup was to investigate the behavior beyond the uncracked regime through to flexural failure in

positive bending. The photographs in Fig. 4.4 show the condition of the specimen at failure, which occurred when *P*=1780 kN (400 kips) per actuator.

Prior to failure, cracks that were 0.05 mm wide first appeared in the bottom flange of Splice 2 at *P*=1000 kN (225 kips). These cracks propagated up from the flange into the web. When each actuator had reached *P*=1200 kN (270 kips), a crack width of 0.1 mm was measured at the bottom flange. At *P*=1245 kN (280 kips), small diagonal shear cracks appeared immediately below the shear key adjacent to the splice region.

When the loads reached P=1485 kN (334 kips) per actuator, the cracks in the bottom flange grew wider to 11.2 mm. The main crack extended to the interface of Splice 2 and the adjacent girder, which led to a shear-flexure interaction displacement of 6.4 mm. Due to a smaller flexural capacity that existed within the CIP splice compared to the adjacent precast girder, most of the cracks appeared within the splice region. One very large flexural crack appeared when the load exceeded *P*=1485 kN as shown in Fig. 4.4 (b). Nearby this large crack, additional flexural cracks and several diagonal shear cracks propagated.

4.5.2 Behavior in Splice 3 Region Under Negative Moment

Fig. 4.5 presents the setup and results when the actuator loads were applied near Splice 3. To generate negative moments in the test specimen, the actuators were relocated to the overhang region of the specimen as depicted in Fig. 4.5 (a). Due to damage that occurred at Splice 2 during the previous test, a tie-down system was provided as shown in Fig. 4.5 (a). To measure the transferred load to the tie down bars, a load cell was placed between the deck and the tie-down beam across the top of the specimen.

Table 4.2 Summary of concrete fresh properties

Description	Slump (mm)	Unit Weight (kN/m^3)	Air Content (%)	Concrete Temp. (°C)	Ambient Temp. (°C)	RH (%)
Girder Segment	660 (flow slump)	22.8	8	35.5	41.9	24.4
Splice Connection	254	23.7	-	-	22.8	48
Deck Slab	95	22.8	5.1	20	21.1	48

Table 4.3 Mechanical properties of concrete material

Description	Age of Concrete on test day (days)	Parameter	At 28 Days (MPa)	At Age of Testing (MPa)
Girder Segments	222	f'_c	68	81
		f_r	7.5	8.1
		E_c	32,700	35,300
Splices	103	f'_c	61	66
		f_r	7.7	7.7
		E_c	40,700	40,600
Deck	95	f'_c	37	45
		f_r	4.7	3.4
		E_c	35,100	35,100

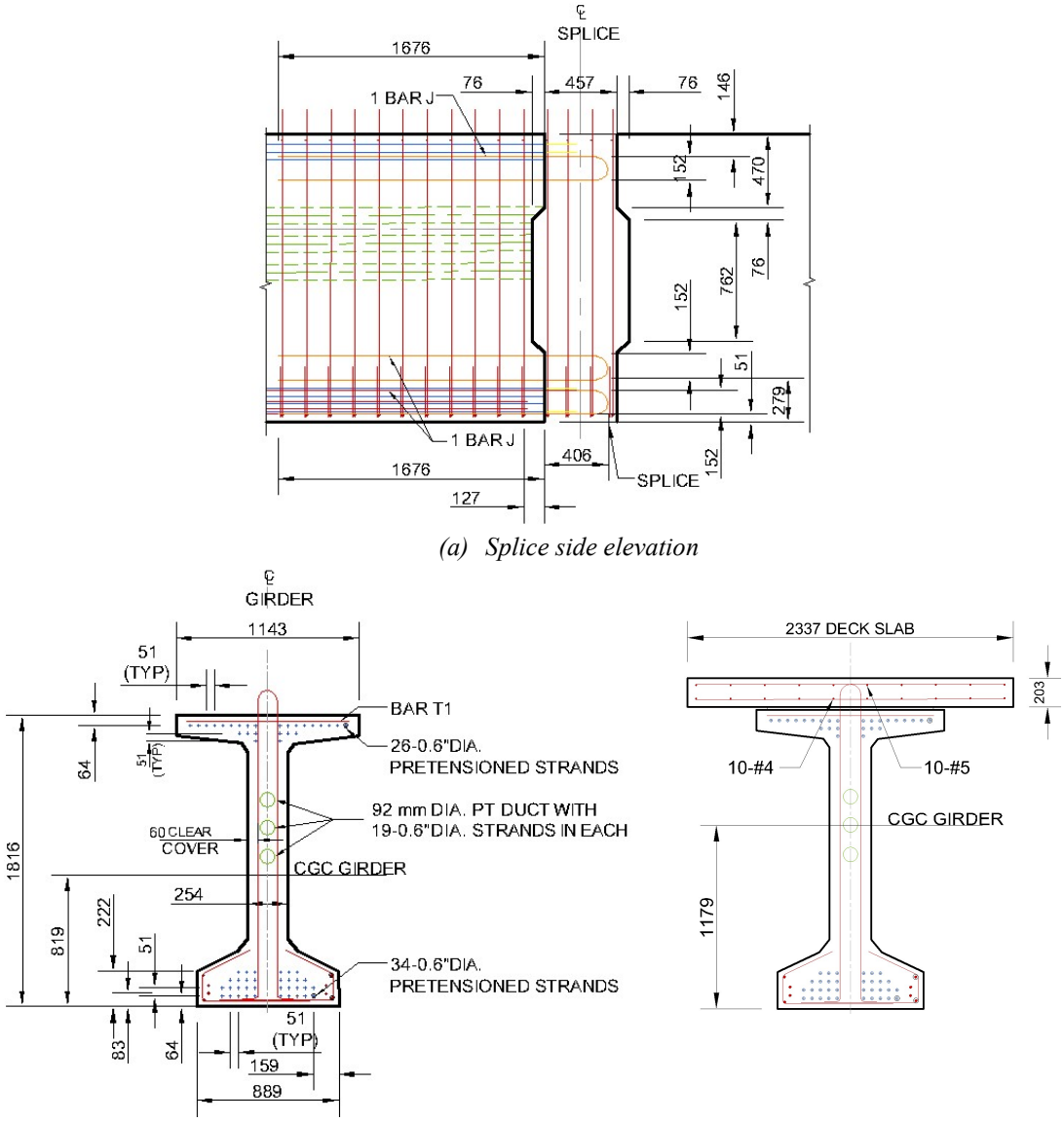

(a) Splice side elevation

(b) Splice cross section

(c) Composite cross section

Fig. 4.3 Splice detail for Modified Tx70 girder- flexural capacity is mainly provided by PT, while minimal mild steel is provided to enhance ductility and load path in top and bottom flanges.

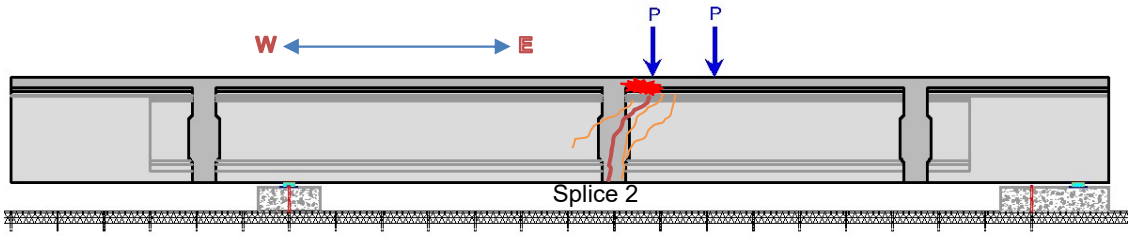

(a) Setup for testing Splice 2

(b) Differential displacement at Splice 2

(c) Buckling of deck reinforcement after failure

(d) Failure at Splice 2 (P= 1780 kN =400 k)

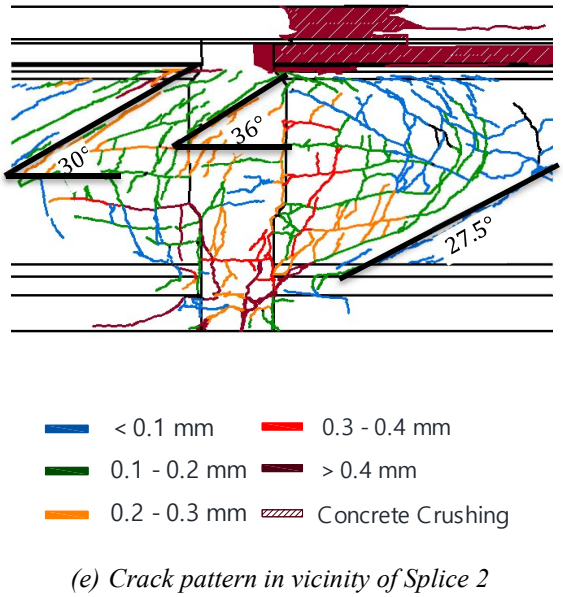

(e) Crack pattern in vicinity of Splice 2

Fig. 4.4 Visual observations for Splice 2 at ultimate conditions.

As before, actuator loads were increased at a rate of 4 kN/s per actuator and first paused at P=690 kN (155 kips) per actuator when the decompression moment was expected in the deck over the interior support. However, no cracks were observed over the interior support. On continued loading, it was observed that at P=1068 kN (240 kips) the specimen reached the cracking moment capacity. As shown in the photograph of Fig. 4.5 (b), cracks emerged on the deck slab over the support region. The crack widths were measured in the range of 0.05 to 0.1 mm.

At P=1557 kN (350 kips), cracks of width 0.1 mm occurred in the top flange above Splice 3. When loads increased to P=1600 kN (360 kips), diagonal shear cracks, 30 degrees from the horizontal, emerged in the web of Splice 3. When reaching P=1780 kN (400 kips), the splitting cracks at the interface of Splice 3 and the adjacent precast girder grew to 0.55 mm. As depicted in the photograph of Fig. 4.5 (c), diagonal cracks propagated when the loads reached *P*=1935 kN (435 kips) and a sudden horizontal compression crack appeared in the bottom flange of the girder, between the interior supports and Splice 3. At this point, based on strain gage monitoring, the transverse bars yielded within the Splice 3 region.

At P=2000 kN (450 kips), the horizontal crack extended and led to a sudden compression failure, as shown in Fig. 4.5 (d). Loading was stopped and cracks were measured over the deck and in Splice 3. Over the deck, cracks of width 0.05 to 0.1 mm spread at approximately 150 mm spacing up to 2.3 m from the point of loading. Beyond that location, cracks were spaced at 300 mm for an additional 3.7 m. The final disposition of cracks in the vicinity of the Splice 3 is shown in Fig. 4.4 (e).

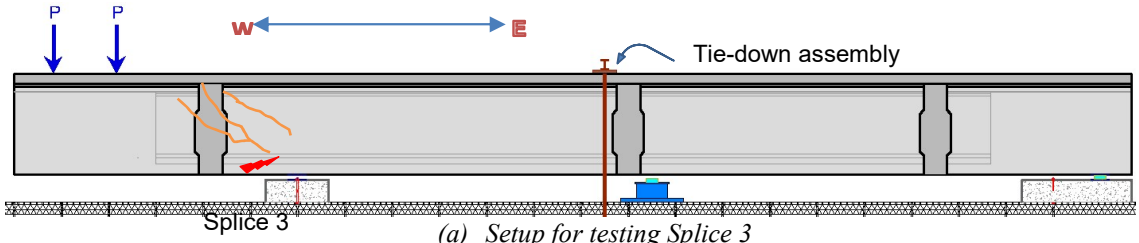

(a) Setup for testing Splice 3

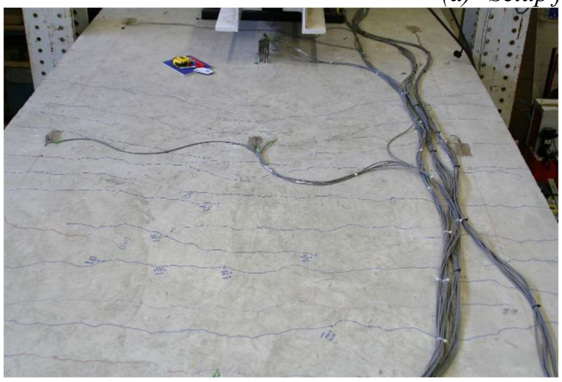

(b) Spread of cracks on deck

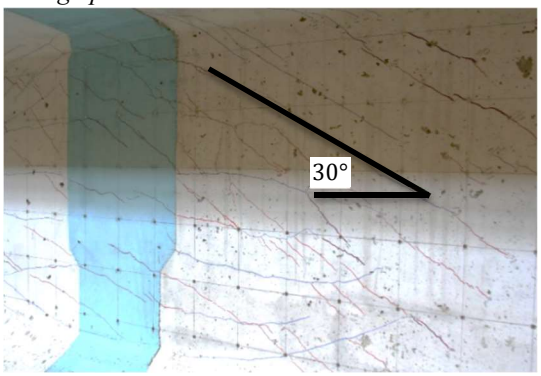

(c) Diagonal cracks in web (P=1935 kN = 435 k)

(d) Compression failure in bottom flange (P=2000 k=450 k N)

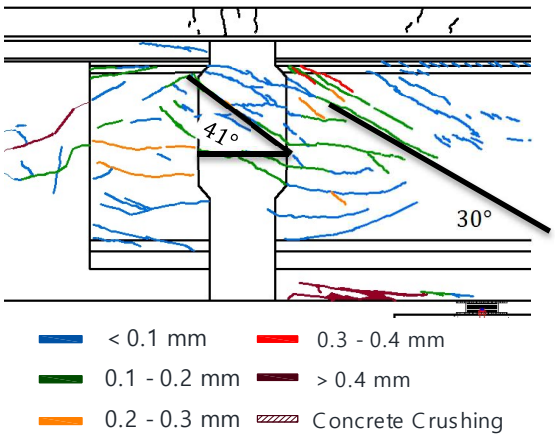

(e) Crack pattern

Fig. 4.5 Visual observation for Splice 3 at ultimate condition.

4.5.3 Behavior of Splice 1 Region Under High Shear

Splice 1 was necessary to enable construction of the overall test specimen due to laboratory crane limitations. This afforded the opportunity to investigate the behavior of a similar splice region under a moderate moment demand but with quite high shear. The general setup and test results are shown in Fig. 4.6. To avoid further damage to Splice 2 and to ensure that loading could attain higher limits, a temporary support beneath the beam soffit adjacent to Splice 2 was provided as shown Fig. 4.6 (a), thereby creating an indeterminate system. Because the precise section properties of the damaged section were not available, the analysis of the indeterminate structure was not feasible. Therefore, to provide a better understanding of the system behavior the specimen was loaded in two stages:

1) Loading up to P=890 kN (200 kips) per actuator without the temporary support (determinate structure) and then unloading to zero.
2) Placing the temporary support and bearing pad with a small clearance of 16 mm and reloading.

Before Stage 2 loading, the temporary support [the central blue support shown in Fig. 4.6 (a)] was placed at 8.5 m from the abutment support and a bearing pad placed over it. The distance between the bearing pad and the soffit of the girder was adjusted to 16 mm.

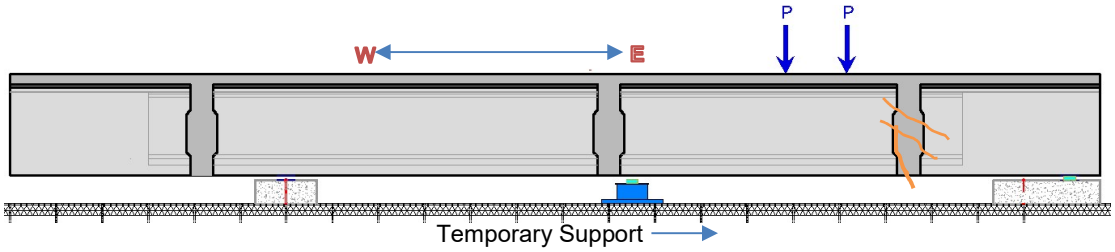

(a) Setup for testing Splice 1

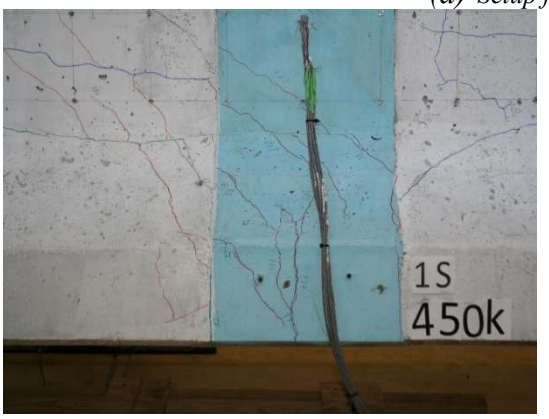

(b) Flexural crack in Splice 1 (P= 2000 kN = 450 k)

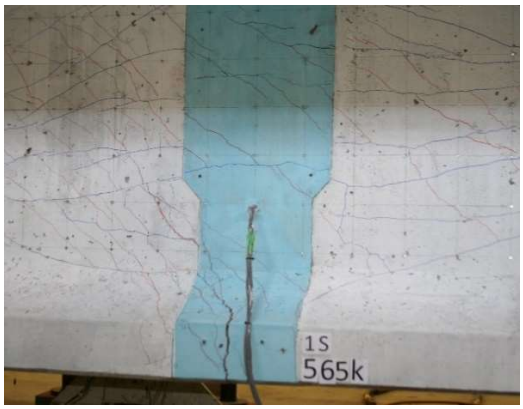

(c) Growth of flexural and shear cracks (d) (P=2515 kN=565 k)

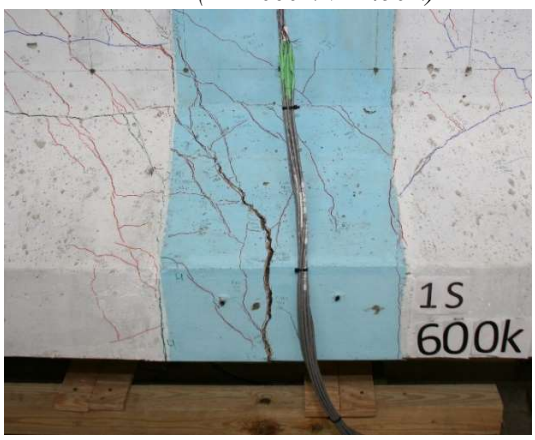

(e) At maximum load (P=2670 kN=600 k)

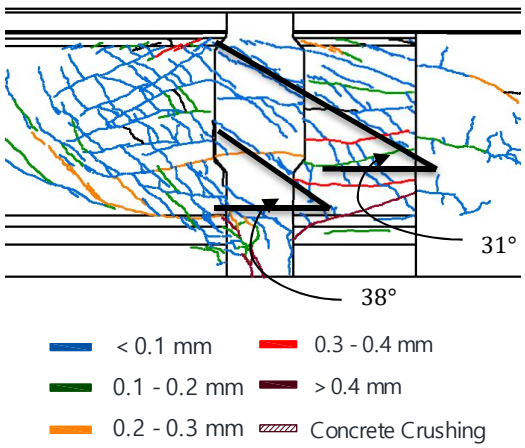

(f) Crack pattern

Fig. 4.6 Visual observation for Splice 1 at maximum loading.

In this test, due to the short span of the girder, Splice 1 experienced a combination of high shear and relatively low moment. Loads were initially applied to the full span length of the specimen. At *P*=955 kN (215 kips) per actuator, the girder soffit met the bearing pad at the temporary support; at higher loads, the specimen became an indeterminate continuous beam.

Prior to reaching the decompression load of *P*=1290 kN (290 kips), no new cracks were observed in Splice 1. At *P*=1780 kN (400 kips), diagonal cracks emerged in the web of Splice 1, aligned toward the loading point and the abutment support. The cracks extended and widened as the load increased to 1780 kN (corresponding to the ultimate design shear strength, $\emptyset V_n$, in the splice for the prototype bridge).

At *P*=1910 kN (430 kips), the lower layer of longitudinal reinforcement yielded and a sudden vertical crack appeared at the center of Splice 1 in the bottom flange. As the loading increased to *P*=2000 kN (450 kips), shear cracks emerged within the web of the girder adjacent to Splice 1 as shown Fig. 4.6 (b). Cracks continued to grow and proliferate as shown in Fig. 4.6 (c) for *P*=2513 kN (565 kips) where crack widths were measured in the range of 0.05 to 0.1 mm.

At *P*=2670 kN (600 kips), the actuators reached their maximum capacity and loading was held for specimen assessment. A significant vertical crack developed at the center of the splice as shown in Fig. 4.6 (d). This crack extended 508 mm up from the soffit and opened to 6.4 mm. The final distribution of cracks in the vicinity of the Splice 1 is presented in Fig. 4.6 (e). Upon removal of the applied loads, the cracks narrowed than 0.5 mm completely closed.

4.5.4 Force-Deformation Behavior and Analysis

Fig. 4.7 presents the force-deformation behavior for each of the test setups. Fig. 4.7 (a) compares the displacement of Splice 2 and the mid-span location when the test specimen is loaded in positive bending. The deformation was essentially linear up to the initial cracking moments. Upon reaching the cracking moment, M_{cr}, a momentary drop in force occurred as the first flexural cracks developed. Following cracking, cracked-elastic behavior occurred as the loading increased to about 85 percent of the ultimate strength. At this level, nonlinear behavior of the strands and longitudinal reinforcement initiated a more marked drop-off in stiffness. Upon reaching the failure, the applied load was dropped rapidly, while additional displacement occurred in the test specimen. After the specimen was fully unloaded, a residual displacement of 36 mm was recorded at midspan.

Fig. 4.7 (b) compares the displacement of Splice 3 and the tip of the overhang when the test specimen was loaded at the overhang to create negative moment. As expected, the specimen exhibited linear behavior up to the cracking moment capacity, when the loads reached P = 1780 kN (400 kips). With the initiation of the first flexural crack, a small drop in applied load occurred. As the loads increased, cracked-elastic behavior governed the deformation of the specimen. Premature compression failure for this test setup led to a sudden drop in applied load, before the specimen exhibited any post-yield behavior. After fully unloading the specimen, a residual displacement of 10 mm was measured at the tip of the overhang.

Fig. 4.7 (c) presents the force-deformation behavior for Splice 1. As mentioned in the previous section, before the loading commenced, a temporary support was placed 8.5

m from the east abutment and the space between the support and the soffit of the girder was adjusted to 16 mm. The apparent increase in stiffness when the loads approached P = 1000 kN (225 kips) per actuator [total of 2000 kN in Fig. 4.7 (c)] was due to the specimen engaging with the temporary support. Later, as the loads increased to P = 1910 kN (430 kips) per actuator [total of 3820 kN in Fig. 4.7 (c)], a vertical crack emerged in the bottom flange of Splice 1 and the longitudinal mild steel (U bars) yielded and the stiffness of the specimen reduced. After the loads were fully removed, a residual offset of 5 mm was recorded at the middle of Splice 1.

The initial dashed lines shown in Fig. 4.7 (a) and (b) represents the behavior of the specimen when loading up to service limit states and then unloaded. While the service load behavior appears to be somewhat nonlinear, this is attributable to the nonlinear behavior of the rubber bearing pads that were unscragged prior to loading. Thus, minor hysteretic performance of the test specimen for service loads should not be interpreted as structural damage.

A comparison between force-deformation graphs for positive and negative moments show that the proposed splice detail is somewhat more ductile under positive moment. In order to improve the ductility in regions with negative moment demands, it is recommended that more compression steel be added to the bottom flange, or the area of the bottom flange in new standard sections be increased. Both options reduce the depth of the concrete compression stress block and thereby provide better ductility in negative moment regions.

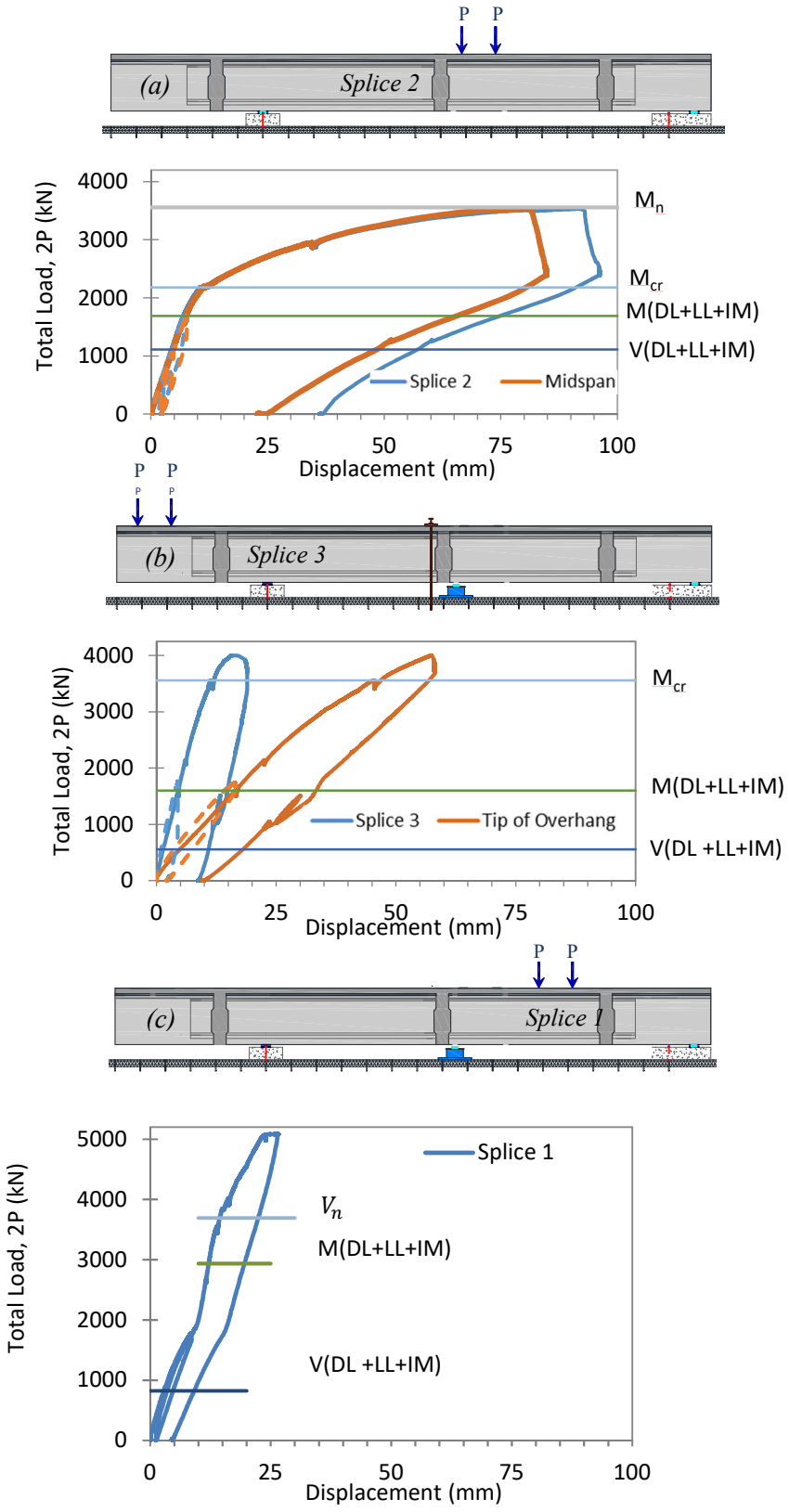

Fig. 4.7 Force-Displacement behavior at different splice locations.

4.5.5 Stress and Strain Profiles

Figs. 4.8 and 4.9 present stress and strain profiles for Splice 2 and 3 during testing at certain key load steps. For both figures the upper row of graphs presents results at service, while the lower row of graphs shows the results at ultimate limit state. The first graph in the upper row presents the stress profile of the splices prior to testing. The analytical prediction includes the effect of time dependent creep, shrinkage, and relaxation losses that were based on the current AASHTO LRFD Bridge Design Specifications (2014). Due to the load balancing effect of the applied prestress, the state of total stress under dead load is observed to be essentially uniform compression, as intended by design.

The center graph in the upper row in Figs. 4.8 and 4.9 plot the effect of loading up to the cracking moment. This result is added to the initial stresses (left-hand graph) to provide the total state of stress in the section shown in the upper right graph. The second row of Figs. 4.8 and 4.9 depict the stress and strain profile of Splice 2 and 3, respectively, just prior to the observed failure.

As it is shown in the second row of Fig. 4.9, stresses in the bottom flange of Splice 3 were well below compression capacity; therefore, failure did not occur in the splice region. On the other hand, tensile strains were slightly beyond the corresponding modulus of rupture and cracks emerged in the top flange of Splice 3.

Concrete strain gage readings may provide reliably crisp data after major cracks occur as the reading depends on the gage location between cracks. Moreover, if a crack passed nearby or through a gage's location, it may have ceased to function properly. It is for this reason the experimental results from the various different gages display scatter. In

spite of this scatter, it is evident that reasonable agreement exists between the predictions of the plane section analysis and the observed strains indicated by gages. The prediction was based on moment-curvature analyses that used the plane sections hypothesis and nonlinear material stress-strain relations (Karthik and Mander, 2011).

4.6 DISCUSSION

As shown in Fig. 4.4 (d), there was an 18 mm differential displacement at the main crack in the middle of the Splice 2. Euler beam theory is not able to predict such an abrupt displacement difference, nor do shear deformations justify such a noticeable change in displacement. The differential displacement is attributed to the outcome of the rigid body kinematics of the diagonally cracked segments at the location of the hinge (Splice 2). As shown in Fig. 4.10, if the failure plane is adjusted to represent the diagonal shear cracks, the plastic rotation of the segments on either side of the hinge results in a differential displacement in the soffit of the girder. The elevation difference at the crack opening is related to the crack angle and rigid body rotation of the two beam segments. From the geometry depicted in Fig. 4.10, the differential displacement may be calculated using

$$y = \frac{x\Delta}{L(\lambda - \lambda^2)} \tag{4.1}$$

where $\Delta =$ the deformation of the beam at the location of compression failure; $x =$ the shift in failure plane due to diagonal cracks; $L =$ the total span length; and $\lambda =$ the ratio of the length of the left segment to the total span length. For Splice 2 test setup, $L = 15.5\ m$ and $\lambda = 0.588$. According to string potentiometer reading, the actuators had a

stroke of 98 mm at the time of failure, which is equal to the deformation of the deck slab at this location.

Based on the location of the main crack in the bottom flange of the Splice 2, and the location of the compression failure, x is estimated as $650\ mm < x < 700\ mm$. Using Eq. (4.1), the resulting differential displacement is calculated to be between 16.9 to 18.2 mm, which agrees well with the experimentally observed displacement of 18 mm, as shown in Fig. 4.4 (c). Therefore, this analysis demonstrates that it is the inclination of the cracked surface that primarily affects the differential displacement on either side of the crack.

In addition to differential displacement, diagonal cracks affected the failure mode of the specimen. The compression failure occurred away from splice region under a slightly lower load than expected with less ductility. Considering the map of vertical and diagonal cracks in the web of the splice region, this phenomenon can be attributed to interaction of shear and flexure. The main flexural crack in the splice extended in the web and merged with a diagonal crack. The compression failure occurred in the top flange and deck area of the section where the diagonal crack was extended. The combination of flexural crack and diagonal crack essentially created a new critical section and shifted the compression face of the critical section from splice to the adjacent girder as shown in Fig. 4.10. Since pretensioning was effective in the top flange of the adjacent girder, the effect of initial compression stresses in the deck and top flange reduced the compressive capacity of the concrete, hence led to failure under lower applied load and lower ductility.

The effect of the shear stresses carried over the diagonal crack can potentially change the equilibrium condition of the new critical section for flexural analysis. While a complete load-deformation analysis may be quite cumbersome, it is straight forward for the ultimate strength condition. At strength limit state, it may be assumed that the width of main crack is sufficiently large so that shear is carried neither by means of aggregate interlock along the crack interface nor by tensile concrete stresses across the crack. Therefore, for this limit state, the horizontal equilibrium requires $C_{sh} = T_{sp}$; where C_{sh} the compression forces in the shifted-shaped failure section, and T_{sp} the tension forces in the splice region.

Based on the moment-curvature analysis, formulated in Chapter 5, results of the calculated capacity for the splice section and the critical section with shifted compression face is summarized in Table 4.4. According to Table 4.4, due to shear-flexure interaction, the nominal capacity of the section is reduced by 3% and the ductility is reduced by 26%.

Table 4.4 Nominal capacity and curvature of splice section and critical section

Section	**Nominal Capacity, M_n kN-m**	**Nominal Curvature, φ_n rad/m**
Splice with no pretensioning	12,780	0.0162
z-shaped Critical section including the top pretensioning	12,390	0.0129

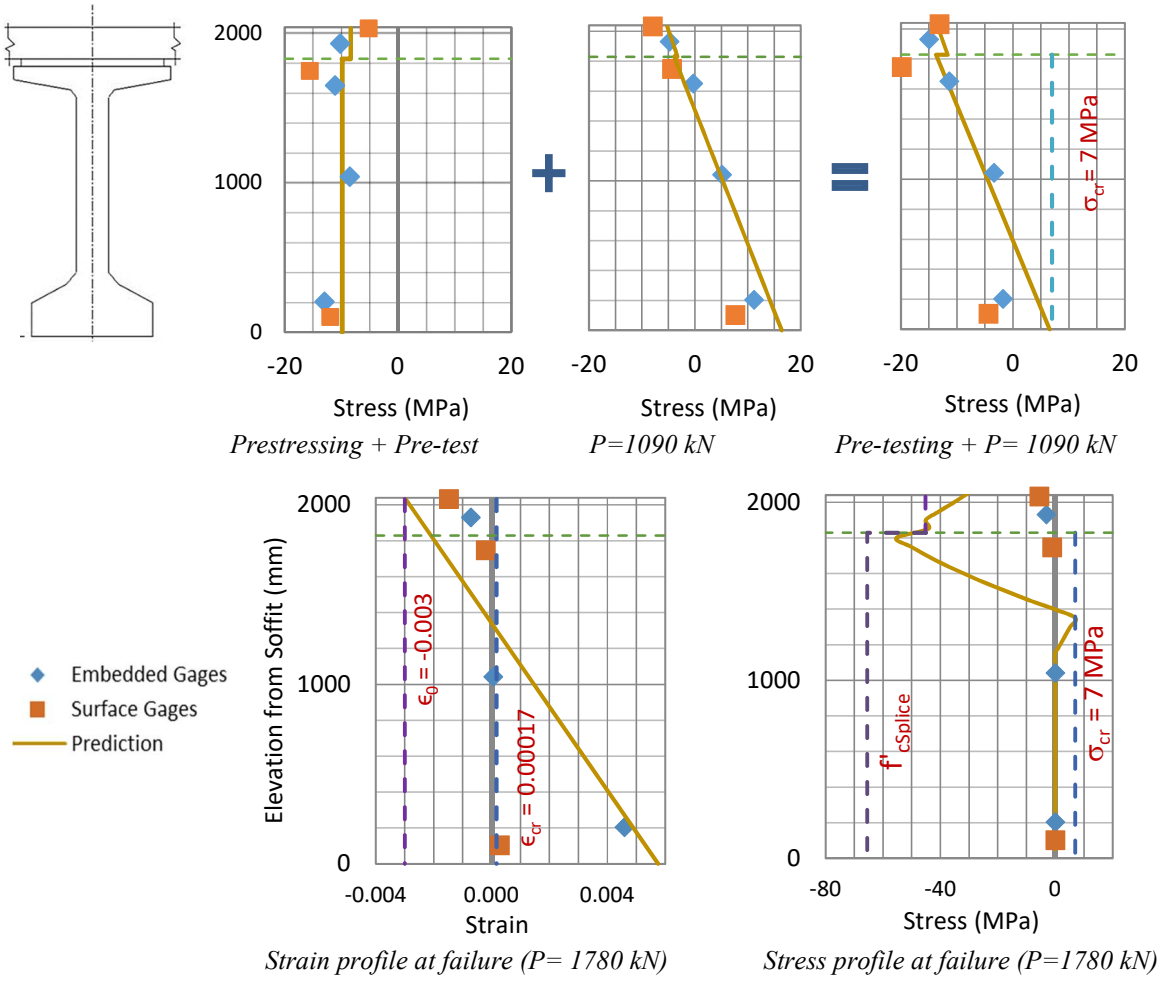

Fig. 4.8 Stress and strain distributions at Splice 2.

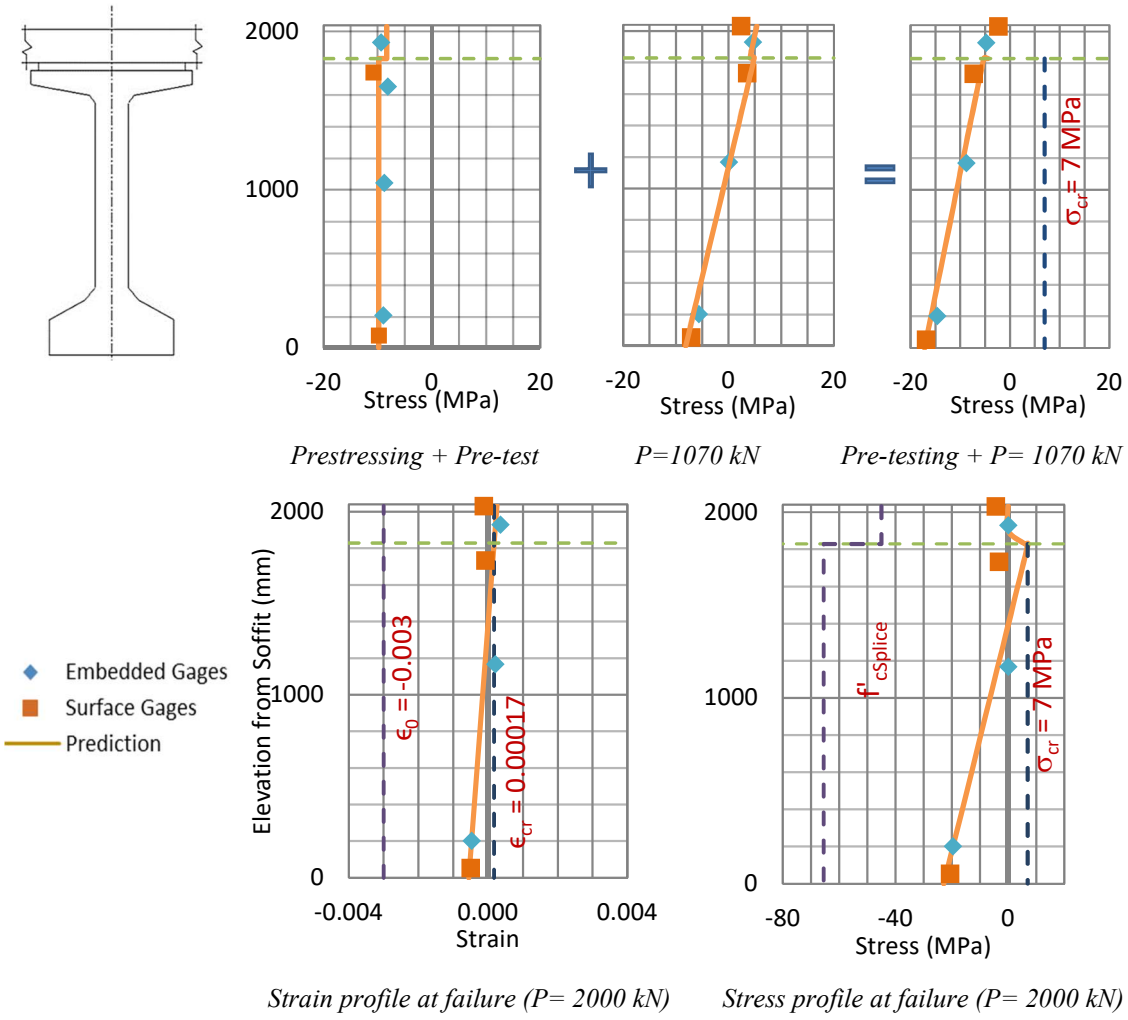

Fig. 4.9 Stress and strain distributions at Splice 3.

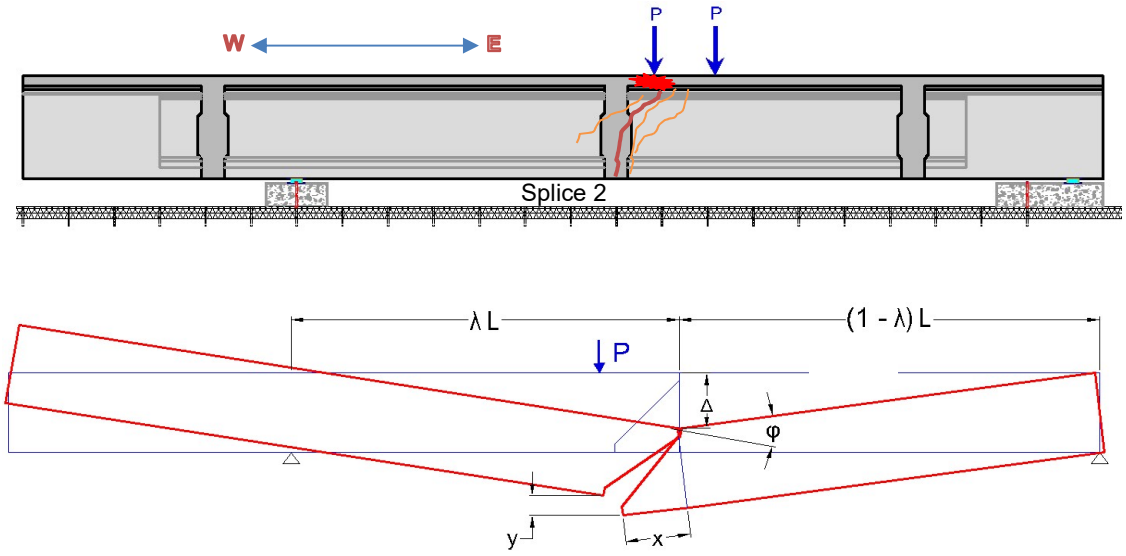

Fig. 4.10 Differential displacement originated from rigid body rotation of segments on either side of the plastic hinge with inclined critical section.

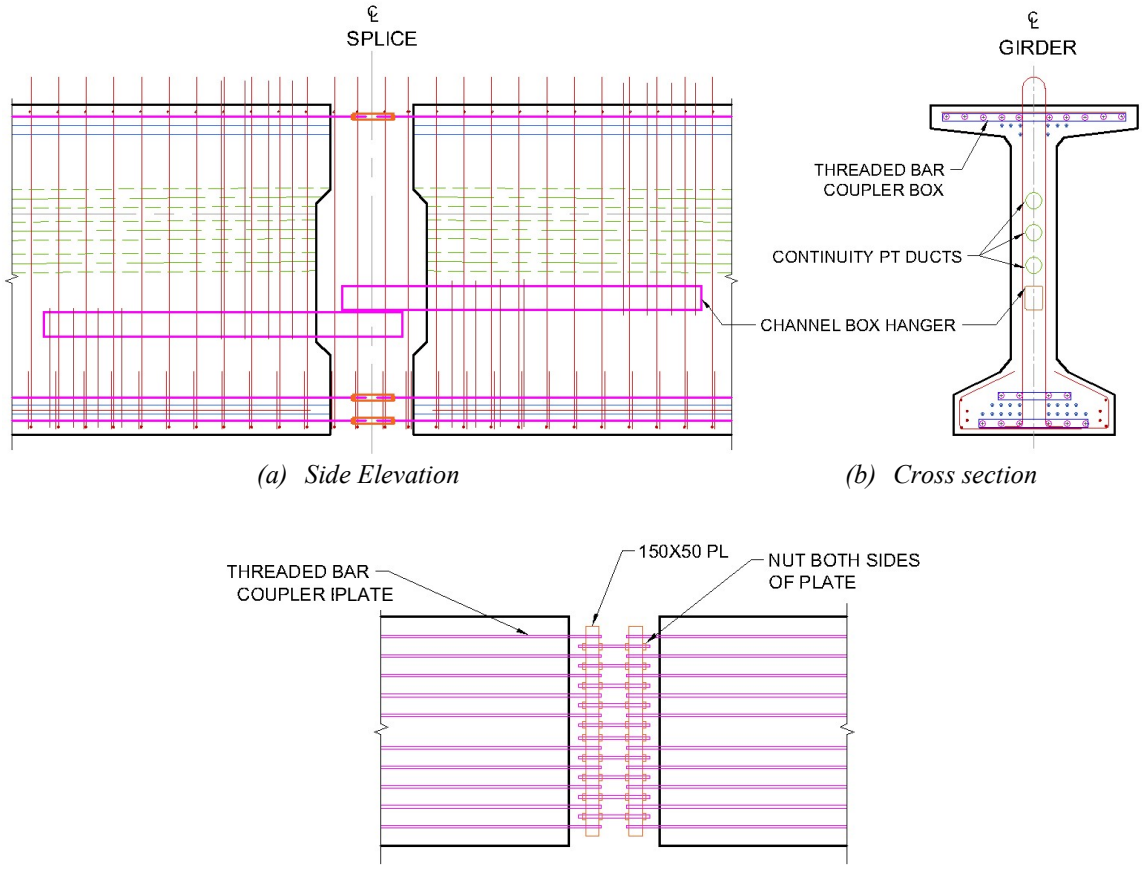

(a) Side Elevation *(b) Cross section*

(c) Girder plan view

Fig. 4.11 Enhanced splice detail with coupled rods in top and bottom flange and channel boxes in web

Results of the experimental analysis revealed that the splice region had significantly lower strength compared to the precast pretensioned concrete girder segments. This lower capacity is attributed to the effect of pretensioning strands which are discontinued in the splice regions. Experimental observations showed that due to lack of a strong load path in the top and bottom flange, the provided minimal reinforcement in the bottom flange yielded shortly after vertical cracks emerged in these regions. Given that the proposed splice detail had only non-contact reinforcement in top and bottom flanges, as soon as cracks opened significantly, the effect of non-contact reinforcement vanished and only the post-tensioning ducts provided flexural capacity in the splice section.

Fig. 4.11 presents an enhanced splice detail where threaded rods are embedded in top and bottom flanges of the precast girder segments and are extended within the splice regions. The threaded bars are then coupled in the splice region using a steel plate and tightened to provide additional load path. In order to make the proposed connection effective in both tension and compression, the threaded rods are fixed to the steel plate using nuts on both sides. On the other hand, in order to enhance the shear capacity of the splice, as well as provide a better alignment, to boxes are embedded in the web area of the precast segments and extended in the splice region (similar to Cazaly hangers).

Angle of diagonal cracks were measured for each test. For each test, a wide range of crack angles were observed, ranging between 28 to 45 degrees. It was observed that generally cracks in the precast girder segments were steeper than in the splice regions. Pre-compression in the splice regions was less than precast segments as pretensioning was

discontinued in these regions. Therefore, under the same moment demand, the tensile strain at mid-height of section is more in splices which leads to less steep angles.

According to Mohr circle, the cracking angle depends on the capacity of concrete before tensile cracking. Mohr circle may be used to define the initial crack angle of an uncracked section, assuming the web area in uncracked until the principal tensile strain reaches the tensile capacity of concrete:

$$\tan\theta = \frac{\tau}{\sigma_1 - \sigma_2} = \frac{\sigma_1}{\tau} \tag{4.2}$$

$$\therefore \quad \tau = \sigma_1 \sqrt{1 - \frac{\sigma_x}{\sigma_1}} = f'_t \sqrt{1 + \frac{f_{ps}}{f'_t}} \tag{4.3}$$

in which $\theta =$ crack angle; $\tau =$ concrete cracking shear stress taken as $\tau = v_{cr}$; $\sigma_1 =$ principal tensile stress taken herein as $\sigma_1 = f'_t$; $\sigma_2 =$ principal compression stress; and $f_{ps} =$ prestress applied to the section where $f_{ps} = -\sigma_x = -F/A =$ the effective uniform compression stress due to prestressing. Substituting (4.3) into (4.2) gives:

$$\tan^2\theta = \frac{f'_t}{f'_t + f_{ps}} \tag{4.4}$$

Given that higher levels of prestressing exist in the precast girders due to the effect of pretensioning, it is understandable that the precast concrete according to Eq. (4.4) has steeper crack angle in the precast girder segments compared to the splice regions.

Kim and Mander (2007) showed that for cracked rectangular columns, the crack angle may be found for pinned-fixed end conditions as:

$$\tan^4\theta = \left(\frac{1.57\,\frac{\rho_v A_v}{\rho_t A_g} + 0.6n\rho_v}{1 + 4n\rho_v} \right) \tag{4.5}$$

in which ρ_v =volumetric ratio of transverse steel where $\rho_v = A_{sh}/sb_w$; $A_v = jd.b_w =$ shear area; s =spacing of transverse steel; $b_w =$ width of the web; and $\rho_t = A_{st}/A_g$ volumetric ratio of longitudinal steel, whereA_{st} =total longitudinal column steel area; and $A_g =$ gross area .

This solution is now adapted for prestressed concrete beams such that the longitudinal tensile steel volume is given by $\rho_l = A_s/A_g$, such that when compared to Kim and Mander's column, $2\rho_l = \rho_t$. Therefore, rearranging Eq. (4.5) to give the crack angle for a prestressed concrete beam results in:

$$\tan^4\theta = \frac{A_{sh}jd/s}{A_s}\left(\frac{0.7854 + 0.6nA_s/(b_w d)}{1 + 4nA_{sh}/(b_w s)}\right) \tag{4.6}$$

where $A_{sh} =$ hoopset area, $n = E_s/E_c$; and $A_s =$ area of the tensile longitudinal reinforcement.

Table 4.5 presents the crack angle for positive and negative bending during Test 1 and 2, respectively. The maximum, minimum and typical observed crack angles during the tests are compared with two theoretical cases: (i) initial shear cracking that is based on a Mohr's circle analysis given by Eq. (4.4); and (ii) crack angle based on elastic compatibility truss model theory adapted from Kim and Mander (2007). It is evident that both models provide satisfactory agreement with typical observed crack angles.

Table 4.5 Comparison of crack angle between observed experimental data and Mohr's circle and Kim and Mander model.

Test #	Experimental Observations			Initial shear cracking prediction	Truss cracking prediction
	Min.	Max.	Typ.		
Test 1 (Positive Bending)	27.5°	45°	37°	35.5°	37.1°
Test 2 (Negative Bending)	32°	46°	35°	35.5°	36.1°
Test 3 (Positive Bending)	31°	38°	36°	35.5°	37.1°

4.7 CONCLUSIONS

Different tests were carried out on the spliced girder test specimen to provide a comprehensive understanding of the behavior of splice connections for precast concrete I-girder under different combinations of positive and negative moment and shear. Based on the results described herein, the following conclusions are drawn.

1. While pretensioned strands provide a significant contribution to the overall flexural capacity of precast prestressed concrete sections, pretensioned prestress is not feasible within the cast-in-place splice region. Thus, the splice region is somewhat weaker than the precast girder sections where the pretensioned prestress is fully developed. Therefore splices, ideally, need to be located in those locations where the overall (positive plus negative) moment demands are lower.
2. Because of the existence of the reinforced concrete deck, the splice sections are inherently ductile under large positive post-yield moments. To add further flexural

capacity and maintain the ductility capability, it is recommended that additional top and bottom reinforcement be added through the splice connection to provide a more integral load path within the splice.

3. Splice and girder sections are inherently less ductile for negative moments. To provide appropriate ductility for negative bending, two options may be considered: either increasing the area of the bottom flange or embedding supplementary compression mild steel in the bottom flange.
4. Small cracks tend to completely close after applied loads are removed due to the presence of post-tensioning. Therefore, post-tensioned concrete girder bridges can potentially provide improved durability.
5. If diagonal cracks form an inclined critical failure plane due to shear-flexure interaction, an apparent differential displacement will emerge on either side of the main crack. This abrupt displacement is not to be attributed to a shear slip or interface slip. This differential displacement mainly originates from the rigid body kinematics of the failure mechanism. This aspect is a key finding in this research as it is essential to consider an inclined crack plane when calculating the ultimate load capacity.
6. Diagonal cracks in the splice regions can potentially reduce the flexural performance of the splices. In these regions, the effect of diagonal cracks will shift the compression face of the splice to the adjacent precast girder segment, where the effect of pretensioning reduces the compression capacity of the top flange for

positive bending, hence reducing the nominal capacity as well as ductility of the section.

5 EFFECT OF FLEXURE-SHEAR INTERACTION ON PERFORMANCE OF IN-SPAN SPLICED CONCRETE GIRDERS

5.1 CHAPTER OVERVIEW

While flexure may commonly govern the design of simply supported prestressed concrete bridge, high flexure-shear interaction arises as a critical condition for continuous spans. Moreover, if prestressed concrete girders are in-span spliced, there may be a discontinuity in strength that affects the ultimate limit state behavior. Results of an experimental investigation suggest that diagonal cracks in the splice regions of prestressed concrete girder bridges may adversely affect the flexural behavior of the splices and reduce their post-cracked ultimate strength and deformability. A generalized moment-curvature approach is developed along a diagonal crack plane to directly account for the effects of flexure-shear interaction. The formulation is provided to calculate the nominal capacity of such sections incorporating the effect of existing shear forces in the critical section. Analyzing the behavior on a critical diagonal section is validated from companion full-scale test results of a slab-on-pretensioned-girder system that was post-tensioned continuously through the splice connections to provide load balancing and continuity.

5.2 INTRODUCTION

The flexural design of continuous beams is based on several widely used well-known methods of structural analysis. However, as new structural typologies arise, detailing complexities require more detailed analysis. While the finite element method may be

employed to analyze such detail complexities, the approach is generally not amenable to routine design office production. Other classic analysis tools such as sectional analysis and fiber element methods for moment-curvature analysis offer a simpler approach of sufficient accuracy to provide the structural designer the required insight into the expected structural behavior and hence the adequacy of a design solution.

Moment-curvature methods have been widely used as an adequate structural analysis approach to predict the flexural behavior of the section. While this method has been greatly enhanced and matured for analysis of general reinforced concrete sections, studies to mainstream the approach for prestressed concrete sections continued over the years (Burns, 1964; Thompson and Park, 1980; Naaman et al., 1986; Shushkewich, 1990; Pirayeh Gar et al., 2012; Cattaneo et al., 2012). Many researchers have provided detailed analysis methods to apply principles of moment-curvature analysis for general structural concrete sections, including the effect of mild steel, prestressing strands, axial forces, and different concrete materials. Various numerical approaches have been proposed to effectively calculate the contribution of concrete in compression, such as fiber elements (Oehlers et al., 2010) and trapezoidal integration (Rodriguez and Aristizabal, 2001).

The customary moment-curvature method is based on taking a transverse section of a beam and assuming plane sections remain plane to conduct the analysis. While this approach remains valid under high moment and low shear, such as at the mid-span region of a simply supported beam, it is prone to break down under the presence of high shear and moment, particularly when large diagonal cracks are prevalent. Several researchers have investigated the coupled effect of shear on the flexural performance of the beams

(Rosenblueth and de Cossio, 1965, Sawyer, 1965, Recupero et al., 2005, Massone et al., 2013, Cladera et al., 2015).

For slab-on-prestressed concrete girder bridges, an added difficulty arises when in-span splices exist. Under traffic loads, these splice regions will always have a measure of high moment and high shear. Splices may have lower flexural capacity due to the lack of pretensioning within the splice regions. This inherent weakness may leave the spliced-girder system predisposed to early failure. Moreover, due to the presence of high flexure and high shear it is inevitable that at the ultimate limit state, diagonal cracks will certainly affect overall flexural performance.

In this chapter, a fiber element based moment curvature analysis is adopted as the basic approach to determine the performance of in-span splices for a slab-on-prestressed concrete girder bridge. Using a conventional transverse section moment-curvature approach, modifications to the analysis method are made to account for the effect of diagonal cracks that encapsulate the shear effect along with the associated compression shift phenomenon on the flexural behavior. Then, the method is formulated to calculate the nominal strength capacity of the section, taking into account the existing shear forces in the critical diagonal section. The modified moment-curvature analysis approach and the results of nominal strength capacity are verified against the full-scale experimental test results of an in-span splice region of a reinforced concrete deck slab on prestressed concrete girder test specimen.

5.3 AN ANALYSIS OF FLEXURE-SHEAR INTERACTION

5.3.1 Problem Identification

Fig. 5.1 presents how a spliced prestressed concrete girder may be analyzed for diagonal cracking that passes through the splice region. Fig. 5.1 (a) presents an elevation of a cracked spliced prestressed concrete girder-on-slab bridge composed of two prestressed precast girders and a wet splice region in between. Precast girders are pretensioned for handling and transportation. A wet joint splice, some 600 mm in length, is cast between the precast girders units. The deck slab is cast over the splice and girders and then continuity prestress provided by post-tensioning over the entire length of the beam.

As shown in Fig. 5.1 (b), the prestressing layout varies from the girder segments to the splice region, leading to different strength capacity between these sections. Section A-A shoes a transverse section with both pretensioning and post-tensioning (a section within the precast girder). Section C-C shows a transverse cross-section through the splice region where only the post-tensioning is in effect. A critical case can be imagined, where due to a combination of diagonal cracks and flexural cracks, a Z-plane is formed that creates a critical section. The tension side of such a Z-plane cross-section is within the splice region where no pretensioning exists, and the compression is located in the adjacent girder section where top pretensioning tendons become fully effective forming the B-C cross section. It is postulated that the large concrete compression forces due to existence of top pretensioning strands and lack of supplementary reinforcement and pretensioning in tension side may lead to a critical failure mechanism along the Z-plane (section B-C).

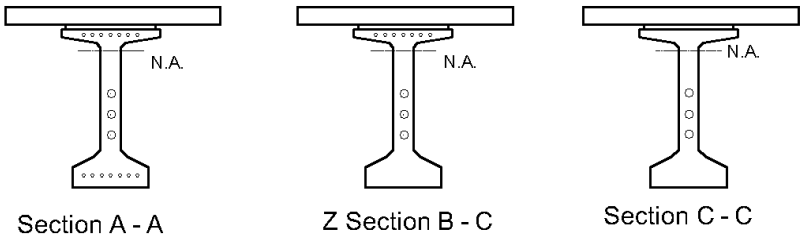

(a) Prestressing detail in different cross sections

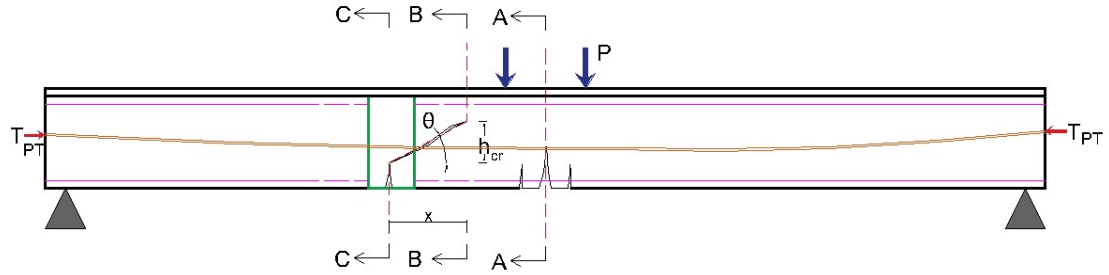

(b) Side Elevation of a beam with vertical and diagonal cracks

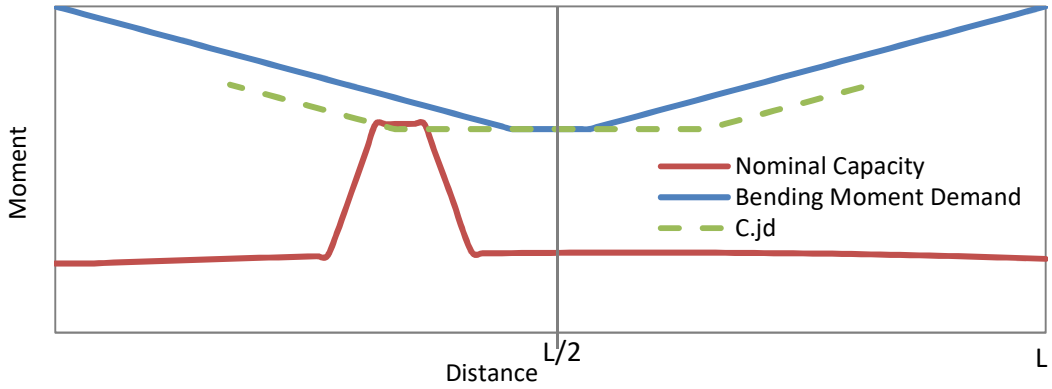

(c) Comparison of bending moment demand and capacity along the length of the beam

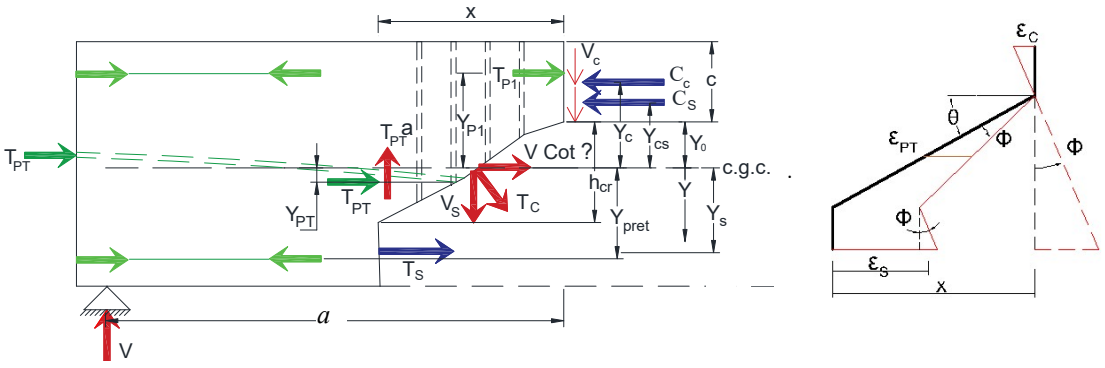

(d) Free-body diagram and strain profile of Z-plane

Fig 5.1. Flexure shear interaction and effect of diagonal cracks

Fig. 5.1 (c) compares the bending moment demand and flexural capacity for each section along the length of the beam. The flexural capacity of the beam is represented by the solid maroon line from which it is evident that the capacity varies such that the precast girder sections maintain a high flexural strength due to existence of both pretensioning and post-tensioning and mild steel reinforcement, while the splice region has substantially lower flexural strength as only post-tensioning contributes in that region.

In Fig. 5.1 (c), two lines represent the ultimate demand along the length of the beam due to applied loads. The solid line represents the bending moment demand calculated based on equilibrium and classical beam theory, which is generally used for design of sections for flexure. Given that diagonal cracks are inevitable in narrow-web members under high flexure and shear, there arises a compression shift along the Z-plane section. This shifted demand is shown in the green dotted line of Fig. 5.1 (c) and is referred to herein as the "C.jd" diagram. The C.jd diagram is analogous to the well-known T.jd diagram that is often used in reinforced concrete design (Park and Paulay, 1975).

Fig. 5.1 (d) depicts the free-body diagram of the beam in Fig 5.1 (a) with a Z-plane cross section. The lower tension side of the section terminates within the comparatively weak splice region; the upper compression side terminates at the location where the upper level tendons fully develop their prestress effect. All parameters are defined in the following section.

In the following, a moment curvature analysis is first presented along the Z-plane. This is then simplified for design purposes to determine the ultimate moment capacity, M_n.

5.3.2 Moment-Curvature Analysis on a Diagonal Crack Plane

Moment curvature analysis can be generalized for situations where the coupled effect of shear and flexure affects the overall behavior of a beam where due to high shear and bending demands lead to excessive flexure cracks as well as diagonal ones. As shown in Fig. 5.1 (d), the potentially critical Z-plane section may be assumed with the associated diagonal flexure-shear crack. In this section, the basic formulation of sectional moment-curvature analysis is generalized to incorporate the existence of shear forces that traverse the critical Z-plane section.

Adopting Bernoulli's plane section hypothesis, the strain profile varies linearly across the section and may be expressed as:

$$\varepsilon(y) = \varepsilon_0 + \emptyset y \tag{5.1}$$

where $\varepsilon(y) =$ strain at distance measured (positive downward) from the reference axis, taken herein as the center of gravity (c.g.c.); $\varepsilon_0 =$ strain at reference axis; and $\emptyset =$ curvature.

For any given increment in curvature, the following coupled relation of axial force and bending moment exists:

$$\begin{Bmatrix} \Delta P \\ \Delta M \end{Bmatrix} = \begin{bmatrix} \dfrac{\partial P}{\partial \varepsilon_0} & \dfrac{\partial P}{\partial \emptyset} \\ \dfrac{\partial M}{\partial \varepsilon_0} & \dfrac{\partial M}{\partial \emptyset} \end{bmatrix} \begin{Bmatrix} \varepsilon_0 \\ \emptyset \end{Bmatrix} \tag{5.2}$$

Based on the free body diagram provided in Fig. 5.1 (d), the equilibrium in the Z-plane section is derived as:

$$M = V.a \tag{5.3}$$

$$M = C_c y_c + C_s y_{cs} + T_{p1} y_{p1} + T_s y_s + T_{PT} y_{PT} + V_s x/2 \quad (5.4)$$

$$P = C_c + C_s - T_{p1} - T_s - T_{PT} - T_c \sin\theta - V\cot\theta \quad (5.5)$$

$$V = V_c + V_s + V_{PT} + T_c \cos\theta \quad (5.6)$$

in which, M = moment taken at the c.g.c. and at distance "a" from the support; V = shear force in the section; P = net axial force in the section; C_c = the compression in concrete; C_s = compression in mild steel; T_{p1} = applied prestress force in the upper level of prestressing strands; T_s = tension force at bottom flange of splice region provided by reinforcing steel (if present); $T_c = x.t_w/\sin\theta$ = tensile force in web concrete; t_w = thickness of the web; T_{PT} = post-tensioned force; V_c = shear carried by concrete in compression zone; V_s =shear carried by transverse reinforcement that crosses the cracked Z-plane; $V_{PT} = T_{PT}.\alpha$ shear carried by vertical component of prestress contributed by harped prestressing strands or post-tensioning tendons; α = drape angle of PT at section; and a = lever arm of the shear force for the given section. It should be noted that the term $V\cot\theta$ which appears in (5.5) and the term $V_s x/2$ that appears in (4.4) represent the coupling effect of shear with flexure in the equilibrium formulation.

In order to solve the equilibrium equations, the strain relations are modified to account for compatibility on the diagonal Z-plane. From the geometry shown in Fig. 5.1 (d):

$$\varepsilon^*(y) = \varepsilon_0 + \emptyset(y + y_0)\text{cosec}\theta \quad (5.7)$$

$$\varepsilon_s = \varepsilon_0 + \emptyset[y + h_{cr}\text{cosec}\theta] \quad (5.8)$$

$$\varepsilon_v = {}^1/_2\, \emptyset h_{cr}\cot\theta \quad (5.9)$$

in which $\varepsilon^*(y)$ = longitudinal strain along the diagonal crack region; ε_s = strain in fibers of bottom flange on tension side; ε_v = strain in vertical transverse reinforcement crossing the diagonal crack; h_{cr} = height of diagonal crack; and θ = angle of the principal diagonal crack. Many researchers have proposed methods to predict the angle of diagonal crack among which, the proposed formula by Kim and Mander (2007) provides quite accurate results for θ.

For moment-curvature analysis, the section is defined with parallel fibers perpendicular to bending moment vector and the curvature is incrementally increased to assure a single valid value for strain. The value of ε_0 is sought so that horizontal equilibrium is achieved in the section. Using constitutive relations for the material for each component, the calculated strains in each fiber are translated into stress and by multiplication of stress and the area of each fiber, the force carried by each fiber can be calculated. The abovementioned compatibility relations would define all equilibrium components except for V_c which afterwards may be calculated using Eq. (5.6), given that V can be calculated using Eq. (5.3). Therefore, for any set of $\emptyset$ and M, all components of equilibrium can be uniquely determined.

The steps in the following algorithm may be used to compute the moment-curvature behavior of a concrete section under coupled effect of shear-flexure interaction. The main aim for each cycle of the analysis is for a specified curvature to find the strain at the reference axis, ε_0.

1. Set $\emptyset_i = \emptyset_{i-1} + \Delta\emptyset$ and assume $V = V_i$ and $\varepsilon_0 = \varepsilon_{0i}$

2. Using Eq. (5.1) and (5.7) to (5.9), calculate the strain in each fiber of the Z-plane section. Subsequently, find the stress and force of each fiber.

3. Using equilibrium, calculate M_i, V_i, and P_i ($V_i^* = {M_i}/{a}$). Check:

   a. $\begin{cases} |P_i - P_{target}| < tolerance \\ |V_i^* - V_i| < tolerance \end{cases}$

4. If tolerance is not met, update ε_{0i} and V:

   a. $\varepsilon_{0i}{}^* = \varepsilon_{0i} - [(P_i - P_{target}) - \frac{\partial P}{\partial \emptyset}\Delta\emptyset]\frac{\partial \varepsilon_0}{\partial P}$

   where $\frac{\partial \varepsilon_0}{\partial P} = \frac{\varepsilon_{0i-1} - \varepsilon_{0i-2}}{P_{i-1} - P_{i-2}}$

   b. $V_i = V_i^*$

5. Calculate V_{ci} and check $V_{ci} < V_{cu} = K\sqrt{f'_c}A_v$

   where $A_v =$ shear area of the compressed concrete; and $f'_c =$ concrete compression strength in MPa. Wolf and Frosch (2007) propose that $K = 0.42$ provides acceptable results for wide range of initial concrete pre-compression.

6. Set $\emptyset_{i+1} = \emptyset_i + \Delta\emptyset$

5.3.3 Nominal Capacity on a Diagonal Failure Plane

Equilibrium and compatibility equations were derived in the previous section to enhance the moment-curvature analysis for load cases where shear-flexure interaction creates a critical Z-plane section. However, for a routine engineering office practice, often the purpose is calculation of nominal capacity at the strength limit state. In this section, the proposed equilibrium and compatibility equations are adopted to calculate the nominal

strength capacity of Z-plane sections and the associated curvature as a general index of capacity and ductility of such sections for the strength limit states.

For nominal moment or flexural strength capacity, the equilibrium and compatibility equations are solved where the specific strain at the extreme compression fiber is set to 0.003 ($\varepsilon_c = 0.003$). In order to solve the problem for nominal capacity, the depth of neutral axis, *c*, is assumed:

$$\emptyset_n = \frac{\varepsilon_c}{c} = \frac{-0.003}{c} = \frac{\varepsilon_0}{y_c - c} \tag{5.10}$$

Given the curvature and strain at extreme compression fiber, the strain for all components may be calculated using Eq. (5.1) and (5.7) to (5.9) where strain at neutral axis can be calculated as:

$$\varepsilon_0 = 0.003\left(\frac{y_c}{c} - 1\right) \tag{5.11}$$

in which y_c = distance from extreme compression fiber to the c.g.c. For nominal bending capacity, the compression force in concrete may simply be calculated using Whitney's equivalent stress block or Karthik-Mander α and β factors (Karthik and Mander, 2011). Strain and stress in steel components as well as shear forces in the section may be calculated using Eq. (5.1), (5.7) to (5.9), and constitutive material relations. By multiplication of the stresses and associated area of each component, the forces may be calculated. By checking the longitudinal equilibrium force, the depth of neutral axis is found by iterating until axial force equilibrium is achieved.

5.4 APPLICATION TO SLAB-ON-SPLICED PRESTRESSED GIRDER TEST SPECIMEN

5.4.1 Test Specimen Description

In this section, the developed principles are applied to predict the behavior of a slab-on-spliced prestressed concrete girder bridge specimen that is post-tensioned for continuity. As shown in Fig. 5.2, the precast girders are pretensioned, and after casting the splice and the deck slab, the entire structure is post-tensioned for continuity. For positive bending (Test Setup 1), the loads are applied at mid-span in the vicinity of Splice 2 (main splice). For negative bending (Test Setup 2), the loads are applied in the overhang portion of the specimen near Splice 3.

Because pretensioning did not exist in the splice region, the flexural capacity of the splices was significantly lower than the adjacent girder. Therefore, for Test 1, the flexural cracks were initiated in the bottom flange of Splice 2 as the bending demand reached the cracking moment. As loads increased, diagonal cracks emerged in the web area and connected with the vertical crack, creating a Z-plane section, where the tension side is located in the splice region and compression side was shifted toward the adjacent girder with pretensioning fully in effect. When the applied loads reached 1870 kN, the specimen failed by crushing of the concrete in the top flange immediately below the applied load.

During Test 2 for negative bending, flexural cracks appeared first in the deck and then extended into the top flange of Splice 3. Due to very high shear demand, diagonal cracks emerged in the web, directed from the applied loads to the interior support. Emergence of vertical flexural cracks and diagonal shear cracks created a critical Z-plane

section, which shifted the compression side of the section into the bottom flange of the adjacent girder. The specimen failed as the loads reached 2000 kN, leading to a premature compression failure with very low ductility.

In the following sections, the developed principles of moment-curvature and nominal strength capacity are applied to predict the behavior of the test specimen. The results are verified by experimental data. Using principles of shear-flexure interaction and the compression shift phenomenon, the failure mode is discussed.

5.4.2 Moment-Curvature Behavior

Fig. 5.3 (a) illustrates the test setup for positive bending. The red line depicts the main crack, which is composed of the vertical flexural crack in the bottom flange of the splice region and the diagonal crack that shifts the compression side of the critical Z-plane section into the adjacent girder segment. The red mark locates the compression failure in the top flange right below one of the applied loads, where pretensioning is fully effective.

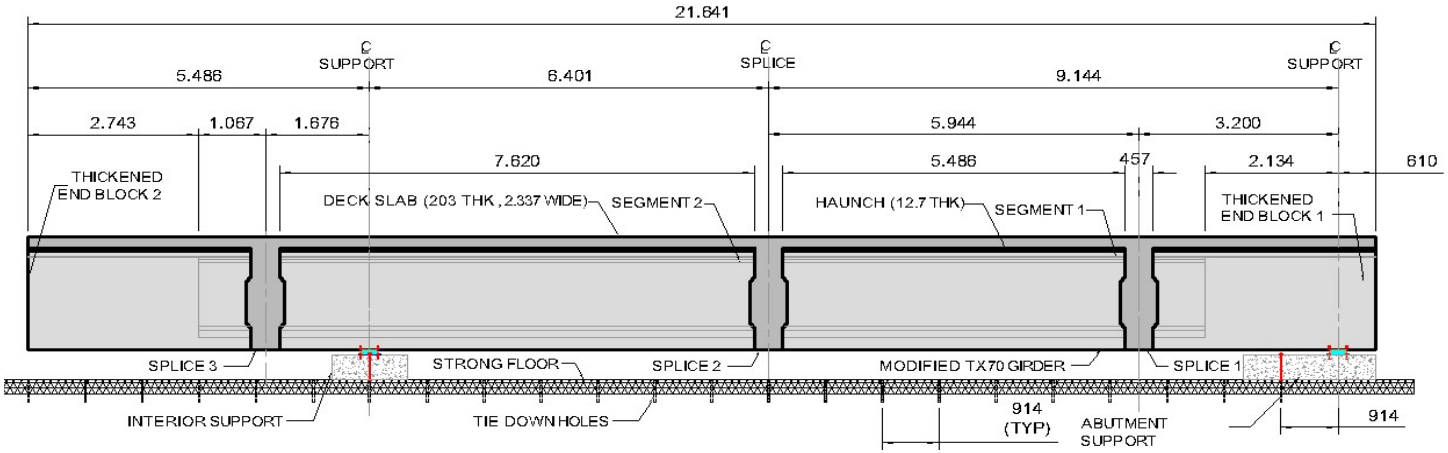

(a) Specimen geometry and splice locations

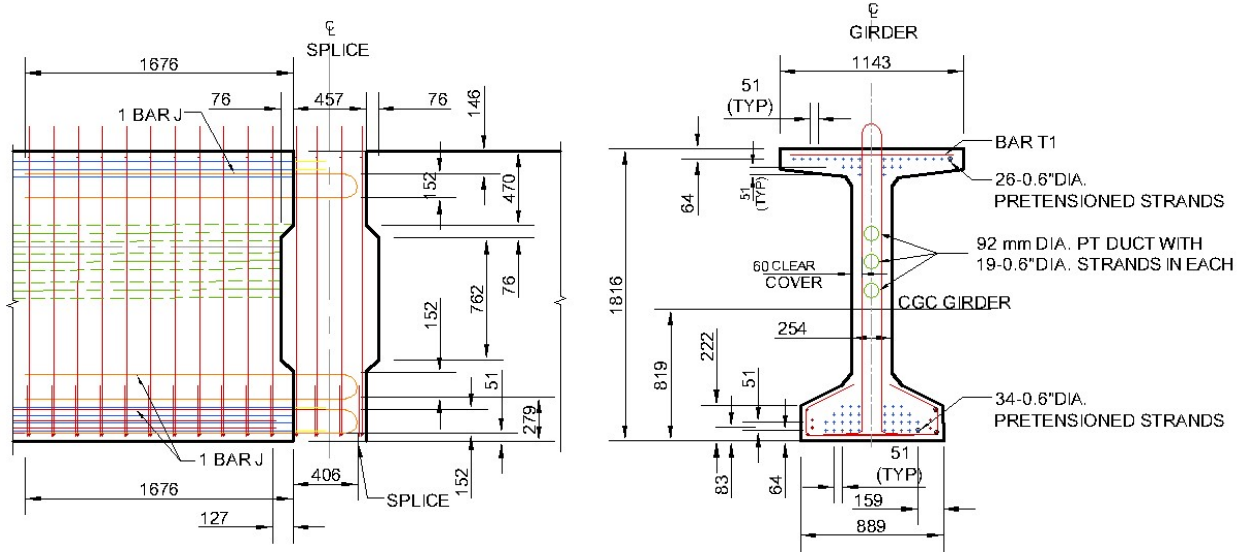

(a) Prestress and reinforcement layout

Fig 5.2. Test Specimen Geometry and Prestress Layout

Fig. 5.3 (b) compares the experimental and numerical results of the moment-curvature for Splice 2 in positive bending. The dotted lines represent the calculated curvature and moment based on the experimental data gathered from the embedded concrete gages and the load cell readings. The solid lines represent the predicted behavior based on generalized moment-curvature analysis. Results of material property tests at the date of testing are used in the prediction model. It is evident that the analysis closely captures the linear behavior of the section. As cracks appear, the section stiffness reduces and the experimental results and numerical prediction follow the same trend. Numerical analysis also closely captures the ultimate strength capacity of the specimen.

In order to understand the effect of shear-flexure interaction on the flexural behavior of a section, the analysis is performed on three sections: (i) the transverse cross-section at Splice 2, (ii) the transverse cross-section at the pretensioned precast section, and (iii) the Z-plane section including the effects of shear-flexure interaction. Fig. 5.3 (c) compares the results of moment-curvature analysis for these three cases. It is evident that the capacity of the precast girder is significantly higher, as pretensioning strands provide high tensile capacity in the bottom flange. However, this higher capacity is limited by a reduction in ductility, as pretensioning provides higher initial compressive stresses in the concrete. The results also reveal that the capacity of the Z-plane section is quite close to the weaker section (splice region), however the ductility of the Z-plane section is less than the splice region. Therefore, it can be inferred that the compression shift phenomenon reduces the capacity of the adjacent girder sections to the capacity of the splice region.

Fig. 5.4 (a) shows the test setup for negative moment where two loads are applied in the overhang portion of the specimen. The red line is the result of emergence of a vertical flexural crack in the deck and top flange of Splice 3 and a diagonal shear crack shifting the compression side of the critical Z-plane section into bottom flange of the adjacent girder segment. Fig. 5.4 (b) compares the experimental and numerical results of moment-curvature analysis for Splice 3 in negative bending. During this test, the failure occurred half-way between Splice 2 and the interior support. Moment-curvature results of Splice 3 suggest that failure occurred out of the splice region. For the interior support, the prediction captures the actual behavior quite well, however, failure occurred before either Splice 3 or the interior support section reach their nominal capacity.

Fig 5.4 (c) compares the moment-curvature behavior of Splice 3, girder segment over the interior support, and the Z-plane section. As expected, the girder segment has higher bending capacity due to the presence of pretensioning strands. Similar to positive bending, the higher capacity of the precast segment is compensated with lower ductility.

Results of moment-curvature analysis for negative bending reveal that the effect of shear-flexure interaction reduces both capacity and ductility of the Z-plane section as compared to the splice region. Given that the compression side of the Z-plane lays in the girder segment, it may be inferred that the capacity of the adjacent girder is also reduced.

The capacity reduction is incorporated in Fig. 5.4. (c), where the bending demand and capacity of the beam are compared. Such capacity reduction leads to premature compression failure occurring half-way between Splice 3 and the interior support, where the compression side of the Z-plane section lies.

5.4.3 Nominal Bending Capacity

For design purposes, the nominal bending capacity of the Z-plane section in both positive and negative bending is calculated as described in Section 5.3.3. Table 5.1 and 5.2 present the strains and forces in each of the components for positive and negative bending, respectively. The strains are defined by setting the depth of neutral axis. Initial strains of concrete and prestressing strands are considered in the calculation for equilibrium.

Table 5.3 and Table 5.4 presents the values of nominal bending capacity calculated using three different methods: (i) from experimental results, (ii) using nominal bending capacity, and (iii) inferred from moment-curvature analysis. It is evident from results that both nominal bending capacity and moment-curvature analysis capture the experimental value with 1.5% error. On the other hand, the results for depth of neutral axis is not very consistent between the nominal capacity calculation and moment-curvature analysis. The former tends to predict a deeper neutral axis, hence predicting lower ductility. The difference may be attributed to the assumptions and simplifications that exists in the calculation of this method.

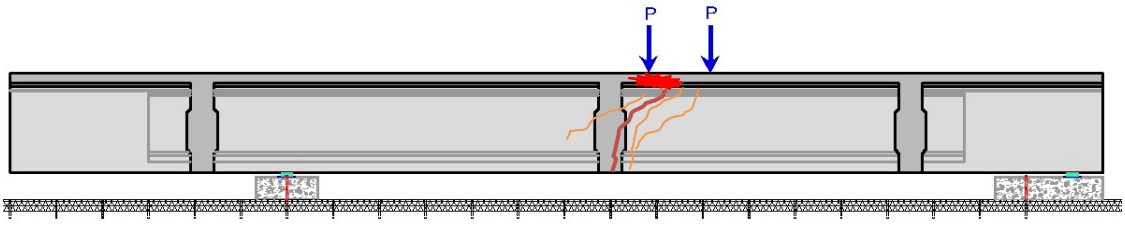

(a) Test Setup and Failure Location

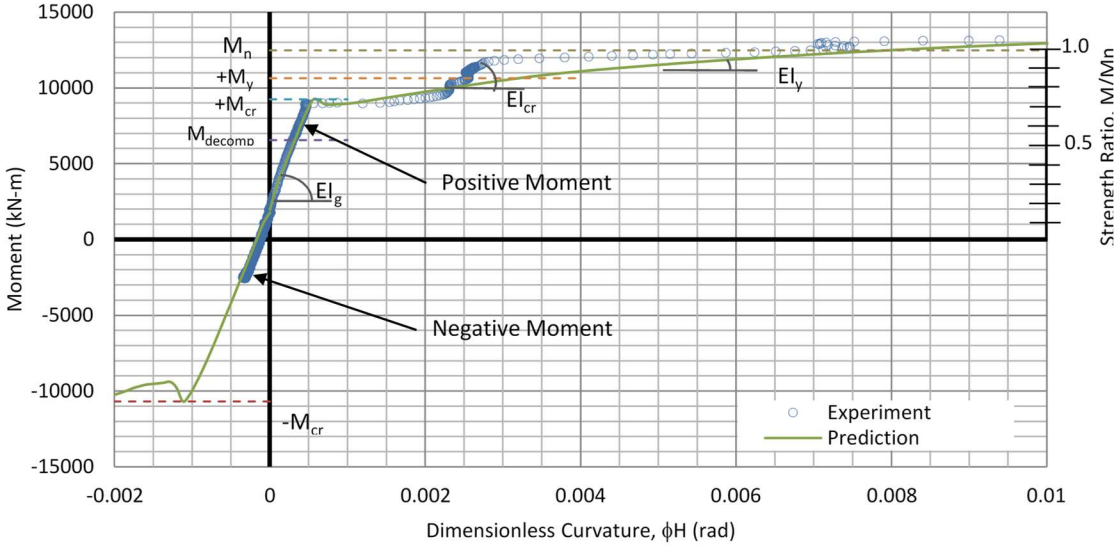

(b) Comparison of experimental and numerical moment-curvature behavior

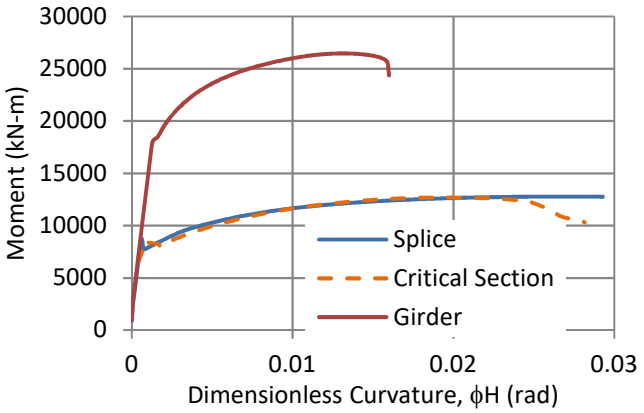

(c) Effect of shear-flexure interaction

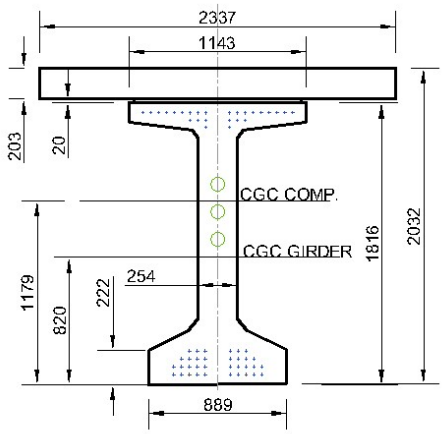

(d) Typical cross section

Fig. 5.3. Moment-curvature analysis of critical Z-plane section in positive bending

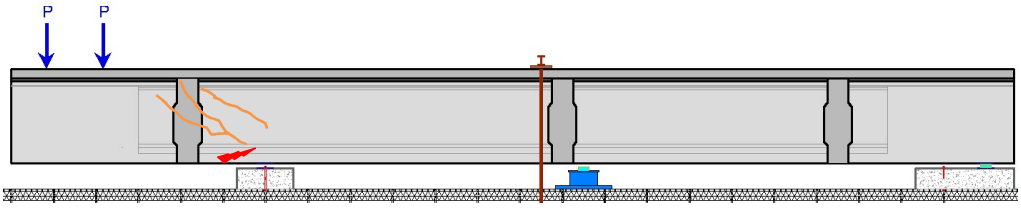

(a) Test Setup and Failure Location

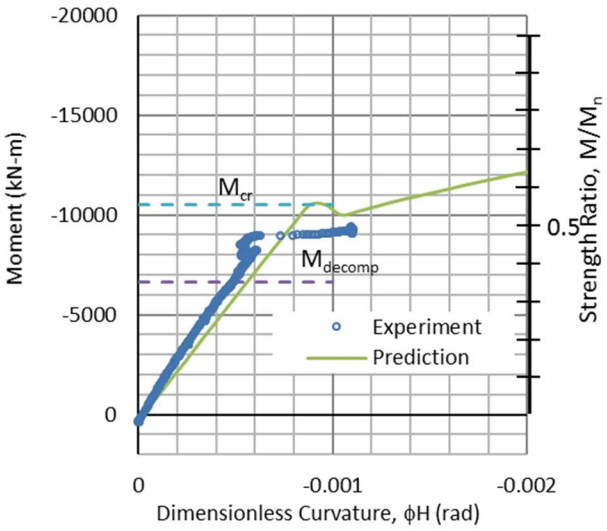

(b) Moment-curvature behavior of Splice 3

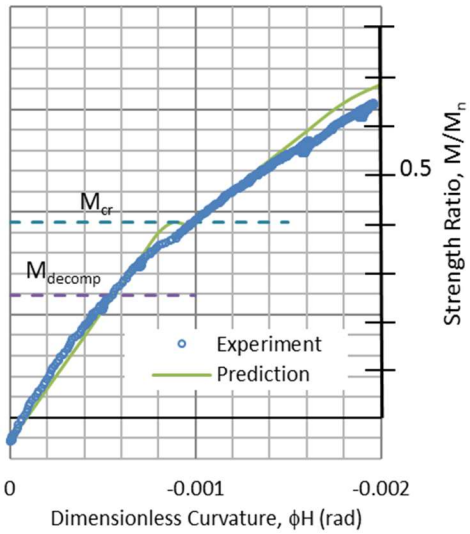

(c) Moment-curvature behavior at Interior support

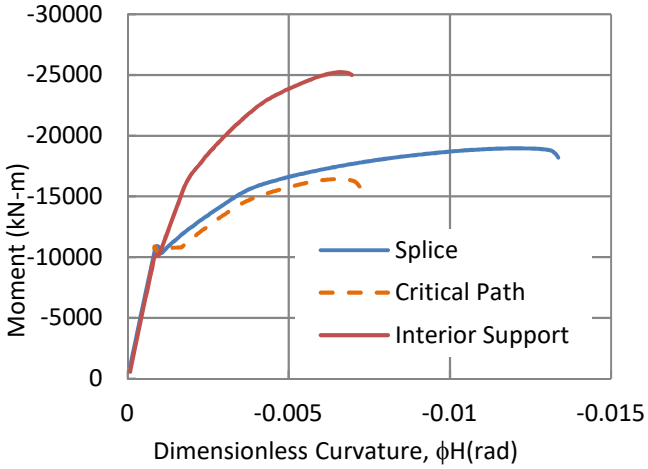

(d) Effect of Shear-flexure interaction

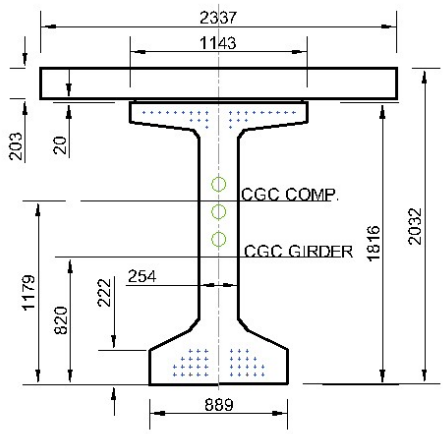

(e) Typical cross-section

Fig. 5.4. Moment-curvature analysis of critical Z-plane section in negative bending

Table 5.1. Strain and forces of Z-plane section components in positive bending

Description	Area (mm)	$Y_{c.g.c.}$ (mm)	Strain (mm/mm)	Force (kN)
Deck Concrete	474,000	-700	-0.003	-13,800
Girder Top Flange	145,000	-520	-0.0005	-5900
Deck Reinforcement	3,290	-700	-0.0021	-1360
Splice Reinforcement	1,136	952	0.0136	480
Top Pretensioning	3,613	-525	0.0055*	3800
Post-tensioning	8,000	152	0.0088*	13,400
$V\cot\theta$	-	-	-	3580

** Initial prestressing strains are included in the final strain profile of the prestressing strands.*

Table 5.2. Strain and forces of Z-plane section components in negative bending

Description	Area (mm)	$Y_{c.g.c.}$ (mm)	Strain (mm/mm)	Force (kN)
Girder Bottom Flange	474,000	-1087	-0.003	-7001
Girder Web Concrete	244,500	-433	-0.0015	-12,925
Deck Reinforcement	3,290	900	0.0014	915
Splice Reinforcement	568	394	0.0008	89
Bottom Pretensioning	4,774	-1118	0.00035	3252
Post-tensioning	8,000	318	0.0063	9930

Table 5.3. Comparison of nominal capacity in positive moment

Description	M_n (kN-m)	Depth of N.A, *c* (mm)
Experimental Result	12,504	-
Nominal Capacity Calculation	12,766	330
Inferred from Moment-Curvature	12,688	298

Table 5.4. Comparison of nominal capacity in negative moment

Description	M_n (kN-m)	Depth of N.A, *c* (mm)
Experimental Result	15,252	-
Nominal Capacity Calculation	15,728	914
Inferred from Moment-Curvature	16,426	790

5.4.4 Beam Deflection Profile

Fig. 5.5 presents the beam deflection profile of the specimen in positive (Fig. 5.5 a) and negative bending (Fig. 5.5 b) for the service limit state as well as ultimate flexural strength. Dots represent the string potentiometer readings while solid lines are the predicted results based on Euler Beam Theory. A total of 36 string potentiometer were placed at 600 mm spacing to accurately measure the deformation of the test specimen. To avoid the effect of side tilting in the recorded data, the string pots were attached to centerline of the soffit of the bottom flange. Possible sources for error are deviation from perpendicular projection after large deformation. To compensate for bearing pad settlements, LVDTs and string pots were placed on either side of the specimen at the location of the supports. Even after the specimen was fully unloaded, some residual deformations were recorded in the elastomeric bearing pads.

For the prediction model, the deformation of the beam was effectively divided in three phases: uncracked (linear elastic behavior), cracked (non-linear elastic behavior) and plastic (non-linear plastic behavior). While the loads remained below cracking limits, the deformation of the beam simply followed the relationship for an elastic beam. As flexural cracks emerge in the splice region, the section modulus of that region is reduced. The reduction factor may be calculated from the moment curvature behavior of the sections (8% for this case). At this stage the beam behaves as a cracked elastic beam. Deformation of this stage can be effectively calculated by reducing the flexural rigidity of the sections in the cracked zone. Table 5.5 summarizes the deformation of specimen in both positive and negative bending in each regime of uncracked, cracked and plastic deformation.

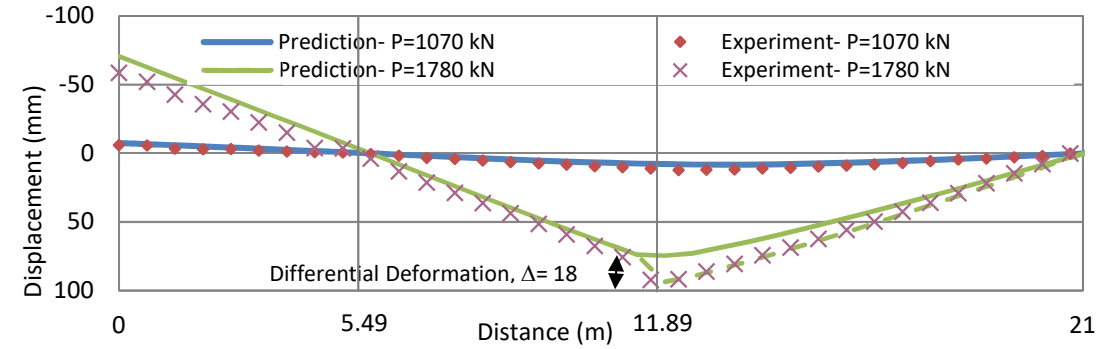

(a) Longitudinal beam deflection profile for positive bending (Test 1)

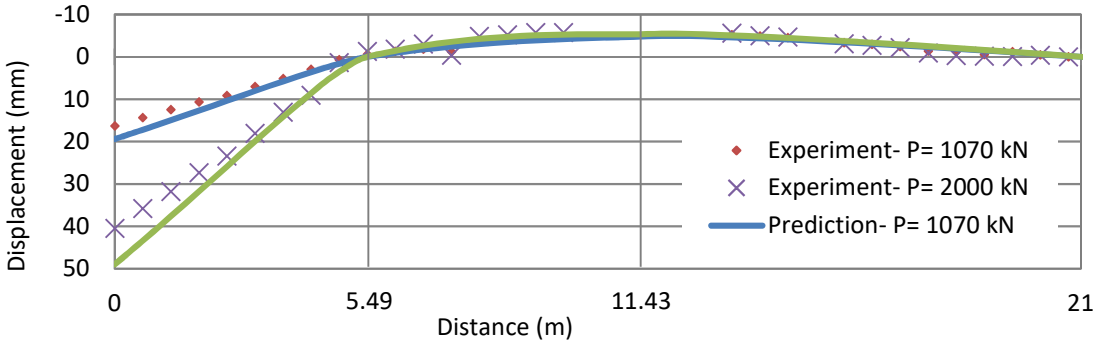

(b) Longitudinal beam deflection profile for negative bending (Test 2)

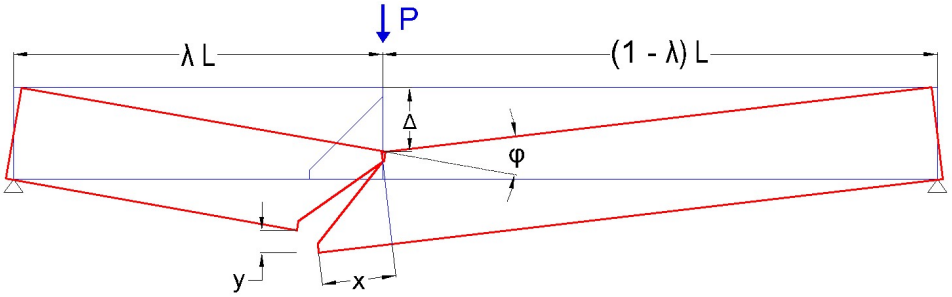

(c) Differential displacement at either side of a Z-plane section

Fig 5.5. Longitudinal deflection profile of test specimen in positive and negative bending.

Table 5.5. Breakdown of maximum deformation of specimen in uncracked, cracked, and plastic phase

Case	Uncracked Deformation (mm)	Cracked Deformation (mm)	Plastic Deformation (mm)
Positive Bending	8.1	9.0	56.1
Negative Bending	10.5	38.1	-

Fig. 5.5 (c) illustrates for a simply supported beam that the differential displacement at both sides of the main crack is simply due to the kinematic rotation of the segments with inclined crack planes. The prediction results are adjusted for this phenomenon in Fig. 5.5 (a) and it is shown by dashed green line. This phenomenon is further discussed in Chapter 4.

5.4.5 Discussion

5.4.5.1 Flexural Strength and Ductility

The results of moment curvature analysis suggest that the test specimen has substantially higher ductility in positive bending. This may be attributed to the compression capacity that the deck concrete provides in positive bending. This fact is also supported by the analysis of nominal bending capacity shown in Table 5.3 for positive bending and in Table 5.4 for negative bending. As presented in Table 5.4, the neutral axis for negative moment remains quite close to the c.g.c. of concrete in the web of the girder to provide adequate concrete area in compression. It may be concluded that in the regions with high negative moment, the area of the bottom flange needs to be increased to provide sufficient compressive capacity as well as to increase ductility by reducing the neutral axis depth. Additional concrete area may be provided by providing thickened sections over the piers and casting integrated diaphragms over the piers.

5.4.5.2 Shear-Flexure Interaction in Splice Design

Comparison of moment-curvature behavior of the transverse section and the Z-plane section reveals that the shear-flexure interaction may adversely affect the flexural performance of the splice regions, where both high bending and shear demands exist. This

effect mainly reduces the ductility of the splice regions, and also substantially reduces the capacity of the adjacent pretensioned girder segments. This reduction in capacity needs to be addressed in the design of such spliced precast girder systems.

Comparison of calculated bending capacity and the experimental data suggests that the effect of shear-flexure interaction can be comprehensively captured if the analysis of Z-plane section is accompanied by the effect of compression shift phenomenon. The compression shift effect can be included in the analysis in two ways: reduction of the capacity of the adjacent precast girder segments in the vicinity of the splice regions; or equivalently, increase of bending demands of the splice regions to match that of the adjacent girder sections.

5.5 CONCLUSIONS AND REMARKS

In this study, moment-curvature analysis and nominal bending capacity of a spliced prestressed concrete girder bridge were developed to incorporate the effects of shear-flexure interaction. The results of proposed models were verified by experimental data from a full-scale in-span spliced prestressed concrete girder test specimen. Based on numerical models and experimental data, the following conclusions are presented:

1. Moment-curvature analysis can be generalized to effectively model the flexural behavior of beams where the shear-flexure interaction may adversely affect the overall behavior of the beams.
2. While detailed finite element analysis or strut-and-tie analysis can effectively capture the effect of shear-flexure interaction, both approaches require more robust and detailed modeling and significantly more calculation time. On the other hand,

shear-flexure interaction can be effectively modeled by modifying the moment-curvature analysis and equilibrium equations. This method provides markedly lower calculation costs.

3. Shear flexure interaction reduces the ductility of the splice regions and substantially reduces the capacity of the adjacent precast girder segments. To take these impacts into account, the bending demand of such regions may be increased to match that of the adjacent girder sections.
4. Slab-on-I-girder bridges have significantly higher ductility in positive bending. In order to avoid brittle compression failure in negative moments, it is recommended that thickened sections be provided over the piers and integrated diaphragms be cast on the girder over the piers to enhance the load carrying capacity and ductility of such sections.
5. One of the impacts of shear-flexure interaction through a diagonal crack is the compression shift phenomenon. The compression side of the critical section is shifted due to the presence of a diagonal crack that can potentially decrease the flexural capacity and ductility of the section. This reduction is more significant where a discontinuity in the beam shifts one side on the critical section to the area with lower or higher flexural capacity. In-span splices in continuous precast prestressed concrete girders is an example of where such an effect can occur.

6 COMPATIBILITY STRUT AND TIE MODELING (C-STM) OF SPLICED PRESTRESSED CONCRETE BRIDGE GIRDERS

6.1 CHAPTER OVERVIEW

Beam theory struggles to accurately predict the behavior of heavily diagonally cracked structural concrete elements particularly when high shear stress demands may adversely affect the overall flexural behavior of such elements. Compatibility Strut-and-Tie Modeling (C-STM) has been introduced as an effective alternative method of structural analysis for members subjected to high moment demands coupled with high shear intensity. In this chapter, the C-STM approach is advanced to model the behavior of slab-on-spliced prestressed concrete girder bridges where shear-flexure interaction may influence system performance particularly near regions that are spliced. Based on previous work on reinforced concrete systems, the C-STM approach is adapted herein to model prestressed concrete systems. The efficacy of the approach is demonstrated by modeling the experimental performance of a reinforced concrete slab-on-prestressed concrete girder super-assemblage that included three spliced regions to consider behavior under high positive moment and moderate shear, high negative moment and high shear, and moderate positive moment and high shear.

6.2 MOTIVATION FOR C-STM ANALYSIS

When structural concrete members are subjected to a combination of high shear force and bending moment demands, both flexural and diagonal cracks may emerge in such regions. While beam theory may effectively model the performance of concrete members where

flexural demands are dominant and shear demands are not so significant, beam theory falls short in capturing the coupling effects of shear and flexure where the presence of diagonal cracks may adversely affect the overall performance of such members.

Flexure-shear interaction is most noticeable in girder members where narrow webs amplify the shear intensity. Therefore, it is not surprising that such a problem may exist in prestressed concrete girder bridges. Moreover, the problem may be further complicated where a prestressed concrete girder system possesses in-span splices. The splice regions also introduce a discontinuity in strength capacity. It follows that an effective analysis method is needed to capture both facets of flexure-shear interaction and strength discontinuity within the modeled structural system.

The concept of strut-and-tie modeling (STM) was introduced as a strength-based design method in the AASHTO LRFD Bridge Design Specifications in 1994 and in ACI 318: Building Code Requirement for Structural Concrete in 2002 for concrete bridges and buildings, respectively. Current methods for STM analysis are based on force-equilibrium only and inevitably, only provide a lower bound limit load solution without providing clear insight as to the expected failure mechanism and location of failure. Throughout decades of research on advancing these models and the STM in particular, the approach has matured and is now well accepted as a conservative design method, particularly for structures with disturbed (D-) regions.

Kim and Mander (1999) enhanced STM methods by also requiring strain compatibility as well as force equilibrium for the analysis of both B and D regions in reinforced concrete elements under combination of flexure and shear. Further

improvements were made by Kim and Mander (2000a; 2000b; 2005; 2007), Scott et al. (2012 a, b), and Karthik et al. (2016). The most recent work of Karthik et al. (2016) includes the effect of concrete tensile capacity as well as tension stiffening, compression softening in concrete struts due to transverse principal tensile strains, and modifications for flexural equivalency. Thus, the Compatibility Strut-and-tie Model (C-STM) is now well developed and verified for reinforced concrete elements under monotonic and cyclic loading.

While numerous studies have investigated the effectiveness of truss modeling for reinforced concrete members, few attempts have been made to incorporate those principles for the analysis of prestressed concrete structures. The literature lacks a validated investigation on modeling of precast prestressed concrete structures with cast-in-place joints and composite beam sections. In this chapter, the C-STM approach is advanced to model the behavior of a reinforced concrete slab-on-spliced prestressed concrete girder bridge that is post-tensioned for continuity. Unlike most of the previous studies, analysis is conducted in displacement control to capture the post-peak behavior followed by static unloading to infer the residual displacement of the structure.

In this chapter, the analysis theory and computational procedures are developed and applied to predict the behavior of the structure in positive bending, negative bending, and high shear. The results of C-STM is then validated through experimental data of a full-scale super-assemblage test specimen. Computational modeling to capture nonlinear behavior is performed using the commercial SAP2000 software (CSI 2016). A three-layered model is developed in 2-D where each of the three layers represent a sub-truss,

specifically: (a) concrete truss action that captures the applied prestress action; (b) concrete arch action that includes post-tensioning effects; and (c) steel truss action that inherently caters for pretensioning actions. Based on the numerical modeling schemes for discrete truss modeling proposed by Kim and Mander (1999), a variable angle truss model is considered to model the behavior of disturbed regions (D-regions), with constant truss modeling representing "beam" region (B-region) behavior.

The efficacy of the approach is demonstrated by modeling the experimental performance of a reinforced concrete slab-on-prestressed concrete girder super-assemblage that included three spliced regions to consider behavior under high positive bending and moderate shear, high negative bending and high shear, and moderate positive bending and high shear.

6.3 THEORY

This section presents the necessary theory to enable one to apply the C-STM technique to a spliced prestressed concrete girder bridge system. The necessary geometric considerations are discussed first as shown in Fig. 6.1. Then the axial stiffness, material strength, and prestressing considerations follow.

6.3.1 Geometry

Fig. 6.1 (a) presents the geometry of a general prestressed concrete girder bridge span with a cast-in-place deck slab. The system shown possesses an in-span splice within a high positive moment region. The structure is post-tensioned for overall continuity. Concrete, mild steel reinforcement, pretensioning strands and post-tensioning ducts are components

that interactively contribute to the load carrying capacity of the structure. As proposed in previous studies (Scott et al. 2012 a, b), loads are transferred through two main actions: truss action and arch actions. In truss action, concrete compression struts and chords are tied with transverse mild steel and tension steel to create a truss action and transfer the loads to supports. Arch action is mainly effective for deep members, were loads are directly transferred to supports through diagonal arch members. While spliced concrete girder bridges are usually composed of long spans, different load combinations may activate the arch actions in such structures. Therefore, in lieu of a more precise and conclusive analysis, the arch action is also considered in the analysis herein.

Fig. 6.1 (b) and (c) present the sub-truss geometries for the general slab-on-spliced prestressed concrete girder bridge. In order to incorporate both truss action and arch action, two main sub-trusses are required. First is the truss effect which incorporates the effects of the concrete compression chord, diagonal concrete compression struts, longitudinal and transverse mild steel, and pretensioning strands (Fig. 6.1 [b]). Second is the arch action effect which also incorporates any effects of post-tensioning (PT) ducts (Fig. 6.1 [c]). Given the draped nature of PT ducts where the c.g.s. elevation may vary along the length of the span, it may not be feasible to lump PT actions at either the top or bottom chord as part of truss action. Therefore, it is necessary to represent the PT as part of the arch sub-truss. In order to provide strain compatibility, the associated nodes of each sub-truss are restrained to move equally.

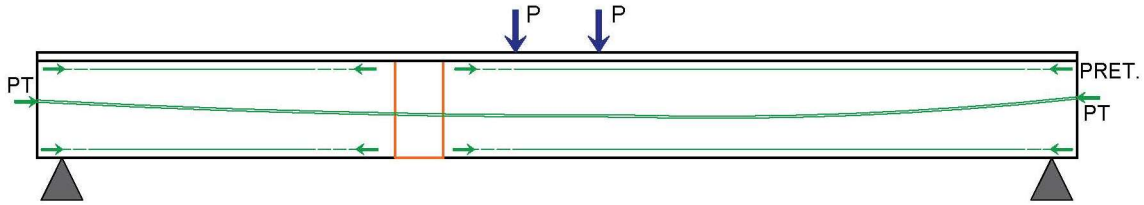

(a) Spliced Prestressed Concrete Girder

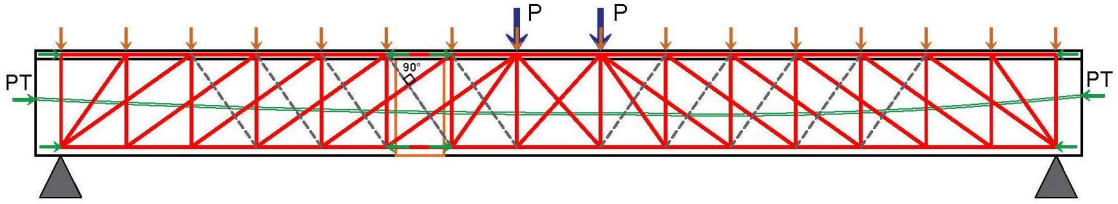

(b) Truss layout and dummy members

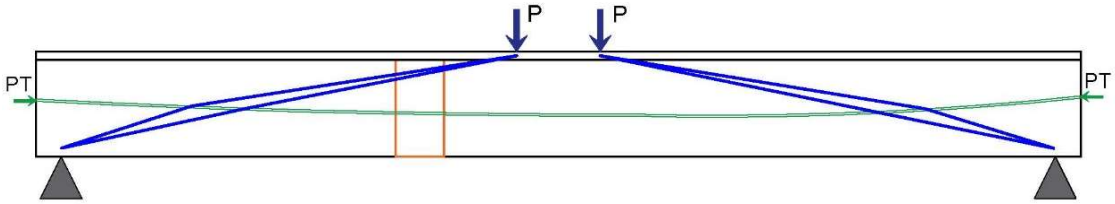

(c) Arch action and post-tensioning effects

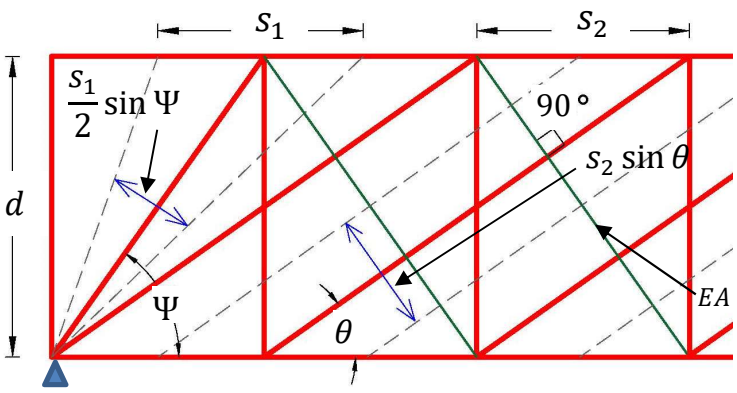

(d) Geometry proportion and strut width calculation in disturbed regions

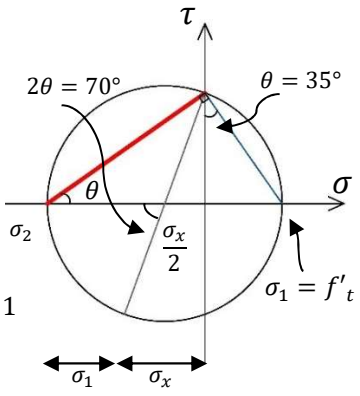

(e) Mohr circle for crack angle calculation (values shown for N=2)

Fig. 6.1. Spliced prestressed girder and truss model geometry development

Fig. 6.1 (d) depicts how one may model end regions (or other disturbed regions near applied loads). As proposed by Kim and Mander (1999), a variable angle truss model is adopted for the analysis of the specimen in the disturbed regions (D-regions) in the vicinity of applied loads and supports. The constant angle truss model is used to model the rest of the beam region (B-regions) away from the D-region.

Karthik et al. (2016) recently demonstrated that softening of concrete struts due to transverse tension may markedly reduce the load carrying capacity of such strut members. Therefore, it is necessary to reduce the strut strength capacity in accordance with the transverse to strut strain ratio, $\varepsilon_1/\varepsilon_2$. Thus, to capture the strain transverse to the struts, a dummy diagonal tension tie member is used that possesses an axial rigidity of $EA = 1$. Therefore, the force in these dummy members is equal to the member strain ε_1.

As shown in Fig. 6.1 (d), in order to make ensure that dummy members are perpendicular to compression struts, the following geometric relation must hold between the depth of the beam (d) and the width of the panels (s_2):

$$s_2 = d/\sqrt{N} \tag{6.1}$$

$$\cot\theta = \sqrt{N} \tag{6.2}$$

in which $N =$ number of panels; and θ is the angle of compression struts. For a single panel ($N = 1$), $\theta = 45°$; for a double panel ($N = 2$), $\theta = 35.26°$; for a triple panel ($N = 3$), $\theta = 30°$; and for four panels ($N = 4$), $\theta = 26.2°$. Diagonal crack angle (θ) may be determined by using methods presented in Chapter 4.

6.3.2 Axial Rigidity

As shown in Fig. 6.1 (b) and (c), truss action and arch action contribute simultaneously to transfer the loads. Scott et al. (2012 a, b) presented a method to apportion the width of the member (width of the web for I-shaped girders), between the truss action and arch action. The ratio is based on the proportionality of the shear force carried by truss and arch action:

$$\eta = \frac{V_{arch}}{V_{arch} + V_{truss}} = \frac{\rho_L}{\rho_L + \rho_T \cot^2\theta} \tag{6.3}$$

in which $\eta =$ arch width scaler, $\rho_L =$ volumetric ratio of longitudinal steel; and $\rho_T =$ volumetric ratio of transverse steel.

Fig. 6.1 (d) illustrates the method for calculating the breadth of struts for both the D-region and B-region:

$$b_{s-B} = s_2 \sin\theta \tag{6.4a}$$

$$b_{s-D} = \frac{1}{2} s_1 \sin\Psi \tag{6.4b}$$

where $b_{s-B} =$ breadth of strut in B-region; $b_{s-D} =$ breadth of strut in D-region; and s_2, s_1, and Ψ are defined in Fig. 6.1 (d).

The width of the arch members, according to Holden et al. (2003), varies as a parabola and may be replaced by a prismatic member whose breadth is:

$$W_A = \frac{3}{8} jd \sqrt{1 + \left(\frac{jd}{L}\right)^2} \tag{6.5}$$

where $L =$ length of arch member; and jd = internal lever arm of tensile force which may be taken as the depth of the truss.

Separate overlaying sub-trusses may be considered to model the contribution of steel elements and concrete elements individually. For the specific problem at hand, the

concrete top chord consists of the transformed area of the deck and area of the prestressed girder top flange. The concrete bottom chord consists of the area of the bottom flange. The area of the narrow web of the prestressed concrete girder may be apportioned between arch and strut members using Eq. (6.3).

It is essential to include the tensile capacity of the concrete for a prestressed concrete system. Therefore, tension concrete ties are included in the model as well. Scott et al. (2012 a, b) proposed the following method to calculate the effective area of concrete tension ties:

$$A_{c-tie} = (4c + 2d_h)N_h s \tag{6.6}$$

in which A_{c-ti} = area of concrete tension tie, c = concrete cover, d_h = diameter of stirrups, N_h = number of stirrups between two ties; and s = spacing of stirrups.

6.3.3 Material Modeling for C-STM

Fig 6.2 presents the tri-linear representation of nonlinear material behavior. While the Mander concrete model (Mander et al., 1988) may be used, it is essential to apply a trilinear simplification for computation that use the likes of the SAP2000 software. An equivalent tri-linear form of the Karthik et al. (2011) model should be more convenient for general use as it also appropriately deals with the tensile behavior in a trilinear fashion.

As discussed above, the top chord of concrete sub-truss is composed of both deck concrete, the haunch concrete (if any), and the upper flange of the girder. A weighted average method based on area and strain at the center of gravity of each component may be used to define the equivalent area and material properties for the top chord:

$$A_{topChord} = A_d n + A_{tf} + A_h \tag{6.7}$$

$$f'_{c-comp} = \frac{(f'_{c-d}(A_d + A_h)n + f'_{c-g}A_{tf})}{A_{topChord}} \tag{6.8}$$

$$\varepsilon_{eff} = \frac{(\varepsilon_c(A_d+A_h)n+\varepsilon_g A_{tf})}{A_{topChord}} \tag{6.9}$$

where A_d = the area of the deck; A_{tf} = the area of top flange of the girder; A_h = the area of the haunch; $n = E_{c-dec}\ /E_{c-girder}$; f'_{c-comp} = the effective compressive strength of top chord before application of flexural equivalency scalar; f'_{c-d} = the measured compressive strength of the deck; f'_{c-g} = the measured compressive strength of the girder; ε_{eff} = the effective equivalent strain in the compression chord; ε_c = strain in extreme compression fiber of the deck; and ε_g = the strain in extreme compression fiber of the top flange of the girder.

The compression capacity of the concrete diagonal struts require adjustment to account for the compression softening arising from transverse tension stresses in the concrete between the diagonal as given by the recent calibration of early data by Karthik et al. (2016) who define the softening coefficient as:

$$\zeta = \frac{f_{2,max}}{f'_c} = \frac{1}{1 - 0.25\varepsilon_1/\varepsilon_2} \tag{6.10}$$

where $f_{2,max}$ = the softened concrete strength in struts; ε_1 = the principal tension strain transverse to a particular compression strut; and ε_2 = the inferred compression strain in the diagonal strut.

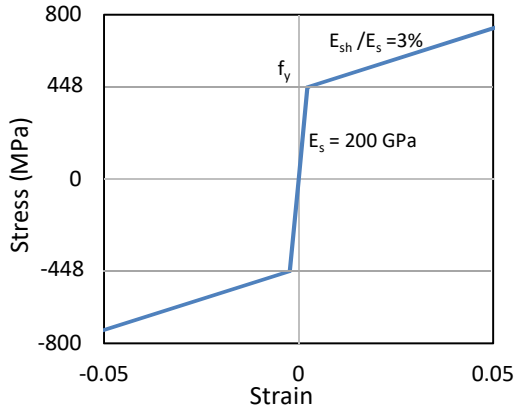

(a) Mild steel

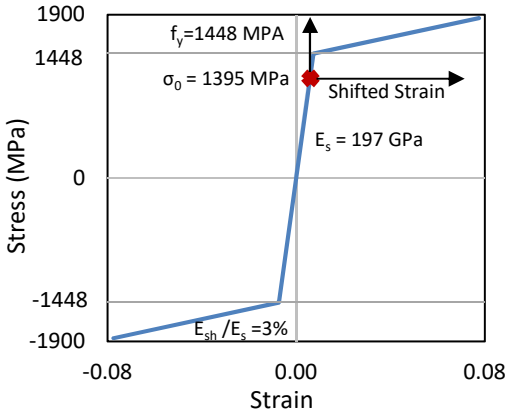

(b) Prestressing strand

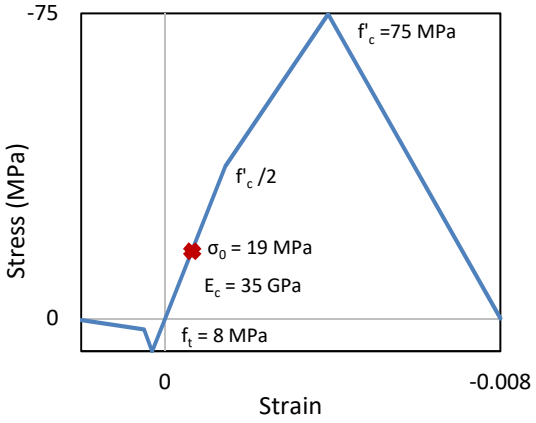

(c) Girder concrete

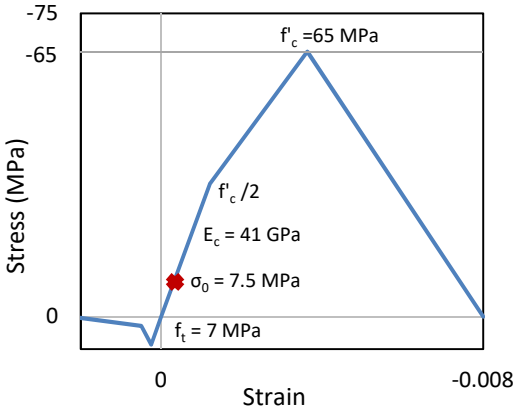

(d) Splice concrete

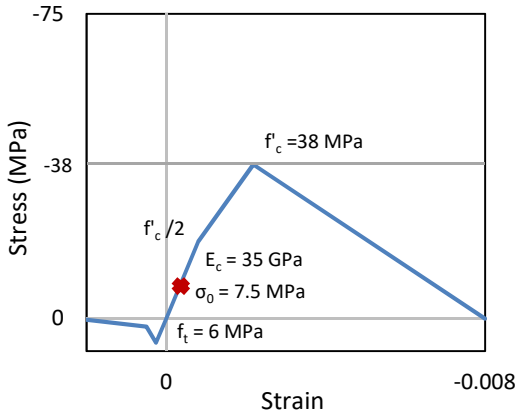

(e) Deck concrete

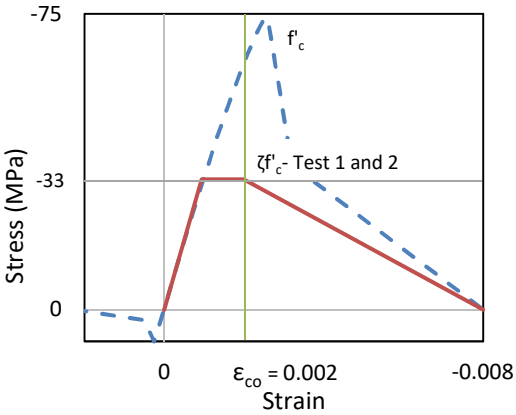

(f) Strut and Arch Concrete

Fig. 6.2. Material properties for C-STM.

For reinforcing mild steel, the constitutive model proposed by Urmson and Mander (2012) is adopted and replaced by an equivalent bilinear curve representing the elastic and post-yield behavior of mild steel material.

For prestressing tendons, the stress-strain model proposed by Menegotto and Pinto (1973) is first adopted and then linearized over the region of expected interest using a bilinear representation to capture the elastoplastic behavior of strands.

Red marks on Fig. 6.2 graphs represent the pre-existing state of strain and stress in members prior to application of live load. Such pre-existing strain (ε_0) is the result of the applied prestress after losses. For each member, ε_0 depends on the prestressing and construction sequence, however for most practical cases it is expected that girders are generally both pretensioned and post-tensioned; while only PT is normally considered present within the splice region.

The stress-strain relation of pretensioning strands and PT ducts must be shifted to incorporate the initial locked-in strains. For pretensioning strands, the locked-in strain is the strain in strand when the girder concrete is cast and after losses. For PT ducts, the locked-in strain is the strain in post-tensioning strands when PT ducts are grouted and after losses.

6.3.4 Analysis Method and Procedure

This study intends to provide a thorough insight of the behavior of slab-on-spliced prestressed concrete girder bridges. In order to capture the post-peak behavior of the structure, it is necessary that analysis is conducted in displacement control (ductile loading). Also, to fully capture the force-deformation behavior of the structure as well as

hysteresis properties of the bridge, unloading is statically applied to assess the residual displacement and thereby infer the damage to the system following overload.

Given that behavior of prestressed concrete girder bridges are highly dependable on the sequence of construction, six steps for executing the modeling are needed:

STEP 1. Application of pretensioning on individual precast girder segments; adjustment of strain in pretensioning strand.

STEP 2. Assemblage of precast segments; casting splices and deck concrete. application of PT; adjustment of strain in PT strands.

STEP 3. Application of dead load.

STEP 4. Application of live load to determine ε_1 and ε_2 in struts and ties; adjustment of strength of struts using Eq. (5.10).

STEP 5. Application of live load up to failure.

STEP 6. Unloading the structure to zero live load.

For *STEP 1*, pretensioning forces are applied at the point where strands are fully bonded to the concrete. For *STEP 2*, the PT forces are applied at the anchorage plate of PT ducts. The load balancing effect of PT is incorporated through application of vertical loads at the nodes of bottom chords. For *STEP 3*, the dead load is applied at nodes of the top chord, and distributed based on the tributary area of each panel.

Given that cracking of concrete or yielding of steel is not expected in the construction stages (under dead load and prestressing effects), for *STEP 1* through *STEP 3*, loads are applied statically and analysis is run in a single stage linear mode.

For *STEP 4*, the stress-strain relation of strands is adjusted to take into account the locked-in initial strains. Live loads are applied and ε_1 and ε_2 in struts and ties are recorded. For *STEP 5*, the strength of the struts is adjusted based on the predicted ε_1 and ε_2 in *STEP 4*, using Eq. (6.10).

Application of live load may be done through force control or displacement control. With the former, the analysis generally converges faster and perfectly captures the behavior of the structure just prior to failure at which time the analysis may not correctly converge.

A displacement control analysis is needed to continue beyond peak load and capture the post-peak behavior of the structure. This approach also enables the unloading analysis (*STEP 6*) to capture the residual displacement and existing stiffness of the structure.

For *STEP 6*, the latest stress-strain state of each member after failure in *STEP 5* is considered as the initial condition of the unloading portion. Given that the main objective for unloading analysis is determination of residual displacement and existing stiffness of the structure after overload, a static single-stage linear analysis should suffice.

6.4 APPLICATION AND VALIDATION

The C-STM approach is adapted to predict the behavior of a reinforced concrete slab-on-spliced prestressed concrete girder test specimen. The test specimen is composed of four prestressed concrete girder segments and three cast-in-place splices with a cast-in-place reinforced concrete deck slab. The entire structure is then post-tensioned for overall

continuity. Each of the three splices were tested in different experimental setups to assess the performance of in-span splices for various load combinations.

For each of these test setups, the C-STM analysis was carried out in three steps:

STEP 1. Dead load and prestressing loads were applied to the structure and the state of stress and strain for each member was recorded.

STEP 2. The initial state of stress and strain in each member was updated based on the results of *STEP 1* and live loads were applied. Transverse and axial strains (ε_1 and ε_2) for each strut were recorded.

STEP 3. Based on the results of ε_1 and ε_2 from *STEP 2* and using Eq. (15), the strength of struts was adjusted and live loads were applied again. A second analysis was done through application of live load. Transverse strain for critical struts were recorded through the dummy members. Using Eq. (6.10), the strength of the struts was adjusted and the analysis was run for the third time to capture the behavior of the specimen.

Application of live load is modeled in two stages: loading and unloading. For the loading portion, load cases are defined as multi-stage nonlinear static loads applied initially in force control and then displacement control. For unloading, the initial condition of stress and strain of the members is set to the last state of the loading portion to capture the post-peak stiffness of the structure. Unloading of the structure is defined as a linear static load case.

Figs. 6.3, 6.4, and 6.5 present the test setup, sub-trusses for C-STM analysis, and comparative results of experimental behavior and C-STM results for each of the testing

stages. In this section, results of each stage of testing is elaborated and the failure mode described. As shown in Fig. 6.3 through 6.5 (a), (b), and (c), three sub-trusses are defined for each test setup, as follows:

1. A concrete sub-truss that incorporates the contribution of concrete in truss action including the top and bottom flanges, concrete tension ties, and concrete compression struts.
2. An arch action and PT sub-truss, that models the contribution of arch action as well as the combined effect of the post-tensioning tendons.
3. A steel and pretensioning strand sub-truss that represents the contribution of transverse mild steel reinforcement as well as top and bottom pretensioning strands and longitudinal deck reinforcement.

6.4.1 Test Setup 1 - Experimental vs. Computational Results

For Test 1, the loads were applied close to mid-span nearby the Splice 2 region to assess the performance of Splice 2 under high positive moment and moderate shear intensity. The diagonal crack angle was $\theta = 35.5°$. Therefore, the two-panel configuration ($\theta = 35.26°$ was chosen that was closest to the crack angle. Based on the first live load analysis, at the time of failure, the transverse strain (ε_1) in the critical strut reached 0.013. Using Eq. (6.10), the strut softening coefficient was determined: $\zeta = 0.44$.

Fig. 6.3 (d) presents two longitudinal displacement profiles for the super-assemblage specimen during Test 1 at two specific loads: (i) $2P = 2140\ kN$ representing the service limit state; and (ii) and $2P = 3560\ kN$ at failure. Very good agreement exists between experimental observation and the computed C-STM results prior to cracking.

Even though the trend is captured quite well at maximum load, a small discrepancy exists close to the splice region, which is attributed to the differential displacement at either side of the main crack, observed to be 18 mm. As discussed in the previous chapter, such differential displacement is attributed to the kinematics of the cracked rigid bodies rotating about a common point in the deck slab. The differences are therefore attributed to a measurement feature rather than a computational modeling deficiency. Evidence of this is shown in Fig. 6.3 (e) where the force-deformation behavior of the specimen at mid-span and Splice 2 is presented. The computational C-STM has captured the initial stiffness, cracking, post-cracked behavior and maximum strength remarkably well. Moreover, due to the displacement controlled analysis, the sudden drop in post-peak resistance was able to be captured.

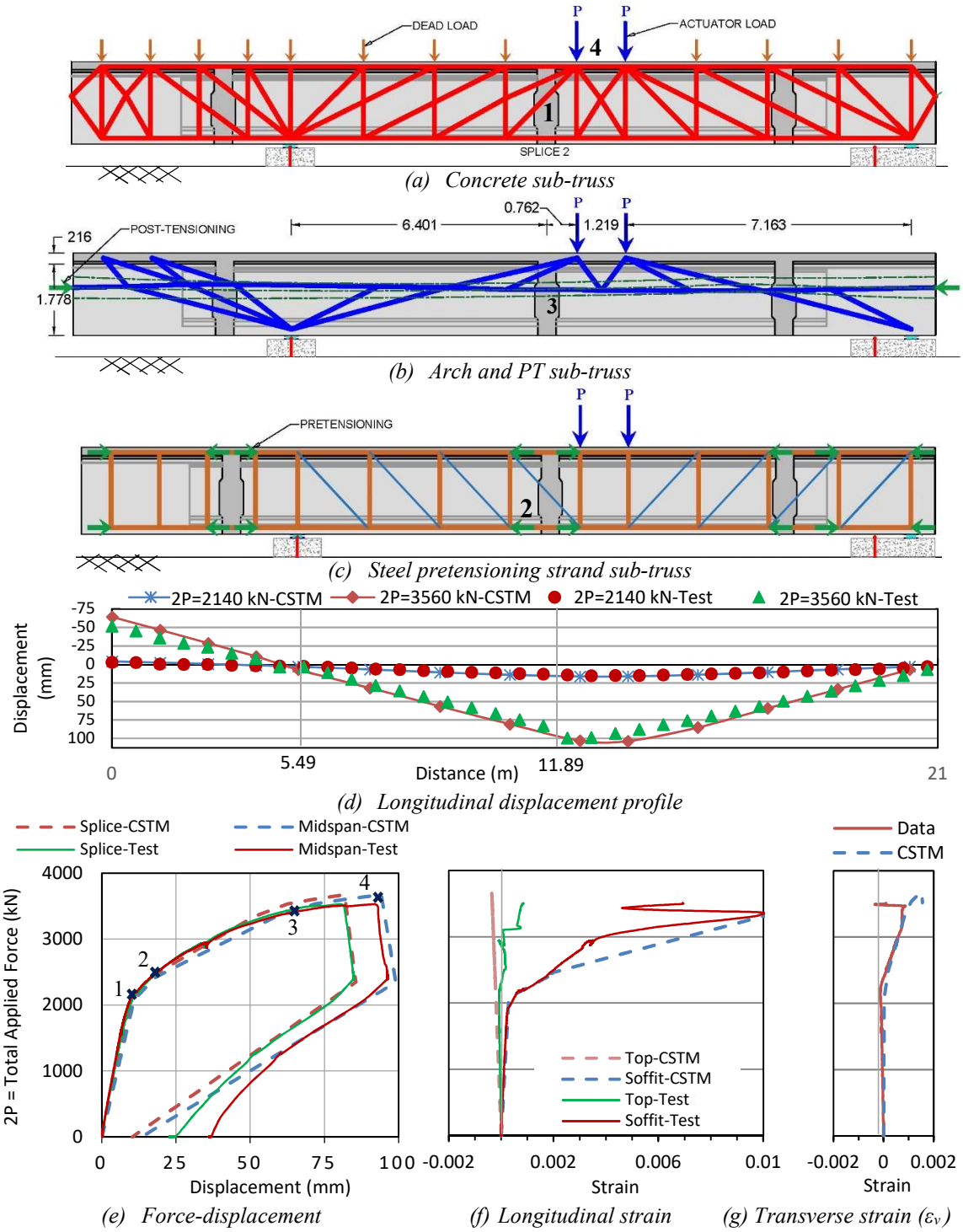

Fig 6.3. Positive moment analysis for Test 1 showing sub-truss configurations for the experimental specimen.

After the specimen achieved its maximum capacity of $2P = 3545\,kN$, the pressure in the actuator was released and the loads removed. This led to a reduction in deflection to 35 mm. The computational reduction in displacement led to a linear drop-off in loads. Initially the unloading test and computed results agree very well, however for loads below $2P = 1200\,kN$ a discrepancy results. This difference is considered to be attributed to partial rather than full crack closure.

Numbers shown on Fig. 6.3 (a), (b), (c), and (e) represent the main events that led to failure. According to C-STM results, when loads reached $2P = 2080\,kN$, concrete in bottom flange of Splice 2 cracked (Event 1). As loads reached $2P = 2430\,kN$, mild steel on bottom flange of Splice 2 yielded (Event 2). Stress in top chord between the applied loads reached $0.5f'_c$, when applied load was $2P = 2740\,kN$. At $2P = 3535\,kN$, PT yielded in the Splice 2 region (Event 3). At this point the stiffness almost plateaued and plastic hinge formed in the splice section. As loads increased, stress in the top flange rapidly increased and reached f'_c and failure occurred (Event 4). At this time, the stress in critical struts reached 93% of the softened capacity.

C-STM results matches the experimental observation as it also follows the same chain of events that led to failure. Also, excessive transverse strain in struts suggests an extended network of diagonal cracks in the web, which also matches the experimental observation.

Fig. 6.3 (f) and (g) compare the strain in longitudinal and transverse reinforcement of Splice 2, respectively. As shown in Fig. 6.3 (f), reinforcement yielded in the bottom flange of splice (Event 2), as only minimal reinforcement is present in bottom flange of

Splice 2; no pretensioning strand passed through the splice region. As for the top flange, strains follow the strain in the compression concrete and does not yield. Results of Fig. 6.3 (g) show the transverse strain measured on a hoop within Splice 2. For both cases, the reading is defined in the vicinity of the maximum loads. While for both cases, linear behavior is evident throughout the entire loading, the rate of change in strain increases when the mild steel in the bottom flange of Splice 2 yields (Event 2).

6.4.2 Test Setup 2 - Experimental vs. Computational Results

Fig. 6.4 presents the results for Test 2, where the loads were applied at the overhang portion of the test specimen to assess the performance of Splice 3 for high negative moment and high shear intensity. The diagonal crack angle was $\theta = 35.5°$. Therefore, the two-panel configuration ($\theta = 35.26°$) was chosen as it is closest to the crack angle. Based on the first live load analysis, at the time of failure, the transverse strain (ε_1) in critical strut reached 0.0122. Using Eq. (15), the strut softening coefficient was determined: $\zeta = 0.46$.

Fig. 6.4 (d) presents two longitudinal displacement profiles for the super-assemblage specimen during Test 2 at two specific loads: (i) $2P = 2140\ kN$ representing the service limit state; and (ii) and $2P = 4000\ kN$ at failure. Results of C-STM are in noticeably good agreement with the experimental observations for both service limit state (uncracked behavior) and at failure. In order to capture the actual displacement of the test specimen, the supports and the tie-down are modeled as flexible springs, rather than rigid supports.

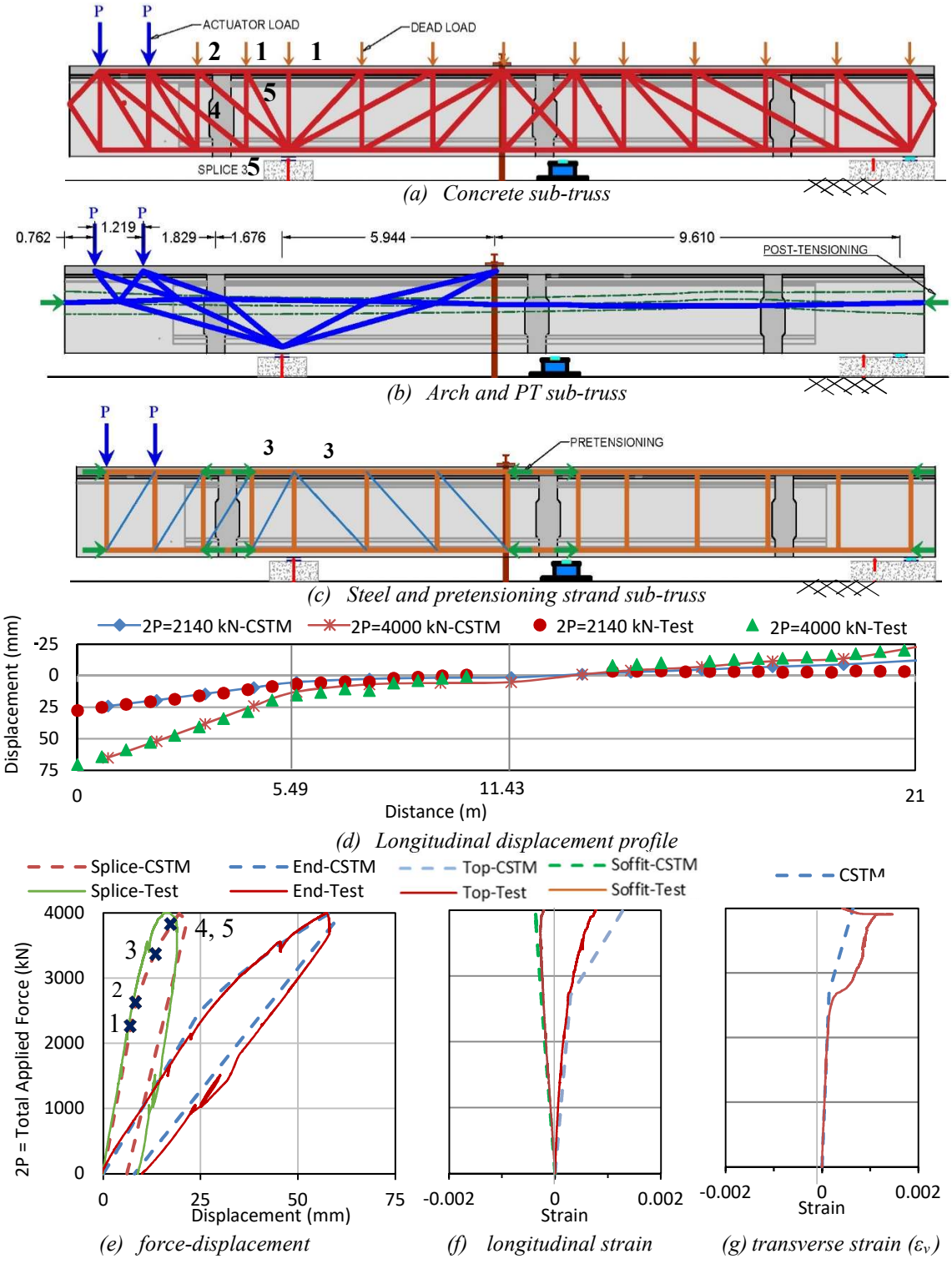

Fig 6.4. Negative moment analysis for Test 2 showing sub-truss configurations for the experimental specimen.

Fig. 6.4 (e) presents the force-deformation behavior of Splice 3 and the end of overhang during Test 2. Solid lines represent the experimental data and dashed lines present the results of C-STM. After the specimen achieved its maximum "failure" displacement, the pressure in the actuator was released and the loads removed. This led to a reduction in deflection to 10 mm. The computational reduction in displacement led to a linear drop-off in loads. The unloading results for the end of the overhang agrees quite well with the experimental results, however, the residual displacement of Splice 3 is slightly underestimated by C-STM model.

The black numbers shown on Fig. 6.4 (a), (b), (c), and (e) represent the main events that led to failure. According to C-STM results, when loads reached $2P = 2472\ kN$, cracks appeared on the deck over the interior support (Event 1). As loads reached $2P = 2709\ kN$, a range of cracks in the deck extended and emerged over the splice region (Event 2). The stress in bottom chord at both sides of interior support reached $0.5f'_c$ when the applied load was $2P = 3508\ kN$. At the same time stresses in two concrete struts reached 90% of softened capacity ($0.9\zeta f'_c$). At $2P = 3880\ kN$, top pretensioning strands yielded over the interior support (Event 3). When applied loads reached $2P = 3980\ kN$ and $2P = 3990\ kN$ the struts reached their softened capacity followed shortly thereafter by the bottom flange becoming overstressed and "failed" in compression (Event 4). Based on the C-STM results, evidently after the top pretensioning yields, the stress in the bottom flange increases rapidly. Unlike for positive moment where the presence of the deck slab leads to lower neutral axis depth, in negative moment only the relatively small area of the bottom flange carries the applied compression stresses. At this point the load transfer

mechanism is a combination of shear transfer through struts and arch members, and flexural load transfer through the top and bottom flanges. As soon as struts reached their maximum capacity and ceased to carry additional load, the overstress in the bottom flange led to "failure" of the specimen in compression.

The C-STM analysis shows the results are in very satisfactory agreement with the experimental observations. Moreover, the C-STM followed the same chain of events that led to failure. The excessive transverse strain in struts also suggests an extended network of diagonal cracks in the web, which is in agreement with the experimental observations.

Fig. 6.4 (f) and (g) compare the strain in the longitudinal and transverse reinforcement of Splice 2, respectively. As shown in Fig. 6.4 (f), reinforcement in both top and the bottom flange of the splice never reach the yield strain, leading to a semi-brittle failure due to the short span. Results of Fig. 6.4 (g) show the transverse strain measured on a hoop within the Splice 3. While for both cases, linear behavior is evident throughout the entire loading, the rate of change in strain increases when crack in the deck expands over the splice region (Event 2).

6.4.3 Test Setup 3 - Experimental vs. Computational Results

Fig. 6.5 presents the C-STM model geometry and results for Test 3, where the actuators were moved to be nearby Splice 1. In order to avoid additional damage to Splice 2, a temporary pedestal was placed adjacent to Splice 2 to create a short span to apply high shear and moderate positive moment to Splice 1. Initially a 10 mm gap existed between the soffit of the girder and the temporary pedestal, which closed up with applied loading. The diagonal crack angle was $\theta = 35.5°$. Therefore, the two-panel configuration ($\theta =$

35.26°) was chosen as it is closest to the crack angle. Based on the first live load analysis, at the time of failure, the transverse strain (ε_1) in the critical strut reached 0.0025. Using Eq. (15), the strut softening coefficient was determined as $\zeta = 0.81$.

Fig. 6.5 (d) presents two longitudinal displacement profiles for the super-assemblage specimen during Test 3 at two specific loads: (i) $2P = 1980\ kN$ representing service limit state; and (ii) and $2P = 5340\ kN$ at maximum actuator capacity. In order to capture the actual displacement of the test specimen, supports are modeled as flexible springs, representing the neoprene bearing pad, rather than rigid supports. Results of C-STM are in very good agreement with the experimental observation for both the service limit state (uncracked behavior) and at maximum loading.

During Test 3, the actuators reached their maximum capacity prior to specimen failure. Therefore, the C-STM is used to predict the failure mechanism of the specimen during Test 3 had there been sufficient actuator capacity available. The results of C-STM up to available data is used to validate the effectiveness of the model, and then loading of the C-STM model is continued until failure.

Fig. 6.5 (e) presents the results of force-deformation behavior of Splice 1. The solid line represents the experimental data and the dashed line presents the C-STM results. Black numbers shown on Fig. 6.5 (a), (b), (c), and (e) represent the main events that led to failure. According to C-STM results, the gap between the soffit of the girder and the temporary pedestal closed when loads reached $2P = 1747\ kN$ (Event 1). This is the reason that specimen shows an increase stiffness at higher loads. Following Event 1, due to the effective shorter span, the shear demands increased significantly. As the applied

loads increased, cracks appeared in the bottom flange of Splice 1 at $2P = 3694\ kN$ (Event 2). When loads reached $2P = 4397\ kN$, the mild steel in the bottom flange of Splice 1 yielded (Event 3). The computational C-STM results predicts that when loads would reach $2P = 5685\ kN$, the stress in the strut shown in Fig. 6.5 (a) would reach its softened capacity and specimen would fail near the temporary pedestal seat (Event 4).

Fig. 6.5 (f) and (g) compare the strain in longitudinal and transverse reinforcement of Splice 2, respectively. As shown in Fig. 6.5 (f), reinforcement in the bottom flange of the splice yields (Event 2), as only minimal reinforcement is present in bottom flange of Splice 1 as no pretensioning strand passed through the splice region. As for the top flange, strains follow the strain in compression concrete and does not yield. Results of Fig. 6.3 (g) show the transverse strain measured on a hoop within Splice 2. Evidently, bars in splice region did not yield throughout the entire course of loading, which is also in agreement with the experimental data.

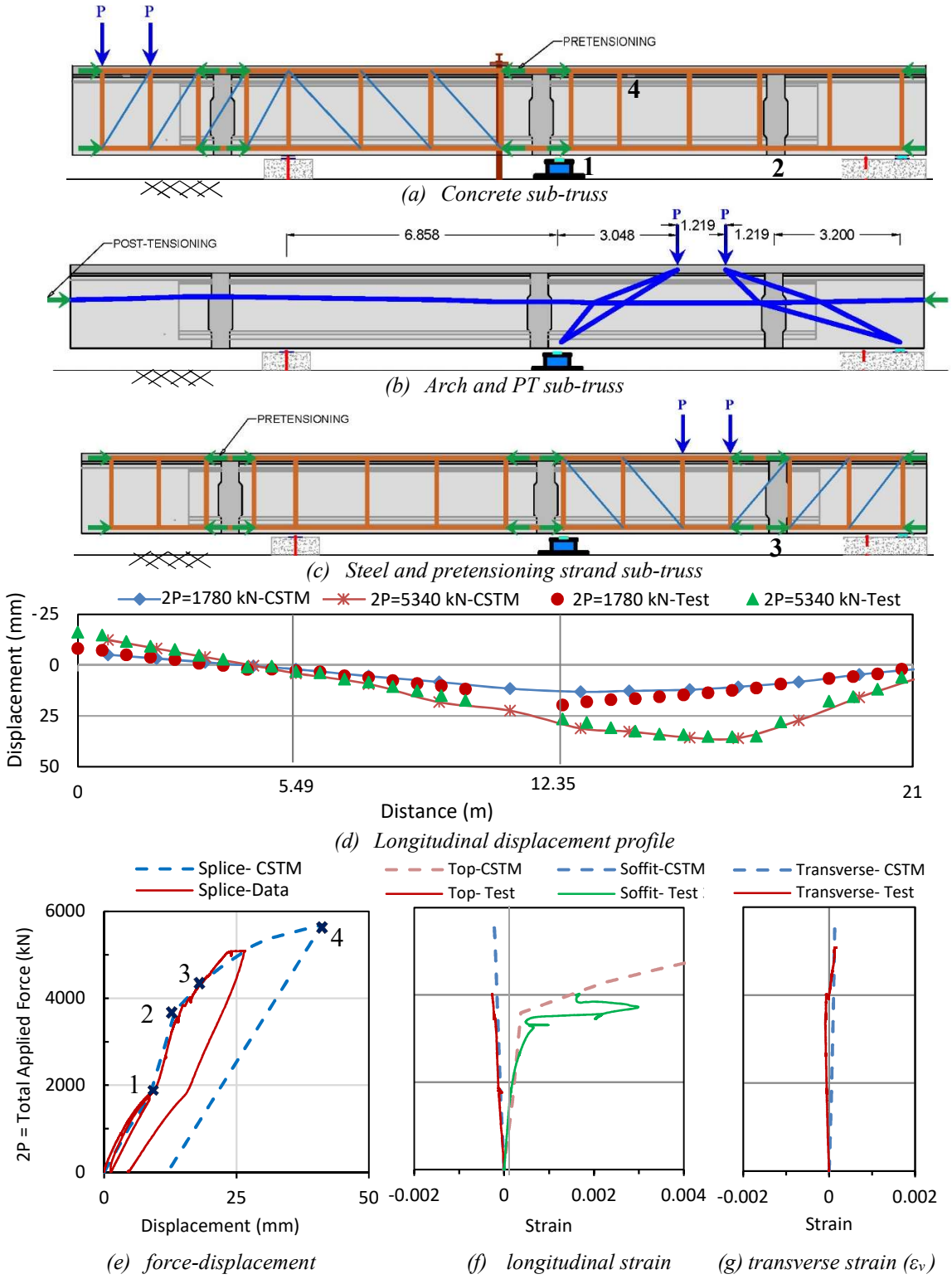

Fig 6.5. High shear analysis for Test 3 showing sub-truss configurations for the experimental specimen.

6.5 DISCUSSION

For the C-STM analysis of the specimen, initially force control method was adopted to apply live loads. The model was then updated to apply loads in displacement control. While the results of force control and displacement control were identical up to failure, the former analysis stopped as soon as the loads reached the maximum capacity of the model. On the other hand, under displacement control, the displacement of specimen continued beyond maximum (peak) load until the target displacement was achieved. During this process, there was a drop in load carrying capacity. In another words, the displacement control approach enables important features such as post-peak behavior of the structure to be captured. Moreover, a displacement control analysis allows the unloading portion of analysis which is not feasible with the force control method.

While displacement control is able to provide more complete information regarding the overall behavior of the structure, the analyst may be required to deal with convergence issues. However, as SAP2000 uses an event-to-event solution strategy, these difficulties can be worked through.

Results of three C-STM analysis suggest that as flexural demand increases in a section, the transverse strain in the struts increases which may effectively reduce the load carrying capacity of the struts. This may be attributed to the increase in tensile strain of tension side of the section, which ultimately affects the transverse strain of the struts. This phenomenon is also in accordance with the of Modified Compression Field Theory (Vecchio and Collins, 1986), where shear capacity of the section is adversely affected by net tensile strain in a section.

6.6 CONCLUSIONS AND CLOSING REMARKS

Compatibility Strut-and-Tie Model (C-STM) was adopted to simulate the behavior of an in-span spliced prestressed concrete girder bridge test specimen. Three test setups were considered for three splices to assess the behavior of each splice under different combination of shear and moment. A prediction model was developed for each test setup and the results of C-STM were compared to the experimental data. The following remarks are results of C-STM and comparison with experimental data.

1. C-STM is a powerful method of analysis for various types of concrete structures, especially for analysis and design of structural systems with different classes of disturbed regions. This research has demonstrated that the C-STM can satisfactorily predict the behavior of prestressed girder structures for different combinations of shear and moment. Results of this investigation suggest that C-STM can successfully capture the force-deformation behavior of structures for both the elastic and inelastic regim under different load combinations.
2. Unlike classical force-based strut-and-tie (plastic truss) modeling and the modified compression field theory, C-STM can effectively predict the global and local behavior of structures in terms of both forces and deformations. Moreover, in contrast with finite element methods, the C-STM is a minimalistic modeling strategy that requires remarkably few members to model structural systems possessing considerable inherent complexity.

3. Application of loads in displacement control enhances the results of C-STM analysis by providing valuable information on post-peak behavior of the structure, as well as unloading stiffness and residual displacement upon load removal.
4. C-STM predicted rather well the performance at the critical sections and effectively captured the failure modes and load transfer mechanisms. Based on the results, for Test 1 (splice 2), the performance of the specimen could be improved by providing a better load path in the bottom flange or by having PT ducts closer to bottom flange to create an alternative load path. For Test 2 (Splice 3), additional compression mild steel as well as transverse reinforcement would effectively increase the ductility of the region and avoid premature failure. For Test 3 (Splice 1), the specimen withstood load as expected and given the short span, shear failure was inevitable, considering that the region was originally designed for flexure and low shear. Additional transverse steel would improve the performance.

7 SUMMARY, CONCLUSIONS AND RECOMMENDATIONS

7.1 SUMMARY

This dissertation has provided a systematic investigation on the design, analysis and performance of in-span spliced prestressed concrete girder bridges by providing design procedures, conducting a full-scale experimental study, and through an analytical and computational modeling investigation using contrasting approaches.

In Chapter 3, the concept of deflection balancing along with the load balancing approach was introduced to provide a platform for design of slab-on-in-span spliced prestressed concrete girder bridges. Three methods of construction were investigated that benefit from in-span splices: shored, partially shored, and heavy-lift (span-by-span) construction. Design procedures and optimal construction sequences were compared and contrasted, and discussed in detail. A prototype bridge geometry was designed for all three methods of construction and the results compared and conclusions drawn.

Chapter 4 presented the experimental performance of a full-scale test specimen that was abstracted from a prototype three-span continuous slab-on-prestressed concrete girder bridge. A super-assemblage test specimen comprised of four precast pretensioned concrete girder segments that were joined together with three cast-in-place in-span splices followed by the casting of a reinforced concrete deck slab. Post-tensioning was applied to the entire super-assemblage structure to provide overall continuity. Three different loading setups were used to investigate the performance of each of the splices. The intention of the different test setups was to investigate splice performance under: (i) high positive

moment and moderate shear; (ii) high negative moment and high shear; and (iii) moderate positive moment and high shear. Results were presented and analyzed for the full-scale laboratory tests on each splice regions under service load through to failure.

Based on the results of the experimental investigation it became evident that within the more lightly prestressed splice regions the diagonal cracking was instrumental in adversely affecting the overall performance and thereby reduce their post-cracked ultimate strength and the deformability of the spliced girder bridge as a system. Therefore, in Chapter 5 a generalized moment-curvature approach was developed along the critical diagonal crack plane to directly account for the effects of flexure-shear interaction. A formulation was also provided to calculate the "nominal capacity" of such sections incorporating the interacting effects of flexure and shear. Analyzing the behavior on a critical diagonal section was validated from companion full-scale test results.

In Chapter 6 Compatibility Strut-and-Tie Modeling (C-STM) was introduced as an effective alternative method of structural analysis when members were subjected to high moment demands coupled with high shear intensity. The C-STM approach was advanced to model the behavior of slab-on-spliced prestressed concrete girder bridges where shear-flexure interaction influenced system performance particularly near disturbed regions as well as those regions that were spliced. The efficacy of the approach was demonstrated by modeling the experimental performance of the test specimen.

7.2 KEY FINDINGS AND CONCLUSIONS

The key conclusions drawn from the experimental testing and analytical modeling are presented in this section.

Based on the results of design case studies, in-span splicing is an effective technique for expanding the span length of slab-on-prestressed precast concrete girder bridges. By providing versatile options for design and construction, in-span splicing may effectively double the span length of simply supported prestressed concrete girder bridges from about 45 m to 90 m. While in current practice, post-tensioning strands are generally stressed prior to casting the deck concrete (due to deck replacement concerns), results of design and analysis suggest that application of part of the PT after casting the deck may enhance the durability of the deck slab.

Results of the experimental study suggest that splices have significantly lower flexural capacity compared to precast prestressed concrete girder segments, which is mainly attributed to the contribution of pretensioning strands to the flexural capacity of precast segments. In general, slab-on-spliced precast concrete girder bridges have higher ductility in positive moment regions compared to negative moment regions, which is attributed to the contribution of the deck in positive bending. Additional compression steel and increased concrete area in the bottom flange would help such sections gain higher ductility. It is observed that small cracks completely close upon removal of the applied load, which may greatly enhance the durability of post-tensioned in-span spliced concrete girder bridges. The experimental observations also suggest that vertical flexural cracks and diagonal shear cracks emerge in the vicinity of splice regions which may give rise to the flexure-shear interaction and adversely affect the overall performance of such regions.

The network of diagonal and vertical cracks in the splice regions may form critical Z-plane sections. Moment-curvature analysis may be generalized to capture the flexure-

shear interaction within the splice regions by incorporating the existing shear forces on the Z-plane sections into the equilibrium equations of moment-curvature analysis. The results of such analysis reveal that the coupled effect of shear and flexure may reduce the overall performance of the sections by reducing the capacity and ductility. Z-plane sections also give rise to the "compression shift" phenomenon, which refers to the shift on the compression side of the Z-plane section. Due to this phenomenon, the demand on the splice section increases which needs to be taken into account for design of in-span splices.

While moment-curvature analysis may provide a satisfactory result for sectional analysis of in-span splices, Compatibility Strut-and-Tie Modeling (C-STM) may effectively simulate the overall behavior of the structure. C-STM analysis results provide remarkably good agreement with the experimental data and can be a powerful approach for analysis of in-span spliced concrete girder bridges. On the other hand, beam theory may fail to accurately predict the behavior of such structures, as it neglects the effect of shear demands on flexural performance of the structure. Application of load through displacement control for C-STM analysis, would provide a thorough understanding of the uncracked, cracked, post-yield, and post peak behavior of the structure.

7.3 ANSWERING THE ORIGINAL RESEARCH QUESTIONS

Based on the literature review presented in Chapter 2, five research questions were presented that this research intended to answer. In this section, the questions are restated and answers are presented.

Question 1: *Given that the standard slab-on-I-girder bridges are one of the most economical options in Texas and the US, is it possible to adopt a splicing*

method to effectively double the span length of existing prestressed concrete girder bridges and reach span lengths of up to 90 m?

Given the limitation on length of individual precast concrete girder segments, the span of simply supported girder bridges is limited to 45 m. However, results of this research suggest that in-span splicing provides versatile practical design options thereby span lengths of such bridges may be expanded up to 90 m. Three methods of construction are identified in this study that adopt in-span splices: (i) shored construction; (ii) partially-shored construction; and (iii) heavy lift (span-by-span) construction. Design procedures and construction sequences are presented to confirm the feasibility and applicability of this technique.

Question 2: *How do the splice and the structure perform under normal service loads? And what is the performance of the structure, and more specifically the splices, if they are overloaded to failure?*

Through an extensive experimental investigation as well as analytical and numerical modeling, the performance of the splice regions as well as the entire bridge system was studied for three different demand combinations: (i) high positive moment and moderate shear; (ii) high negative moment and high shear; and (iii) moderate positive moment and high shear. From the experimental performance as well as computational results, it was deduced that structural integrity was entirely satisfied during service limit states and no cracks were observed under service live loading. It was observed that at the ultimate limit state, the coupling effect of shear and flexure adversely affected the performance of the splice regions, reducing their capacity and ductility.

Question 3: *Given that in-span splices are generally located in the regions with minimal flexural demands, the shear demands at splice locations remain high. Therefore, how would the interaction of shear and flexure in splice regions be affected by the post-cracking performance of in-span splices?*

The splice regions possess significantly lower flexural capacity, as the pretensioning strands are discontinued in these regions. Therefore, splices are generally positioned at locations with lower flexural demands, which subsequently carry relatively higher shear demands. On the other hand, while flexural demands are relatively lower than at the mid-span (for positive moment) and at the pier (for negative moment), they remain relatively high for the splice sections, due to their significantly lower flexural capacity. Hence, generally splice regions experience both high shear and flexural demands. Experimental observations revealed that this coupled effect may emerge as a new critical state, where the flexure-shear interaction may adversely affect the performance of in-span splices particularly at ultimate conditions.

During the experimental study, it was observed vertical flexural cracks in the splice regions were followed by diagonal shear cracks in the narrow web of the splice and adjacent precast girders. The combination of vertical and diagonal cracks created a Z-plane section where the tension side resided in the splice region, and the compression side was shifted to the adjacent precast girder segment. An analytical and computational approach was developed in the form of moment-curvature analysis to incorporate the effect of existing shear forces on the Z-plane in the equilibrium formulation of original moment-curvature analysis. The result of the enhanced moment curvature analysis

revealed that the coupling effect of shear and flexure may reduce the capacity and ductility of the splice region.

Furthermore, a Compatibility Strut-and-Tie (C-STM) approach was adapted and further developed to capture the overall performance of the structure. Computational models were made for three splices under three different load combinations, simulating the experimental testing investigation. Results were found to agreeable reasonably well with the experimental data and the performance of the test specimen was captured quite well for all three cases. It was deduced that for in-span spliced continuous prestressed concrete girder bridge systems, the C-STM approach may effectively capture the overall performance of the structure.

Question 4: *Given that due to the narrow web of I-girder sections, and the existence of post-tensioning ducts within the web, high inelastic shear deformations are possible; how well can existing methods of analysis predict the performance of a spliced girder bridge?*

Prediction models were developed prior to the testing phase of the experimental study based on Euler beam theory. Moment curvature analysis was developed to predict the performance of the splice regions as well as the precast girder segments. Experimental results revealed that while predicting models were able to capture the performance of the structure in the service limit state (uncracked behavior), they over-estimated the capacity and ductility of the splices. As discussed before, the lower capacity and ductility was mainly attributed to the coupling effects of shear and flexure. Given that beam theory does not consider the contribution of shear in the flexural behavior of the structure, it was

deduced that this method was not able to capture the flexure-shear interaction and, hence, failed to correctly predict the nominal capacity of the structure.

Question 5: *Considering that splice regions are prone to diagonal cracks, how would the design demands of this regions and the adjacent girder sections be affected?*

As discussed before, the coupling effect of shear and flexure may adversely impact the capacity and ductility of the splice region. The concept of "compression shift" was introduced to describe the critical state where failure occurred along the Z-plane sections. It was deduced that the reduction in capacity of the splice regions may be adjusted for design purposes using the compression shift concept.

7.4 RECOMMENDATIONS FOR CURRENT PRACTICE AND FUTURE RESEARCH

This research was conducted to provide technical answers and solutions to the research questions presented in Chapter 2. Based on the results of experimental investigations and computational modeling, the following recommendations are proposed for current practice as well as for future research.

7.4.1 Current Practice

1. While current practice is skeptical about stressing a portion of the post-tensioning strands after casting the deck concrete due to deck replacement issues, pre-compression of the deck concrete may significantly increase the durability of the deck. Results of the experimental study show that even if minor cracks emerge in the deck, the effect of post-tensioning would close those cracks in a compressed state. Therefore, it is recommended that a portion of post-tensioning be applied

after the deck concrete is cast (Stage II PT) and provisions be made to temporarily de-tension Stage II PT if deck replacement is needed.

2. While splices with minimal reinforcement may be designed to provide the required capacity at service load conditions and up to ultimate loading, lack of a sufficiently strong load path may adversely affect the performance of splices. It is recommended that splices be designed to provide stronger load paths in top and bottom flanges to withstand the flexural demands.
3. Given that splices have lower capacity due to the lack of pretensioning, they are generally placed in locations with lower flexural demands, which corresponds to increased shear demands in such regions. The coupled effect of shear and flexure may give rise to a new critical state where diagonal cracks shift the compression side of the critical section. It is recommended that splice sections be designed for higher flexural demands.
4. Given that flexure-shear interaction arises new critical state in the splice regions, and considering that beam theory neglects the effect of shear on flexural performance of the structures, it is recommended that more sophisticated methods, such as the C-STM approach be used for analysis of in-span spliced prestressed concrete girder bridges.
5. Prestressed girders and splices have shown lower ductility in negative moment regions compared to positive moment regions. This is mainly attributed to the contribution of deck slab concrete in providing enhanced compression capacity which is absent in negative regions. In order to improve the compression capacity

of the continuous prestressed concrete girder bridges in negative moment regions, it is recommended that thickened sections be used over the piers with high negative moment demands.

7.4.2 Future Research

To expand the current state-of-art and practice, the following research questions are proposed regarding in-span spliced concrete girder bridges:

Question 1: *Given that in-span splices generally possess lower flexural capacity due to lack of pretensioning strands, what methods may be used to provide a strong load path through the top and bottom flanges of such regions?*

Results of this study proposed that lack of a strong load path in the splice regions may create critical failure states where the overall performance of the structure is adversely affected as loads approach ultimate conditions. Over the past decades, researchers have proposed various splice details to enhance the performance of those regions, especially for on-pier splices. However, the effectiveness of such details is not clear for in-span splices, given that shear-flexure interaction may affect the performance of such regions. A comprehensive study is required to consider different enhanced splice details for in-span splices and experimentally and analytically investigate the effectiveness of each detail.

Question 2: *Results of this study suggest that the moment curvature analysis may be effectively enhanced to incorporate the effects of flexure-shear interaction as an integrated analysis method. How can this method be further developed to provide more accurate and reliable results?*

Shear-flexure interaction can be a potential critical state for in-span spliced concrete girder bridges. Generalized moment-curvature analysis that incorporates the effects of flexure-shear interaction may be adapted to provide a better understanding of such effects. However, the current theory does not provide a general approach on the initiation of diagonal cracks. Also, it assumes that no shear is transferred between the diagonal struts through aggregate interlock and only considers the shear contribution of concrete in the uncracked compression region. While the current theory with both shortcomings may still capture the lower bound solution and ultimate strength, it may be further improved to provide a thorough understanding of the overall performance of the cracked section.

Question 3: *Compression shift phenomenon is identified in this research as an effect of flexure-shear interaction, which may adversely reduce the capacity and ductility of the Splice regions. How can this phenomenon be incorporated in a routine design practice?*

Based on the experimental data and the results of the computational modeling, the capacity of the splices may be adversely affected by flexure-shear interaction. Through emergence of a critical state on a Z-plane section, the compression side of the critical section may be shifted to the adjacent girder segment, which is herein referred to as the "compression shift effect". Results of moment-curvature analysis suggest that the compression shift phenomenon would decrease the capacity and ductility of the splice region. While this effect may be analyzed by the proposed methods in this study, a design approach is required to facilitate a routine office designed. The results of the moment-curvature analysis suggest that the splice region should be design for the higher demand between the

compression side and tension side of the Z-plane section, but the extension of the Z-plane is dependent on the diagonal crack angle and the height of the diagonal crack. Further investigation and parametric studies are required to ensure a safe and practical design approach to compensate for the compression shift phenomenon.

Question 4: *While current practice, as well as result of this study suggest that in-span splicing may effectively extend the span length of precast concrete girder bridges, it is mainly considered for bridges with straight girder lines. How can this technique be further developed to provide a feasible option for curved bridges?*

While I-shaped girders are the subject of this study, the in-span splicing technique may also be adopted for U-shaped beams as several examples of in-span spliced U-girder bridges exist in current practice. Given that torsion is one of the biggest challenges in curved structures, U-shaped sections (with a cast-in-place lid on top) provide an appealing solution to overcome the torsion demands. However, many engineers as well as DOTs have been skeptical about adapting such a technique to curved bridges. It would be very beneficial to conduct an experimental study along with a sophisticated 3-D analysis to support the current specifications to ensure a safe and economical design.

REFERENCES

AASHTO (2012). AASHTO LRFD Bridge Design Specifications. 6th Edition, American Association of State Highway and Transportation Officials (AASHTO), Customary U.S. Units, Washington, D.C.

Abdel-Karim, A. and Tadros, M.K. (1992). Design and Construction of Spliced I-Girder Bridges. *PCI Journal*, 33, 114–122.

Alawneh, M. (2013). Curved Precast Prestressed Concrete Girder Bridges. *Ph.D. Dissertation*, University of Nebraska, Lincoln, Nebraska, August 2013, 359 pp.

Bishop, E.D. (1962). Continuity Connection for Precast Prestressed Concrete Bridges. *ACI Journal*, 585–599.

Burns, N. H. (1964). Moment Curvature Relationships for Partially Prestressed Concrete Beams. *PCI Journal*, 9(1), 52-63.

Caroland, W.B., Depp, D., Jenssen, H., and Spaans, L. (1992). Spliced Segmental Prestressed Concrete I-Beams for Shelby Creek Bridge. *PCI Journal*, 37(5), 22–33.

Castrodale, R.W. and. White, C.D (2004). Extending Span Ranges of Precast Prestressed Concrete Girders. Transportation Research Board, *National Cooperative Highway Research Program*, Report No. 517, 603 pp.

Cattaneo, S., Giussani, F., and Mola, F. (2012). Flexural Behaviour of Reinforced, Prestressed and Composite Self-Consolidating Concrete Beams. *Construction and Building Material*s, 36, 826-837.

Cladera, A., Marí, A., Ribas, C., Bairán, J., and Oller, E. (2015). Predicting the Shear–Flexural Strength of Slender Reinforced Concrete T and I Shaped Beams. *Engineering Structures*, 101, 386-398.

Collins, M. P., Bentz, E. C., and Sherwood, E. G. (2008). Where Is Shear Reinforcement Required? Review of Research Results and Design Procedures. *ACI Structural Journal*, 105(5), 590-600.

Dimmerling, A., Miller, R., Castrodale, R., Mirmiran, A., Hastak, M., and Baseheart, T. (2005). Connections Between Simply Supported Concrete Beams Made Continuous: Results of NCHRP Project 12-53. *Transportation Research Record: Journal of the Transportation Research Board*, (1928), 126-133.

Endicott, W.A. (1996). Precast Super Bulb Tees Create Innovative Bridge. Ascent Winter, PCI publication, 30–32.

Ficenec, J. A., Kneip, S. D., Tadros, M. K., and Fischer, L. G. (1993). Prestressed Spliced I-Girders: Tenth Street Viaduct Project, Lincoln, Nebraska. *Precast/Prestressed Concrete Institute Journal*, 38(5).

Fitzgerald, J.B. and Stelmack, T.W. (1996). Spliced Bulb-Tee Girders Bring Strength and Grace to Pueblo's Main Street Viaduct. *PCI Journal*, 41(6), 40–54.

Holden, T., Restrepo, J., Mander, J. B. (2003). "Seismic Performance of Precast Reinforced And Prestressed Concrete Walls." *Journal of Structural Engineering*, 129(3), 286-296.

Hueste, M.D., Mander, J.B., and Parkar, A.S. (2011). Continuous Prestressed Concrete Girder Bridges, Volume 1: Literature Review and Preliminary Designs. *Texas Department of Transportation*, Report No. 0-6651-1, 176 pp.

Hueste, M.D., Mander, J.B., Baie, R., Parkar, A.S., Parchure, A., Prouty, M., and Sarremejane T. (2016). Continuous Prestressed Concrete Girder Bridges, Volume 2: Analysis, Testing, and Recommendations. *Texas Department of Transportation*, Report No. 0-6651-2, 278 pp.

Janssen, H.H. and Spaans, L. (1994). Record Span Spliced Bulb-Tee Girders Used in Highland View Bridge. *PCI Journal*, 39(1), 12–19.

Kaar, P. H., Kriz, L. B., Hognestad, E. (1960). Precast-Prestressed Concrete Bridges: 1. Pilot Tests of Continuous Girders. *Journal of PCA Research and Development Laboratories*, 2(2), pp. 21–37.

Karthik, M. M., and Mander, J. B. (2011). "Stress-Block Parameters for Unconfined and Confined Concrete Based on a Unified Stress-Strain Model." *ASCE Journal of Structural Engineering*, 137(2), 270–273.

Karthik, M. M., Mander, J. B., and Hurlebaus, S. (2016). Displacement-Based Compatibility Strut-and-Tie Method and Application to Monotonic and Cyclic Loading. *Journal of Structural Engineering*, 142(6), 04016010.

Kim, J. H., and Mander, J. B. (1999). Truss Modeling of Reinforced Concrete Shear-Flexure Behaviour. *Technical Report MCEER - 99-0005*, University at Buffalo, New York.

Kim, J. H., and Mander, J. B. (2000a). Cyclic Inelastic Strut-Tie Modeling of Shear-Critical Reinforced Concrete Members. *American Concrete Institute*, SP 193, 707-728.

Kim, J. H., and Mander, J. B. (2000b). Seismic Detailing of Reinforced Concrete Beam-Column Connections. *Structural Engineering and Mechanics*, 10(6), 589-601.

Kim, J. H., and Mander, J. B. (2005). Theoretical shear strength of concrete columns due to transverse steel. Journal of Structural Engineering, 131(1), 197-199.

Kim, J. H., and Mander, J. B. (2007). Influence of Transverse Reinforcement on Elastic Shear Stiffness Of Cracked Concrete Elements. *Engineering Structures*, 29(8), 1798-1807.

Lin, T. Y., Kulka, Yang and Associate (1968). Prestressed Concrete for Long-Span Bridges. *Prestressed Concrete Institute*. Chicago, IL.

Mander, J. B., Priestley, M. J., and Park, R. (1988). Theoretical Stress-Strain Model for Confined Concrete. *Journal of Structural Engineering*, 114(8), 1804-1826.

Marti, P. (1985, January). Basic Tools of Reinforced Concrete Beam Design. *In Journal Proceedings*, 82(1), pp. 46-56.

Mattock, A.H. and Kaar, P.H. (1960). Precast-prestressed Concrete Bridges III: Further Tests of Continuous Girders. *Journal of PCA Research and Development Laboratories*, 2(3), pp. 51–78.

Menegotto, M., Pinto, and P. E. (1973). Method Of Analysis For Cyclically Loaded RC Frames Including Changes In Geometry And Non-Elastic Behaviour Of

Elements Under Combined Normal Force And Bending. *In IABSE Congress Reports of the Working Commission* (Vol. 13).

Miller, R.A., R.W. Castrodale, A. Mirmiran, and M. Hastak (2004). Connection of Simple Span Precast Concrete Girders for Continuity. *National Cooperative Highway Research Program*, Report No. 519, 203 pp.

Mirmiran, A., Kulkarni, S., Miller, R., Hastak, M., Shahrooz, B., and Castrodale, R. (2001b). Positive Moment Cracking in the Diaphragms of Simple-Span Prestressed Girders Made Continuous. SP 204 Design and Construction Practices to Mitigate Cracking, E. Nawy, Ed., *American Concrete Institute*, Detroit, 117–134 pp.

Moore, A., Williams, C., Al-Tarafany, D., Felan, J., Massey, J., Nguyen, T., Schmidt, K., Wald, D., Bayrak, O., Jirsa, J., and Ghannoum, W. (2015). Shear Behavior of Spliced Post-Tensioned Girders. *Center for Transportation Research*, Report. no. 0-6652-1.

Mörsch, E. (1902) Der Eisenbetonbau: seine Theorie und Anwendung. Stuttgart : Verlag Konrad Wittwer

Mumber, J., Foster, D. M., Lambert, E. D., and Saunders, C. A. (2003). Ocean City-Longport Replacement Bridge Requires Precast Concrete Durability for Harsh Marine Conditions. *PCI journal*, 48(6), 32-45.

Naaman, A. E., Harajli, M. H., and Wight, J. K. (1986). Analysis of Ductility in Partially Prestressed Concrete Flexural Members. *PCI Journal*, 31(3), 64-87.

Newhouse, C.D., Roberts-Wollmann, C.L., and Cousins, T.E. (2005). Development of an Optimized Continuity Diaphragm for New PCBT Girders. FHWA/VRTC 06-CR3, *Virginia Transportation Research Council*, 77 pp.

Nicholls, J. J., and Prussack, C. (1997). Innovative Design and Erection Methods Solve Construction of Rock Cut Bridge. *PCI Journal*, 42(4), 42-55.

Nikzad, K.A., Trochalakis, T., Seguirant, S.J., and Khaleghi, B. (2006). Design and Construction of the Old 99 Bridge – An HPC Spliced Girder Structure. *PCI Journal*, 23(18), 98–109.

Oehlers, D., Haskett, M., Ali, M., Lucas, W., and Muhamad, R. (2011). Our Obsession with Curvature in RC Beam Modelling. *Advances in Structural Engineering*, 14(3), 391-404.

Oesterle, R. G., Glikin, J. D., Larson, S. C. (1989). Design of Precast-Prestressed Bridge Girders Made Continuous. National Cooperative Highway Research Program, Report No. 322, *Transportation Research Board*, Washington, D.C.

Park, R., Paulay, T. (1975). Reinforced concrete structures. *John Wiley & Sons,* Hoboken, New Jersey.

Park, R., Thompson, K. J. (1980). Ductility of Prestressed and Partially Pretressed Concrete Beam Sections. *PCI Journal*, 25(2), 46-80.

Paulay, T. (1971a). Coupling Beams of Reinforced Concrete Shear Walls. *Journal of the Structural Division*, 97(3), 843-862.

Pirayeh Gar, S., Head, M., and Hurlebaus, S. (2011). Tension Stiffening in Prestressed Concrete Beams Using Moment-Curvature Relationship. *Journal of Structural Engineering*, 138(8), 1075-1078.

Recupero, A., D'Aveni, A., and Ghersi, A. (2005). Bending Moment–Shear Force Interaction Domains for Prestressed Concrete Beams. *Journal of Structural Engineering*, 131(9), 1413-1421.

Ritter, W. (1899). Die Bauweise Hennebique, *Hennebiques Construction Method*.

Rodriguez-Gutierrez, J. A., and Aristizabal-Ochoa, J. D. (2001). M-P-φ Diagrams for Reinforced, Partially, and Fully Prestressed Concrete Sections under Biaxial Bending and Axial Load. *Journal of Structural Engineering*,127(7), 763-773.

Ronald, H.D. (2001). Design and Construction Considerations for Continuous Post-tensioned Bulb Tee Girder Bridges. *PCI Journal*, 46(3), 44–66.

Rosenblueth, E., and de Cossio, R. D. (1965). Instability Considerations in Limit Design of Concrete Frames. *ACI Special Publication*, 12, 439-463.

Russo, G., and Zingone, G. (1991). Flexure-Shear Interaction Model for Longitudinally Reinforced Beams. *Structural Journal*, 88(1), 60-68.

Sawyer, H. A. (1965). Design of Concrete Frames for Two Failure Stages. *ACI Special Publication*, 12, 405-437.

Schlaich, J., Schäfer, K., and Jennewein, M. (1987). Toward a consistent design of structural concrete. *PCI journal*, 32(3), 74-150.

Scott, R.M. (2010). Experimentally Validated Compatibility Strut and Tie Modeling of Reinforced Concrete Bridge Piers. *Master of Science Thesis*, Texas A&M University, 188 pp.

Scott, R. M., Mander, J. B., and Bracci, J. M. (2012). Compatibility strut-and-tie modeling: Part I-Formulation. *ACI Structural Journal*, 109(5), 635.

Scott, R. M., Mander, J. B., and Bracci, J. M. (2012). Compatibility Strut-and-Tie Modeling: Part II-Implementation. *ACI Structural Journal*, 109(5), 645.

Shushkewich, K. W. (1990). Moment-Curvature Relationships for Partially Prestressed Concrete Beams. *Journal of Structural Engineering*, 116(10), 2815-2823.

Sritharan, S., and Ingham, J. M. (2003). Application of strut-and-tie concepts to concrete bridge joints in seismic regions. *PCI Journal*, 48(4), 66-90.

Sun, C. (2004). High Performance Concrete Bridge Stringer System. *Ph.D. Dissertation*, The University of Nebraska- Lincoln, 228 pp.

Tadros, M.K. (2007). Design Aids for Threaded Rod Precast Prestressed Girder Continuity System. *Nebraska Department of Roads Research Report*, 103 pp.

Tadros, M.K. and Sun, C. (2003). Implementation of the Superstructure/Substructure Joint Details. University of Nebraska, Omaha, Department of Civil Engineering, *Nebraska Department of Roads Research Report*, Project No. SPR-PL-1(038), 514 pp.

To, N. H. T., Ingham, J. M., and Sritharan, S. (2001). Monotonic Nonlinear Strut-And-Tie Computer Models. *Bulletin of the New Zealand Society for Earthquake Engineering*, 34(3), 169-190.

To, N. H. T., Ingham, J. M., and Sritharan, S. (2002). Strut-And-Tie Computer Modelling of Reinforced Concrete Bridge Portal Frames. *Bulletin of the New Zealand Society for Earthquake Engineering*, 35(3), 165-189

To, N. H. T., Ingham, J. M., and Sritharan, S. (2003). Strut-And-Tie Computer Modelling of Reinforced Concrete Bridge Joint Systems. *Journal of Earthquake Engineering*, 7(4), 581-590.

TxDOT (2010). TxDOT Bridge Design Manual. Bridge Division, *Texas Department of Transportation*, Austin, Texas.

Urmson, C. R., and Mander, J. B. (2011). Local Buckling Analysis of Longitudinal Reinforcing Bars. *Journal of Structural Engineering*, 138(1), 62-71

Williams, C., Moore, A., Al-Tarafani, D., Massey, J., Bayrak, O., Jirsa, J., and Ghannoum, W. (2015). Behavior of the Splice Regions of Spliced I-Girder Bridges. *Texas Department of Transportation*, Report No. 0-6652-2, 226 pp.

Wolf, T. S., Frosch, R. J. (2007). Shear Design of Prestressed Concrete: A Unified Approach. *Journal of Structural Engineering*, 133(11), 1512-1519.

Zhu, R. R. H., Wanichakorn, W., Hsu, T. T. C., and Vogel, J. (2003). Crack Width Prediction Using Compatibility-Aided Strut-And-Tie Model. *ACI Structural Journal,* 100(4), 413-421.

APPENDIX A

DESIGN EXAMPLE

A.1 OVERVIEW

An important design principle for post-tensioning is to balance the dead load as much as practical. Different stages of prestressing are necessary and should be applied in such a sequence to ensure that the girders perform properly through all fabrication and construction stages, including casting, hauling, erection, and deck construction, until the bridge is open to traffic. Therefore, different methods of construction and different construction stages may require different approaches for selecting the prestress profile and the stressing sequence.

Two broad methods of construction are commonly used for continuous prestressed concrete girder bridges: shored and partially shored construction. Because the method of supporting girders in each case is different, construction loads may vary for each segment and location along the girder length. Therefore, the prestress design is not likely to be identical for both cases, even though the aim of load balancing may exist through the entire design procedure for both methods of construction.

Appendix A outlines the basic design information that is common for both methods of construction. This is followed by a design example for shored construction. The design example includes prestress design, stress checks, ultimate flexural strength checks, deflection checks, and shear design. The *AASHTO LRFD Bridge Design Specifications* (AASHTO 2012) are referenced in the design examples.

A.2 DESIGN PARAMETERS

Fig. A.1 (a) presents a side elevation of one-half of the bridge, which is symmetrical about its centerline. In consultation with a TxDOT panel of engineers, the following parameters were selected for the design examples:

- A three-span configuration using 190-240-190 ft.
- Based on transportation limitations, the length of the drop-in and end girder segments was 140 ft, while that of on-pier segment was 96 ft.
- Length of splice connections is 2 ft.
- Tx70 girder sections were modified such that a 9 in. web was used to accommodate PT ducts, instead of the standard 7 in. web.

Fig. A.1 (b) shows the bridge cross-section at the midspan. The bridge has a total width of 46 ft and total roadway width of 44 ft. The bridge superstructure consists of six Tx70 girders spaced 8 ft center-to-center, with 3 ft overhangs on each side designed to act compositely with an 8 in. thick cast in place (CIP) concrete deck. The wearing surface thickness is 2 in. TxDOT standard T501 type rails are considered in the design. Three design lanes are considered for the purpose of design in accordance with the AASHTO LRFD Specifications (AASHTO 2012).

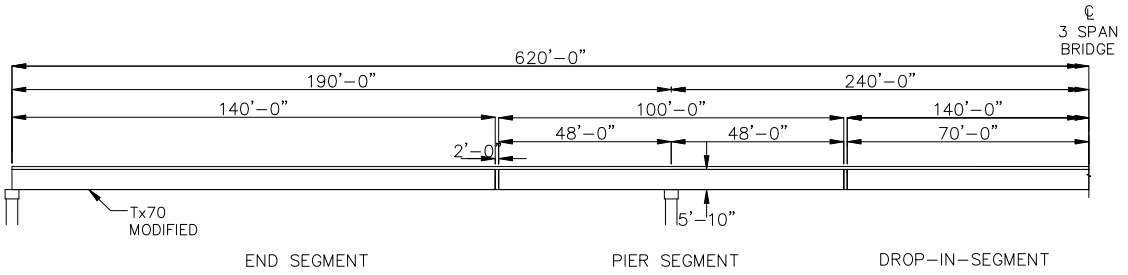

(a) Side Elevation of the Bridge

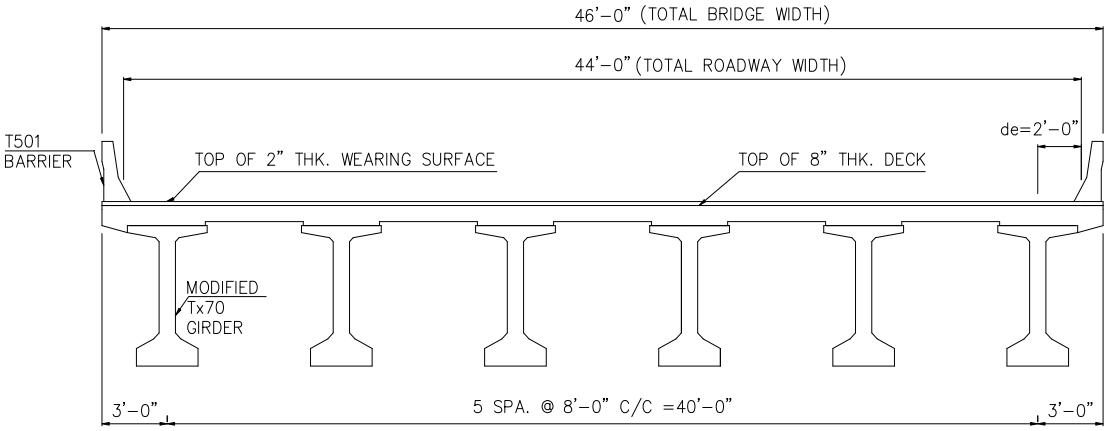

(b) Cross-Section of the Bridge

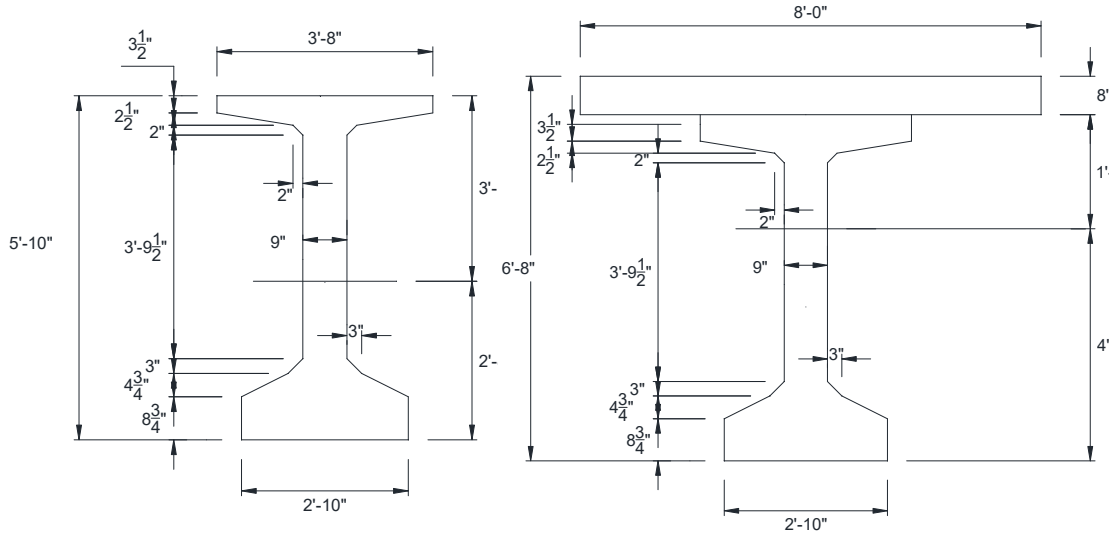

(c) Non-Composite Section *(d) Composite Section*

Fig. A.1 Bridge Geometry and Cross-Section Properties

A standard Tx70 girder was adopted for the design and modified to comply with the requirements for continuity and post-tensioning effect. The web width of the standard Tx70 girder was increased to 9 in. so as to enable accommodation of the post-tensioning ducts. The width of top flange was increased to 44 in. and that of the bottom flange was increased to 34 in. Table A.1 gives the composite and non-composite section properties for the modified Tx70. Fig. A.1 (a) and (b) show the details of non-composite and composite section for the prismatic modified Tx70 girder, respectively.

Table A.1. Section Properties for Prismatic Modified Tx70 Girder (9 in. Web).

Girder Type	Depth of N.A. from Top, y_t (in.)	Depth of N.A. from Bottom, y_b (in.)	Area, A (in.^{2})	Moment of Inertia, I_x (in.^{4})
Tx70 Modified	37.75	32.25	1106	687,111
Tx70 Modified Composite	31.75	48.25	1842	1,461,059

A.3 MATERIAL PROPERTIES

Table A.2 gives the design parameters selected for the application examples. The design parameters such as concrete strength are based on standard practices that are followed throughout Texas. A relative humidity of 65 percent is assumed based on the average value in Texas as specified in AASHTO LRFD Specifications (AASHTO 2012) Article 5.4.2.3. The other parameters, which include prestressing steel and mild steel, are based on the AASHTO LRFD Specifications (AASHTO 2012).

Table A.2. Design Parameters.

Parameter		Selected Value
Concrete strength at service for deck slab, f'_c		4 ksi
Precast Concrete strength at release, f'_{ci}		6.5 ksi
Precast Concrete strength at service, f'_c		8.5 ksi
Coefficient of thermal expansion of concrete		$6x10^{-6}$/° F
Relative humidity		65%
Mild steel	Yield strength, f_y	60 ksi
	Modulus of elasticity, E_c	29,000 ksi
Prestressing steel	Strand diameter	0.6 in.
	Ultimate tensile strength, f_{pu}	270 ksi – low relaxation
	Yield strength, f_{py}	0.9 f_{pu}
	Stress limit at transfer, f_{pi}	$f_{pi} \geq 0.75\ f_{pu}$
	Stress limit at service, f_{pe}	$f_{pe} \geq 0.8\ f_{py}$
	Modulus of elasticity, E_p	28,500 ksi
	Coefficient of friction, μ	0.25
	Wobble coefficient	0.0002/ ft
	Anchor set	0.375 in.

Table A.3. Dead Loads for Modified Tx70 Girder.

Load Type	Value (kip/ft)	Applied to
Self-weight prismatic	1.152	Girder Section
Self-weight haunch (for pier segment-hybrid case)	1.152–2.488	Girder Section
Deck weight	0.800	Girder Section
Haunch weight (between girder and deck)	0.079	Girder Section
Barrier weight	0.109	Composite Section
Wearing surface	0.187	Composite Section

A.4 DEAD LOADS

Dead loads for design are addressed in the AASHTO LRFD Specifications (AASHTO 2012) Article 3.5.1. Dead loads considered in the design include girder self-weight and weights of the haunch, slab, barrier, and wearing surface. For the haunch segment, self-weight varies linearly with increasing depth from a prismatic section at the splice to the centerline of pier. The load due to the deck is distributed to the individual girders based on the center-to-center spacing between girders. The loads due to the wearing surface and barrier loads act on the composite section and are distributed equally to all the girders. Table A.3 gives the dead loads acting on each individual girder for the bridge considered.

A.5 LIVE LOADS

AASHTO LRFD Specifications (AASHTO 2012) Article 3.6 describes the HL-93 truck live load model. Three traffic lanes are considered for the design in accordance with the AASHTO LRFD Specifications (AASHTO 2012). The live load is to be taken as one of the following combinations, whichever yields maximum stresses at the section considered.

A.5.1 Design Truck and Design Lane Load

The HL-93 design truck consists of one front axle weighing 8 kips and two rear axles weighing 32 kips each, spaced 14-30 ft apart. A dynamic load allowance factor of 33 percent is considered for the design truck. The design lane load consists of 0.64 klf uniformly distributed in the longitudinal direction and is not subjected to a dynamic load allowance. Fig. A.2 shows the details for design truck and design lane load.

The design tandem load consists of a pair of 25 kip axles spaced 4 ft apart and is subjected to a dynamic load allowance. The design lane load consists of 0.64 klf uniformly

distributed in the longitudinal direction and is not subjected to a dynamic load allowance. Fig. A.3Fig. A.3 shows the details for design tandem and design lane load.

The live load moments and shear forces, including the dynamic load effects, are distributed to the individual girders using distribution factors (DFs). AASHTO LRFD Tables 4.6.2.2.2 and 4.6.2.2.3 specify the DFs for moment and shear for I-shaped girder sections. The use of these DFs is allowed for prestressed concrete girders having an I-shaped cross-section with a composite slab, if the conditions outlined below are satisfied. For bridge configurations not satisfying the limits below, refined analysis is required to estimate the moment and shear DFs. Table A.4 gives the LRFD live load DFs for the case of a concrete deck on an I-girder.

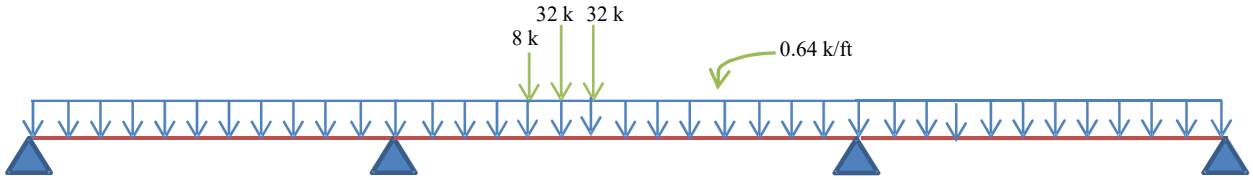

Fig. A.2 Design Truck and Design Lane Load.

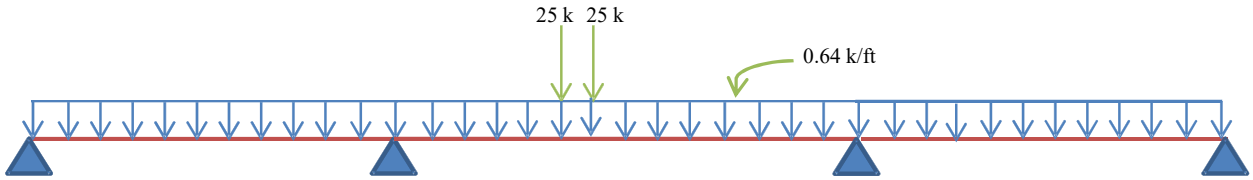

Fig. A.3 Design Tandem and Design Lane Load.

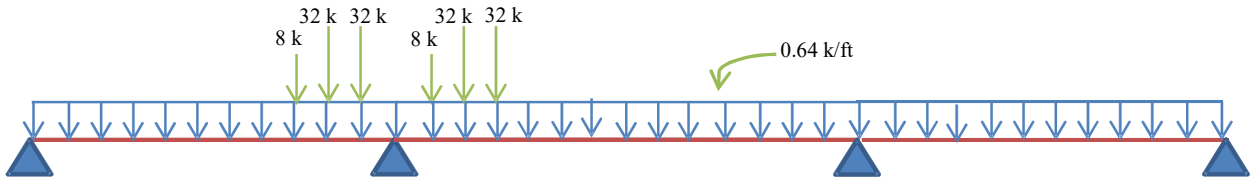

(*a) Design Truck and Design Lane Load*

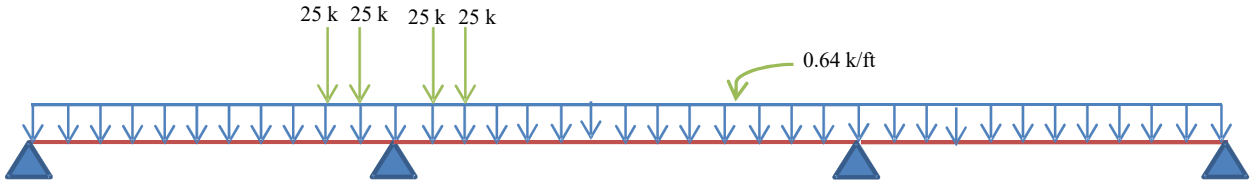

(b) Design Tandem and Design Lane Load

Fig. A.4 Critical Load Placement of HL-93 Vehicular Live Load over Continuous Span for Maximum Shear Demand

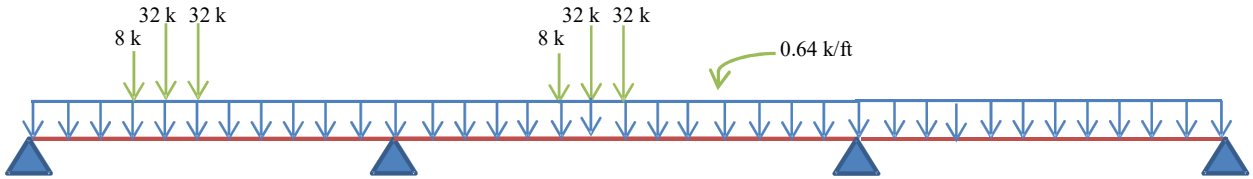

Fig. A.5 Critical Load Placement of HL-93 Vehicular Live Load over Continuous Span for Maximum Deflection.

Table A.4. LRFD Live Load DFs for Concrete Deck on I-Girder.

Category	DF Formulas	Range of Applicability
Live Load Distribution per Lane for Moment in Interior Beam	One Design Lane Loaded: $0.06 + \left(\frac{S}{14}\right)^{0.4}\left(\frac{S}{L}\right)^{0.3}\left(\frac{K_g}{12.0Lt_s^3}\right)^{0.1}$ Two or More Design Lanes Loaded: $0.075 + \left(\frac{S}{9.5}\right)^{0.6}\left(\frac{S}{L}\right)^{0.2}\left(\frac{K_g}{12.0Lt_s^3}\right)^{0.1}$	$3.5 \le S \le 16.0$ $4.5 \le t_s \le 12.0$ $20 \le L \le 240$ $N_b \ge 4$ $10000 \le K_g \le 7000000$
Live Load Distribution per Lane for Moment in Interior Beam	One Design Lane Loaded: Lever Rule Two or More Design Lanes Loaded: $g = eg_{interior}$ $e = 0.77 + \frac{d_e}{9.1}$	$-1.0 \le d_e \le 5.5$
Live Load Distribution per Lane for Shear in Interior Beam	One Design Lane Loaded: $0.36 + \frac{S}{25}$ Two or More Design Lanes Loaded: $0.2 + \frac{S}{12} - \left(\frac{S}{35}\right)^{2.0}$	$3.5 \le S \le 16.0$ $4.5 \le t_s \le 12.0$ $20 \le L \le 240$ $N_b \ge 4$
Live Load Distribution per Lane for Shear in Interior Beam	One Design Lane Loaded: Lever Rule Two or More Design Lanes Loaded: $g = eg_{interior}$ $e = 0.6 + \frac{d_e}{10}$	$-1.0 \le d_e \le 5.5$

Note: The abovementioned terms in Table A.4 are defined as follows:

K_g = $n(I + Ae_g^2)$.

n = Modular ratio between the girder and slab concrete.

A = Area of the girder cross-section, in^2.

e_g^2 = Distance between the centroid of the girder and the slab, in.

S = Beam Spacing, ft.

L = Span Length, ft.

N_b = Number of beams.

d_e = Distance from exterior web of exterior beam to the interior edge of curb or traffic barrier, in.

t_s = Thickness of slab, in.

The following conditions must be met to use the DFs of Table A.4:

1. Width of slab is constant.
2. Number of girders (N_b) is not less than four.
3. Girders are parallel and of the same stiffness.
4. The roadway part of the overhang, $d_e \leq 3.0$ ft.
5. Curvature in plan is less than 4 degrees.
6. Cross-section of the bridge girder is consistent with one of the cross-sections given in LRFD Table 4.6.2.2.1-1.
7. $3.5 \leq S \leq 16.0$.
8. $4.5 \leq t_s \leq 12.0$.
9. $20 \leq L \leq 240$.
10. $10{,}000 \leq K_g \leq 7{,}000{,}000$.

According to AASHTO LRFD Specifications (AASHTO 2012) Article 3.6.1.3.1, the maximum shear and negative moment under vehicular live load is calculated as the larger of:

1. 90 percent of the effect of (Two Design Trucks + Design Lane Load).

2. 100 percent of the effect of (Two Design Tandems + Design Lane Load).

The two design trucks or tandems are spaced a minimum of 50 ft between the lead axle of one truck/tandem and the rear axle of the other truck/tandem on either side of the interior support to produce the maximum negative moment demand and shear demand. The two design trucks/tandems must be placed in adjacent spans to produce maximum force effects. Fig. A.4 shows the details for design truck tandem and design lane load, and design tandem and design lane load.

A.6 ALLOWABLE STRESS LIMITS

The design of spliced girder bridges involves various stages. It is necessary to ensure that the girder stresses are within the allowable stress limits during all stages of construction. Table A.5 and Table A.6 summarize the allowable stress limits as given in the AASHTO LRFD Specifications (AASHTO 2012). The allowable stress limits have been computed for the girder for a specified concrete compressive strength at service (f'_c) of 8.5 ksi and a specified concrete compressive strength at transfer (f'_{ci}) of 6.5 ksi based on practical limits used by TxDOT. For the deck, a specified concrete compressive strength (f'_c) of 4 ksi is used. The reduction factor, ϕ_w, for the compressive stress limit at the final loading stage is taken equal to 1.0 when the web or flange slenderness ratio, calculated according to the AASHTO LRFD Specifications (AASHTO 2012) Article 5.7.4.7.1, is less than or equal to 15. When either the web or flange slenderness ratio is greater than 15, the provisions of the AASHTO LRFD Specification*s* (AASHTO 2012) Article 5.7.4.7.2 are used to calculate the value for the reduction factor ϕ_w (see AASHTO LRFD Article 5.9.4.2).

Table A.5. Summary of Allowable Stress Limits in Girder.

Stage of Loading	Type of Stress	Allowable Stress Limits	
		f'_c or f'_{ci} (ksi)	Limiting Value (ksi)
Initial Loading Stage at Transfer	Compressive	$-0.60\, f'_{ci}$	−3.90
	Tensile	$0.24\sqrt{f'_{ci}}$	0.612
Intermediate Loading Stage at Service	Compressive	$-0.45\, f'_c$	−3.83
	Tensile	$0.19\sqrt{f'_c}$	0.554
Final Loading Stage at Service	Compressive: Case I	$-0.60\Phi_w\, f'_c$	−5.10
	Compressive: Case II	$-0.40\, f'_c$	−3.40
	Tensile	$0.19\sqrt{f'_c}$	0.550

Note: Tension stresses are positive.

Table A.6. Summary of Allowable Stress Limits in Deck.

Stage of Loading	Type of Stress	Allowable Stress Limits	
		f'_c *(ksi)*	Limiting Value
Final Loading Stage	Compressive	$-0.60\, f'_c$	−5.10
	Tensile	$0.19\sqrt{f'_c}$	0.554

Note: Tension stresses are positive.

A.7 LIMIT STATES

[AASHTO Art. 3.4.1, Table 3.4.1-1]

A.7.1 Service Limit State

For prestressed concrete members, the service load design typically governs; therefore, the design satisfying the service load criteria usually meets the flexural strength limit state. Service load stresses are checked during various stages of construction based on the limits given in Table A.5 and Table A.6. Tension in prestressed concrete members is checked considering the Service III limit state while compression is checked using the Service I limit state as specified in the AASHTO LRFD Specifications (AASHTO 2012).

Service I – checks compressive stresses in prestressed concrete components:

$$Q = 1.00(DC + DW) + 1.00(LL + IM) \quad \text{(A.1)}$$

where:

Q = Total load effect.

DC = Self-weight of girder and attachment (slab and barrier) load effect.

DW = Wearing surface load effect.

LL = Live load effect.

IM = Dynamic load effect.

Service III – checks tensile stresses in prestressed concrete components:

$$Q = 1.00(DC + DW) + 0.80(LL + I \quad \text{(A.2)}$$

A.7.2 Flexure Strength Limit State

The flexural strength limit state needs to be checked to ensure safety at ultimate load conditions. The flexural strength limit state design requires the reduced nominal moment capacity of the member to be greater than the factored ultimate design moment, expressed as follows:

$$\phi M_n \geq M_u \tag{A.3}$$

where:

M_u = Factored ultimate moment at a section, kip-ft.

M_n = Nominal moment strength at a section, kip-ft.

ϕ = Resistance factor.

= 1.0 for flexure and tension of prestressed concrete members.

The total ultimate design bending moment for the Strength I limit state, according to the AASHTO LRFD Specifications (AASHTO 2012) is as follows:

$$M_u = 1.25\ (M_{DC}) + 1.5\ (M_{DW}) + 1.75(M_{LL+IM}) \tag{A.4}$$

where:

M_{DC} = Bending moment due to all dead loads except wearing surface, kip-ft.

M_{DW} = Bending moment due to wearing surface load, kip-ft.

M_{LL+IM} = Bending moment due to live load and impact, kip-ft.

A.7.3 Shear Limit State

[AASHTO Art. 5.8]

The AASHTO LRFD Specifications (AASHTO 2012) specify use of the Modified Compression Field Theory (MCFT) for transverse shear reinforcement. MCFT takes into account the combined effect of axial load, flexure, and prestressing when designing for shear. Shear in prestressed concrete members is checked through the Strength I limit state. The shear strength of concrete is based on parameters β and θ. The transverse reinforcement is based on demands of both transverse and interface shear. The interface shear design is based on shear friction theory where the total resistance is based on the cohesion and friction maintained by shear friction reinforcement crossing the interface shear plane.

The AASHTO LRFD Specifications (AASHTO 2012) require that transverse reinforcement is provided at sections with the following condition:

$$V_u > 0.5\phi(V_c + V_p) \qquad \text{[AASHTO Eq. 5.8.2.4-1]}$$

where:

V_u = Factored shear force at the section, kips.

$$V_u = 1.25(DC) + 1.5(DW) + 1.75(LL + I$$

DC = Shear force at the section due to dead loads except wearing surface load, kips.

DW = Shear force at the section due to wearing surface load, kips.

$LL + I$ = Shear force at the section due to live load including impact, kips.

V_c = Nominal shear strength provided by concrete, kips.

V_p = Component of prestressing force in the direction of shear force, kips.

ϕ = Strength reduction factor.

= 0.9 for shear in prestressed concrete members.

The nominal shear resistance at a section is the lesser of the following two values:

$$V_n = V_c + V_s + V_p \qquad \text{[AASHTO Eq. 5.8.3.3-1]}$$

and

$$V_n = 0.25 f_c' b_v d_v + V_p \qquad \text{[AASHTO Eq. 5.8.3.3-2]}$$

Shear resistance provided by the concrete, V_c, is given as:

$$V_c = 0.0316 \beta \sqrt{f_c'} b_v d_v \qquad \text{[AASHTO Eq. 5.8.3.3-3]}$$

Shear resistance provided by the transverse steel reinforcement, V_s, is given as:

$$V_s = \frac{A_v f_y d_v (\cot\theta + \cot\alpha) \sin\alpha}{s} \qquad \text{[AASHTO Eq. 5.8.3.3-4]}$$

where:

d_v = Effective shear depth, in.

b_v = Girder web width, in.

f_c' = Girder concrete strength at service, ksi.

V_p = Component of prestressing force in the direction of shear force, kips.

β = Factor indicating ability of diagonally cracked concrete to transfer tension.

θ = Angle of inclination of diagonal compressive stresses (slope of compression field), radians.

A_v = Area of shear reinforcement within a distance, s, in.^{2}

s = Spacing of stirrups, in.

f_y = Yield strength of shear reinforcement, ksi.

α = Angle of inclination of diagonal transverse reinforcement to longitudinal axis, taken as 90 degrees for vertical stirrups.

A.8 DEFLECTION

[AASHTO Art. 2.5.2.6.2]

As a final check for service conditions, the girders are checked for allowable deflection under live load and impact as specified in the AASHTO LRFD Specifications (AASHTO 2012) Section 2.5.2.6.2. The deflection limit state ensures that there are no undue vibrations in the bridge and also limits cracking in concrete members. In order to investigate maximum deflections for straight girder systems, all the design lanes are loaded and all the supporting components are assumed to deflect equally. The composite bending stiffness of an individual girder can be taken as the stiffness of the design cross-section, divided by the number of girders.

The limits for maximum deflection as specified in AASHTO LRFD Specifications (AASHTO 2012) Article 2.5.2.6.2 for concrete construction are based on the span length L as follows:

1. Vehicular load, general = $L/800$.
2. Vehicular and/or pedestrian loads = $L/1000$.

The live load is considered as specified in AASHTO LRFD Specifications (AASHTO 2012) Article 3.6.1.3.2, according to which, the deflection is calculated under the larger of the following:

- Design Truck Load alone.
- 25 percent of Design Truck Load and full Design Lane Load.

Fig. A.5 shows the critical load arrangement for vehicular live loads to produce maximum deflections in the continuous girders. Note that the axle loads shown are the full values, but should be reduced for the second load case provided above.

A.9 PRESTRESS LOSSES

[AASHTO Art. 5.9.5]

Prestressing operations are accompanied with losses that result in reduction of the total prestressing force with time. The prestress losses are classified into instantaneous losses and long-term losses. The losses due to elastic shortening and initial steel relaxation are grouped into instantaneous losses. The losses due to creep, shrinkage, and steel relaxation after transfer are long-term losses. The losses due to creep and shrinkage are time dependent. Along with these losses, friction and anchor set losses also need to be

accounted for in post-tensioned members. Based on previous research, empirical formulas are provided for computation of prestress losses. An approximate method can be used for computation of prestress losses for preliminary design. The general equations for approximate estimation of prestress losses in prestressed concrete members are given below.

A.9.1 Approximate Estimation of Losses

[AASHTO Art. 5.9.5.3]

A.9.1.1 Elastic Shortening

The AASHTO LRFD Specifications (AASHTO 2012) provide the following expression to calculate loss in prestress due to elastic shortening.

For pretensioned members:

$$\Delta f_{pES} = \frac{E_p}{E_{ci}} f_{cgp} \tag{A.5}$$

For post-tensioned members:

$$\Delta f_{pES} = \left(\frac{N-1}{2N}\right) \frac{E_p}{E_{ci}} f_{cgp} \tag{A.6}$$

where:

Δf_{pES} = Prestress loss due to elastic shortening, ksi.

E_p = Modulus of elasticity of prestressing reinforcement, ksi.

E_{ci} = Modulus of elasticity of girder concrete at release, ksi.

= $33{,}000\, w_c^{1.5} \sqrt{f'_{ci}}$.

w_c = Unit weight of girder concrete, kcf.

f'_{ci} = Girder concrete strength at transfer, ksi.

f_{cgp} = Sum of concrete stresses at the center-of-gravity of the prestressing steel due to the prestressing force at transfer and self-weight of the member at sections of maximum moment, ksi.

N = Number of identical prestressing tendons.

A.9.1.2 Steel Relaxation

The AASHTO LRFD Specifications (AASHTO 2012) specify the following expressions to estimate the loss in prestress due to relaxation of steel.

[AASHTO Eq. 5.9.5.4.2c-1]

At transfer – low-relaxation strands initially stressed in excess of $0.5f_{pu}$:

$$\Delta f_{pR1} = \frac{\log(24.0t)}{40}\left[\frac{f_{pj}}{f_{py}} - 0.55\right] f_{pj} \quad \text{(A.7)}$$

where:

Δf_{pR} = Prestress loss due to steel relaxation at transfer, ksi.

t = Time estimated in days from stressing to transfer.

f_{pj} = Initial stress in tendon at the end of stressing, ksi.

f_{py} = Specified yield strength of prestressing steel, ksi.

After transfer – low-relaxation strands:

$$\Delta f_{pR2} = 0.3\left[20.0 - 0.4\Delta f_{pES} - 0.2\left(\Delta f_{pSR} + \Delta f_{pCR}\right)\right] \quad \text{(A.8)}$$

where:

Δf_{pR2} = Prestress loss due to steel relaxation after transfer, ksi.

Δf_{pES} = Prestress loss due to elastic shortening, ksi.

Δf_{pSR} = Prestress loss due to concrete shrinkage, ksi.

Δf_{pCR} = Prestress loss due to concrete creep, ksi.

A.9.1.3 Concrete Creep

The AASHTO LRFD Specifications (AASHTO 2012) provide the following expression to estimate the loss in prestress due to creep of concrete:

$$\Delta f_{pCR} = 12 f_{cgp} - 7\Delta f_{cdp} \geq 0 \quad \text{(A.9)}$$

where:

Δf_{pCR} = Prestress loss due to concrete creep, ksi.

f_{cgp} = Sum of concrete stresses at the center-of-gravity of the prestressing steel due to prestressing force at transfer and self-weight of the member at sections of maximum moment, ksi.

Δf_{cdp} = Change in concrete stresses at the center-of-gravity of the prestressing steel due to permanent loads except the dead load present at the time the prestress force is applied calculated at the same section as f_{cgp}, ksi.

A.9.1.4 Concrete Shrinkage

The AASHTO LRFD Specifications (AASHTO 2012) provide the following expression to estimate the loss in prestress due to concrete shrinkage:

$$\Delta f_{pSR} = 17 - 0.15H \tag{A.10}$$

where:

Δf_{pSR} = Prestress loss due to concrete shrinkage, ksi.

H = Mean annual ambient relative humidity in percent, taken as 65 percent for this preliminary study.

A.9.1.5 Losses due to Friction

AASHTO LRFD Specifications (AASHTO 2012) Article 5.9.5.2.2 provides the following expression to estimate the loss in prestress due to friction between internal post-tensioning tendons and the duct:

$$\Delta f_{pF} = f_{pj}(1 - e^{-(Kx+\mu\alpha)}) \tag{A.11}$$

where:

Δf_{pF} = Prestress loss due to friction, ksi.

f_{pj} = Stress in the post-tensioning tendons at jacking, ksi.

x = Length of a tendon from the jacking end to any point under consideration, ft.

K = Wobble friction coefficient, per ft of tendon.

μ = Coefficient of friction.

α = Sum of the absolute values of angular change of the tendon path from the jacking end, or from the nearest jacking end if tensioning is done equally at both ends, to the point under investigation, radians.

A.9.2 Refined Estimate of Time Dependent Losses

For complex prestressed concrete bridges, exact evaluation of prestress losses is desired. A more exact estimate of prestress losses can be made using the time step method. An approximate method can be used for computation of prestress losses for preliminary design. However, for final design, AASHTO LRFD Specifications (AASHTO 2012) Article 5.9.5.4.1 specifies a time step method for computation of prestress losses for spliced girder bridges. In refined estimate of time dependent losses, prestress losses are calculated at different stages of load application. The general equation for computing time dependent prestress losses is as follows:

$$\Delta f_{pLT} = \left(\Delta f_{pSR} + \Delta f_{pCR} + \Delta f_{pR}\right)_{id} + \left(\Delta f_{pSD} + \Delta f_{pCD} + \Delta f_{pR} - \Delta f_{pSS}\right)_{df} \quad \text{(A.12)}$$

where:

Δf_{pSR} = Prestress loss due to shrinkage of girder concrete between transfer and deck placement, ksi.

Δf_{pCR} = Prestress loss due to creep of girder concrete between transfer and deck placement, ksi.

Δf_{pR} = Prestress loss due to relaxation of prestressing strands between time of transfer and deck placement, ksi.

Δf_{pR2} = Prestress loss due to relaxation of prestressing strands in composite section between time of deck placement and final time, ksi.

Δf_{pSD} = Prestress loss due to shrinkage of girder concrete between time of deck placement and final time, ksi.

Δf_{pCD} = Prestress loss due to creep of girder concrete between time of deck placement and final time, ksi.

Δf_{pSS} = Prestress gain due to shrinkage of deck in composite section, ksi.

$\left(\Delta f_{pSR} + \Delta f_{pCR} + \Delta f_{pR}\right)_{id}$ = Sum of time dependent prestress losses between transfer and deck placement, ksi.

$(\Delta f_{pSD} + \Delta f_{pCD} + \Delta f_{pR} - \Delta f_{pSS})_{df}$ = Sum of time dependent prestress losses after deck placement, ksi.

However, the exact computation of prestress losses is cumbersome for spliced girder bridges because of multiple stages of prestressing and combined pretensioning and post-tensioning. According to AASHTO LRFD Specifications (AASHTO 2012) Article 5.9.5.2.3, whenever combined pretensioning and post-tensioning is involved and when post-tensioning is not applied in identical increments, the effect of subsequent post-tensioning on previously stressed members should be considered. Accordingly, multiple stages of prestressing will have an effect on creep and elastic shortening of members,

which needs to be included in the losses. A time step analysis that includes the effects of multiple stages of prestressing will provide a more accurate evaluation of prestress losses. The following expressions show the effect of multiple stages of prestressing on prestress losses.

A.9.2.1 Losses in Pretensioning

The following expression may be used to estimate the total prestress losses in the pretensioning strands due to pretensioning plus two stages of post-tensioning.

$$\Delta f_{pT} = \Delta f_{pES} + \Delta f_{pR} + \Delta f_{pCR} + \Delta f_{pSR} + \left(\Delta f_{pES} + \Delta f_{pCR}\right)_{\mathrm{PT1}} + \left(\Delta f_{pES} + \Delta f_{pCR}\right)_{\mathrm{PT2}} \quad \text{(A.13)}$$

where:

Δf_{pT} = Total loss of prestress, ksi.

Δf_{pES} = Loss due to elastic shortening, ksi.

Δf_{pR} = Loss due to relaxation, ksi.

Δf_{pCR} = Loss due to creep, ksi.

Δf_{pSR} = Loss due to shrinkage, ksi.

$(\Delta f_{pES} + \Delta f_{pCR})_{PT1}$ = Elastic shortening and creep loss due to Stage I PT, ksi.

$(\Delta f_{pES} + \Delta f_{pCR})_{PT2}$ = Elastic shortening and creep loss due to Stage II PT, ksi.

A.9.2.2 Losses in Stage I Post-tensioning

The following expression may be used to estimate the total prestress losses in the Stage I post-tensioning strands when two stages of post-tensioning are used.

$$\Delta f_{pT} = \Delta f_{pES} + \Delta f_{pR} + \Delta f_{pF} + \Delta f_{pCR} + \Delta f_{pSR} + \left(\Delta f_{pES} + \Delta f_{pCR}\right)_{\mathrm{PT2}} \quad \text{(A.14)}$$

where:

Δf_{pF} = Loss due to friction, ksi.

The remaining variables are the same as defined above.

A.9.2.3 Losses in Stage II Post-tensioning

The following expression may be used to estimate the total prestress losses in the Stage II post-tensioning strands when it is the final stage of post-tensioning.

$$\Delta f_{pT} = \Delta f_{pES} + \Delta f_{pR} + \Delta f_{pF} + \Delta f_{pCR} + \Delta f_{pSR} \quad \text{(A.15)}$$

A software analysis may be performed to compute prestress losses for spliced girder bridges and various design programs are available for this purpose. An input of all the time-dependent material properties is required along with a description of geometric section properties, prestressing tendons, construction stages, and applied loads. Time intervals between various stages of construction are required. An exact estimation of prestress losses is not practical during the preliminary design stage. However, for detailed

design, a more precise evaluation of prestress losses using the time step method is recommended.

A.10 DESIGN OF PROTOTYPE BRIDGE FOR SHORED CONSTRUCTION

The following example gives the details for design of the three-span continuous precast prestressed concrete girder bridge described in Section A2 and A3 using shored construction. As noted above, a modified Tx70 girder section is used for this bridge. The design is based on the *AASHTO LRFD Bridge Design Specifications* (AASHTO 2012). In shored construction, shoring towers are provided in both the end span and the center span at each splice location. The length of an individual girder segment is selected based on the length and weight limitations during handling at the precast plant and transportation. The girder spacing is based on typical practice followed by TxDOT. The design parameters such as material properties, strand diameter, and concrete strength are representative of typical values used in Texas. Details are provided in Section A1.

A.11 DESIGN PHILOSOPHY

The principle of post-tensioning (PT) is to balance the dead load. After construction is complete, the net load on the prestressed members will consist primarily of the transient live load. Because the self-weight of the segments is significant, the post-tensioning is applied in two stages. Stage I post-tensioning (PT1) will balance the self-weight of the segments for transportation, erection, and the first stages of construction. PT1 tendons are place in the individual segments. Stage II post-tensioning (PT2), on the other hand, is the continuity post-tensioning and is continuous along the entire length of the girder line to balance the deck weight and super-imposed dead loads. Pretensioning strands will also be

provided within the individual girder segments to counteract the moments that are produced because of the eccentricity of the Stage I PT at the ends of the segments.

To reduce the cost of construction, the required force for post-tensioning should be minimized. The required PT force is proportional to the balanced load and inversely proportional to the drape of the tendons, such that:

$$(F * \delta) = \frac{W * L^2}{8} \tag{A.16}$$

where:

F = Required post-tensioning force, kips.

W = Balanced dead load, kips/ft.

L = Span length, ft.

δ = Eccentricity of tendons, ft.

Because the balanced load is the dead load of the structure and is fixed for a specific type of girder and bridge geometry, the drape should be maximized to minimize the prestressing force. The sequence of construction defines the loads that each girder and segment carry; therefore, the proposed stages for shored construction are described below. Then, the girder loads and required prestressing forces for balancing them are calculated.

A.12 HANDLING AND ERECTION – PRETENSIONING AND FIRST STAGE OF POST-TENSIONING DESIGN

Pretensioning and Stage I post-tensioning are provided to balance the self-weight of the girders. One important issue during the hauling and erection is the location of the supports and lifting points. The lifting points and support locations should be determined according to the support locations for the segments during construction. For shored construction, the drop-in segments and end segments are supported at their ends, so end supports are used when they are transported from the precast plant to the construction site. The girder segments are pretensioned for self-weight during handling and transportation. Stage I post-tensioning is applied to balance the self-weight of the girders. Fig. A.6 shows the support details during transportation of the drop-in and end segments.

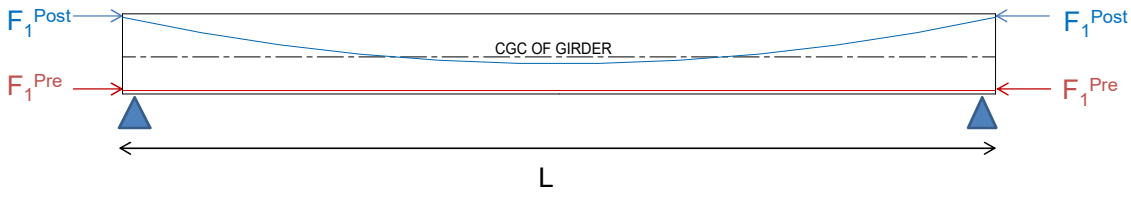

Fig. A.6 Transportation of Drop-in and End Segments.

On the other hand, the on-pier segment is supported at its midpoint, and will be seated on shore towers at its ends, so the post-tensioning profile will be selected to balance loads that produce negative moments. Hence, these segments are not designed to carry significant positive moments. To avoid any positive moments in the on-pier segments, they are transported by supporting it at the quarter span points from ends. The amount of prestress force required in the top flange of the on-pier segment is high because these segments cantilever over the piers and eventually support the ends of the drop-in and end segments. The on-pier girder segment is pretensioned for self-weight plus the girder reactions from the drop-in segment and end segment. Stage I post-tensioning is applied to balance the self-weight and the reaction from the drop-in and end segments. Also, until the stage when the pier segment supports the drop-in girder segment, the stresses in the bottom flange are high. This is offset by providing temporary Dywidag bars in the bottom flange. Fig. A.7 shows the details for support locations and prestressing during transportation of the on-pier girder segment.

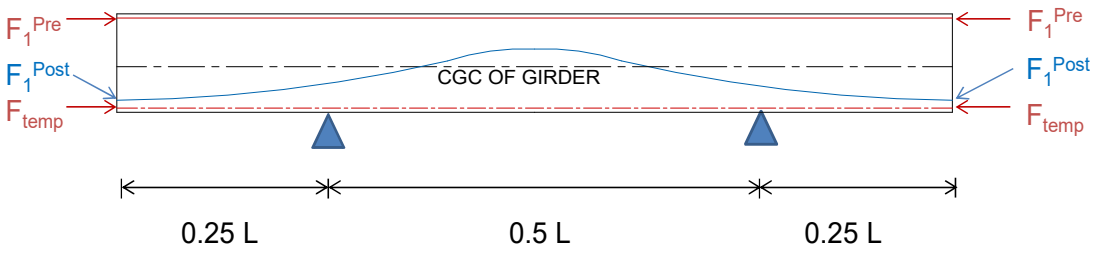

Fig. A.7 Transportation of On-Pier Segment.

The span lengths and weights of the girder segments are taken into consideration during handling and transportation. In Texas, the maximum span length should be limited

to 160 ft, and the maximum weight limited to 200 kips based on input from precasters and contractors (Hueste et al. 2012). These values are primarily due to lifting limits at the precast plant and transportation limits to the construction site. Table A.7 gives the span lengths and weights for the girder segments. Sheet A-1 provides a sample calculation on design of pretensioning and Stage I post-tensioning for the drop-in segment.

Table A.7. Segment Lengths and Girder Weights.

Girder Segments	Length (ft)	Weight (kips)
End Segment	140	161
Drop-in-Girder Segment	140	161
On-Pier Segment	96	111
Recommended Limit	160	200

Following the same procedure for design of pretensioning and Stage I PT strands, the end segments can be designed. The same procedure can also be used for the on-pier segments, but it should be kept in mind that the on-pier segments also carry half of the weight of the drop-in segments and end segments; therefore, their effect on the total negative moment should be considered in the design of on-pier segments. Table A.8 and Table A.9 summarize the pretensioning and Stage I PT requirements, respectively.

Table A.8. Pretensioning Design.

Pretensioning	Drop-in Segment	End Segment	On-Pier Segment
	Bottom Flange	Bottom Flange	Top Flange
Tendons (0.6 in. dia.)	24	32	26
Prestress at Transfer (kips)	1054	1406	1142
Effective Prestress (kips)	843	1125	913

Table A.9. Stage I Post-Tensioning Design.

Post-Tensioning	Drop-in Segment	On-pier Segment	End Segment
Tendons (0.6 in. dia.)	19 (1 duct of 19)	38 (2 ducts of 19)	19 (1 duct of 19)
Prestress at Transfer (kips)	779	1558	779
Effective Prestress (kips)	662	1324	662

Sample Calculation: Pretensioning and PT1, for Drop-in Segment:

Pretensioning:

Material: 0.6" dia, low relaxation strand,

f_{pu}= 270 ksi;

Initial pretensioning at transfer (f_{pi}) = $0.75f_{pu}$ = 202.5 ksi

Loss Estimate: 20 percent

Post-tensioning:

Material: 0.6" dia, low relaxation strand,

f_{pu}= 270 ksi

Initial pretensioning at transfer (f_{pi}) = $0.70f_{pu}$ =189 ksi

Loss Estimate: 15 percent

Note: Center of prestressing steel (c.g.s.) is calculated, considering pretensioning and PT1 together:

$$c.g.s.=\frac{\sum F_i y_i}{\sum F_i}=\frac{F_{pre}y_{pre}+F_{PT1}y_{PT1}}{F_{pre}+F_{PT1}}$$

Because the number of pretensioning strands is more flexible than for PT strands, first the number of ducts for PT1 is decided:

For one duct of 19 strands for PT1, and solving the above equation for no eccentricity at the ends, and required eccentricity for balancing dead load, the number of strands for pretensioning and the profile of PT1 is defined:
(Note that the area of 0.6" dia strands is 0.217 in^2, y_b=32.3 in., y_{tc}=-37.7 in., minimum distance from girder face to centerline of pretensioning is assumed to be 6 in.)

a) At ends (x=0):

$F_{pre}y_{pre}+F_{PT1}y_{PT1}=0$

$n*0.8*202.5*0.217*(32.25-6)+19*0.85*189*0.217*(-37.75+6)=0$

n=23 (For symmetry, use 24 strands)

b) At x=L/2 = 70 ft:

$$F=\frac{w*L^2}{8*\delta}$$

$$24*0.8*202.5*0.217+19*0.85*189*0.217=\frac{1.15\ k/ft*(140\ ft)^2}{8*\delta}$$

δ=1.87 ft=22.47 in.

Note: Maximizing the drape will minimize the force, but it should be kept in mind that PT2 ducts will be running under the PT1 ducts. Assuming 3 ducts for PT2, and considering 6 in. clear cover from the soffit, 2 in. clear cover between ducts, the location of PT1 ducts will be as follows when the diameter of ducts is assumed to be 4 in.:

$$y=32.25-6-3*4-3*2-\frac{4}{2}=6.25\ in.$$

Therefore the elevation of PT1 duct from top of the girder is:

y_{top}= 6.25+37.75 = 44 in.

For the pretensioning strands, the centroid from top of the girder will be:

y_{top} = 62 in.

$$y_{avg}=\frac{24*62+19*44}{24+19}=54\ in.$$

δ= 54-37.75=16 in < 22.5 in. N.G.

Considering that 24 pretensioning strands can be placed in 2 rows, the centroid of the pretensioning strands can be taken down to 3.5 in. from soffit (2.5 in. to centroid of first row, and on a 2 in. spacing grid).

Also, the PT duct may be taken to the top of the girder and be anchored on top of the girder (as shown in Fig. A.11) so that the c,g,s at the end is equal to 34 in. from top.

$$y_{avg}=\frac{24*66.5+19*44}{24+19}=56.6\ in.$$

δ= 56.6-34=22.6 in > 22.5 in. O.K.

For the purpose of handling and transportation, temporary unbonded Dywidag threadbars are provided in the bottom flange of the pier segments. Once the pier segment is erected on site, it behaves as a cantilever, and the Dywidag bars are released. Dywidag threaded bars of 1.25 in. diameter and f_{pu} equal to 150 ksi are considered for the design.

A.13 CONSTRUCTION ON SITE

After the girders are transported to the job site, the girders are lifted and placed on piers and temporary shoring towers. Then Stage II post-tensioning is carried out to balance the weight of the deck and to provide compression in the deck. Fig. A.8 shows the details of various stages of construction. The step-by-step construction procedure is as follows:

1. Erect piers, abutments, and temporary supports.
2. Place on-pier girder segments on the piers and secure the girders to the temporary shoring towers.
3. Attach strongbacks to each end segment. Erect the end girder segments on the abutments and shoring towers. Connect the strongbacks to the on-pier girder segments. The shoring towers should be capable of transferring the reaction from the end girder segment to the foundation.
4. Attach strongbacks to the ends of the drop-in girder segment. Erect the drop-in-girder segment and connect the strongbacks to the on-pier girder segment. It is necessary that the end girder segments are installed prior to this step. This ensures that there is less rotation of the on-pier segment caused by the reaction of the drop-in-girder segment. Tie-downs could also be used to prevent uplift at the end of the on-pier segment.

5. After all the segments have been placed, check the vertical alignment of the girders. Strongbacks help in maintaining the vertical alignment of the adjacent girders prior to threading the post-tensioning tendons through the ducts. Provide couplers between the ducts of adjacent girders at the splice locations. Then, thread the continuous Stage II PT tendons through the ducts in the webs of the girder segments.
6. Cast the splices between the girder segments. Once the splices have cured and gained sufficient strength, remove the strongbacks.
7. Construct the formwork for the deck and place the precast concrete deck panels and deck reinforcement. Pour the concrete for the deck. After the deck concrete has reached sufficient strength, stress the Stage II PT and then grout the tendons.
8. Remove the temporary shoring towers. Cast the barriers and wearing surface and, after a suitable time interval, the bridge can be opened to traffic.

Table A.10 provides the values for the Stage II post-tensioning design.

Table A.10. Stage II Post-Tensioning Design.

Post-Tensioning	**Drop-in Segment**	**On-pier Segment**	**End Segment**
Tendons (0.6 in dia.)	57 (3 ducts of 19)	57 (3 ducts of 19)	57 (3 ducts of 19)
Force at Transfer (kips)	2337	2337	2337
Force Final (kips)	1987	1987	1987

The Stage II post-tensioning is designed to act continuously to balance the deck and superimposed dead load. Stage II PT will be carried out on site after the girders are erected on temporary supports and piers. Service stresses may control the amount of post-tensioning provided. For the Stage II PT, 0.6 in. dia. low relaxation strands with f_{pu} of 270 ksi are considered. The jacking force in post-tensioning tendons is assumed to be 0.70 f_{pu}, which is equal to 189 ksi. The force at transfer is calculated after taking the losses into account. Prestress losses of 15 percent are assumed in selection of the Stage II post-tensioning.

A.14 PRESTRESSING LAYOUT

Fig. A.9 shows an overview of the longitudinal prestressing profiles for the shored case. Cross-sections are provided at several key locations illustrating the pretensioning and post-tensioning layout. Fig. A.11 (g) shows profile details of the post-tensioning layout for the three-span bridge.

A.15 MOMENTS DURING VARIOUS STAGES OF CONSTRUCTION

The moments during the various stages of construction considered are computed at selected locations along the structure and are provided in Table A.11. The moments are computed at 0.4*L* from the abutment support of end span (Section A-A), at the end span splice (Section B-B), at the face of the pier (Section C-C), at the interior span splice (Section D-D), and at midspan of the interior span (Section E-E) as shown in the Fig. A.10. The moments due to girder self-weight, precast concrete panels (PCPs), and the wet CIP deck act on the non-composite girder section. The moments due to removal of shoring towers, superimposed dead load, and live load act on the composite girder section. The moments due to prestressing are computed before losses. Table A.11 provides a summary of the moments at each of these locations. Fig. A.11 and Fig. A.12 show the moments due to the permanent loads acting on the non-composite girder section and the composite girder section, respectively.

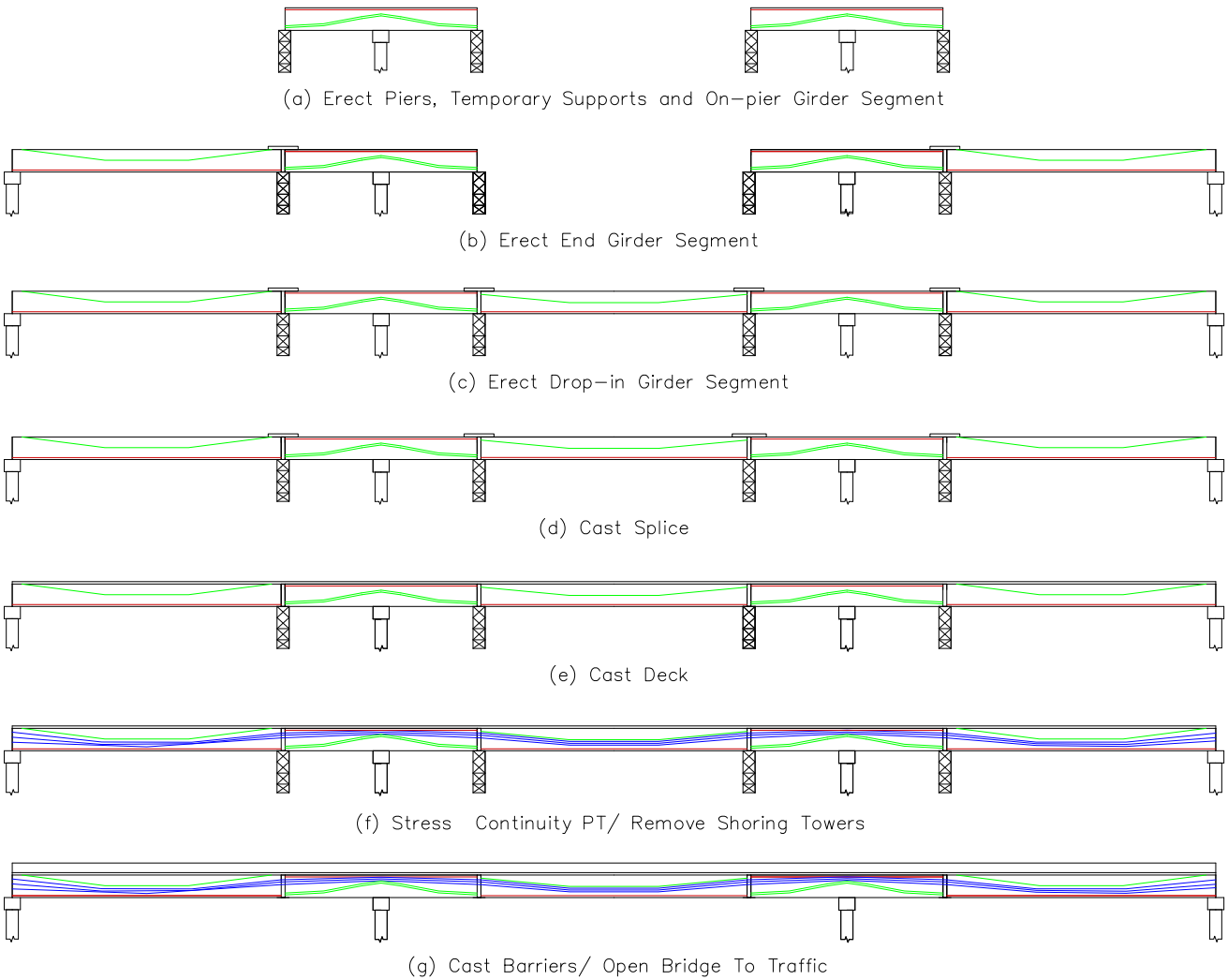

Fig. A.8 Stages of Construction.

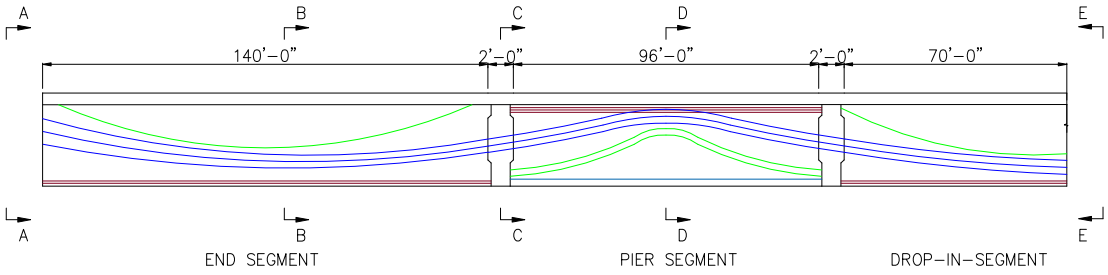

(a) Prestressing Profiles

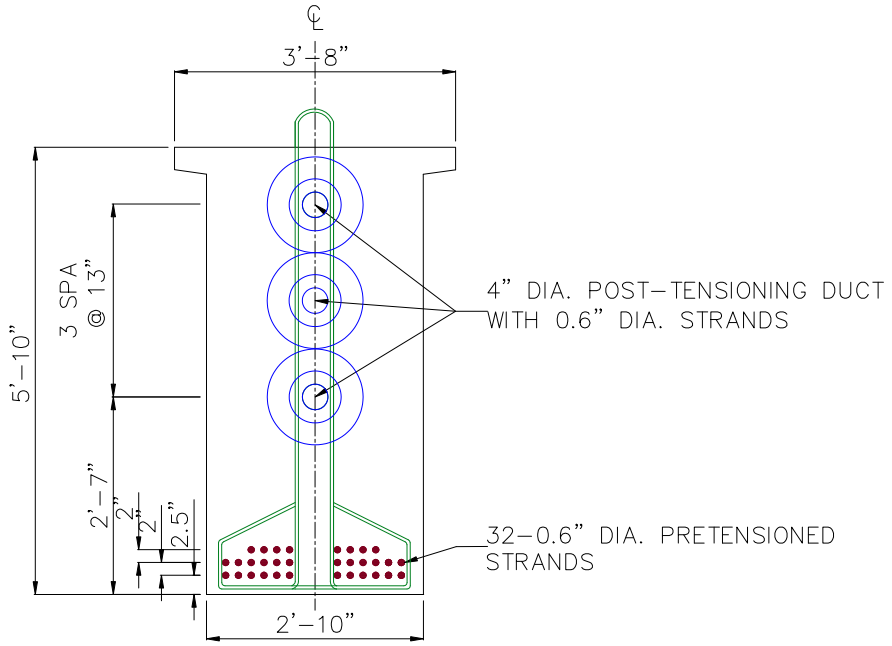

(b) Prestressing Layout at Section A-A at Anchor End

Fig. A.9 Prestressing Details for Shored Three-Span Girder.

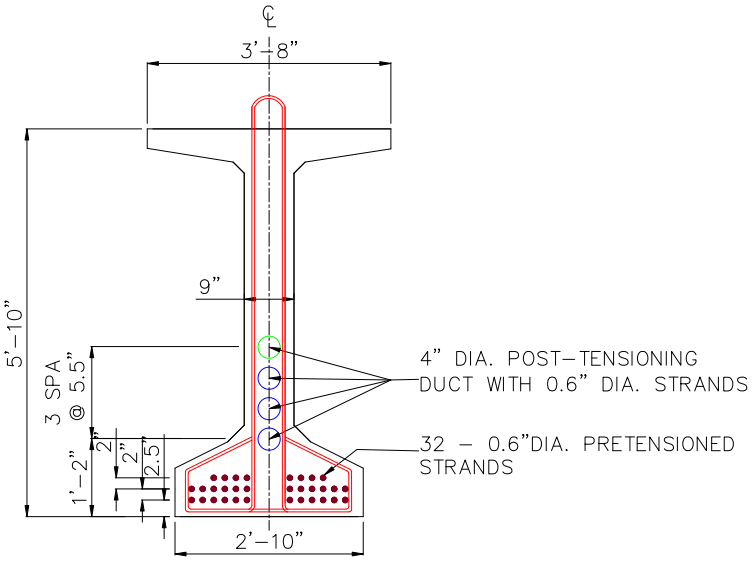

(c) Prestressing Layout at Section B-B Near Midspan of End Span

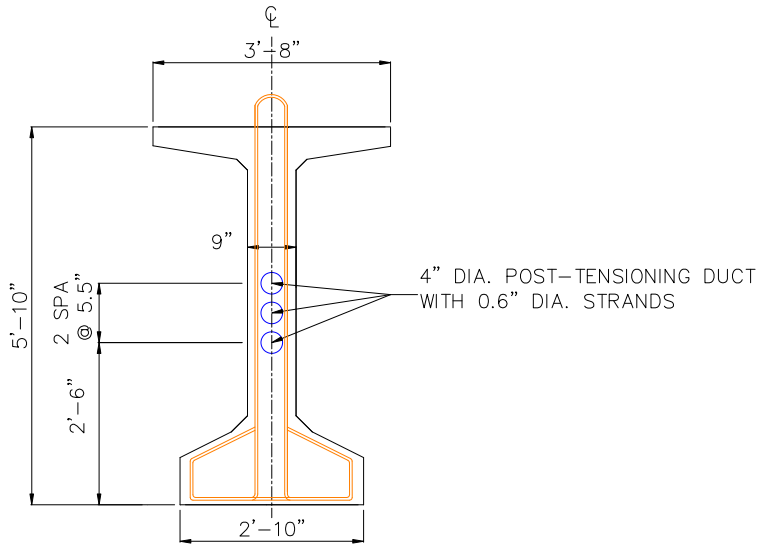

(d) Prestressing Layout at Section C-C at Splice Connection in End Span

Fig. A.9 Continued.

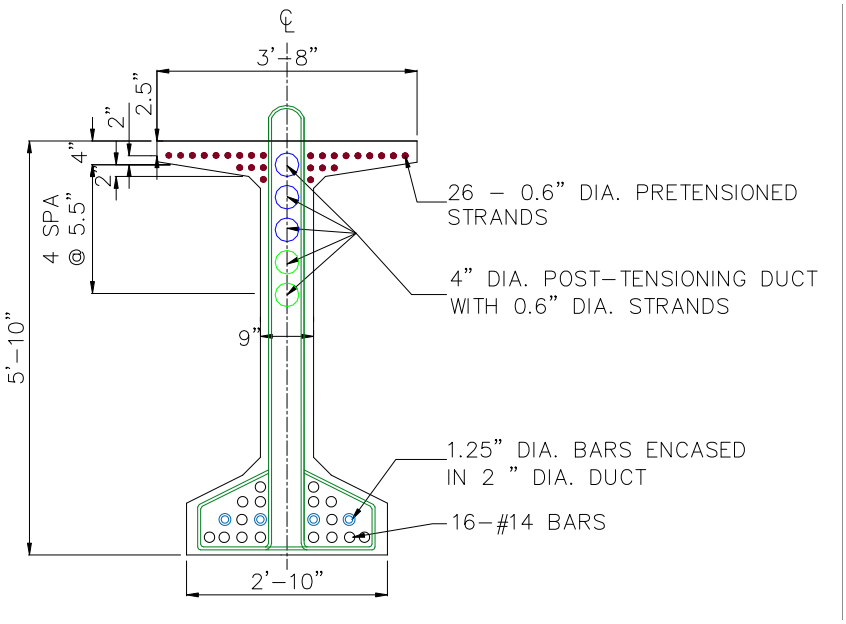

(e) Prestressing Layout at Section D-D at Interior Pier

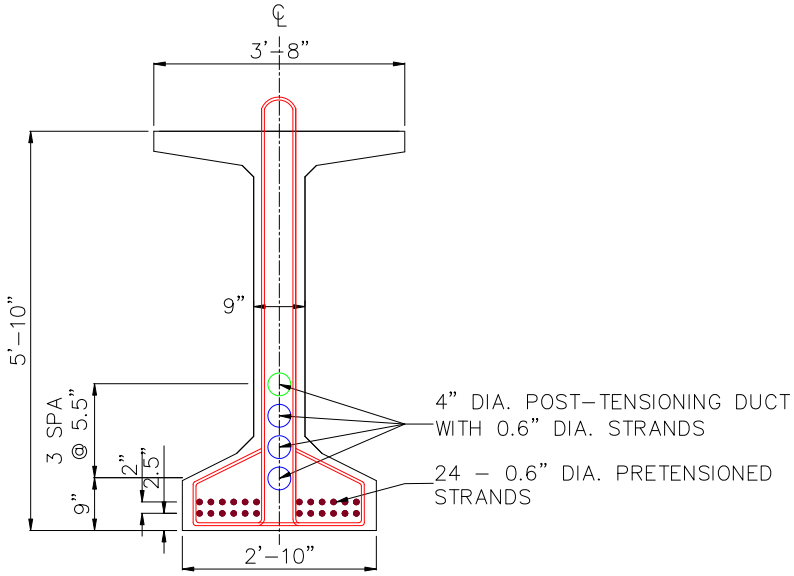

(f) Prestressing Layout at Section E-E Near Midspan of Drop-In Segment

Fig. A.9 Continued.

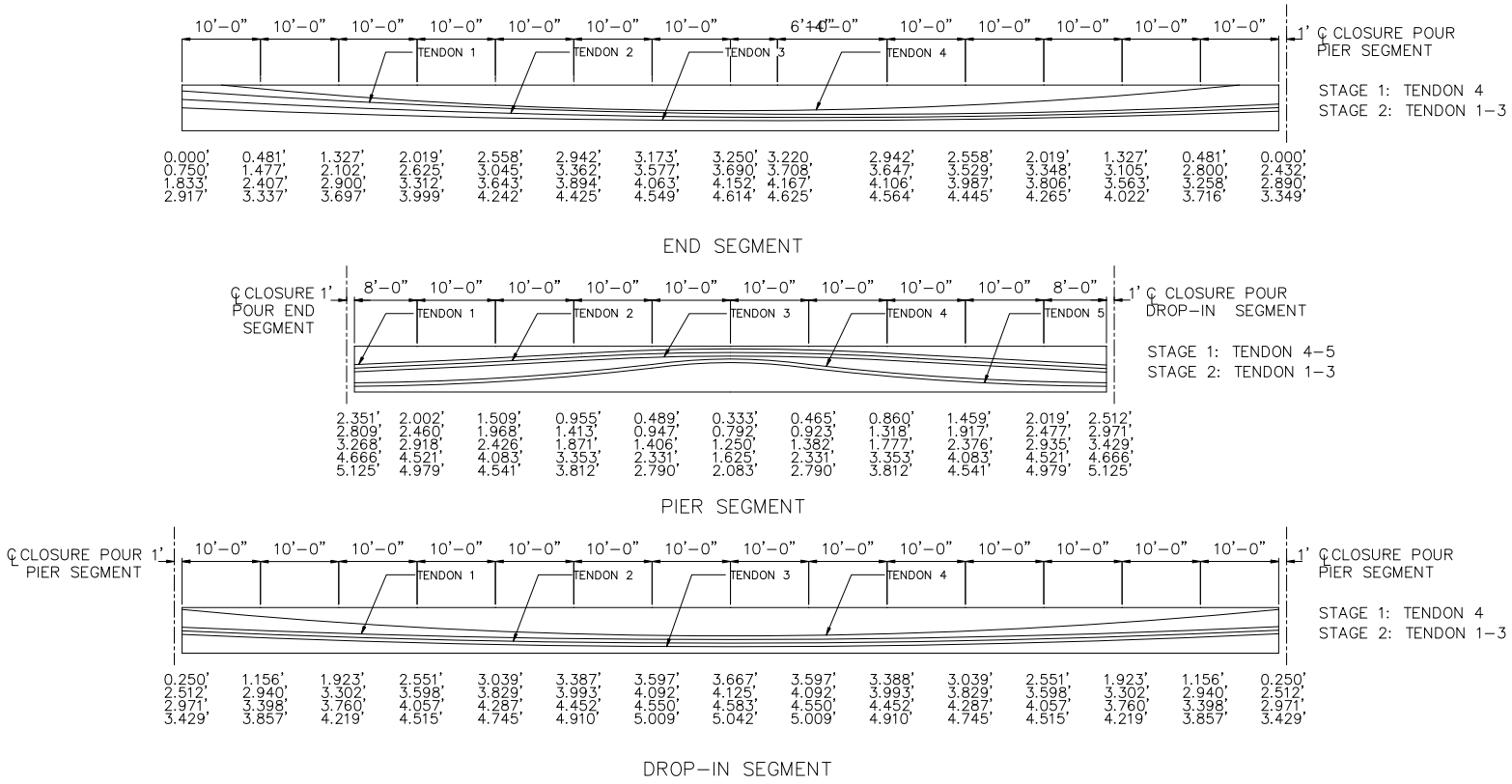

(g) Post-Tensioning Layout

Fig. A.9 Continued.

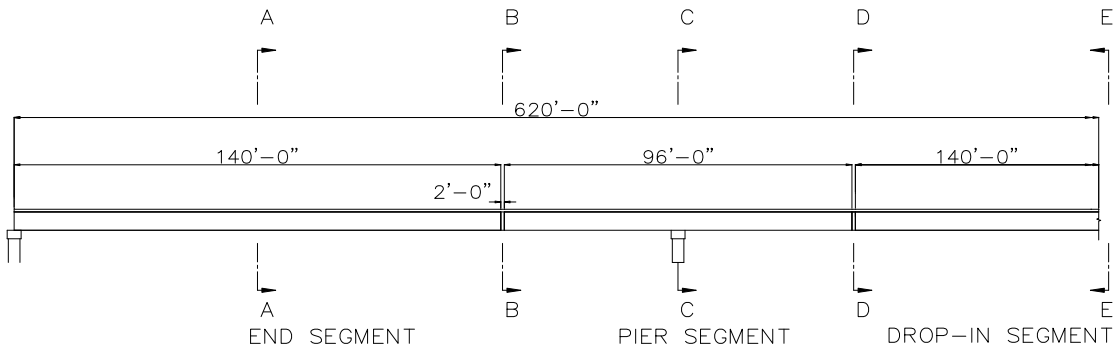

Fig. A.10 Section Locations for Girder Moments.

Table A.11. Girder Moments at Various Sections (kip-ft).

Loading	Section				
	A-A (End Segment)	**B-B (Splice Exterior)**	**C-C (Pier)**	**D-D (Splice Interior)**	**E-E (Drop-in segment)**
Girder Self-Weight	2822	-	−1383	-	2822
Pretensioning and Stage I PT	−3281	-	5185	-	−2896
Reaction from Drop-in Segment	-	-	−3871	-	-
Haunch and Deck	1293	−1719	−467	−1256	896
Stage II Post- tensioning	−4161	+195	5436	−327	−3344
Shoring Support Removal	942	1763	−4593	1306	1306
Superimposed Dead Load	725	11	−1391	15	739
Live Load	5736	3660	−5391	2371	6109

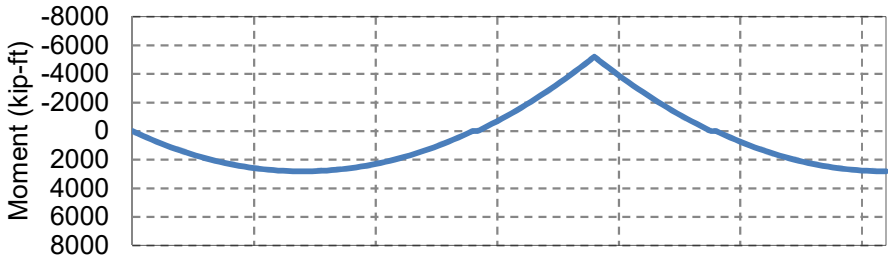

(a) Self-weight and Girder Reaction

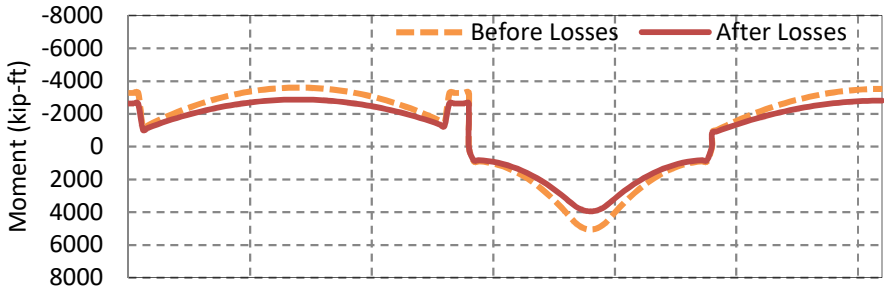

(b) Pretensioning and Stage I Post-Tensioning

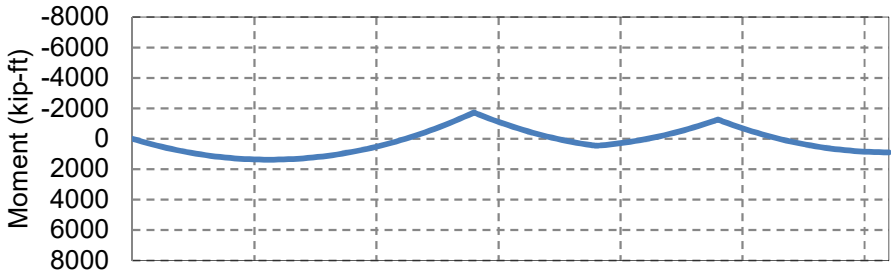

(c) Wet Deck Weight

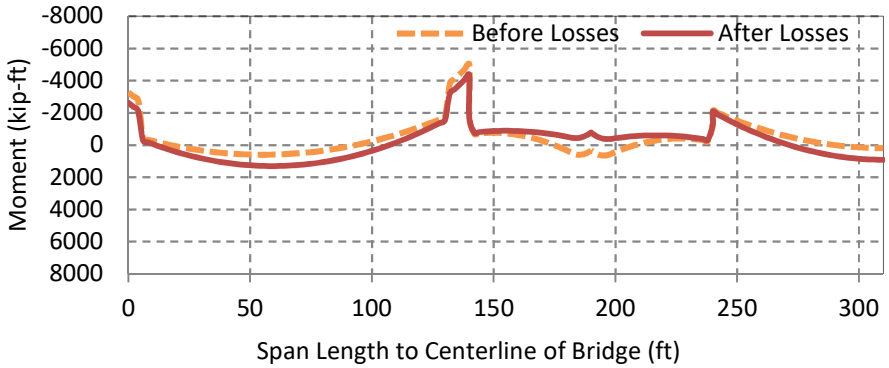

(d) Girder Moments with Wet Deck

Fig. A. 11 Moments Acting on Non-Composite Girder.

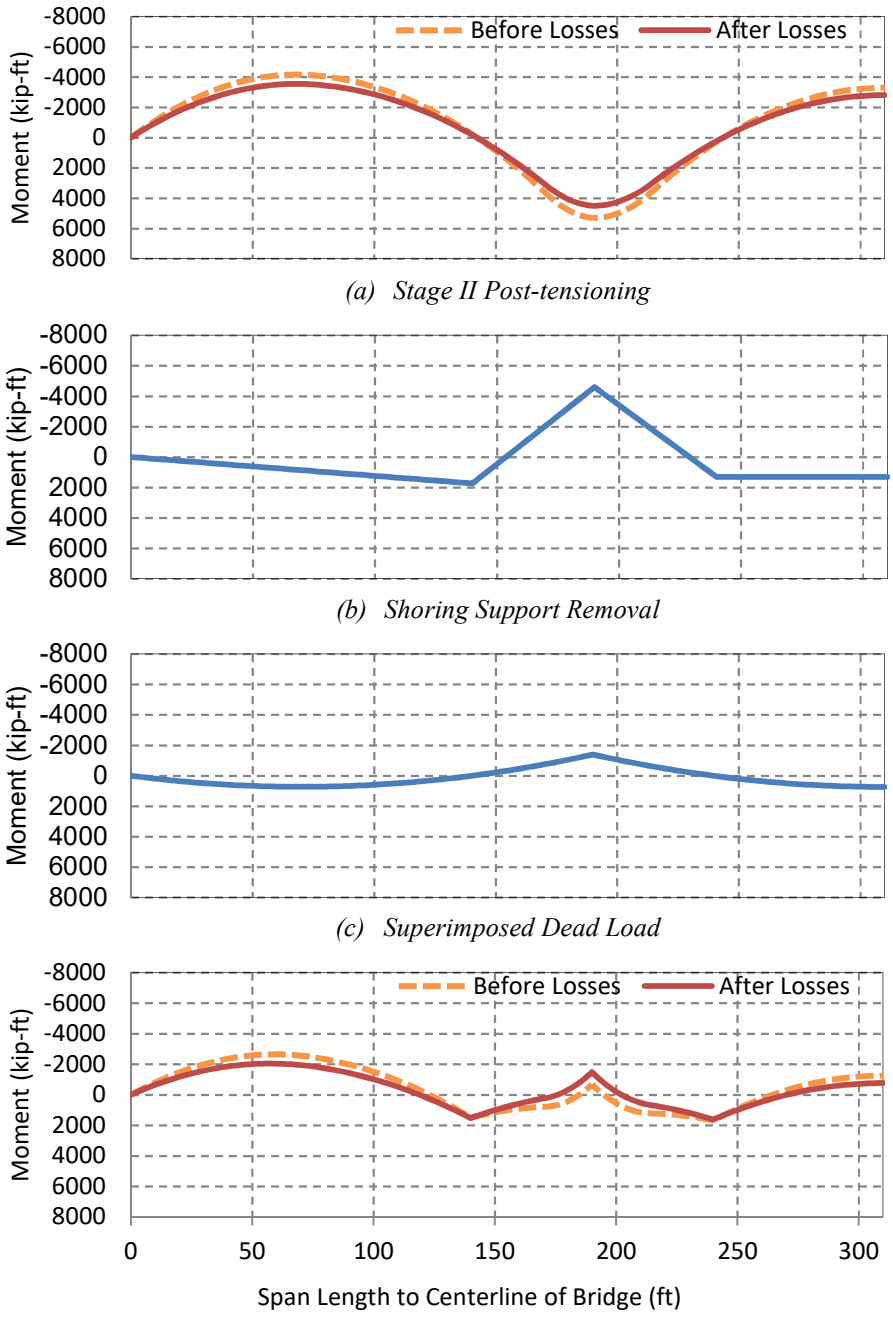

(a) Stage II Post-tensioning

(b) Shoring Support Removal

(c) Superimposed Dead Load

(d) Total Composite Section Moments

Fig. A.12 Moments Acting on Composite Girder.

A.16 SERVICE STRESS ANALYSIS

Service stress analysis is carried out under the effect of dead loads, prestress, live loads, and temperature and thermal gradient. The stresses are checked at various stages of construction. The important construction stages for checking girder stresses are identified as follows:

- Stage I: Support girder segments on piers and temporary supports.
- Stage II: Girders support weight of PCPs and wet CIP deck.
- Stage III: Apply Stage II post-tensioning, remove shoring towers, and cast barriers.
- Stage IV: Open bridge to service.

For the various stages of construction, stress checks are provided at the following points: (1) 0.4L of the end span, (2) at the splice in the end span, (3) at the face of pier, and (4) at a splice in the center span, and (5) at the midspan of center span. Compression in prestressed concrete girders is evaluated using the AASHTO Service I limit state while tension in prestressed concrete girders is evaluated using the AASHTO Service III limit state.

Fig. A.14 through Fig. A.18 present the stress blocks at Section A-A (0.40L of the end span), Section B-B (at the splice in the end span), Section C-C (at the face of the pier), Section D-D (at the splice in the center span), and Section E-E (at the midspan of the center span), as shown in Fig. A.13. Table A.12 provides a summary of the stresses at various sections.

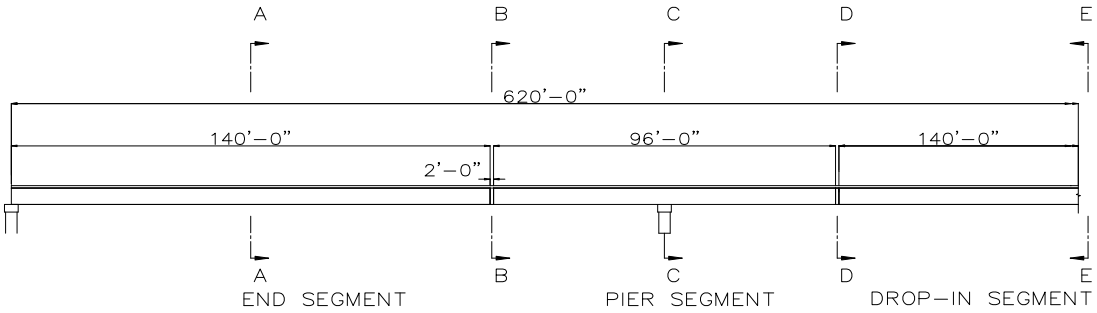

Fig. A.13 Section Locations for Stress Checks.

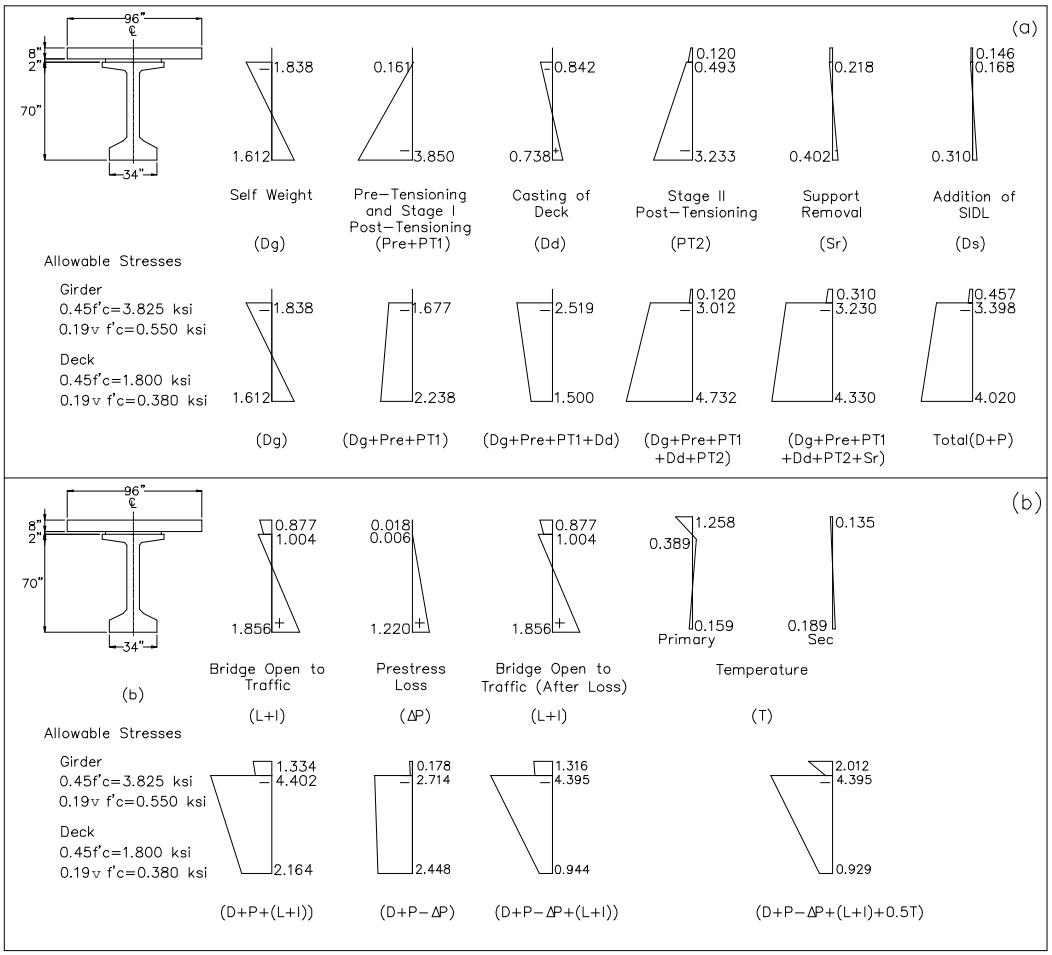

Fig. A.14 Stress Check at Section A-A (End Segment) for (a) Construction and (b) In-Service before and after Losses.

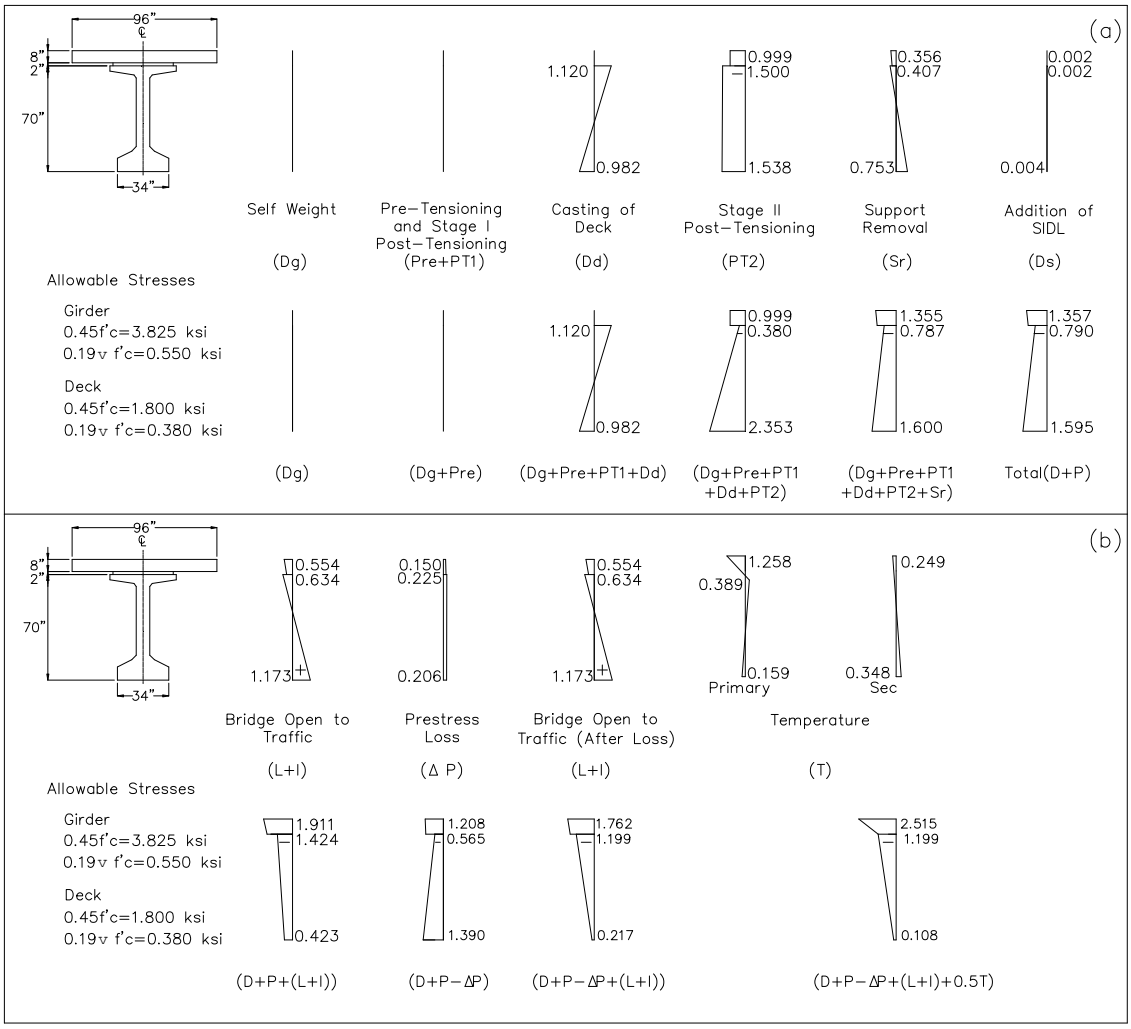

Fig. A.15 Stress Check at Section B-B (Splice in Exterior Span) for (a) Construction and (b) In-Service before and after Losses.

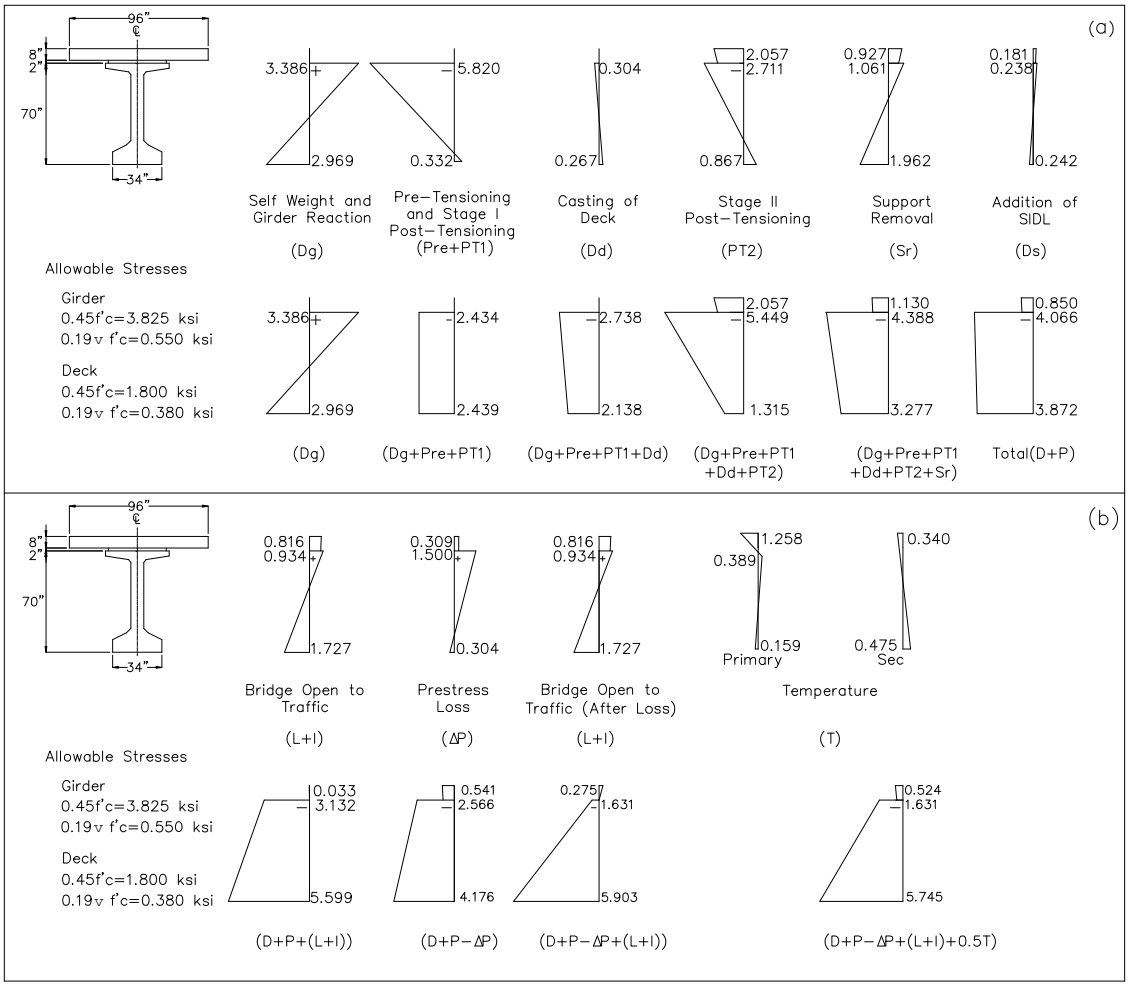

Fig. A.16 Stress Check at Section C-C (Over Pier) for (a) Construction and (b) In-Service before and after Losses.

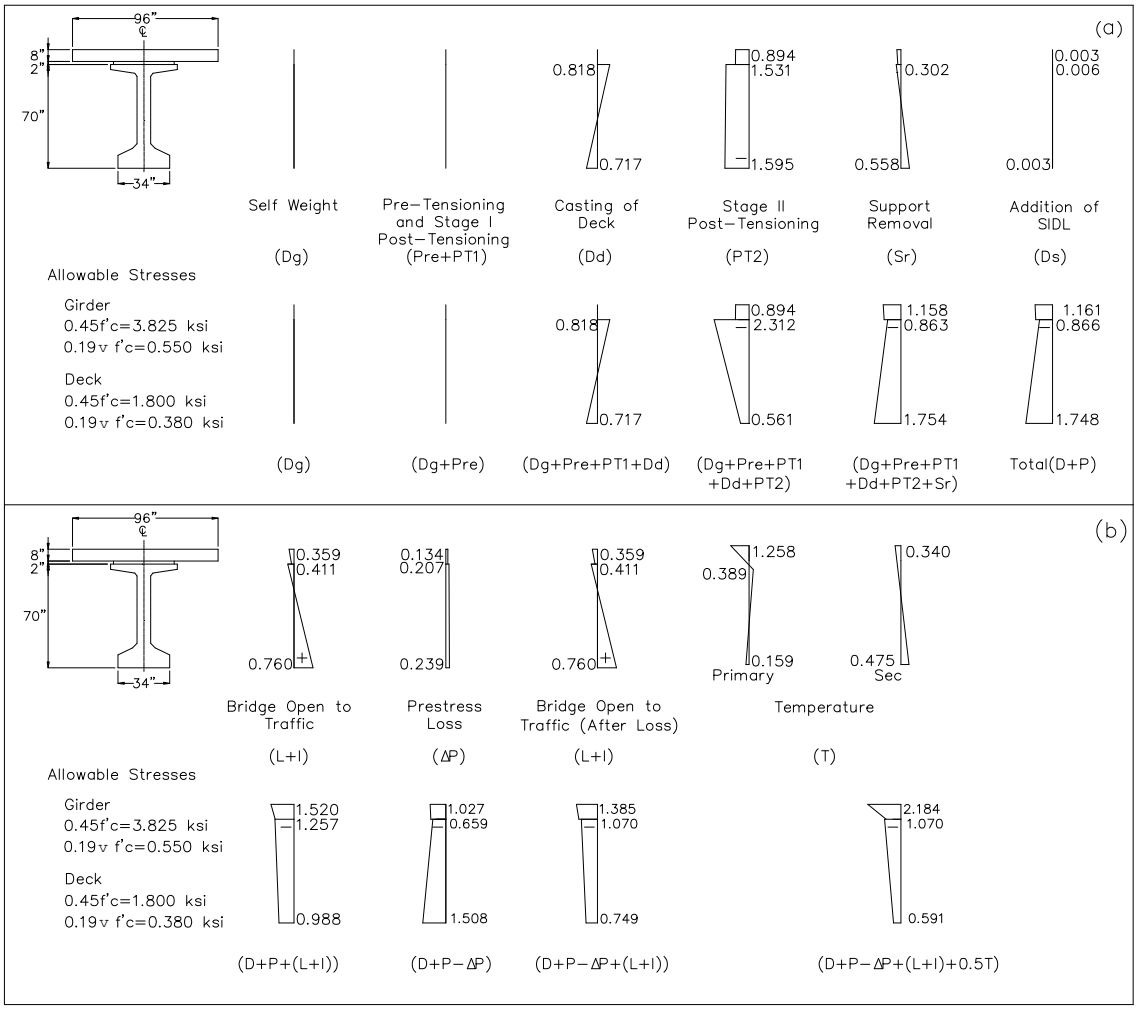

Fig. A.17 Stress Check at Section D-D (Splice in Interior Span) for (a) Construction and (b) In-Service before and after Losses.

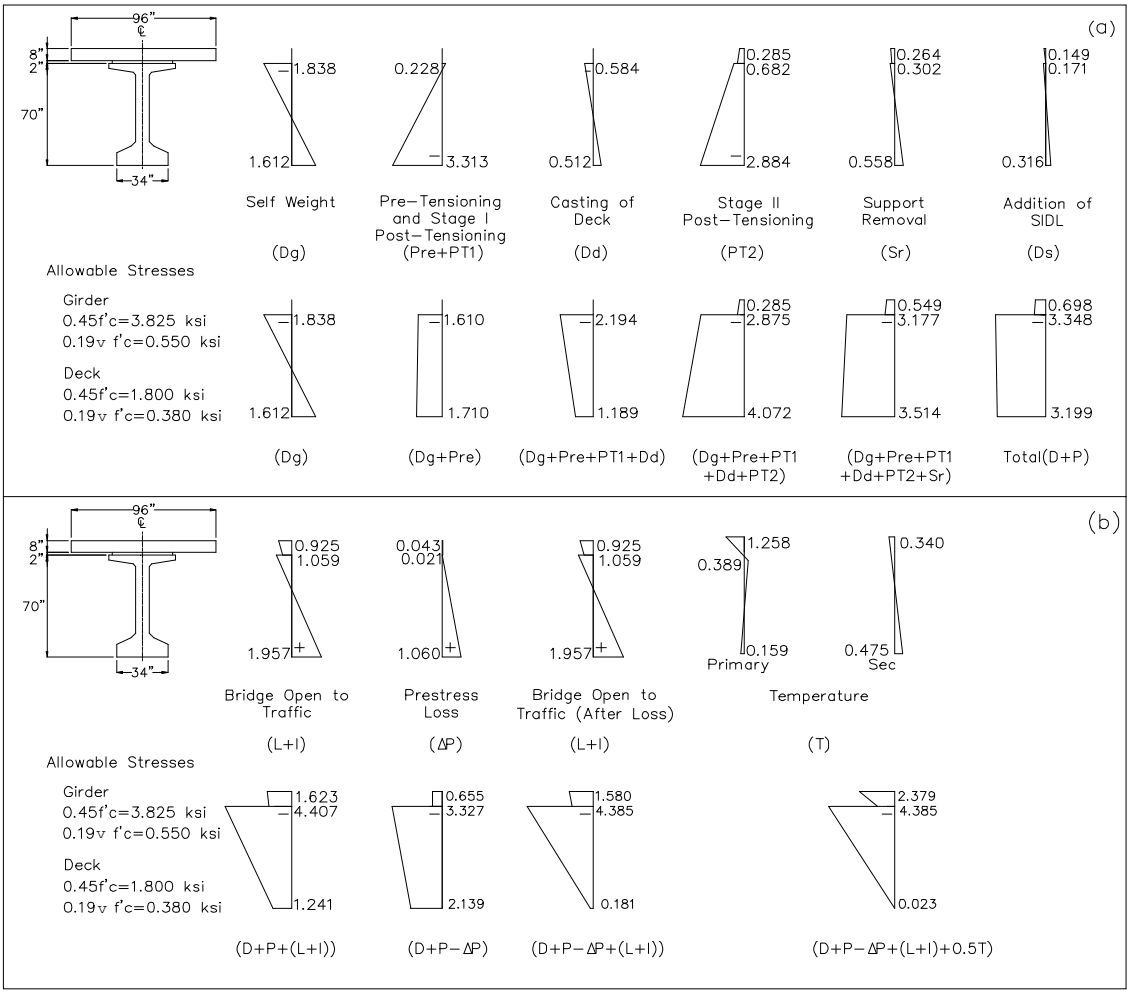

Fig. A.18 Stress Check at Section E-E (Drop-in Segment) for (a) Construction and (b) In-Service before and after Losses.

Table A.12. Girder Stresses at Various Sections (ksi).

Loading	Component	Location	Section					Limit	
			A-A (End Segment)	B-B (Splice Exterior)	C-C (Pier)	D-D (Splice Exterior)	E-E (Drop-in Segment)	Compression (Service I)	Tension (Service III)
Step I (Before Loss)	Girder	Top	−1.677	-	−2.434	-	−1.610	−3.825	+0.550
		Bot	−2.238	-	−2.449	-	−1.700		
Step II (Before Loss)	Girder	Top	−2.519	**+1.120**	−2.738	**+0.818**	−2.194	−3.825	+0.550
		Bot	−1.500	−0.982	−2.183	−0.717	−1.189		
Step III (After Loss)	Girder	Top	−3.391	−0.565	−2.566	−0.659	−3.327	−3.825	+0.550
		Bot	−2.800	−1.390	−4.176	−1.508	−2.139		
	Deck	Top	−0.439	−1.208	−0.541	−1.027	−0.655	−2.400	+0.380
		Bot	−0.531	−1.112	−0.608	−0.975	−0.694		
Step IV - Service (After Loss)	Girder	Top	−4.395	−1.199	−1.631	−1.070	−4.385	−5.100	+0.550
		Bot	−0.944	−0.217	**−5.903**	−0.481	−0.181		
	Deck	Top	−1.316	−1.762	0.275	−1.385	−1.580	−2.400	+0.380
		Bot	−1.194	−1.531	0.009	−1.246	−1.393		

Bold font indicates stress values that exceed stress limits.

Both splice locations experience tensile stresses that exceed the allowable tensile stresses at service conditions when the deck is poured (Step II). This stress exceedance is addressed by providing two #6 U bent mild steel reinforcement in the top flange. In addition, any cracks that may form will close when the Stage II PT operation is carried out.

The compressive stresses in the girder soffit at the interior support in the negative moment region were exceeded due to the large amount of PT tendons in the section. This stress exceedance may be addressed by increasing the specified concrete compressive strength to stay within the allowable compressive stress limit. Another option is to provide additional mild steel reinforcement in the compression zone. For this design, 16-#14 bars and four Dywidag bars were added in the bottom flange of the girder to improve the nominal capacity of the section as specified in the ultimate strength check. This additional mild steel reinforcement is also adequate to serve as compression reinforcement in the girder soffit at the interior support over the pier for the computed stress exceedance at service load conditions.

The deck in the pier region experiences tensile stresses due to negative bending under service conditions. However, these tensile stresses are within the allowable tensile stress limits.

A.17 DEFLECTION CHECK

The girders are to be checked for allowable deflection under live load and impact as specified in AASHTO LRFD Specifications (AASHTO 2012) Article 2.5.2.6.2. Composite section properties are used in computing deflections that occur under service

loadings. According to AASHTO LRFD Specifications (AASHTO 2012) Article 3.6.1.3.2, the deflection is calculated as the larger of:

1. Design truck alone, or
2. 25 percent of Design Truck Load and full Design Lane Load.

The design truck load is multiplied with the dynamic amplification factor to compute deflections. The limit for maximum live load deflection is specified as $L/800$ where L is the span length in inches (AASHTO 2012, Article 2.5.2.6.2). Table A.13 provides the allowable and actual deflection values for the three-span bridge. The computed live load deflections are observed to be within the limits for both the exterior and interior spans.

Table A.13. Live Load Deflection Check.

Deflection	Exterior Span	Interior Span
Allowable (in.)	2.85	3.60
Actual (in.)	1.21	1.34

A.18 FLEXURAL STRENGTH CHECK

The flexural strength limit state must be checked to ensure safety at ultimate load conditions, and requires that the reduced nominal moment capacity of the member be greater than the factored ultimate design moment, expressed as follows:

$$M_u \leq \phi M_n \tag{A.17}$$

where:

M_u = Factored ultimate moment at a section, kip-ft.

M_n = Nominal moment strength at a section, kip-ft.

ϕ = Resistance factor.

= 1.0 for flexure and tension of prestressed concrete members.

The total factored moment at ultimate according to the AASHTO LRFD Specifications (AASHTO 2012) is given by:

$$M_u = 1.25\,(M_{DC}) + 1.5\,(M_{DW}) + 1.75\,(M_{LL+IM}) \quad \text{(A.18)}$$

where:

M_{DC} = Bending moment due to all dead loads except wearing surface, kip-ft.

M_{DW} = Bending moment due to wearing surface load, kip-ft.

M_{LL+IM} = Bending moment due to live load and impact, kip-ft.

The moment capacity and demand is checked at the following points: (1) $0.4L$ of the end span, (2) at the face of pier, and (3) at the midspan of the center span. The moment capacity at ultimate depends on the number of strands, diameter of strands, stress in the stands, design strength of concrete, and the cross-section properties of the section. Table A.15 gives the moment demand and capacity for the three-span bridge. The capacity is greater than demand at each section considered.

Table A.14. Moment Capacity and Demand at Ultimate.

Capacity and Demand	End Segment	On-Pier Segment	Drop-in Segment
M_u, kip-ft	14,940	20,680	15,330
ϕM_n, kip-ft	22,780	24,180	24,430

Table A.15. Moment Capacity and Demand at Ultimate.

Capacity and Demand	End Segment	On-Pier Segment	Drop-in Segment
M_u, kip-ft	14,940	20,680	15,330
ϕM_n, kip-ft	22,780	24,180	24,430

The negative moment capacity provided by the pretensioning strands and post-tensioning tendons at the interior supports is supplemented by adding mild steel reinforcement. For this design, 16-#14 bars and four 1.0 in. diameter Dywidag bars are added in the bottom flange of the girder to provide the additional capacity and meet the moment demand at the interior support over the pier. The mild steel reinforcement provided in the bottom flange acts as compression steel.

A.19 SHEAR STRENGTH CHECK

MCFT is used for transverse shear design as specified in the AASHTO LRFD Specifications (AASHTO 2012). MCFT takes into consideration the combined effect of axial load, flexure, and prestressing when determining the shear strength provided by the concrete section. Fig. A.19 (a) shows the shear demand and shear design for the three-span prototype bridge from the abutment to the centerline of the symmetric structure. Fig. A.20 shows the details of the shear reinforcement. The stirrup layout is as follows:

- End girder segment:
  - #5 double-legged stirrups at a spacing of 4 in. are provided for a distance of 10 ft from the abutment end of the end segment.
  - #5 double-legged stirrups at a spacing of 6 in. are provided from 10–20 ft from the abutment end of the end segment.
  - #5 double-legged stirrups at a spacing of 12 in. are provided in the remaining portion of the end segment.
- Pier girder segment:
  - #5 double-legged stirrups at a spacing of 4 in. are provided for a distance of 29 ft from the centerline of pier toward the center span and 24 ft from the centerline of pier toward the end span in the ends of the pier segment.
  - #5 double-legged stirrups at a spacing of 6 in. are provided in the remaining portions of the pier segment.
- Drop-in girder segment for center span:

- #5 double-legged stirrups at a spacing of 6 in. are provided for a distance of 20 ft from each end of the drop-in segment.
- #5 double-legged stirrups at a spacing of 12 in. are provided in the remaining portion of the drop-in segment.

The transverse bars were extended above the top flange to provide shear resistance for interface shear between the deck and the girder segments. The provided shear resistance at the interface plane was calculated based on Article 5.8.4.1-3 of the AASHTO LRFD Specifications (AASHTO 2012). The interface shear resistance is compared with the factored interface shear demand in Fig. A.19 (b).

A.20 SPLICE DESIGN

A.20.1 Splice Details

Splices are located at the dead load point of contraflexure in the prototype bridge to minimize the load demands at the splice. The width of the splice connection should be kept as small as possible because there is no pretensioning in this region and a minimal amount of mild steel reinforcement is provided. However, the splice width should be large enough to splice the continuity PT tendon ducts and allow for proper vibration of the cast-in-place concrete for the splice. The width of the splice connection detail is 24 in. (2 ft) per TxDOT recommendations. Fig. A.21 shows the splice connection detail considered for the design.

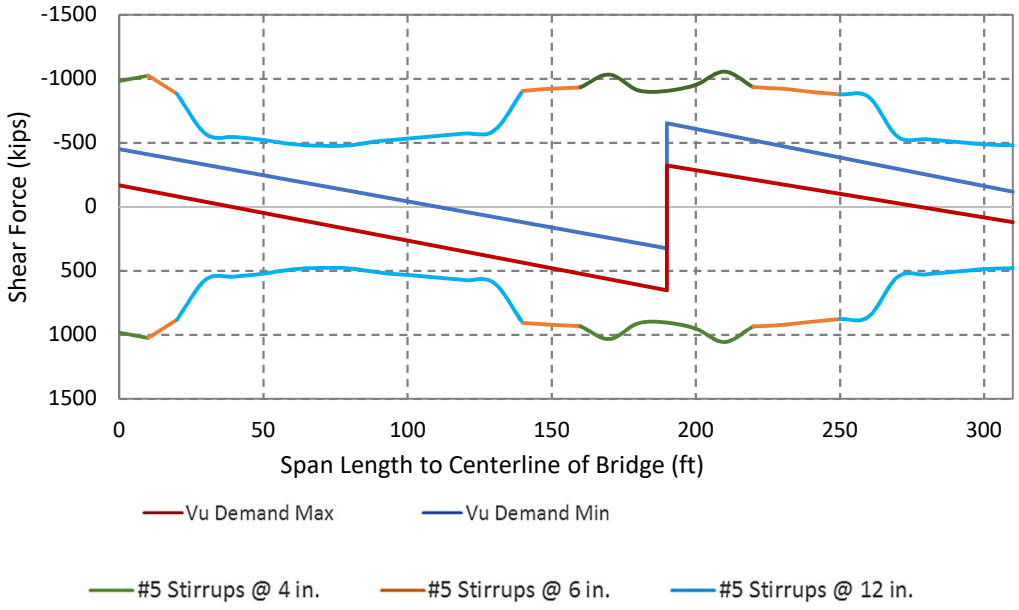

(a) Transverse Shear Demand and Capacity

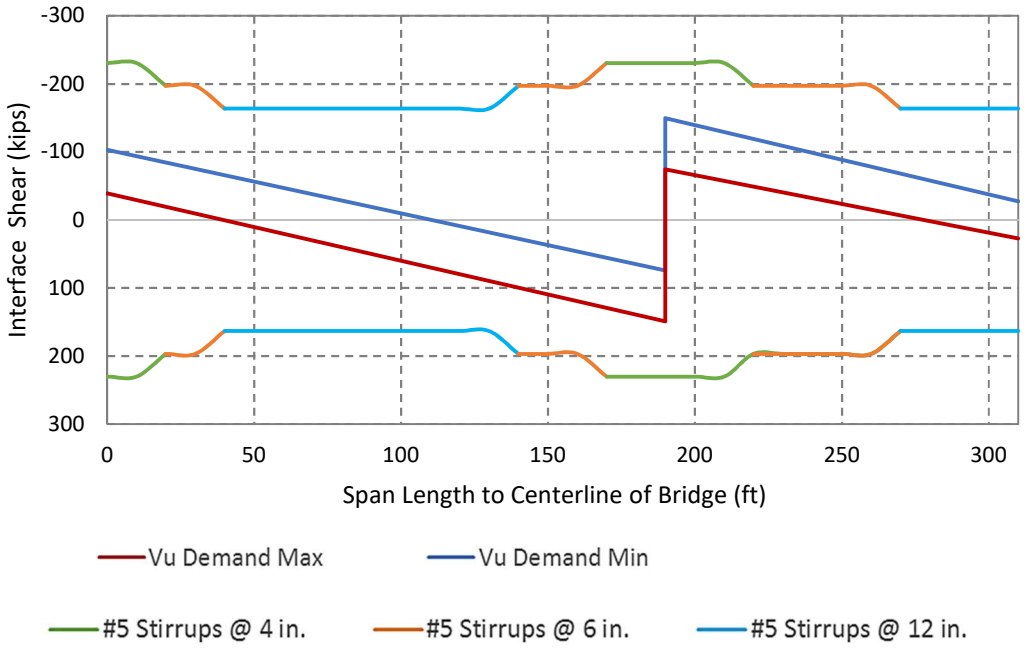

(b) Interface Shear Demand and Capacity

Fig. A.19 Transverse and Interface Shear Demand and Capacity.

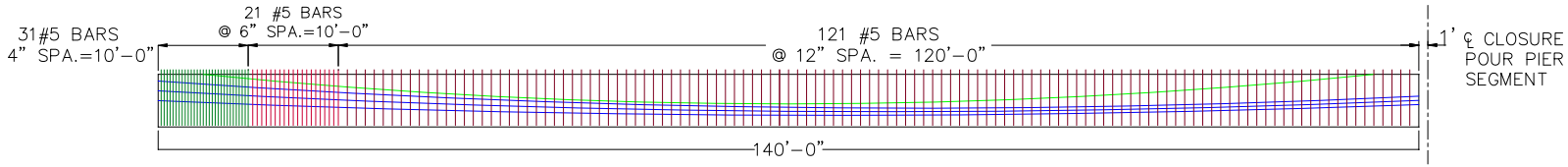

(a) END SEGMENT

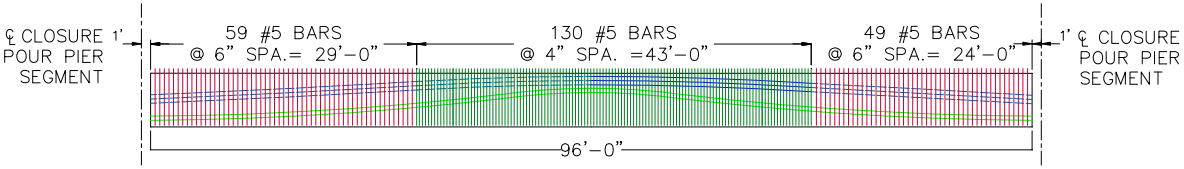

(b) ON-PIER SEGMENT

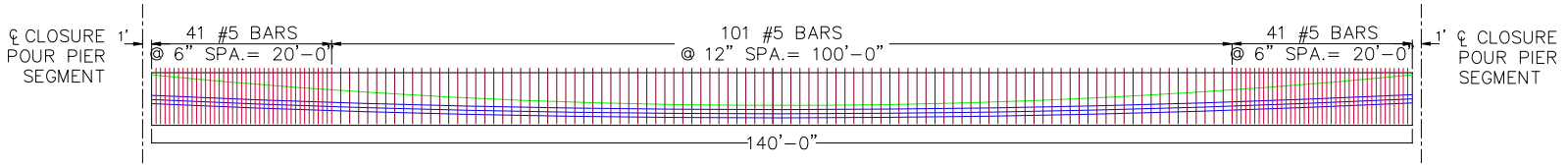

(c) DROP-IN SEGMENT

Fig. A.20 Shear Reinforcement Details.

A partially prestressed splice connection detail is used at all splice locations. Mild steel reinforcement is provided in addition to continuity PT through the splice connection. The mild steel reinforcement consists of 180° bent hooked bars anchored into the adjacent girder flanges and extending into the joint. The mild steel bent bars are designed for the maximum factored design loads. The combination of PT and mild steel is expected to provide better durability and performance. Vertical reinforcement is provided to strengthen the splice connection for shear. The integrity of the splice connection largely depends on the shear transfer mechanism at the interface of the precast girder and closure pour. This shear transfer mechanism is mainly provided by the compressive force provided by the continuous PT, the lapped 180° bent hooked bars in the connection, and a single shear key.

Prestressing and Reinforcement Details for the Splice

Only the Stage II PT tendons are continuous through the splice connections. The pretensioned strands and the Stage I PT tendons terminate at the girder segment ends adjacent to the splice. Therefore, additional mild steel reinforcement was needed to achieve flexural strength at the splices. For the proposed splice connection detail, additional capacity is provided by mild steel 180° bent bars with details as presented in Table A.16 (see Fig. A.21). Table A.17 presents the prestressing design summary for the splices.

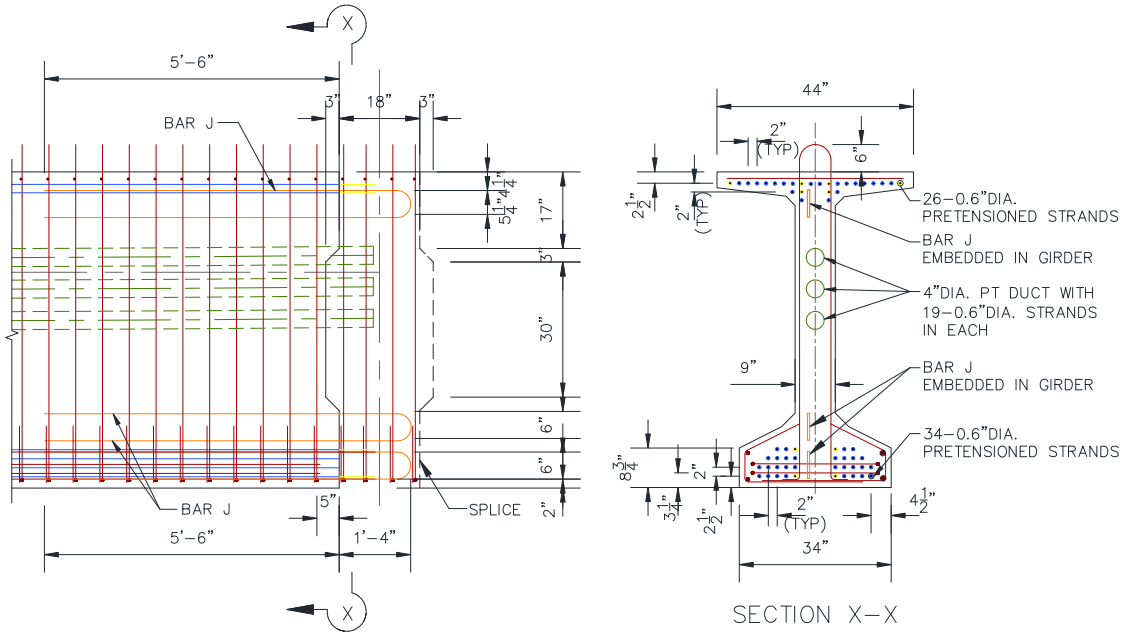

Fig. A.21 Partially Prestressed Splice Connection Detail.

Table A.16. Reinforcement Details for the Splices.

Reinforcement Details		**Splices**
180° bent bars embedded in each girder segment at splice	Top flange of each girder segment	1 - #6
	Bottom flange of each girder segment	2 - #6

Table A.17. Prestressing Details for the Splices.

Prestressing Details		**Splices**
Stage II Post-tensioning	Tendons (0.6 in. dia.) (19 strands in each duct)	57 (3 ducts)
	Force at Transfer	2337 kips

A.20.2 Flexural Strength Check

The strength limit state of the splice connection is checked to ensure safety at ultimate load conditions based on the AASHTO LRFD Specifications (AASHTO 2012). The total ultimate bending moment for the interior splice, corresponding to the in-span splice in the end span of the prototype bridge, is $M_u = 4874$ kip-ft. Only the Stage II PT tendons run continuously through the splice connection, while the pretensioning strands and the Stage I PT tendons terminate at the girder segment ends adjacent to the splice. To enhance the flexural capacity and for crack control, 180° mild steel bent bars are provided in the splice with details as follows (see Fig. A.21):

- Top flange steel: 1 - #6 180° bent bar embedded.
- Bottom flange steel: 2 - #6 180° bent bars embedded.

For capacity calculation under the strength limit state, the stress distribution in the compression concrete is approximated with an equivalent stress distribution of intensity $0.85f_c'$ over a zone bounded by the edges of the cross-section and a straight line located parallel to the neutral axis at a distance $a = \beta_1 c$, where β_1 is the stress block factor. The value of β_1 depends on the compressive strength of concrete and is given by the following expression (the permissible values for β_1 range from 0.65 to 0.85):

$$\beta_1 = 0.85 - 0.05(f_c' - 4) \geq 0.65 \quad \text{(A.19)}$$

where f_c' = Specified concrete compressive strength at service, ksi.

According to AASHTO LRFD Specifications (AASHTO 2012) Article 5.7.2.2, the actual values of β_1 are used for each portion of the cross-section. The stress block factor for the slab, β_{1s}, is calculated corresponding to f_{cs}', and the stress block factor for the precast girder, β_{1b}, is calculated corresponding to f_{cb}'.

$$\beta_{1s} = 0.85 - 0.05(4 - 4) \geq 0.65 = 0.85$$

$$\beta_{1b} = 0.85 - 0.05(8.5 - 4) \geq 0.65 = 0.65$$

The AASHTO LRFD Specifications (AASHTO 2012) specify the following expression to estimate the stress in prestressing steel with bonded tendons at ultimate conditions. This expression is applicable when the effective prestress after losses, f_{pe}, is not less than 0.5 f_{pu}, where f_{pu} is the ultimate tensile strength of the prestressing strands (AASHTO Eq. 5.7.3.1.1-1) :

$$f_{ps} = f_{pu}\left(1 - k\frac{c}{d_p}\right) \quad \text{(A.20)}$$

where:

f_{ps} = Average stress in prestressing steel, ksi.

f_{pu} = Specified tensile strength of prestressing steel, ksi.

k = $2\left(1.04 - \frac{f_{py}}{f_{pu}}\right) = 0.28$ for low-relaxation strands. (AASHTO Eq. 5.7.3.1.1-2)

c = Distance between neutral axis and the compressive face, in.

d_p = Distance from extreme compression fiber to the centroid of the prestressing tendons, in.

The provisions of AASHTO LRFD Specifications (AASHTO 2012) Article 5.7.3.1.1 are used for calculating the depth of neutral axis and the nominal moment resistance. The flexural behavior of the section at ultimate conditions is classified as rectangular or flanged, based on the depth of the neutral axis relative to the section geometry. Rectangular section behavior is first assumed to determine the depth of neutral axis, as illustrated in the following calculations.

The expressions for the forces acting in the girder section are as follows:

$$C = 0.85 f'_{cs} \beta_{1s} c\, b_{eff} \quad \text{(A.21)}$$

$$T = A_{ps} f_{ps} \quad \text{(A.22)}$$

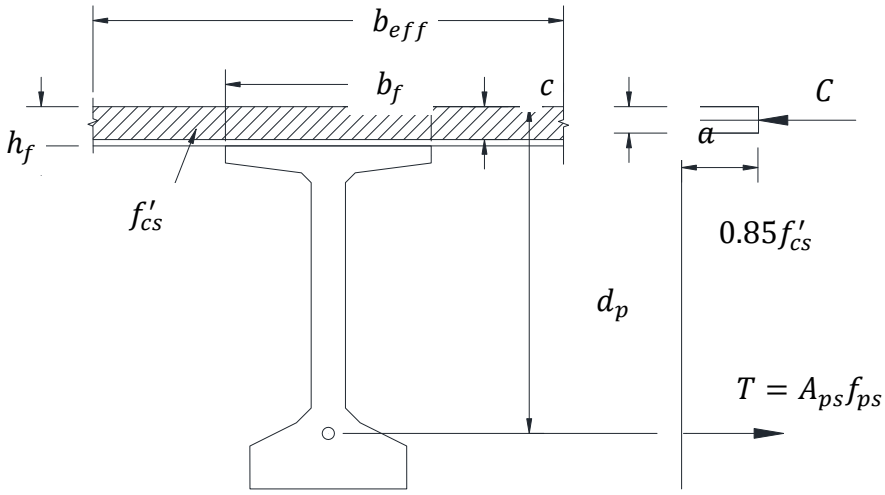

Figure A.1. Rectangular Section Behavior.

$$T = A_{ps} f_{pu} \left(1 - k \frac{c}{d_p}\right) \quad \text{(A.23)}$$

(AASHTO Eq. 5.7.3.1.1-1)

Applying equilibrium and solving for the neutral axis depth, gives the following.

$$T = C \quad \text{(A.24)}$$

$$c = \frac{A_{ps} f_{pu} + A_s f_y - A_s' f_y}{0.85 f'_{cs} \beta_{1s} b_{eff} + k A_{ps} \frac{f_{pu}}{d_p}} \quad \text{(A.25)}$$

(AASHTO Eq. 5.7.3.1.1-4)

where:

c = Distance between neutral axis and the compressive face, in.

A_{ps} = Area of prestressing steel = 12.369 in.^{2}

A_s = Area of non-prestressed tension reinforcement = 1.76 in.^{2}

A_s' = Area of non-prestressed compression reinforcement = 6.448 in.^{2}

f'_{cs} = Specified compressive strength of slab concrete at service = 4.0 ksi

β_{1s} = Stress factor for compression block (computed for f'_{cs}) = 0.85

b_{eff} = Effective width of compression flange = 96.0 in. (AASHTO table 4.6.2.1.3-1)

f_{pu} = Specified tensile strength of prestressing steel = 270.0 ksi

f_y = Specified yield strength of reinforcement = 60.0 ksi

$k = 2\left(1.04 - \frac{f_{py}}{f_{pu}}\right) = 0.28$ for low-relaxation strands (AASHTO Eq. 5.7.3.1.1-2)

d_p = Distance from extreme compression fiber to the centroid of the prestressing tendons, in.

h_f = Depth of compression flange = 8.0 in.

$$c = \frac{(12.369)(270.0) + (52.8+52.8) - (52.8+417.6)}{0.85(4.0)(0.85)(96) + (0.28)(270.0)\left(\frac{4.123}{26.53} + \frac{4.123}{33.53} + \frac{4.123}{40.53}\right)} = 9.72 \text{ in.}$$

a = Depth of the equivalent rectangular stress block

$$= \beta_{1s} c = (0.85)(9.72) = 8.3 \text{ in.}$$

Therefore, the assumption of rectangular section is not valid. When the neutral axis lies in the girder, the section is found to behave like a flanged section (see Fig. A.23), and the equations for determining the depth of the neutral axis and the design flexural strength of the section are outlined below.

$$f_{ps} = (270.0)\left(1-(0.28)\frac{12.41}{d_p}\right) \quad \text{(AASHTO Eq. 5.7.3.1..1-1)}$$

From the summation of moments about C_1, the reduced nominal flexural moment strength at the section is obtained as follows.

$$\phi M_n = \phi\left[T\left(d_p-0.5h_f\right)-C_2(0.5a)\right] \qquad (A.32)$$

where:

T = Tensile force in the prestressing strands =

(236.8+242.0+246.86)*0.217*19

= 2983.1 kips

C_1 = Compressive force in the slab, kips

C_2 = Compressive force in the girder flange within the stress block depth, kips

f'_{cs} = Compressive strength of slab concrete at service = 4.0 ksi

f'_{cb} = Compressive strength of girder concrete at service = 8.5 ksi

b_{eff} = Effective flange width = 96.0 in.

b_f = Girder flange width = 44.0 in.

h_f = Thickness of slab = 8.0 in.

t_f = Thickness of girder flange = 3.5 in.

β_{1b} = Stress factor of compression block (computed for f'_{cb}) = 0.65

$a = \beta_{1b}c$ = Depth of the equivalent rectangular stress block, in.

$$T\left(d_p-0.5h_f\right) = [(967.44)(26.53-(0.5)(8.0))+(997.44)(33.53-(0.5)(8.0))+$$
$$(1017.79)(40.53-(0.5)(8.0))+(66.67)(73.00-(0.5)(8.0))$$
$$+(66.67)(64.5-(0.5)(8.0))-(66.67)(12.5-(0.5)(8.0))$$
$$-(417.60)(4.00-(0.5)(8.0))]/12$$

= 8038.49 kip-ft

$$C_2(0.5a) = \left[0.85(8.5)(44)\left((0.65)(12.41)-8.0\right)\left((0.5)(8.1)\right)\right]/12$$

= 6.91 kip-ft

$$\phi M_n = \phi\left[8038.49-6.91\right] \approx 8030 \text{ kip-ft} > M_u = 7817 \text{ kip-ft OK}$$

A.20.3 Shear Design

A.20.3.1 Transverse Shear Design

MCFT is used for transverse shear design as specified in the AASHTO LRFD Specifications (AASHTO 2012). The total ultimate shear demand for the splice in the end span of the prototype bridge was $V_u = 420$ kips. Table A.18 presents shear design details for the end-span splice.

Table A.18. Shear Design Details for Splices.

Girder Segment	Shear Reinforcement	Nominal Capacity, V_n (kips)
End-Span Splice	4 - #5 Stirrups @ 6 in. spacing	900
Main Span Splice	4 - #5 Stirrups @ 6 in. spacing	900

Note: All shear reinforcement consists of double legged stirrups.

Due to the significant amount of shear reinforcement, TxDOT engineers recommended checking the principal tensile stress in the web of the Tx70 girder at the splice locations. AASHTO LRFD Specifications (AASHTO 2012) Article 5.8.5 requires checking the principal tension stress to verify the adequacy of the webs of segmental concrete bridges for longitudinal shear and torsion. This article states that the principal tensile stress resulting from long-term residual axial stress and maximum shear at the neutral axis of the critical web shall not exceed the tensile stress limit provided by AASHTO LRFD Specifications (AASHTO 2012) Table 5.9.4.2.2-1 ($0.11\sqrt{f_c'}$) for the Service III limit state at all stages during the life of the structure, excluding those during

construction. When investigating principal stresses during construction, the tensile stress limits of Table 5.14.2.3.3-1 ($0.11\sqrt{f_c'}$) shall apply.

The principal stress was checked at the splice location in the end span and main span, as shown in Table A.19. Shear and bending stresses in the concrete at the neutral axis of the web were calculated for the Service III limit state. The principal stress is calculated using classical beam theory and the principles of Mohr's Circle.

Table A.18 shows the principal tension stress at the end span and main span splice locations with and without considering the vertical force component of draped longitudinal tendons V_p. AASHTO LRFD Specifications (AASHTO 2012) Article 5.8.5 specifies that V_p shall be considered as a reduction in the shear force due to the applied loads. Also, from the load-balancing approach, the total dead load of the girder and deck slab is balanced by the prestressing and PT tendon profiles. Therefore, the principal tension stress values considering V_p are below the AASHTO LRFD Specifications (AASHTO 2012) specified allowable limit.

Table A.19. Principal Tension Stress Calculation.

Location	**Principal Tension Stress at Service (Not Considering V_p) (ksi)**	**Principal Tension Stress at Service (Considering V_p) (ksi)**	**Principal Tensile Stress Limit ($0.11\sqrt{f_c'}$)**
End Span Splice	0.242	0.066	0.321
Main Span Splice	0.249	0.068	0.321

A.20.3.2 Interface Shear Design for Girder-to-Splice Interface

The provisions for interface shear design as specified in AASHTO LRFD Specifications (AASHTO 2012) Article 5.8.4 are followed for the design of the girder-to-splice interface. The required nominal interface shear strength at the interface plane is given as follows:

$$V_{nreqd} = \frac{V_u}{\phi} \tag{A.33}$$

where:

V_{nreqd} = Required nominal shear strength at the interface plane, kips.

V_u = Factored shear force at the girder-to-splice interface, kips.

ϕ = Resistance factor for shear in prestressed concrete members equal to 0.9 for normal weight concrete members per AASHTO LRFD Specifications (AASHTO 2012) Article 5.5.4.2.

The required nominal interface shear strength at the interface plane is $V_{nreqd} =$ 467 kips. The interface shear resistance at the girder-to-splice interface is calculated per the AASHTO LRFD Specifications (AASHTO 2012) Article 5.8.4 based on shear friction theory. The nominal shear resistance of the interface plane is based on the cohesion factor, c, friction factor, μ, and the area of concrete engaged in interface shear transfer, A_{cv}. For the parametric design cases, the values of parameters specified in AASHTO LRFD Article 5.8.4 are cohesion factor c = 0.24 ksi, friction factor μ = 1.0, fraction of concrete strength available to resist interface shear K_1 = 0.25, and limiting interface shear resistance K_2 = 1.5 ksi. These values of parameters are selected based on the *TxDOT Bridge Design Manual* (2013).

The nominal shear resistance of the interface plane is provided by the mild steel 180° bent bars, area of concrete engaged in interface shear transfer, and permanent net compressive force normal to the interface plane. The expression for nominal shear resistance of the interface plane is given as follows:

$$V_n = cA_{cv} + \mu\left[A_{vf}f_y + P_c\right] \quad \text{(A.34)}$$

where:

V_n = Nominal shear resistance of the interface plane, kips.

c = Cohesion factor = 0.24 ksi.

μ = Friction factor = 1.0.

A_{cv} = Area of concrete engaged in interface shear transfer, in.^{2}

A_{vf} = Area of shear reinforcement crossing the shear plane within A_{cv}, in.^{2}

P_c = Permanent net compressive force normal to the shear plane = 1753 kips.

f_y = Yield strength of shear reinforcement, ksi = 60 ksi.

In this case of the girder-to-splice interface:

$$A_{cv} = A_g - A_{duct}$$

A_g = Area of girder = 1106 in.^{2}

A_{duct} = Area of PT ducts = 3 (12.57) = 37.71 in.^{2}

$$A_{cv} = 1106 - (3)(12.57) = 1068.30 \text{ in.}^2$$

The minimum interface shear reinforcement is determined as follows:

$$A_{vf} \geq \frac{0.05 \ \ cv}{f_y} \quad \text{(A.35)}$$

where:

A_{cv} = Area of concrete engaged in interface shear transfer = 1068.30 in.^{2}

A_{vf} = Area of shear reinforcement crossing the shear plane within A_{cv}, in.^{2}

f_y = Yield strength of shear reinforcement = 60.0 ksi.

$$A_{vf} \geq \frac{0.05(1068.30)}{60} = 0.89 \text{ in.}^2$$

For the provided 3 - #6 mild steel 180° bent bars (double legged) at each girder-to-splice interface, the area of interface shear reinforcement is given as follows:

$$A_{vf} = (3)(2)(0.44) = 2.651 \text{ in.}^2 > 0.89 \text{ in.}^2 \qquad \text{(OK)}$$

The nominal shear resistance of the interface plane is calculated as follow:

$$V_n = (0.24)(1068.30) + (1.0)[(2.651)(60) + 1753] = 2160 \text{ kips}$$

The nominal shear resistance, V_n used in the design shall not be greater than the lesser of the following two expressions:

$$V_n \leq K_1 f_c' A_{cv} \qquad \text{(A.36)}$$

$$V_n \leq K_2 A_{cv} \qquad \text{(A.37)}$$

where:

f_c' = The 28-day compressive strength at service of the weaker concrete at the interface plane, ksi.

K_1 = Fraction of concrete strength available to resist interface shear = 0.25.

K_2 = Limiting interface shear resistance = 1.5 ksi.

$$V_n \leq (0.25)(8.5)(1068.30) \approx 2270 \text{ kips}$$

$$V_n \leq (1.5)(1068.30) \approx 1600 \text{ kips}$$

Therefore, the nominal shear resistance at the girder/splice interface is taken as 1600 kips, which is much larger than the required nominal interface shear strength of 467 kips at the interface plane.

The embedment length of the mild steel 180° bent bars into the girder flanges is determined based on the design recommendations for optimized continuity diaphragms (Koch and Roberts-Wollmann, 2008). Their design recommendation for embedment length is based on the angle of inclination of the diagonal compressive stress or crack angle, θ, computed using MCFT used for transverse shear design. Using MCFT, as specified in AASHTO LRFD Specifications (AASHTO 2012) Article 5.8.3, a variable angle truss analogy is adopted in which the angle of the diagonal compressive stress, θ, is considered to be variable and is determined in an iterative manner. MCFT takes into account different factors such as strain condition of the section and shear stress in the concrete to predict the shear strength of the section. At the splice location, the angle of the diagonal compressive stress is $\theta = 29°$. Therefore, the required embedment length of the provided #6 mild steel 180° bent bars at each girder-to-splice interface is 5 ft-6 in (see Fig. A.2).

AASHTO LRFD Specifications (AASHTO 2012) Article 5.8.4.1 requires that shear friction reinforcement shall be anchored to develop the specified yield strength on both sides of the shear plane by embedment, hooks, or welding. The splice connection detail is designed to develop the specified yield strength of the reinforcement on both sides of the shear plane. Therefore, the embedment length of the 180° bent bars is also checked to satisfy the development length requirements specified in *AASHTO LRFD Specifications*

(AASHTO 2012) Article 5.11. The required development length for the #6 mild steel 180° bent bars at each girder-to-splice interface is 10 in. The provided 180° hook extends into the splice equal for a distance of 1 ft-4 in. The recommended embedment length of the bent bars into the girder segments is 5 ft-6 in., as determined above based on Koch and Roberts-Wollmann (2008). This length is larger than the standard AASHTO straight bar development length of 2 ft-2 in. for top bars. Therefore, the detailing of the connection #6 mild steel 180° bent bars on both sides of the shear plane provides full development of reinforcement.

APPENDIX B

DESIGN AND CONSTRUCTION OF TEST SPECIMEN

B.1 INTRODUCTION

The results of the parametric design and analysis study suggest that in-span splicing can be used to extend the span lengths of precast prestressed concrete girder bridges. But limited experimental data are available to evaluate the performance of in-span splices. Appendix B provides details for an experimental program conducted to evaluate the performance of the in-span splice connections under varying levels of demand and different combinations of positive moment, negative moment, and shear. The prototype bridge and the abstraction of the specimen are described, followed by an overview of the specimen design, construction, post-tensioning process, and instrumentation plan.

B.2 SPECIMEN ABSTRACTION

B.2.1 Prototype Bridge

Chapter 3 of dissertation describes the three-span prototype bridge. The bridge has a 190-240-190 ft span configuration, with the end spans being 190 ft long and the middle span being 240 ft long. Fig. B.1 shows the abstraction of the specimen from the prototype bridge. The splice corresponding to the splice in the end span of the prototype bridge was tested. The locations of the PT tendons at the corresponding splice location in the specimen were kept similar to those in the prototype bridge. Though shored construction was used for the prototype design, the proposed connection detail is also a representative of a partially shored construction technique where a temporary tower and/or strong-backs are

provided at the in-span splice location and the on-pier girder segments need to be tied back for stability purposes.

Fig. B.2 shows the cross-section of the bridge. The bridge has a total width of 46 ft and a total roadway width of 44 ft. The bridge superstructure consists of six modified Tx70 girders spaced 8 ft center-to-center, with a 3 ft overhang on each side, designed to act compositely with an 8 in. thick CIP concrete deck. The deck includes 4 in. thick precast concrete stay-in-place precast concrete panels between girders that serve as formwork for the deck. The asphalt wearing surface thickness is 2 in. A T501 traffic barrier was considered as presented in the standard drawings of the *TxDOT Bridge Design Manual* (2013). Three design lanes were considered for the purpose of design in accordance with the AASHTO LRFD Specifications (AASHTO 2012). The specimen represents a typical interior girder as indicated in Fig. B.2.

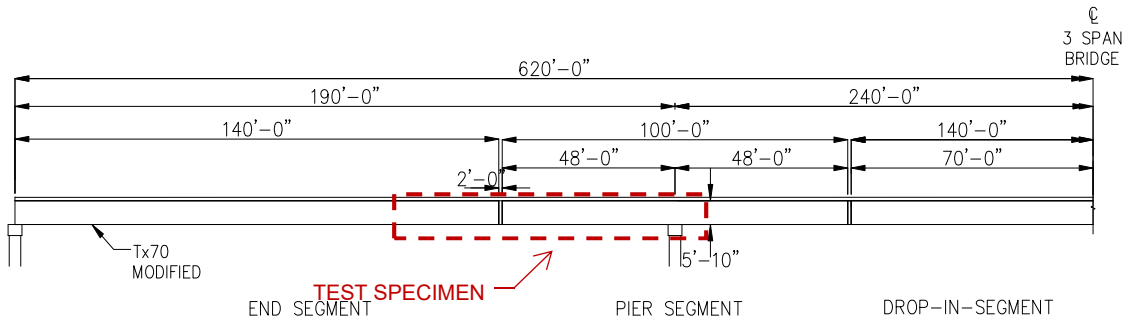

Fig. B.1 Elevation of the Prototype Bridge Showing the Test Specimen.

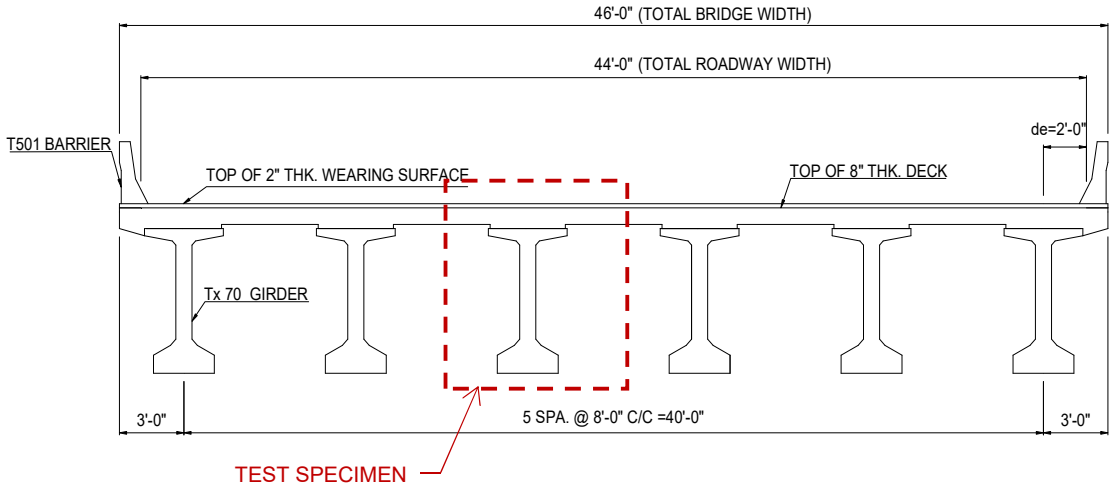

Fig. B.2 Cross-section of the Prototype Bridge Showing the Test Specimen.

Researchers conducted experimental testing to evaluate the performance of this specimen with a focus on the splice connection performance. The requirements for service limit state design, flexural strength limit state design, and shear strength limit state design were evaluated.

B.2.2 Specimen Details

The experimental program took place in the High Bay Structural and Materials Testing Laboratory (HBSMTL) at Texas A&M University. This facility has a 72-ft long strong floor and tie down locations are available on a 3-ft grid. Therefore, the length of the specimen was limited to 71 ft. Different options were considered by the research team to arrive at the final specimen presented in this Appendix. Specimen geometry and tests setups were designed to simulate the same demand on the main splice (middle splice, Splice 2). Fig. B.3 presents the comparison for demand moment and shear between the prototype bridge and the test specimen.

Fig. B.4 and Fig. B.5 show the elevation and plan views of the test-setup, respectively, providing the location of tie downs, pedestals, and splices. An interior splice was provided corresponding to the in-span splice within the end span of the prototype bridge, shown in Fig. B.1. However, due to the weight capacity limit of the crane in the HBSMTL, two additional splices were provided, connecting the girder segments to the thickened end blocks. Overall, the three splices divided the specimen into four segments. Appendix B provides detailed drawings for each girder segment within the specimen. Table B.1 provides the weights of girder segments.

The research team tested all three splices in the specimen during five stages of testing. The first two test stages were non-destructive and were intended to evaluate the performance of the girder up to the service limit for positive and negative moment and shear. The next three tests focused on each splice and were intended to evaluate the post-cracking behavior of the girder up to ultimate strength. The finalized test specimen facilitated testing splice connections within the span (approximately at the dead load point of contraflexure), near the interior pier (high moment and high shear region), and near the abutment (low moment and high shear region) of the continuous bridge.

Table B.1. Weight of Girder Segments.

Components		**Length**	**Weight (kips)**	**Total Weight * (kips)**
Thickened End Blocks 1 and 2	End Block Portion	9'-0"	23.9	28.4
	Tx70 Girder (Modified) Portion	2'-9"	4.5	
Segment 1	Tx70 Girder (Modified)	18'-0"	25.2	25.2
Segment 2	Tx70 Girder (Modified)	25'-0"	34.3	34.3

** Limiting lifting weight in the HBSMTL is 36 kips.*

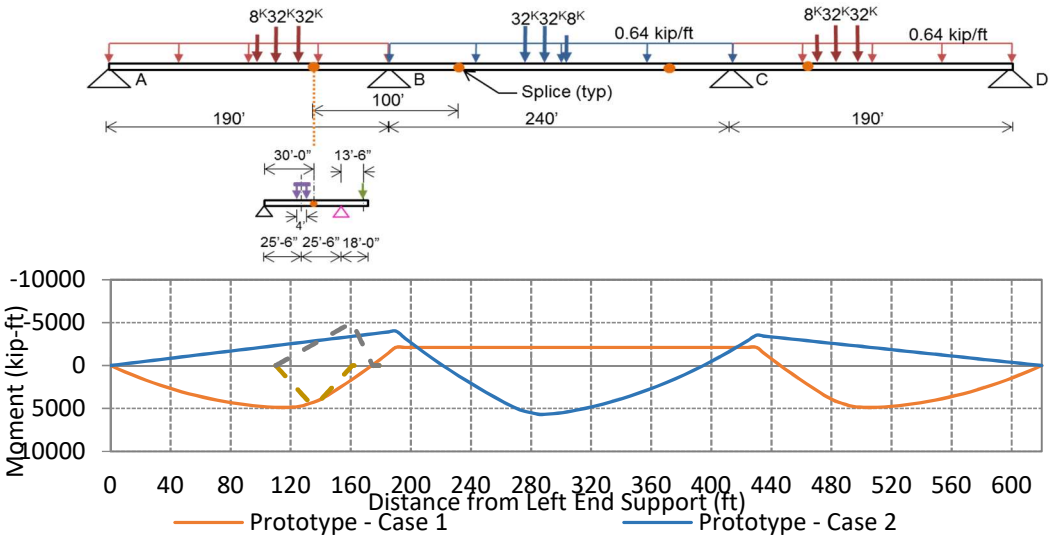

(a) Maximum Service Moment under Live Load with Impact from Prototype Bridge

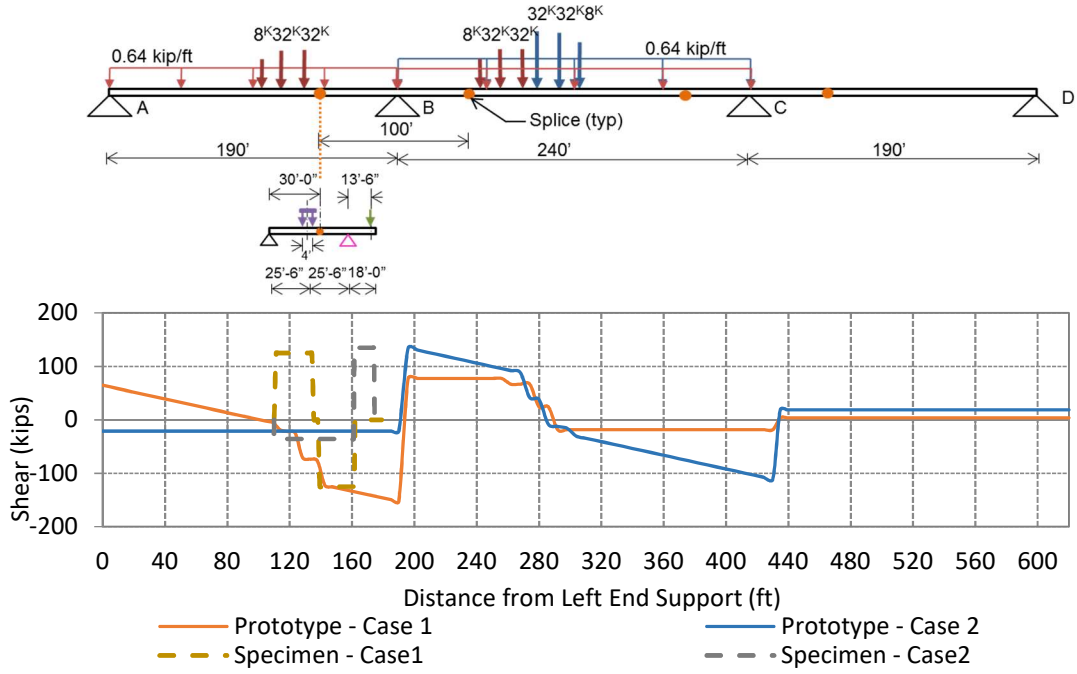

(b) Maximum Service Shear under Live Load with Impact from Prototype Bridge

Fig. B.3 Replication of Maximum Moment and Shear at Service in Test Specimen.

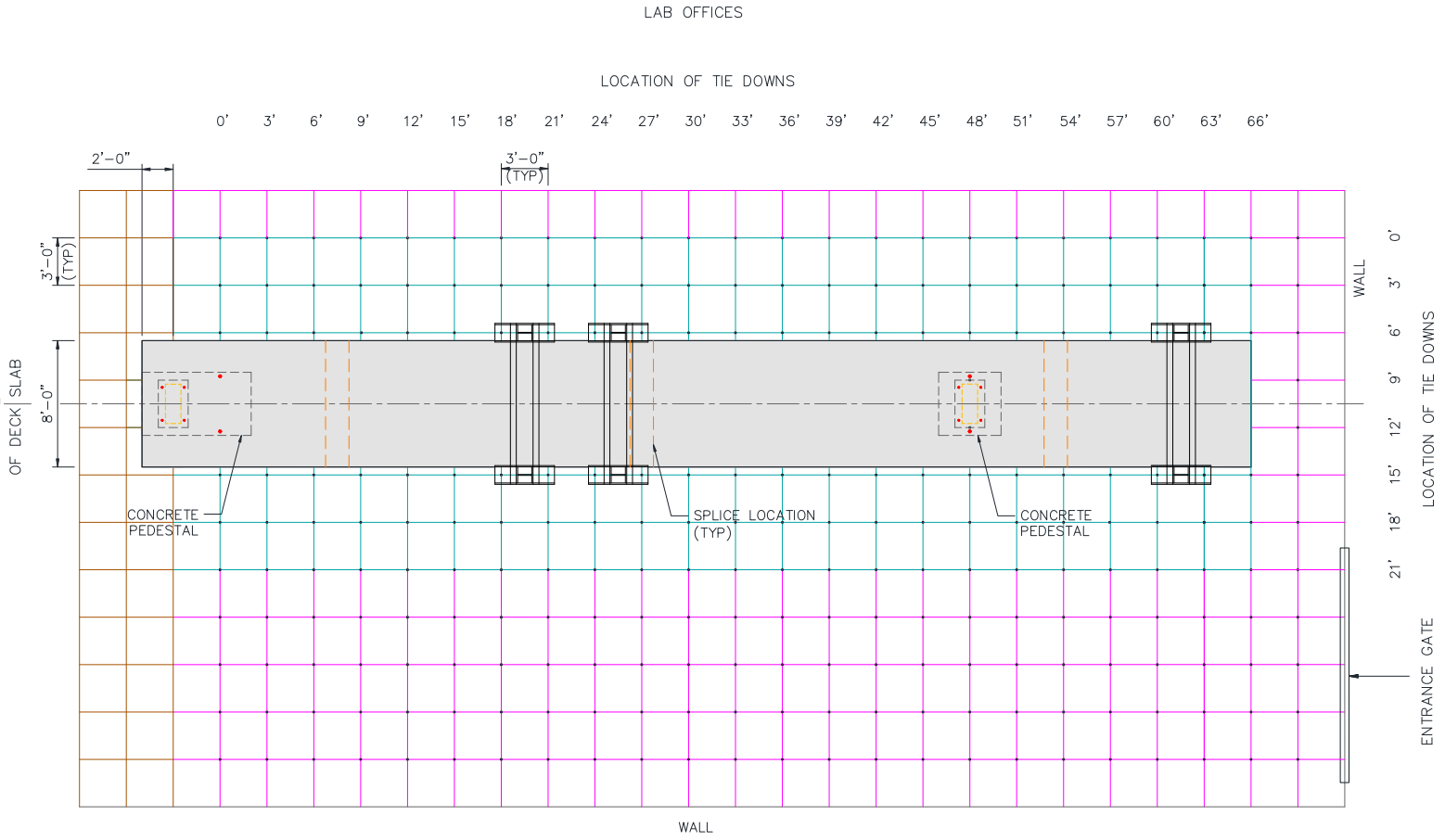

Fig. B.4 Plan View of the Test Specimen in the High Bay Laboratory.

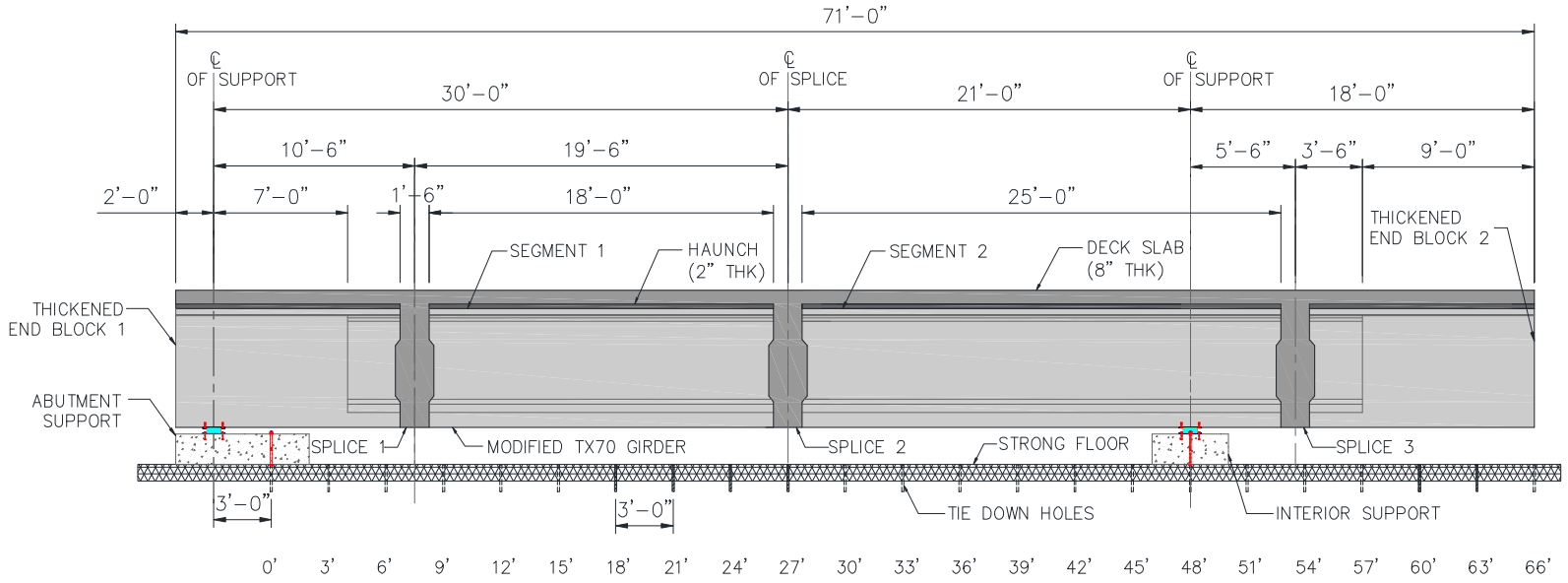

Fig. B.5 Elevation View of Test Specimen.

The basic characteristics of the specimen are as follows:

- A modified Tx70 girder cross-section was used for the specimen to match the prototype bridge at full-scale. Modifications of the original section based on precaster requirements and preferences included: (1) widening the modified web width from 9 in. to 10 in., which also resulted in widening the top and bottom flange by 1 in.; (2) use of 3-5/8 in. diameter PT ducts rather than 4 in. diameter; and (3) increasing the top flange thickness to 5 in. minimum to accommodate the top pretensioning strands.
- An interior splice was provided corresponding to the in-span splice in the prototype bridge. Due to the weight capacity limit of the crane in the HBSMTL, two additional splices were provided connecting the girder segments to the thickened end blocks.
- Thickened end blocks were provided at both ends of the specimen to accommodate the necessary PT anchorage systems. The girder segments and end blocks were fabricated at a precast plant and transported to the laboratory.
- The concrete used for the prestressed concrete girder segments was specified as TxDOT Class H self-consolidating concrete with a required initial compressive strength at release f'_{ci} of 6.5 ksi and a required compressive strength at service f'_c of 8.5 ksi.

- The concrete used for the splice connections was selected after considering several alternative mixes and conducting trial batches. A conventional concrete mixture with 0.75 in. maximum size aggregate, river gravel coarse aggregate, a 9.5 in. slump, and a 28-day target f'_c of 8.5 ksi was used.
- A partially prestressed splice connection detail was used at all three splice locations. Mild steel reinforcement was provided in addition to continuity PT running through the connection. The mild steel reinforcement consisted of 180° bent hooked bars anchored into the adjacent girder flanges and extending into the joint. Additionally, two #6 transverse bars were placed inside each of the bent hooked bars to increase the effective bearing area.
- A reinforced concrete CIP deck slab, 92 in. wide and 8 in. thick, was cast in the laboratory. TxDOT Class S conventional concrete with a specified 28-day f'_c of 4 ksi was used for the deck slab. Deck reinforcement details for the specimen were provided in accordance with TxDOT construction practices. Typical clear cover provided was 2 in. and 1.25 in. for the top and bottom reinforcement, respectively.
- The continuity PT tendons were installed, stressed, and grouted in the laboratory by a post-tensioning contractor.

B.2.3 Modified Tx70 Girder

Fig. B.6 shows the details of the modified Tx70 girder cross-section used for the specimen. Table B.2 presents the non-composite section properties of the modified Tx70 section. The standard Tx70 girder is 70 in. deep with top flange 42 in. wide, bottom flange 32 in. wide, and web thickness of 7 in. The web for the modified Tx70 girder segments was

widened to 10 in. by spreading the standard girder side forms. An increased web width is required to accommodate the 19-strand PT ducts. The width of the top and bottom flanges was also increased by 3 in., making the top flange 45 in. wide and the bottom flange 35 in. wide. The top flange thickness was also increased to 5 in. minimum to accommodate the top pretensioning strands.

Table B.3 presents the design parameters used for the specimen. These parameters are the same as those used for the modified Tx70 girder prototype bridge design. The design parameters are selected based on the current TxDOT state-of-practice and values commonly available from Texas precasters.

Table B.2. Section Properties for Modified Tx70 Girder with Widened Web.

Girder Type	Depth of N.A. from top, y_{top} (in.)	Depth of N.A. from bottom, y_{bot}	Area, A (in.^{2})	Moment of Inertia, I_x (in.^{4})	Weight (plf)
Modified Tx70	36.96	34.54	1243.5	805,053	1295
Composite Section	24.99	46.51	1980.0	1,424,995	2062

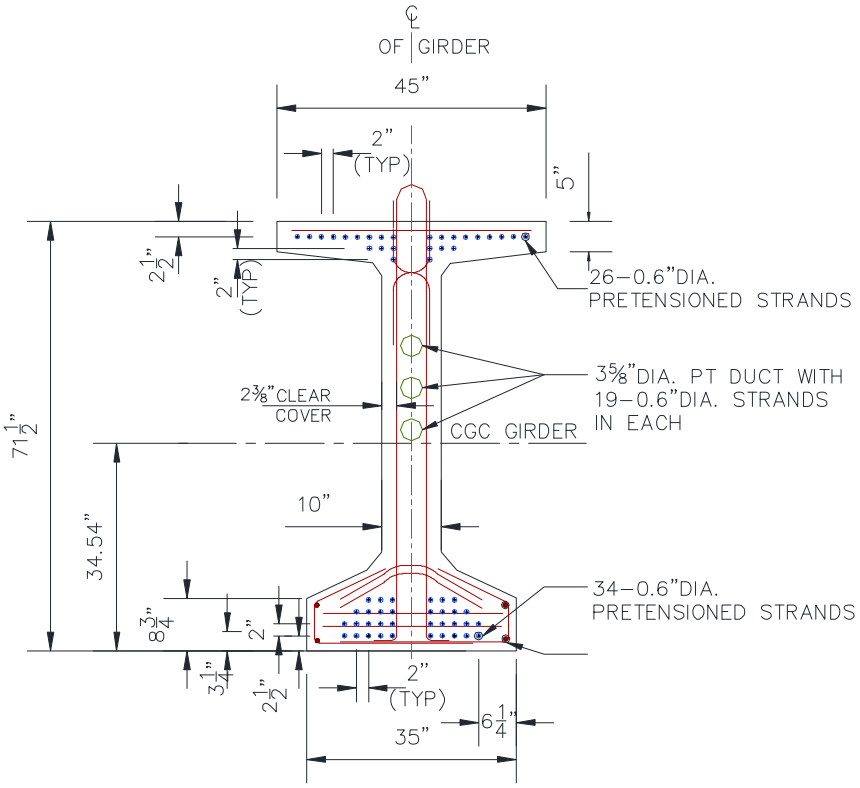

Fig. B.6 Typical Section Geometry of Modified Tx70 Girder with Widened Web (Adapted from TxDOT 2010).

Table B.3. Design Parameters for Specimen.

Parameter		Description/Selected Values
Specified Concrete Strength at Service for Deck (CIP), f'_c		4 ksi
Specified Concrete Strength at Service (Precast), f'_c		8.5 ksi
Specified Concrete Strength at Release (Precast), f'_{ci}		6.5 ksi
Coefficient of Thermal Expansion of Concrete		$6x10^{-6}/^oF$
Mild Steel (ASTM A615 Grade 604)	Yield Strength, f_y	60 ksi
	Modulus of Elasticity, E_s	29,000 ksi
Prestressing Steel	Strand Diameter	0.6 in.
	Ultimate Tensile Strength, f_{pu}	270 ksi (Low Relaxation)
	Yield Strength, f_{py}	$0.9\,f_{pu}$
	Stress Limit at Transfer, f_{pi}	$f_{pi} \geq 0.75\,f_{pu}$
	Stress Limit at Service, f_{pe}	$f_{pe} \geq 0.8\,f_{py}$
	Modulus of Elasticity, E_p	28,500 ksi
	Wobble Coefficient, K	0.0002/ft
	Coefficient of Friction, μ	

B.3 SPECIMEN DESIGN

B.3.1 Design Philosophy and Modifications

Appendix A presents the design of the prototype bridge, which serves as the basis of the specimen design. This subsection describes how the experimental test specimen was designed to capture certain key features of the prototype. Due to the different span lengths, the PT drape of the duct is not so pronounced in the test specimen. However, the duct curvatures remain essentially the same because the load that is balanced (per unit length) is the same between the prototype bridge and the physical test specimen.

The specimen was designed to simulate the performance of the prototype bridge; however, minor changes were made of necessity as follows:

1. The prototype has four PT ducts, three for continuity and one to balance segment self-weight. The test specimen had only three ducts for continuity and overall load balancing; the fourth duct was replaced by concentric pretensioning (additional strands top and bottom).
2. The prototype bridge was designed for the modified Tx70 with a 9 in. web thickness. The web thickness was increased to 10 in. to match the precaster's available formwork. As a result, the width of the top and bottom flange also increased by 1 in.
3. To accommodate the pretensioning strands in the top flange, the thickness of the top flange was increased by 1.5 in. To maintain the total depth of the composite section, the thickness of the haunch between the slab and the girder was reduced from 2 in. to 0.5 in., maintaining the overall depth of 80 in. for the composite section.
4. The prototype bridge was designed for a deck slab width of 96 in. Due to lab constraints, the width of the specimen deck slab was slightly narrower (92 in.).
5. The shear transfer at the splice connections of the prototype bridge was checked based on intentionally roughening the surface of the girder faces at the splice connections to a 0.25 in. amplitude. The specimen, however, did not have intentionally roughened surfaces, which reduced the shear transfer capacity of the specimen compared to the prototype bridge design.
6. The thickened end blocks for the end segments in the prototype bridge were designed to be tapered off to the adjacent standard cross section. For the specimen, however,

the end regions were squared off for ease of construction and due to constraints in the precast plant.

B.3.2 Girder Segment Design

Top and bottom pretensioning strands were designed based on the amount of steel provided in prototype bridge for pretensioning and Stage I PT. Stresses were checked to ensure they satisfied the limits for transportation and construction loads. Stage II PT was designed considering the same amount of steel (number of strands) as for the prototype bridge, but the drape was designed to balance the dead weight of the girder segments, splices, and deck slab. Table B.4 presents the design summary for the specimen.

Table B.4. Prestressing Summary for the Specimen.

Design Parameters		**Description**
Pretensioning	Strands (0.6 in. dia.)	26 strands
	Force at Transfer, F_{1i}	1143 kips
Stage I PT (Replaced by Pretensioning in the Specimen)	Strands (0.6 in. dia.)	34 strands
	Force at Transfer, F_{2ai}	1494 kips
Stage II PT	Tendons (0.6 in. dia.) (19 strands per duct)	57 strands (3 ducts)
	Force at Transfer, F_{2bi}	2337 kips

Fig. B.7 and Fig. B.8 show the prototype bridge moments at different loading and design stages, for the non-composite and composite girder sections, respectively. The load-balancing design moments at each design stage and service stresses were checked. In

the load-balancing approach, the girder segments were designed such that the prestress moments in the girders were balanced at each stage throughout the loading history of the specimen construction. The different loading and design stages considered are as follows:

- Girder Section.
    - Self-weight + Pretensioning.
    - Self-weight + Pretensioning + Non-composite Deck Weight.
- Composite Girder and Deck Section.
    - Stage II PT + Superimposed Dead Load.
    - Stage II PT + Superimposed Dead Load + Removal of Shoring Towers.

B.3.2.1 Flexure Considerations

Flexural stress analysis was carried out for the specimen girder segments under the total dead loads and prestressing force as well as construction loads during different stages of specimen construction. Fig. B.9 shows the stresses in the specimen at various steps of construction.

The specimen was also analyzed for actuator load beyond cracking up to ultimate conditions, or the maximum actuator load. Chapter 4 and 5 of the dissertation presents the results of the analysis, along with the experimental results.

Deck reinforcement details for the specimen were provided in accordance with current TxDOT construction practice for continuous bridge decks. The typical clear cover provided was 2 in. and 1.25 in. for top and bottom reinforcement, respectively. The reinforcement details are as follows:

- Transverse steel: #5 bars at 6 in. spacing at top and bottom

- Longitudinal steel: #4 bars at 9 in. spacing at top

  #5 bars at 9 in. spacing at bottom

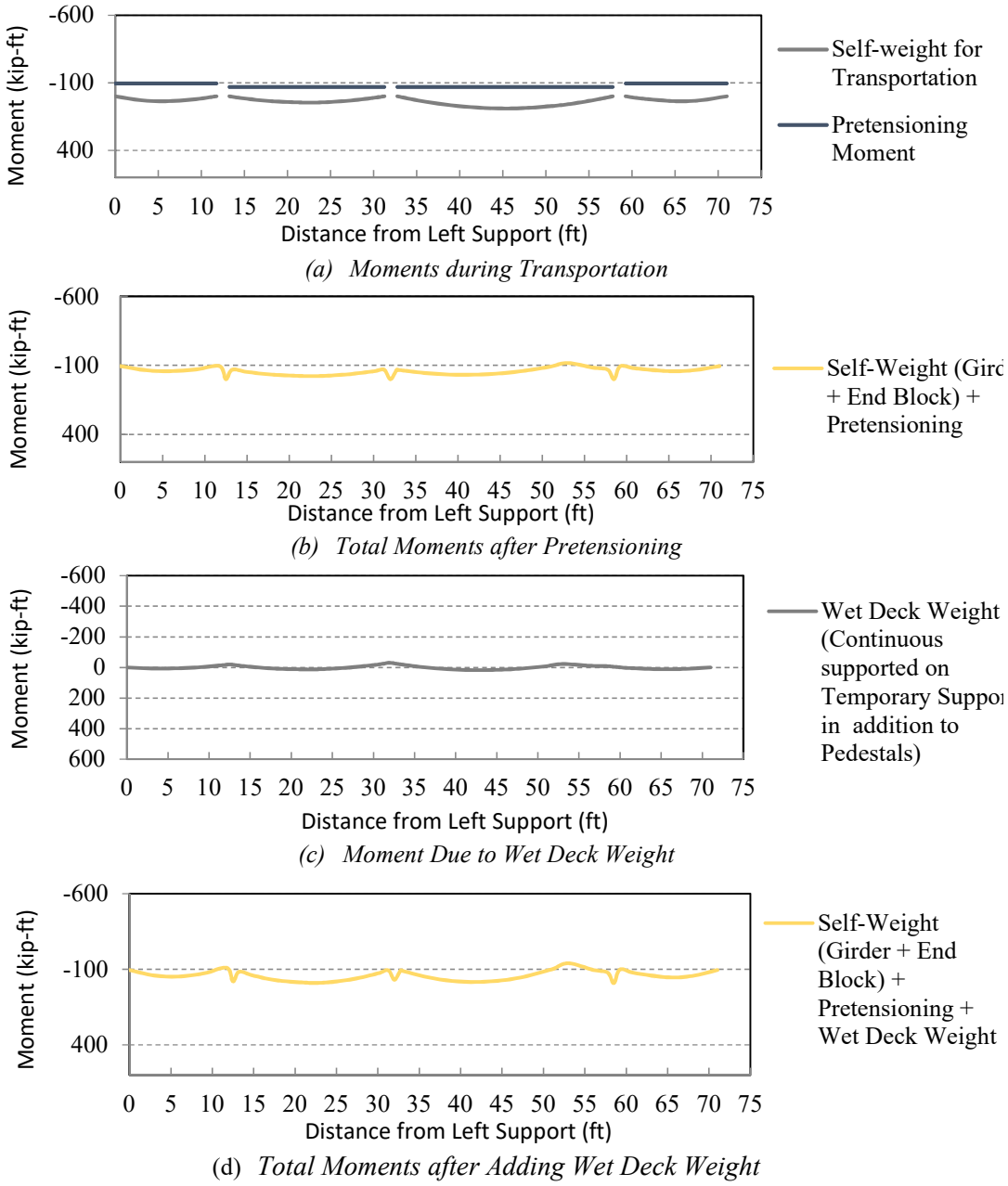

Fig. B.7 Test Specimen Design Moments Acting on Non-composite Girder.

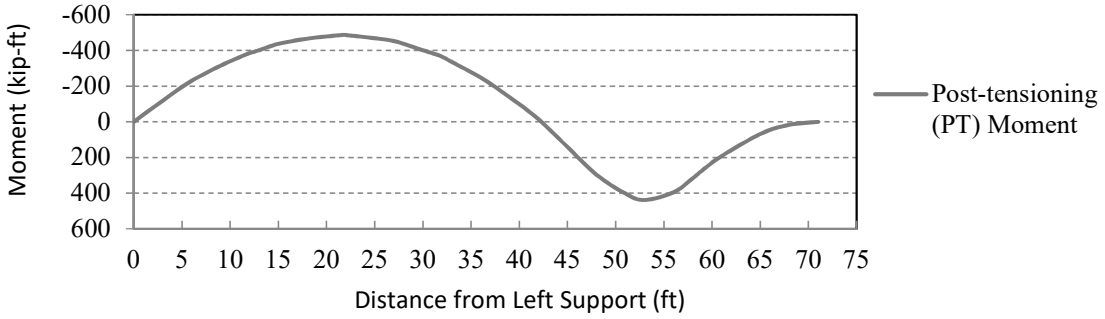

(a) Moment due to Stage 2 PT

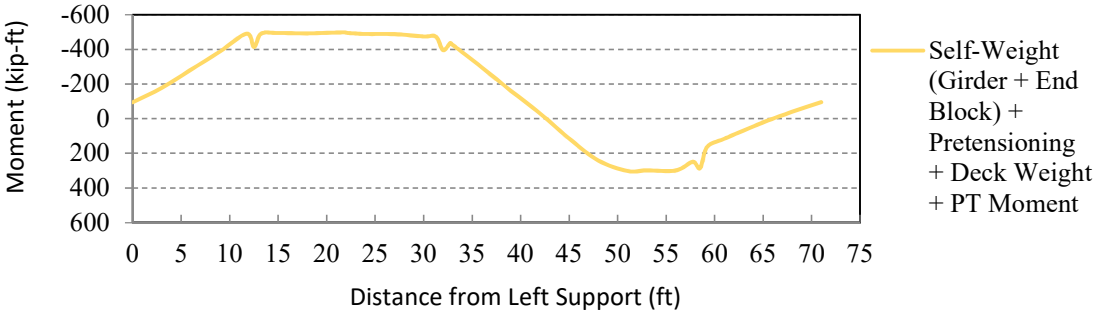

(b) Total Moments after Stage 2 PT

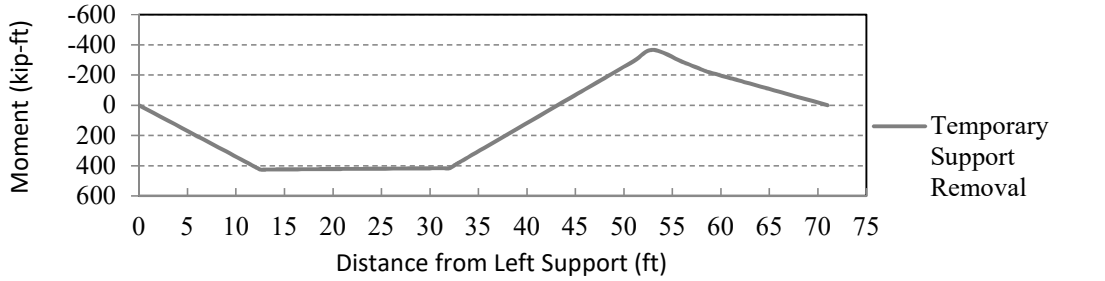

(c) Moment due to Temporary Support Removal

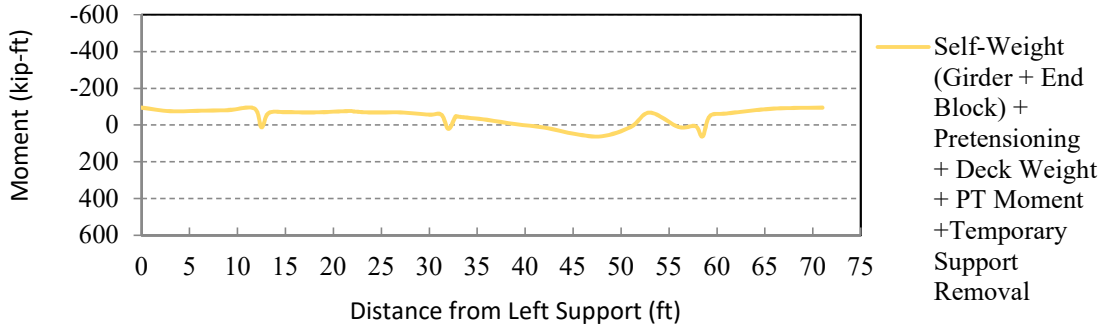

(d) Total Moments after Temporary Support Removal

Fig. B.8 Test Specimen Design Moments Acting on Composite Girder.

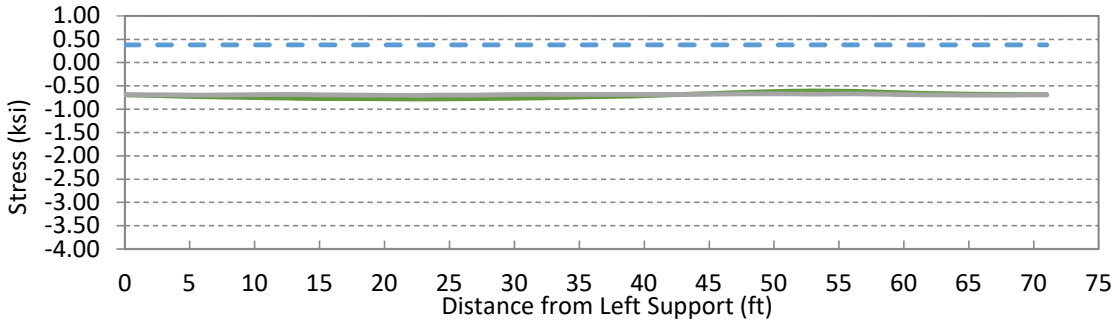

(a) Stresses at Top of CIP Deck

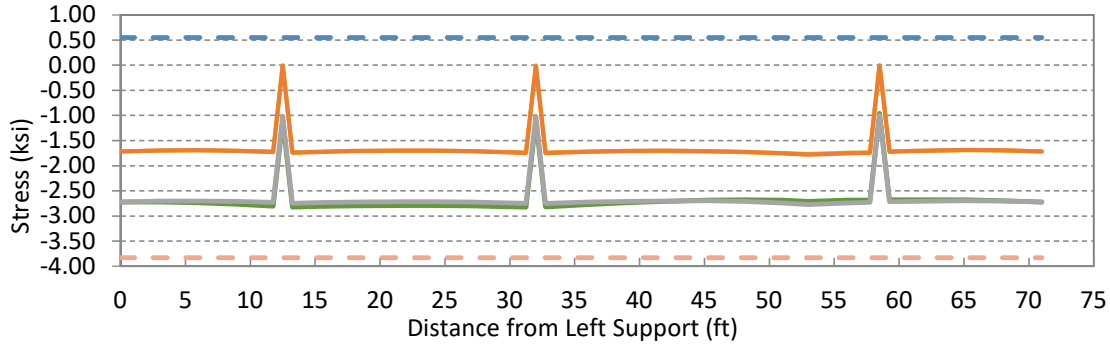

(b) Stresses at Top of Girder

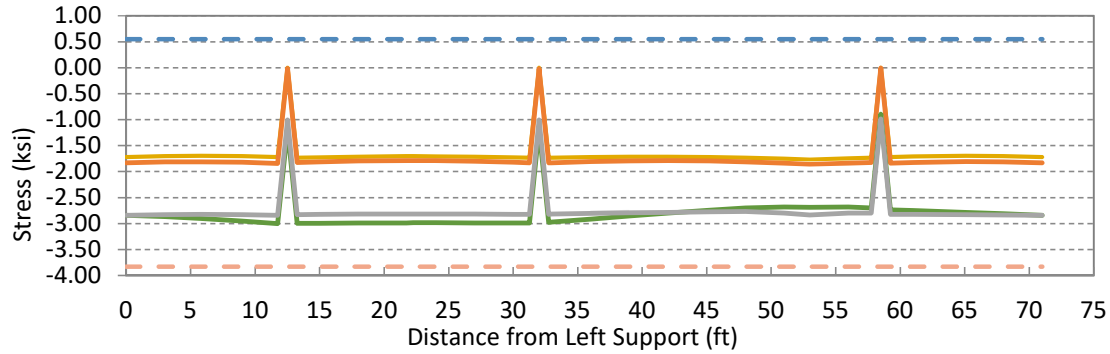

(c) Stresses at Bottom of Girder

Fig. B.9 Service Stress Analysis for Specimen.

B.3.2.2 Shear Considerations

Transverse Shear Design: MCFT was used for transverse shear design as specified in the AASHTO LRFD Specifications (2012). MCFT takes into consideration the combined effect of axial load, flexure, and prestressing when designing for shear. Table B.5 presents the shear reinforcement details for the specimen, which are the same as those provided for the prototype bridge presented in Appendix A.

Table B.5. Shear Reinforcement Details for Specimen.

Location Description	Shear Reinforcement	Dimension from Segment End
Thickened End Block 1	#5@4 in.	0'-0" to 11'-6"
Splice 1 near End Support	#5@4 in.	0'-0" to 2'-0"
Segment 1	#5@4 in. #5@6 in.	0'-0" to 2'-8" 2'-8" to 17'-6"
Interior Splice 2	#5@6 in.	0'-0" to 2'-0"
Segment 2	#5@6 in. #5@4 in.	0'-0" to 8'-10" 8'-10" to 24'-6"
Splice 3 in Overhang	#5@4 in.	0'-0" to 2'-0"
Thickened End Block 2	#5@4 in.	0'-0" to 11'-6"

Note: All shear reinforcement consists of double legged stirrups.

Principal Tensile Stresses: AASHTO LRFD Article 5.8.5 (2012) requires that the principal tension stress be checked to verify the adequacy of the webs of segmental concrete bridges for shear and torsion. This article states that the principal tensile stress resulting from long-term residual axial stress and the maximum shear at the neutral axis

of the critical web shall not exceed the tensile stress limit for the Service III limit state ($0.11\sqrt{f_c'}$) at all stages during the life of the structure, excluding those during construction. When investigating principal stresses during construction, the tensile stress limit in AASHTO LRFD Table B.14.2.3.3-1 ($0.11\sqrt{f_c'}$) is used.

For the specimen, the principal stress was checked at the critical sections over the interior support and the three splice locations. Shear and bending stresses in the concrete at the neutral axis of the web were calculated for the Service III limit state. The principal tension stress was calculated using classical beam theory and the principles of Mohr's Circle.

Table B.6 shows the principal tension stress for service limit states at the selected locations with and without considering the effect of prestressing. The vertical component of the draped longitudinal tendons V_p will counteract the shear force in the section and reduces the shear demand carried by the concrete and transverse steel. For the case of load balancing, the effect of the vertical component of the PT cancels the dead load shear demand for the service limit state. AASHTO LRFD Article 5.8.5 (2012) specifies that V_p may be considered as a reduction in the shear force. The principle tension stress values considering V_p are below the AASHTO specified allowable limit. Note that the principal tension stress at service for Splice 3 is above the limit when V_p is not considered.

Table B.6. Principal Tension Stress Calculations for Specimen.

Critical Location	Principal Tension Stress at Service (not Considering V_p) (ksi)	Principal Tension Stress at Service (Considering V_p) (ksi)	Principal Tensile Stress limit ($0.11\sqrt{f'_c}$) (ksi)
Interior Support	0.224	0.039	0.321
Splice 1 near End Support	0.126	0.015	0.321
Interior Splice 2	0.242	0.066	0.321
Splice 3 in Overhang	0.433	0.095	0.321

B.3.3 Splice Connection Design

Flexural Considerations: The interior splice (Splice 2) in the specimen represents the splice located in the end span of the prototype bridge. This splice location corresponds to the dead load point of contraflexure in the prototype bridge so as to minimize the load demands at the splice. The width of the splice connection should be kept as small as possible because there is no pretensioning in this region and a minimal amount of mild steel reinforcement is provided. However, the splice width should be large enough to splice the continuity PT tendon ducts and allow for proper vibration of concrete. The width of the splice connection detail was a maximum of 24 in. per TxDOT recommendations. Fig. B.10 shows the splice connection detail used for the test specimen.

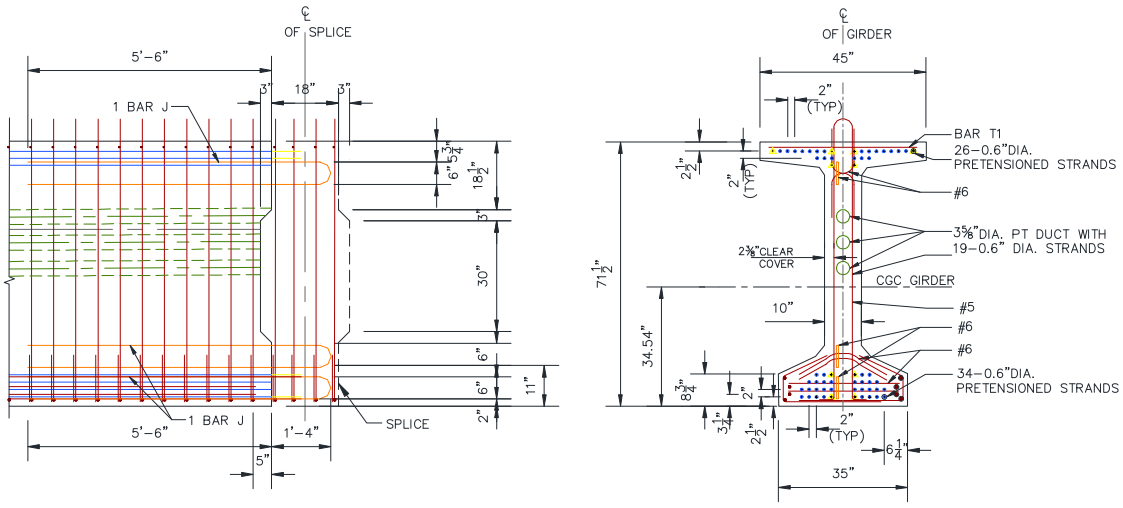

(a) Elevation *(b) Cross-Section*

Fig. B.10 Splice Detail Used for Test Specimen.

Because it is not feasible to pretension the splice region, a minimalist partially prestressed concrete solution was designed where the continuity PT provides most (approximately 90 percent) of the flexural strength, with some supplementary capacity provided by several top and bottom mild steel U-bars that formed a non-contact splice within the splice region. The same connection detail was used at all three splice locations. The mild steel reinforcement consisted of #6 180° hooked bars anchored into the adjacent girder flanges and extending into the joint. This connection detail was considered appropriate for the prototype bridge because thickened ends of girders were not used at the splice connection.

The factored moment capacity of the splice was calculated based on the number, diameter, location, and stress in the tendons, along with the design strength of concrete

and properties of the girder cross-section. Additional capacity was provided by the #6 mild steel 180° bent bars with details as follows (see J bars in Fig. B.10):

- Top flange steel: 1 - #6 180° bent bar.
- Bottom flange steel: 2 - #6 180° bent bars.

The embedment length of these bent bars was 5 ft 6 in. following the design recommendations of Koch and Roberts-Wollmann (2008). Their design recommendations for embedment length are based on the angle of inclination of the diagonal compressive stress computed using MCFT. In addition, two #6 transverse bars were tied inside each of the bent bars to increase the bearing capacity of the non-contact splice. The design capacity of the splice connection was calculated at three locations. Table B.7 shows the ultimate moment capacity for the splice locations in the specimen. The mild steel contributes a minimal amount of flexural strength, ranging from approximately 4–8 percent of the total reduced nominal strength in bending.

Table B.7. Reduced Nominal Moment Capacity for Splice Connections.

Description	Splice 1 Near End Support	Interior Splice 2	Splice 3 in Overhang
Continuity PT, ϕM_n (kip-ft)	7460	7400	10,310
Splice Reinforcement (180° bent bars), ϕM_n (kip-ft)	630	630	380
Total Capacity, ϕM_n (kip-ft)	8090	8030	10,690

Interface Shear Considerations: The integrity of the splice connection largely depends on the shear transfer mechanism at the interface of the precast girder and closure pour. This shear transfer mechanism was mainly provided by the shear key and the lapped 180° bent hooked bars in the connection. The interface shear resistance at the girder/splice interface was calculated as per AASHTO LRFD Article 5.8.4 based on shear friction theory. The nominal shear resistance of the interface plane is based on the cohesion factor, c, friction factor, μ, and the area of concrete engaged in interface shear transfer, A_{cv}. For the specimen, the case of normal-weight concrete placed against a clean concrete surface, free of laitance, without the roughened surface was used. The values of parameters specified in AASHTO LRFD Article 5.8.4 are cohesion factor c = 0.075 ksi, friction factor μ = 0.6, fraction of concrete strength available to resist interface shear K_1 = 0.2, and limiting interface shear resistance K_2 = 0.8 ksi. Due to the relatively high concrete strength and high level of prestressing, the K_2 value is the critical parameter and limits the shear

transfer capacity to 800 kips while shear demand for strength limit state is 448 kips in the prototype bridge.

B.4 SPECIMEN PREPARATION

The PT ducts and anchorages introduced some new details in the girder fabrication. A precast plant having experience with a recent spliced girder project agreed to fabricate the segments. After fabricating the girder segments and transporting them to the HBSMTL, significant preparation was necessary prior to testing. A brief review of the construction process is presented below.

B.4.1 Bearing Pad, Pedestal Design, and Pedestal Construction

The specimen was supported on two concrete pedestals in the lab. The pedestals were tied down to the strong floor using threaded rods. The size of the pedestal was based on the 3 ft spacing between the tie downs in the strong floor. The height of the pedestals was selected to facilitate installation of string potentiometers below the girder and to accommodate the girder deflection during testing. Fig. B.11 presents detailed dimensions and details of the pedestals.

Laminated steel-reinforced elastomeric bearing pads were selected for the supports based on the reaction forces at the supports during testing. In addition, because these bearing pads are commonly used by TxDOT in practice, they are intended to simulate the condition at supports similar to the prototype bridge on site. Fig. B.12 presents the bearing pad dimensions.

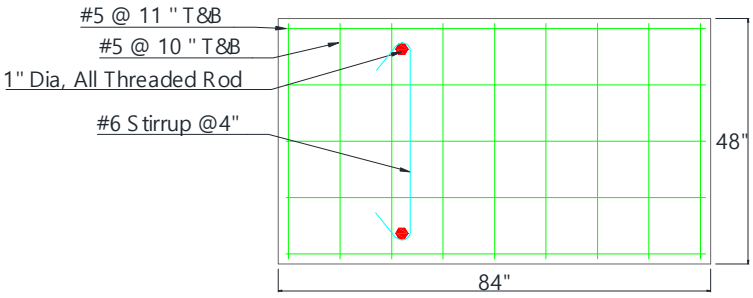

(a) 4x8 ft Pedestal, Plan View

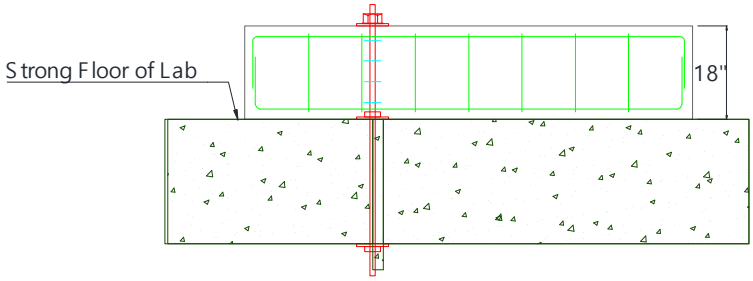

(b) 4x8 ft Pedestal, Elevation View

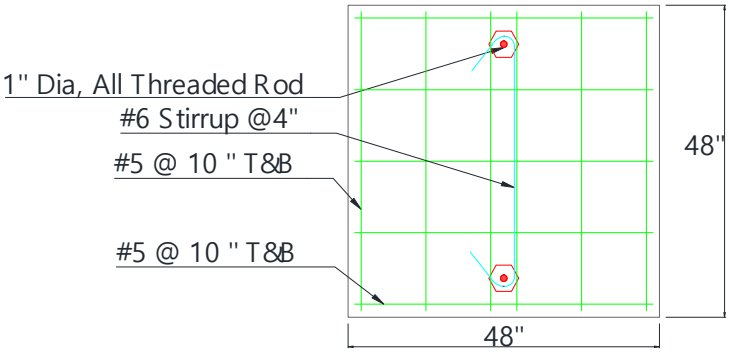

(c) 4x4 ft Pedestal, Plan View

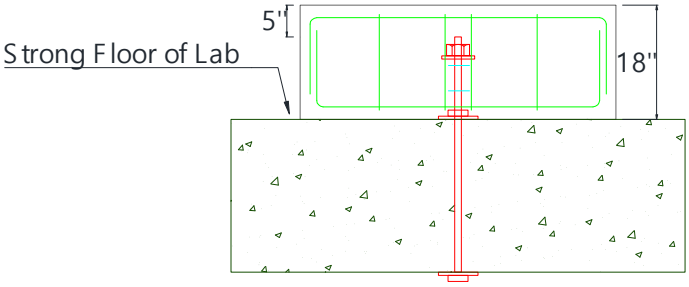

(d) 4x4 ft Pedestal, Elevation View

Fig. B.11 Details of Concrete Pedestals.

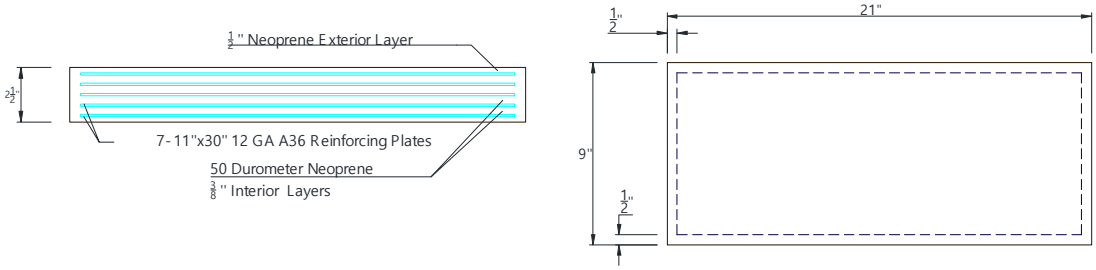

(e) 9x21 in. Bearing Pad, Elevation View *(b) 9x21 in. Bearing Pad, Plan View*

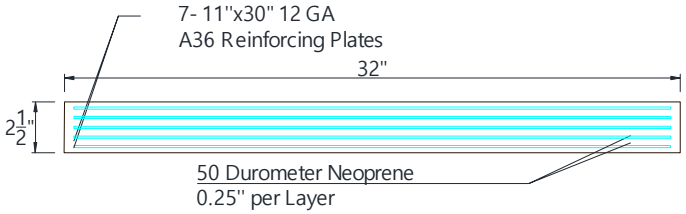

(c) 9x32 in.^{2} Bearing Pad, Elevation View

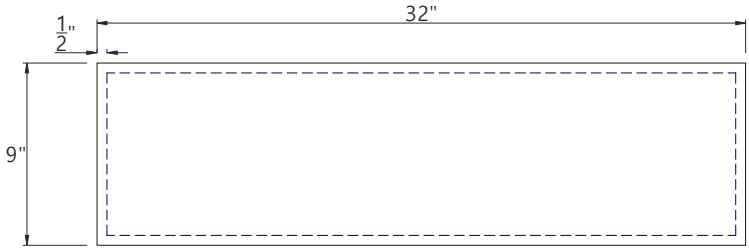

(d) 9x32 in. Bearing Pad, Plan View

Fig. B.12 Bearing Pad Details.

B.4.2 Casting the Girder Specimen at the Precast Plant

The four girder segments and end blocks for the specimen were fabricated at a precast plant. The gaged bars were prepared by the research group and placed in the girder according to the instrumentation plan. Gage wires were carefully tied to the closest vertical bars to protect them during the concrete placement. The wires were taken out of the formwork at the top of the segments. Fig. B.13 shows the placement and monitoring of the reinforcement. Casting of the specimen and concrete sample fabrication can be seen in Fig. B.14. A total of 156 cylinders, 13 MOR beams, and 12 shrinkage prism samples were taken from the different batches to monitor the mechanical properties of the concrete.

The girder segments were released two days after the pour. They were then hauled to the HBSMTL after they reached the required concrete strength at service f_{ci} of 6.5 ksi (see Fig. B.15). Fig. B.16 shows the final alignment of the girder segments in the HBSMTL with temporary supports in place to support each end of the girder segments.

(a) Installing Reinforcement

(b) Strain Gage

(c) Protecting Gage Wires

(d) Prestressing Strands

(e) Checking Gages

Fig. B.13 Installing Reinforcement at the Precast Plant.

(a) Installing Formwork

(b) Casting Concrete Transported from Batch Plant

(c) Molds for Hardened Property Samples

(d) Preparing Samples

Fig. B.14 Casting Girder Segments and Samples at the Precast Plant.

(a) Girder Segments with Lifting Points

(b) Placing Girder Segments

(c) Verifying Segment Spacing and Placement

Fig. B.15 Transporting Girder Segments to the High Bay Laboratory.

(a) Top View - Girder Alignment

(b) Side View - Girder Alignment

Fig. B.16 Final Girder Segment Placement and Alignment in the High Bay Laboratory.

B.4.3 Fabricating Wooden Connection Formwork

Three pairs of wooden formwork for the splice connections were fabricated by the research group in the lab. The formwork was cut and screwed together to maintain the actual shape of the modified Tx70 cross section through the splices. Gage wires were sent through openings in the formwork with care to avoid gage losses. Fig. B.17 shows the splice reinforcement with gaging and the formwork attached on the back side.

B.4.4 Building Falsework and Deck Formwork

Wooden falsework was designed and constructed to provide support for the deck formwork and walkway, as presented in Fig. B.18. A railing was also provided alongside the walkway and at the end of the formwork for safety.

B.4.5 Casting Splices in the Laboratory

After the connection formwork was fabricated and properly lubricated, the high strength conventional concrete splices were cast in the laboratory. Different options were considered for mixture proportions for the concrete, and after 10 trial batches the final mixture proportions were selected. Table B.8 summarizes the mixture proportion summary for the splice concrete. A concrete ready mix truck was hired and loaded with the appropriate amounts of 0.75 in. maximum size river gravel (coarse aggregate) and manufactured sand (fine aggregate) from a local batch plant. The gradation of the aggregates met TxDOT specifications. The remaining water, admixtures, and Type III cement were added to the concrete mix truck at the HBSMTL, as shown in Fig. B.19. The splices were cast in the laboratory as depicted in Fig. B.20.

Table B.8. Splice Concrete Mixture Proportions.

Material		Type	Quantity
Cement (lb/yd^3)		III	700
Water (lb/yd^3)		-	200
w/c ratio		-	0.29
Aggregate (lb/yd^3)	Coarse (MNAS ¾ in.)	River Gravel	1935
	Fine	Mfd. Sand	1232
HRWRA/Superplasticizer (oz/yd^3)		PS 1466	91

B.4.6 Casting Reinforced Concrete Deck in the Laboratory

After the splice gained sufficient strength, the mild steel and concrete for the deck was placed, as shown in Fig. B.21. A TxDOT Class S concrete with specified 28-day strength of 4 ksi was used for the deck concrete. A smooth finish was provided after casting. The deck concrete cured for one week and then the formwork was removed.

B.4.7 Fresh Concrete Properties

Fresh properties of concrete were measured after the concrete was cast. Measured parameters included slump, unit weight, temperature, and relative humidity. Table B.9 summarizes the average fresh concrete properties for the girder segments, splice connections, and the deck concrete.

(a) Splice 1 (End) *(b) Splice 2 (Middle)*

Fig. B.17 Splice Reinforcement and Formwork.

(a) South Side Formwork

(b) North Side Formwork

Fig. B.18 Falsework and Deck Formwork.

(a) Measuring Cement into Hopper

(b) Adding Cement to Truck

(c) Adding Admixture and Water to Truck

Fig. B.19 Adding Materials to Concrete Mixture for Connections.

Table B.9. Summary of Fresh Properties of Concrete.

Component	Slump or Slump Flow (in.)	Unit Weight (kcf)	Air Content (%)	Concrete Temperature (°F)	Ambient Temperature (°F)	RH (%)
Girder Segment	24.8	0.145	8	96	107.4	24.4
Splice Connection	9.75	0.151	not measured	not measured	70 (typical)	48
Slab Deck	3.75	0.146	5.1	67.5	70 (typical)	40

(a) Casting Splices

Fig. B.20 Placing Concrete for Splice Connections.

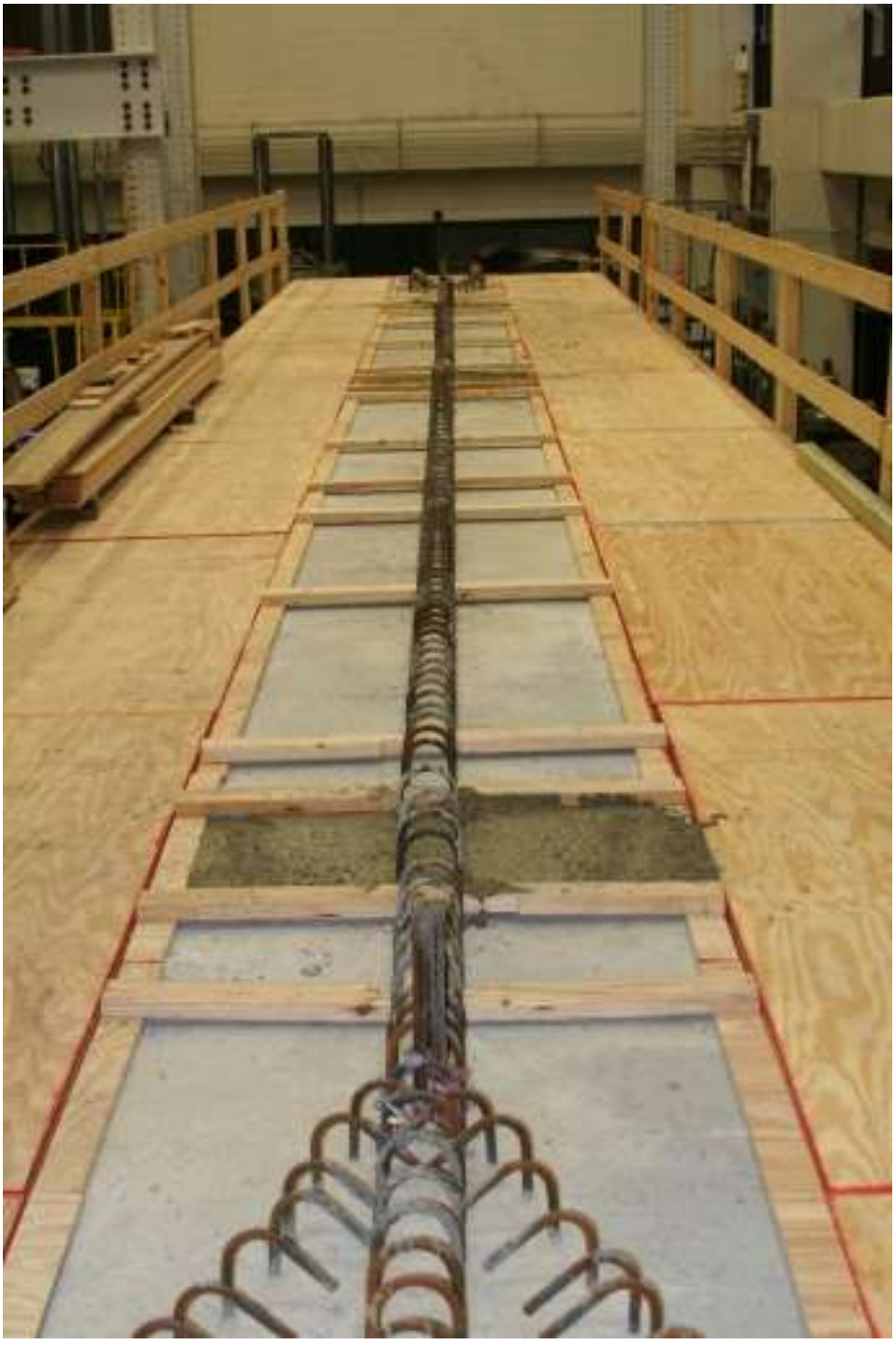

(b) Casting Splices Complete

Fig. B.20 Placing Concrete for Splice Connections (Continued).

(a) Casting the Deck

(b) Finishing the Deck

(c) Curing the Deck and Removing the Deck Formwork

Fig. B.21 Construction of the Deck Slab.

B.4.8 Installing Gages, Linear Variable Differential Transformers, String Pots, and Demountable Mechanical Points

Surface gages were attached on the top surface of the deck and to the sides of the top and bottom flanges of the precast girder according to the instrumentation plan described in Section 5.5. String potentiometers were placed 2 ft apart below the specimen to capture the deformation profile of the specimen.

A complete set of six linear variable differential transformers (LVDTs) was also mounted on the webs at each splice connection to map the deformed configuration of the splices and to measure the cracks. Demountable Mechanical (DEMEC) points made from thin aluminum sheets were installed on the webs of the splice regions. DEMEC readings were carried out at specific load levels during each test to fully map the deformation of the web and formation of cracks. Fig. B.22 shows the DEMEC and LVDT configurations for Splice 2.

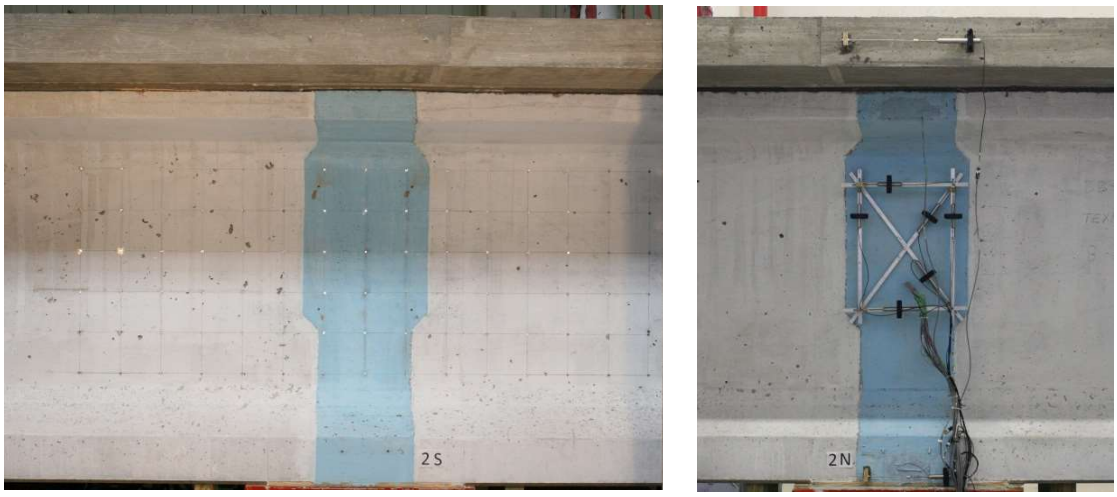

(a) DEMEC Points *(b) Splice LVDTs*

Fig. B.22 Splice DEMEC and LVDT Layouts.

B.4.9 Post-Tensioning

After the concrete deck and splice concrete gained their design strength of 4 ksi and 8.5 ksi, respectively, the PT operation was carried out. A PT contractor cut and placed the strands, stressed the strands, and grouted the ducts. Strands were fed through the three ducts and were stressed from End Block 1, after being anchored at End Block 2.

A hydraulic self-reacting jack was used to stress the strands. A simple conversion factor was used to translate the desired force per tendon into the required pressure. The desired force was also translated into strand elongation, which was double checked to ensure the target force per tendon was applied.

Table B.10 provides a summary of the target values for the PT operation. The three PT tendons were stressed one at a time. The middle tendon was stressed first, and then the top and the bottom tendons were stressed, respectively. While calculating the target force, instantaneous and time-dependent losses were considered. The order of stressing each duct

affects the instantaneous elastic shortening for each tendon. While calculating the stress for the first duct, the elastic shortening due to tensioning the second and third tendons was considered. In addition, the instantaneous loss due to anchorage set was considered. For the specific setup that was used for the specimen, the anchorage set was assumed to be 3/8 in.

Table B.10. Post-tensioning Calculation.

Tendon Location (Sequence)	Target Applied Stress (ksi)	Target Applied Force (kips)	Elongation (in.)
Middle (First)	206	850	6-1/8
Top (Second)	203	836	6
Bottom (Third)	200	822	6

After the strands were stressed, the ducts were grouted. Two holes at the top of each end cap served to monitor the filling of the tendon. When grout flowed out of the top hole, the grouting was stopped, as the grout had fully filled the ducts.

Grout was fed through each duct from End Block 2, using an air compressor to provide sufficient pressure throughout the length of the duct and to avoid formation of voids in the ducts. A pre-bagged NA Grout was used, which is a high flow, non-aggregate, and non-shrink grout. Every 400 lb of grout cement were mixed with 15.5 gallons of water, based on common practice. A mud flow test was carried out to measure the flowability of the grout. A large range of 11 to 30 seconds is acceptable based on the Post-tensioning Institute Specifications (2001). The grout mix was observed to be highly flowable and had

a flow time of 8.5 seconds, which was lower than the acceptable limit. However, according to EN 447 (European Committee for Standardization, 1996) any value lower than 25 seconds is acceptable.

Samples from each the three grout batches used for filling the PT ducts were taken for compressive strength testing. Standard 2 in. × 2 in. × 2 in. grout cube samples were made according to ASTM C109 (2013).

B.5 INSTRUMENTATION

Different types of instruments were used to record data to investigate and understand the behavior of the specimen under the test loads described in the experimental program. The instrumentation included strain gages, embedded concrete gages, LVDTs, string potentiometers, and DEMEC points. The instruments were used to capture the deflections along the specimen length and the strain profiles at critical sections of the specimen. In addition, reinforcement was monitored to determine if yielding occurred.

(a) Stressing Tendons

(b) Anchorage Plate and Anchor Wedges

(c) Measuring Pressure during Stressing

(d) Mixing Grout Mix and Water

(e) Grouting Ducts Using Air Pressure

Fig. B.23 Tendon Post-tensioning and Grouting Process.

B.5.1 Rebar Strain Gages

Fig. B.24 shows the locations of the rebar strain gages in the specimen. The strain gages were attached to reinforcement bars in the splice region and in the thickened end blocks.

Table B.11 summarizes rebar strain gage details according to the type of reinforcement bar. Because the research study was primarily focused on monitoring and assessing the performance of the proposed splice connection detail, most of the strain gages were attached in this area. The splice connection detail includes 180° bent hooked bars, and it was important to capture the stress, strain, and elongation in these bars. Two strain gages were attached on one leg of the 180° bent hooked bars at the top and bottom of each splice. Also, one strain gage was attached on one leg of each transverse shear reinforcement bar to measure shear demands. Ten strain gages were attached in the thickened end block to investigate the effect of post-tensioning and bursting forces during post-tensioning in this area.

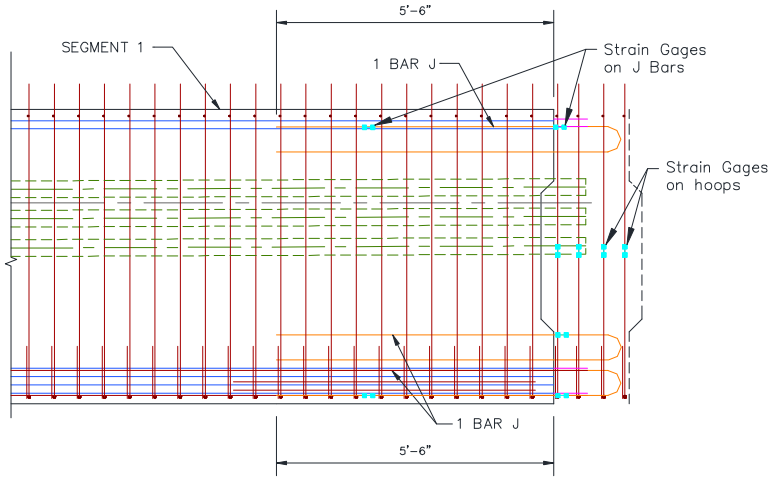

(a) Strain Gage Locations in the Splice Region (typical)

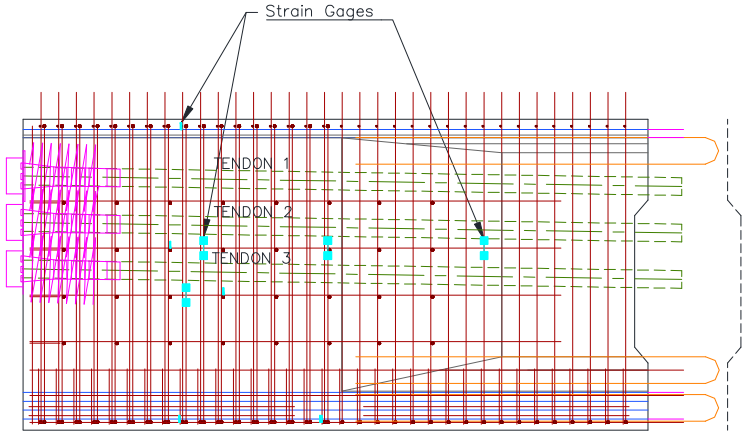

(b) Strain Gage Locations in Thickened End Block 1

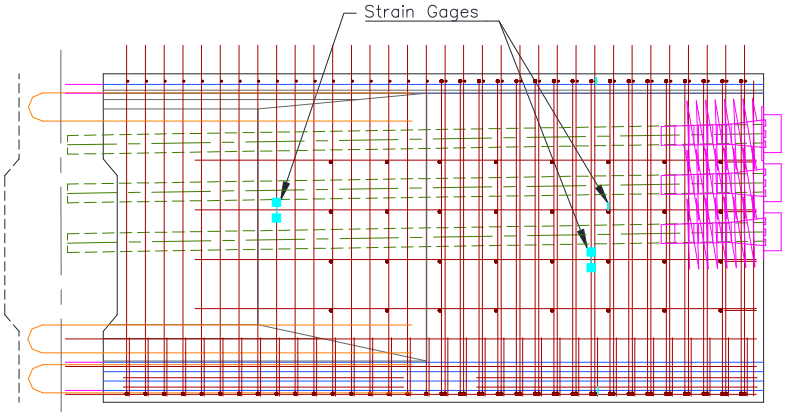

(c) Strain Gage Locations in Thickened End Block 2

Fig. B.24 Rebar Strain Gages in the Specimen.

Table B.11. Summary of Rebar Strain Gages.

Description	No. of Gages per Splice	Total No. of Gages	Installation Notes
On 180° bent hooked bars in girder	4	12	Pre-installed on the reinforcement bars, which were placed at the precast plant before the girder segments were cast.
On 180° bent hooked bars in splice	6	18	Installed in laboratory before casting splices.
On transverse shear reinforcement bars in splice	4	12	Installed in laboratory before casting splices.
Total	14	42	

A commonly used general purpose strain gage (CEA-06-250UW-350) with a gage length of 0.25 in. was used for measuring rebar strain in select locations. To make a half-bridge or full-bridge configuration, strain gages are usually attached to the point of interest as a pair of two or in a set of four, respectively. The advantage of using a half-bridge or full-bridge configuration to measure strain is the ability to compensate for a secondary type of strain. For the specimen, the rebar at critical locations were primarily subject to axial strain. The temperature during the testing program in the laboratory was nearly constant, so no compensation for temperature induced strains was needed. In this case, the strain gages were attached to the rebar at the points of interest and a quarter-bridge configuration was used to read the strain.

B.5.2 Surface Strain Gages

Surface strain gages (PL-60-11-3LT) were also used to capture the strain profile at important sections of the specimen during the loading and post-tensioning stages. Surface gages are similar to rebar gages, but because they are used on concrete, they are usually longer than those used for rebar (gage length = 2.36 in.). As shown in Fig. B.25, surface gages were attached on the top surface of the CIP concrete deck and on the side surfaces of the girder flanges. Three lines of strain gages were attached on top of the deck along the length of the specimen (see Fig. B.25 [a]). Two lines of strain gages measured the strain and deformation on the deck near the edges, and the central line of gages measured the strain on top of the deck along the centerline of the girder. Two surface strain gages were attached on the side surfaces of the top and bottom flanges of the girder at each critical location to capture the strain profile of those sections during post-tensioning and loading the specimen (see Fig. B.25 [b]).

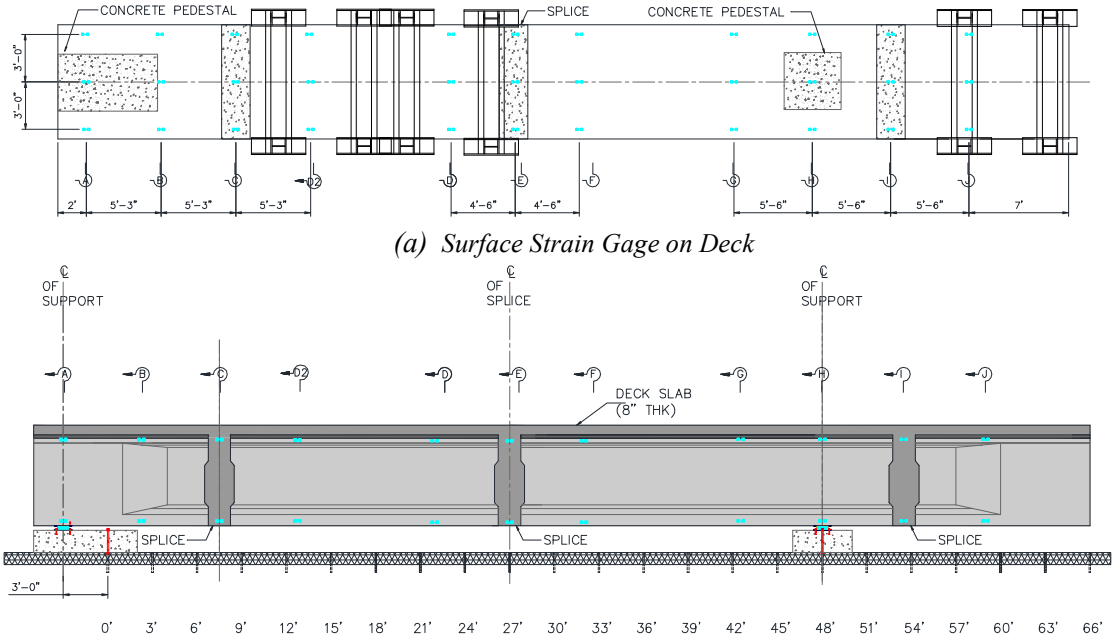

(a) Surface Strain Gage on Deck

(b) Surface Gages on Side of Girder Flanges

Fig. B.25 Surface Gages on the Specimen.

B.5.3 Embedded Concrete Gages

Embedded concrete gages were used to capture the strain and stress in the concrete, especially in the anchorage zones and the splice connections. The concrete gages around the PT ducts captured the effect of post-tensioning on the girder and the splice connection. Unlike the rebar strain gages, the embedded concrete gages were placed by attaching to the adjacent reinforcement using wires and then were embedded when the concrete was cast. These gages measured the axial strain in concrete. There are two different types of embedded concrete gages: one that only measures compressive strain and the other that measures both compressive and tensile strain in concrete. Within the specimen, the

concrete was subjected to tensile stresses in some areas and cracked, therefore embedded concrete gages with the ability to measure both compression and tension were used.

In order to measure the strain profile in the splice section, three embedded concrete gages were placed in the splice region. Fig. B.26 shows the typical locations for the embedded concrete gages within the splice region and end blocks. These gages were used to observe the effect of post-tensioning at the splices and the anchorage zone. They were also used in the splice sections to capture the strain profile at different loading stages during laboratory testing.

B.5.4 Linear Variable Differential Transformers

LVDTs are capable of measuring relative displacement between two specific points and are typically used to measure the average strain over a longer length. LVDTs were used to map the splice deformation at different loading stages during testing. Fig. B.27 (a) shows the location of mounted LVDTs on the specimen. Fig. B.27 (b) shows the configuration detail of the mounted LVDTs.

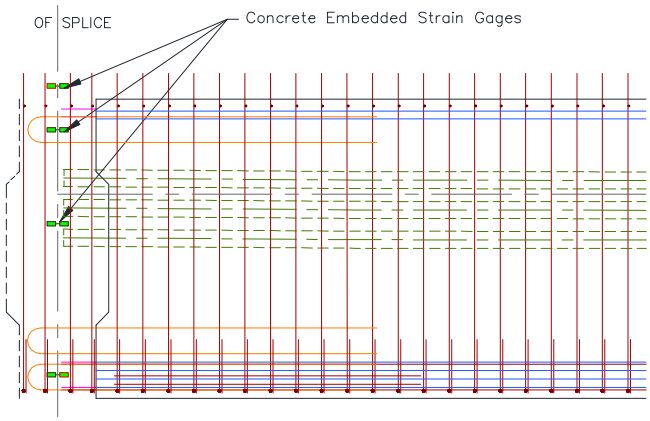

(a) Typical Strain Gage Locations in the Splice Region

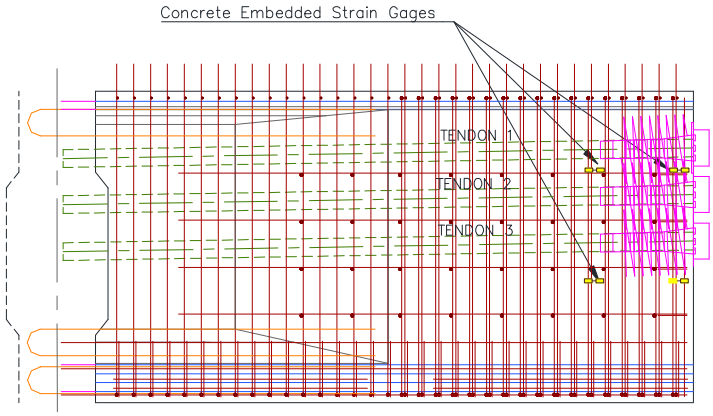

(b) Typical Strain Gage Locations in the Thickened End Block

Fig. B.26 Embedded Concrete Gages in the Specimen.

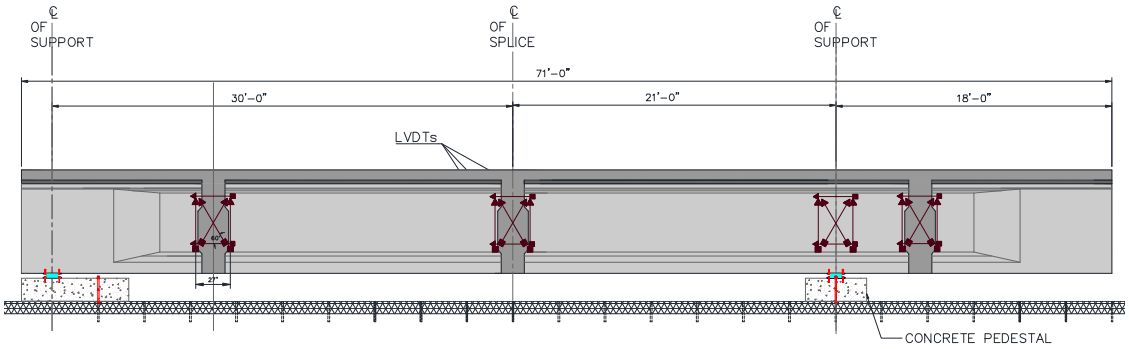

(a) Locations of LVDTs

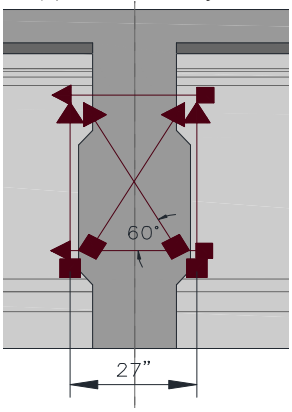

(b) Configuration of LVDTs

Fig. B.27 LVDTs Mounted on the Web of Specimen.

B.5.5 String Potentiometers

String potentiometers (string pots) are used to measure displacements and movements from a constant origin. String pots were placed under the girder at 2 ft increments to record the deformation profile of the girder during load testing. Fig. B.28 shows the layout of the string pots. The string pots were also used to capture the effect of post-tensioning, which introduced camber in the girder specimen.

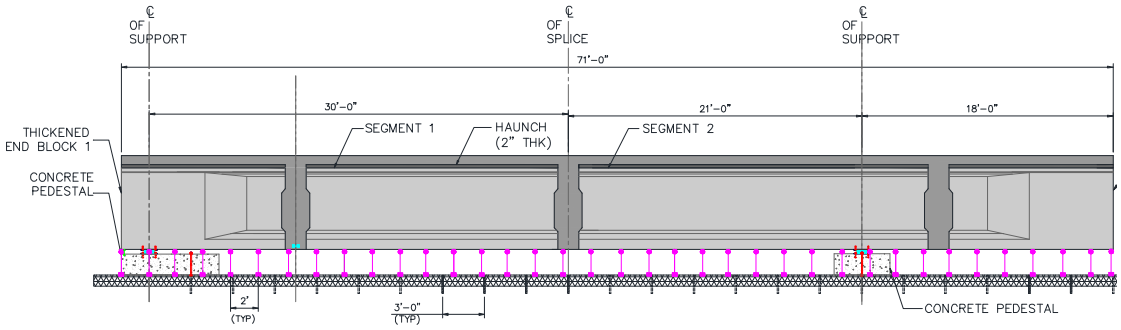

Fig. B.28 String Potentiometers Mounted on the Specimen.

B.5.6 Demountable Mechanical Points

DEMEC points were also used to map the deformation on the surface of the specimen. DEMEC points have several advantages including economy, reliability, and ease of installation. One disadvantage is that it is time consuming to measure and record all the distances between the DEMEC points and to map the deformed surface. Also, because there is no continuous data logging using the DEMECs, the experiment needs to be stopped at specific instances of interest in order to measure and record the useful data.

B.5.7 Summary of Instrumentation

Table B.12 presents a summary of the number of gages used for the specimen.

Table B.12. Instrumentation Summary.

Instrument Type	Location in the Specimen	Quantity	Measurement
Rebar Strain Gages	Splices	42	Strains in transverse reinforcement and 180° bent hooked bars in splices
Rebar Strain Gages	Thickened end blocks	10	Effect of PT forces on rebar in thickened end block
Concrete Strain Gages (Embedded)	Splice, thickened end blocks	20	Concrete strains in thickened end blocks and splice regions
Concrete Strain Gages (Surface)	Top and bottom flanges of girder segments and on top surface of deck	49	Strain in extreme fiber, moment-curvature relationship, load-displacement relationship
LVDTs	Splices, over interior support	24	Strains at splice regions and interior support
DEMEC Points	Splices, over interior support	280	Mapping the deformation in the splice region and at the interior support
String Pots	Movement of bottom girder face relative to strong floor along the length of the specimen	37	Deflection along the length of the specimen for moment-curvature relationship and load-displacement relationship
3-Wire Cable	Strain gages and string pots	10 (1000 ft each)	-
4-Wire Cable	LVDTs	2 (1000 ft each)	-

B.6 SUMMARY OF MATERIAL PROPERTIES

B.6.1 Concrete

Fresh and hardened properties of concrete for girder segments, splice connections, and slab deck was measured. More than 200 samples were taken from all batches of concrete

to provide a thorough understanding of the material properties of concrete. Samples were tested for day 1, 3, 14, 28, 56, and the day of testing. Appendix A of Report FHWA/0-6651-2 provides details of the measured properties at each stage. Table B.13 presents the summary of the material properties for the age of 28 days and the day of testing. The values for the day of testing was used in numerical models.

Table B.13. Concrete Properties for Numerical Analysis.

Part	Age of Concrete (days)	Parameter	At 28 Days (ksi)	At Age of Testing (ksi)
Girder Segments	222	f'_c	9.860	11.730
		f_r	1.084	1.170
		E_c	4742	5126
Splices	103	f'_c	8.790	9.500
		f_r	1.112	1.112
		E_c	5896	5895
Deck	95	f'_c	5.360	6.555
		f_r	0.685	0.500
		E_c	5089	5089

Stress-strain tests were carried out on #5 and #6 bars based on the ASTM A370-A8 standard. Tests were conducted on five #5 and five #6 bars. The grip-to-grip distance of the device was 16 in. An extensometer consisting of three LVDTs was used to measure the elongation, and the average of the three readings is report. The gage length was set to 8 in. as recommended in Article A9.3.1 of the ASTMA370. A MTS hydraulic jack with displacement control was used to load the specimen. Fig. B.30 shows the test setup and a typical failure of a reinforcing bar.

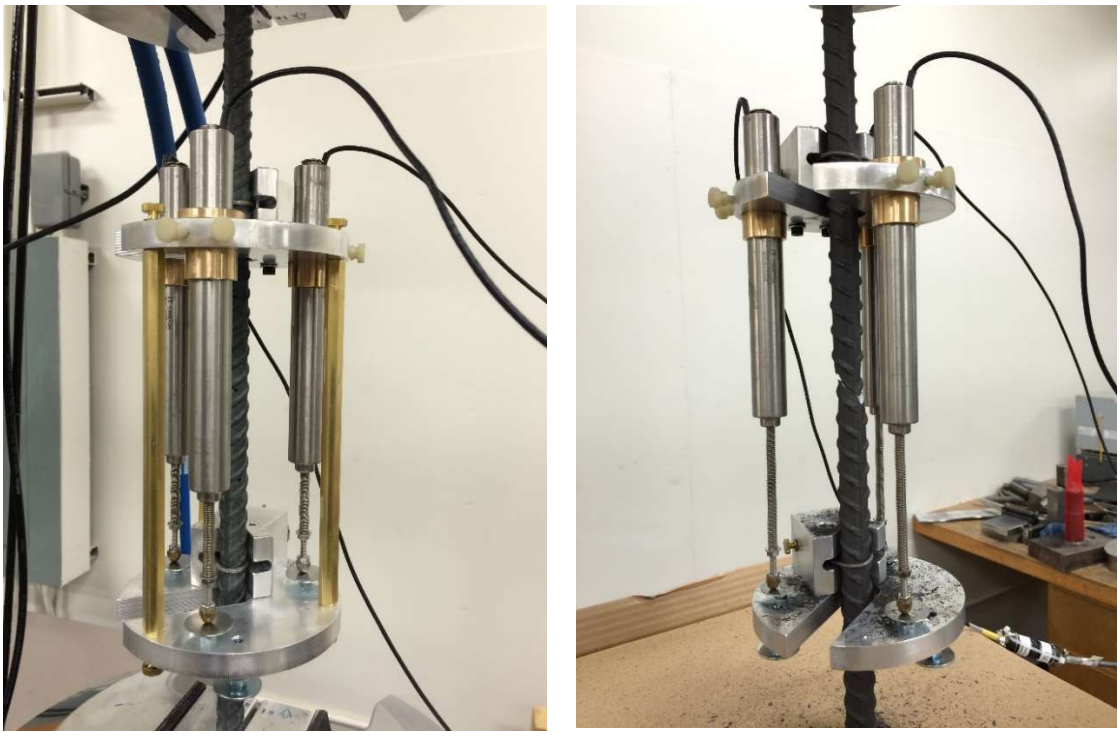

(a) Test Setup *(b) Failure within the Gage Area*

Fig. B.29 Mild Steel Stress-Strain Test.

Table B.14 and Table B.15 present the results of the stress-strain tests on the #5 and #6 bars, respectively. Fig. B.31 depicts typical stress-strain curves for the #5 and #6 mild steel bars based on experimental results and compares it with the Urmson-Mander (2012) model that was used in the numerical modeling.

Table B.14. Mechanical Properties of #5 Bars.

Test #	Loading Rate, in./sec.	Yield Stress (f_y), ksi	Young's Modulus (E), ksi	Ultimate Stress (f_{su}), ksi
1	0.0167	65.1	29,868	101.6
2	0.0084	63.5	27,578	105.8
3	0.0020	60.5	28,900	99.1
4	0.0050	61.7	27,753	101.3
5	0.0050	62.3	27,273	102.0
Average	-	62.6	28,275	102.0

Table B.15. Mechanical Properties of #6 Bars.

Test #	Loading Rate, in./sec.	Yield Stress (f_y), ksi	Young's Modulus (E), ksi	Ultimate Stress (f_{su}), ksi
1	0.0167	68.1	29,109	107.5
2	0.0084	68.0	29,096	107.5
3	0.0050	67.5	30,299	107.3
4	0.0050	67.9	29,587	107.3
5	0.0084	68.2	28,599	107.6
Average	-	67.9	29338	107.4

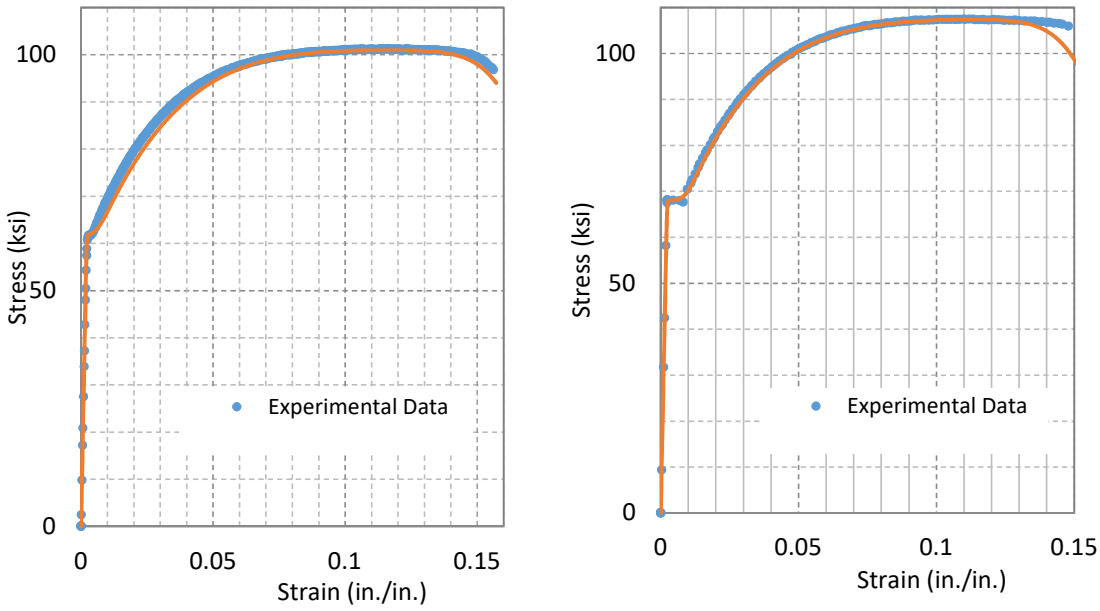

(a) #5 Rebar *(b) #6 Rebar*

Fig. B.30 Stress-Strain Curve for Mild Steel.

A.1 PRESTRESSING STRAND

Tensile strength test was carried out on five 0.6 in. diameter prestressing strands. An MTS hydraulic jack was used to pull the specimens. The grip-to-grip distance was 16 in., as specified by ASTM A370-A8. An extensometer with three LVDTs having a gage length of 8 in. was used to measure the strain. Because the wires started untwisting after reaching their yield strength, the gage was removed after yielding occurred. Fig. B.31 presents the test setup and failure of the specimen. Table B.16 summarizes the loading rates for each test and mechanical properties of the strands. Stresses were determined using the nominal area.

(a) Test Setup *(b) Untwisting after Yielding* *(c) Failure at Grip*

Fig. B.31 Prestressing Strand Tensile Test.

Table B.16. Mechanical Properties of Prestressing Strands.

Test #	Loading Rate, in./sec	Yield Stress (f_y), ksi	Young's Modulus (E), ksi	Ultimate Strength, ksi
1	0.0167	213	27,936	272.6
2	0.0167	211	28,635	271.9
3	0.0084	207	28,581	271.8
4	0.0084	203	28,538	273.3
5	0.0050	201	28476	272.7

APPENDIX C

DERIVATION OF DEFLECTION BALANCING

C.1 Deflection Theory

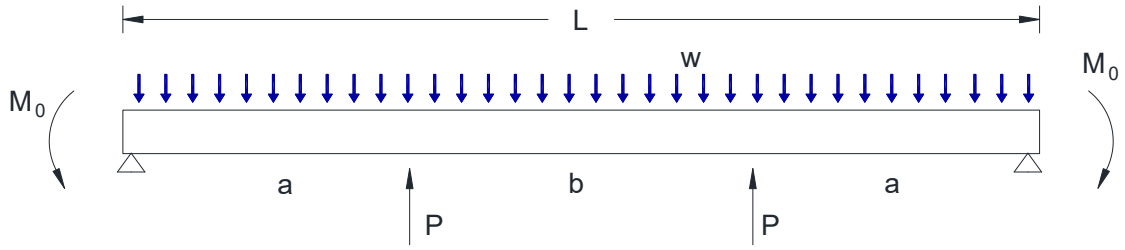

Let $Pa = m_p \frac{wL^2}{8} = m_p \frac{WL}{8}$ $\quad \therefore P = \frac{m_p}{a}\frac{wL^2}{8} = \frac{m_p}{a}\frac{WL}{8}$ (Note $W = wL$)

and $M_0 = m_0 \frac{wL^2}{8}$ and $y_f = \frac{wL^4}{384EI} = \frac{WL^3}{384EI}$ with $Y = \frac{y}{y_f}$ and $X = \frac{x}{L}$

Using free body diagram and moment equation:

$$-EI\,Y" = M(x) = (W/2 - P)x + P\langle x - a\rangle - M\_0 - (wx^2)/2$$

$$-\frac{wL^4}{348y_f}Y" = \frac{wLx}{2} - \frac{wx^2}{2} - P[x - \langle x - a\rangle] - M_0$$

$$-\frac{WL^3}{348y_f}Y" = \frac{Wx}{2} - \frac{wx^2}{2} - m_0\frac{WL}{8} - \frac{M_p}{a}\frac{WL}{8}[x - \langle x - a\rangle]$$

Simplifying:

$$\left(\frac{L}{48y_f}\right)Y" = \frac{4}{L^2}x^2 - \frac{4}{L}x + m_0 + \frac{M_p}{a}[x - \langle x - a\rangle]$$

Integrating to find slope y'

$$\frac{L^2}{48y_f}Y' = \frac{4}{L^2}\frac{x^3}{3} - \frac{4}{L}\frac{x^2}{2} + m_0x + \frac{m_p}{2a}[x^2 - \langle x - a\rangle^2] + C_1$$

at $x = {}^{L}/_{2}\,;\ Y' = 0$

$$0 = \frac{4}{L^2}\frac{L^3}{24} - \frac{4}{L}\frac{L^2}{8} + m_0\frac{L}{2} + \frac{m_p}{2a}\left[\frac{L^2}{4} - \langle\frac{L}{2} - a\rangle^2\right] + C_1$$

$$-C_1 = L\left(\frac{1}{6} - \frac{3}{6}\right) + m_0\frac{L}{2} + \frac{m_p}{2a}L^2\left[\frac{1}{4} - \langle\frac{1}{2} - \frac{a}{L}\rangle^2\right]$$

$$C_1 = \frac{L}{3} - m_0\frac{L}{2} + \frac{m_pL}{{}^{a}/_{L}}\left[1 - \left(1 - \frac{2a}{L}\right)^2\right]$$

$$C_1 = \frac{L}{3} - m_0\frac{L}{2} - \frac{m_pL}{2}\left(1 - \frac{a}{L}\right)$$

$$Y' = \frac{4}{L^2}\frac{x^3}{3} - \frac{4}{L}\frac{x^2}{2} + \frac{L}{3} - m_0\left\{\frac{L}{2} - x\right\} - m_p\left\{\frac{L-a}{2} - \frac{1}{2a}[x^2 - \langle x-a\rangle^2]\right\}$$

Integrating

$$\frac{L^2}{48y_f}\,Y = 4\frac{x^2}{12} - \frac{4}{L}\frac{x^3}{6} + \frac{Lx}{3} - m_0\left\{\frac{Lx}{2} - \frac{x^2}{2}\right\} - m_p\left\{\left(\frac{L-a}{2}\right)^x - \frac{1}{6a}[x^3 - \langle x-a\rangle^3]\right\}$$

Multiplying by $\frac{48}{L^2}$

$$Y = \frac{Y}{y_f} = 16\left(\frac{x}{L}\right)^4 - 32\left(\frac{x}{L}\right)^3 - 24m_0\left\{\left(\frac{x}{L}\right) - \left(\frac{x}{L}\right)^2\right\} + 16\left(\frac{x}{L}\right) - m_p\left\{24\left(1 - \frac{a}{L}\right)\left(\frac{x}{L}\right) - \frac{8}{{}^{a}/_{L}}\left[\left(\frac{x}{L}\right)^3 - \langle\frac{x}{L} - \frac{a}{L}\rangle^3\right]\right\}$$

And setting $X = \frac{x}{L}\ and\ set\ \ \alpha = \frac{a}{L}$

$$Y = [16X^4 - 32X^3 + 16X] - m_0\,24\{X - X^2\} - m_p\left\{24(1-\alpha)X \quad - \frac{8}{\alpha}[X^3 - \langle x-a\rangle^3]\right\} \qquad \text{(C.1)}$$

Differentiating

$$Y' = 64X^3 - 96X^2 + 16 - m_0\,24\{1-2X\} - m_p\,24\left\{(1-\alpha) - \tfrac{1}{\alpha}[X^2 - \langle x-a\rangle^2]\right\} \quad \text{(C.2)}$$

Specific Case for $\alpha = \frac{1}{3}$

$$Y = [16X^2 - 32X^3 + 16x] - m_0\,24\{X - X^2\} - m_p\left\{16X - 24\left[X^3 - \langle X - \tfrac{1}{3}\rangle^3\right]\right\} \quad \text{(C.3)}$$

$$Y' = 64X^3 - 96X^2 + 16 - m_0\,24\{1-2X\} - m_p\left\{16 - 96\left[X^2 - \langle X - \tfrac{1}{3}\rangle^2\right]\right\} \quad \text{(C.4)}$$

C.2 SPECIFIC SOLUTIONS

C.2.1 Eccentric only solution $(\boldsymbol{m_p = 0})$

Boundary condition with $y' = 0$ @$X = 0$. From Eq. (C.2):

$$Y' = 0 = 16 - 24m_0 \rightarrow\ m_0 = \frac{2}{3}$$

$$\therefore \qquad M^F = Fe_0 = \frac{2}{3}\frac{WL}{8} = \frac{WL}{12} = 0.0833\,WL$$

which is the well-known solution for a fixed-fixed beam.

C.2.2 Zero central deflection with eccentric only solutions $(\mathbf{m_p = 0})$

From Eq. (C.1) $\quad X = \frac{1}{2}$

$$Y = 0 = \left[16.\frac{1}{2}^4 - 32.\frac{1}{2}^3 + 16.\frac{1}{2}\right] - m_0 24\left\{\frac{1}{2} - \frac{1}{2}^2\right\} = 5 - 6m_0$$

$$m_0 = \frac{5}{6}$$

$$\therefore \qquad Fe_0 = \frac{5}{6} \times \frac{WL}{8} = 0.1042\,WL = \frac{WL}{9.6}$$

C.2.3 Harped only solution $(\mathbf{m_o = 0})$, $\boldsymbol{\alpha = 1/3}$

For zero slope at support: $X = 0,\ \ Y' = 0$. From Eq. (C.4):

$$Y' = 16 - m_p\{16 - 96[0]\} = 16 - 16m_p$$

$$m_p = 1$$

$$\therefore \qquad Fe_0 = \frac{WL}{8}$$

Associated central deflection with $m_p = 1$ and $X = 1/2$:

$$Y = \left[16.\frac{1}{2}^4 - 32.\frac{1}{2}^3 + 16.\frac{1}{2}\right] - \left\{16.\frac{1}{2} - 24[\frac{1}{2}^3 - \frac{1}{6}^{1/3}\right\} = -\frac{1}{9}(upward)$$

C.2.4 Harp Only: Zero central deflection $(\mathbf{m_p} = ?)$, $\boldsymbol{\alpha = 1/3}$

From Eq. (C.3):

$$Y = [5] - m_p 1\{5\ {}^1/_9\} = 0$$

$$m_p = {}^{45}/_{46} = 0.9783$$

$$\therefore \qquad Fe_c = \frac{45}{46} \times \frac{WL}{8} = 0.1223\, WL = \frac{WL}{8.177}$$

C.2.5 Mixed Solution

With both harping and end eccentricity, what are the values of m_p and m_0 so that the precast beam has zero slope at each end and zero mid-span deflection for the specific case where $\alpha = 1/3$.

From Eq. (C.4) for $Y' = 0$ and $X = 0$:

$$Y' = 0 = 16 - 24m_0 - 16m_p \qquad \text{(C.5)}$$

From Eq. (C.3) for $Y = 0$ and $X = 1/2$:

$$Y = 0 = 5 - 6m_0 - 5\ {}^{1}/_{9}\ m_p \qquad \text{(C.6)}$$

Solving Eq. (C.5) and (C.6) simultaneously:

$$m_p = {}^{9}/_{10} = 0.9$$

$$m_0 = {}^{1}/_{15} = 0.0667$$

$$\therefore \qquad F(e_c - e_0) = \frac{9}{10} \times \frac{WL}{8} = 0.1125\ WL$$

$$\therefore \qquad F(e_0) = \frac{1}{15} \times \frac{WL}{8} = \frac{WL}{120} = 0.00833\ WL$$

Total moment at center:

$$\therefore \qquad Fe_c = (0.1125 + 0.00833)WL = 0.12083\ WL$$

C.2.6 Optimal Location of Harping (α_{opt})

To Obtain zero central deflection (with $m_0 = 0$), and full moment balancing $m_p = 1$, solve for α when $Y = 0$ and $X = 1/2$:

$$Y' = 0 = 5 - \left\{12(1 - \alpha) - {}^{8}/_{\alpha}\left[{}^{1}/_{8} - \left({}^{1}/_{2} - \alpha\right)^{3}\right]\right\}$$

Solving for α numerically:

$\alpha = 0.353553$

APPENDIX D

C-STM GEOMETRY PROPORTION DERIVATION

Fig. D.1 presents the geometric proportion of truss panels, so that the transverse dummy members are perpendicular to compression concrete struts. The geometric proportion may be derived as:

$$AC \perp BD \;\&\; AD \perp BE$$
$$\therefore \angle CAD = \angle EBD = \theta$$

$$\tan\theta = \frac{ED}{BD} = \frac{CD}{AC}$$
$$\therefore \frac{d}{N.s} = \frac{s}{d}$$
$$\therefore s = \frac{d}{\sqrt{N}}$$
$$\cot\theta = \frac{N.s}{d} = \frac{N.s}{s\sqrt{N}} = \sqrt{N}$$

Results of such proportionality is presented in Table D.1 for the cases of $N = 1, 2, 3,$ and 4. The last row of Table D.1 presents the cases and where, due to geometric restrains or a different calculated crack angle, geometric proportion does not follow Eq. (6.1) of Chapter 6. Karthik et al. (2016) proposed that the following equation based on Mohr's circle may be used to calculate the value of $\frac{\varepsilon_1}{\varepsilon_2}$ for any given value of θ:

$$\left|\frac{\varepsilon_1}{\varepsilon_2}\right| = \left(\tan^2\theta + \frac{\left|\frac{\varepsilon_1}{\varepsilon_{2i}}\right|}{\cos^2\theta}\right)$$

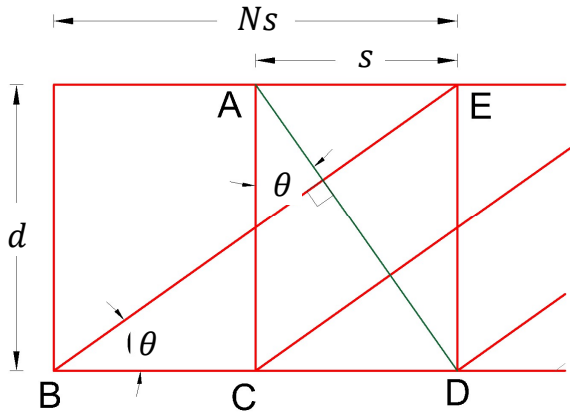

Fig. D.1 Geometric proportion of panels.

Table D.1. Truss geometry for 1 thru 4 panel configurations.

Panel Configuration	Truss Geometry
$N = 1$ $\theta = 45°$ $\cot\theta = 1.0$	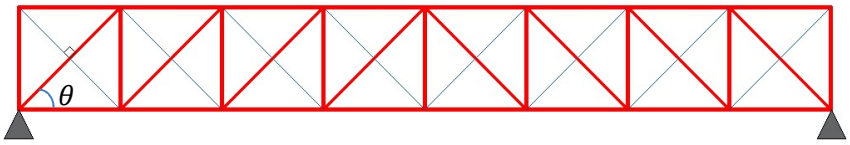
$N = 2$ $\theta = 35.5°$ $\cot\theta = 1.402$	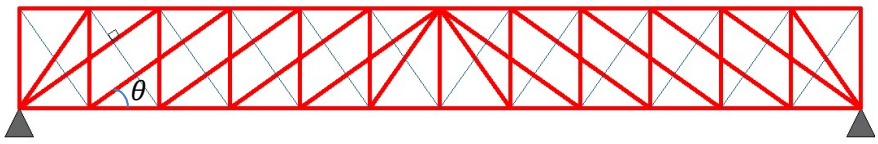
$N = 3$ $\theta = 30°$ $\cot\theta = 1.732$	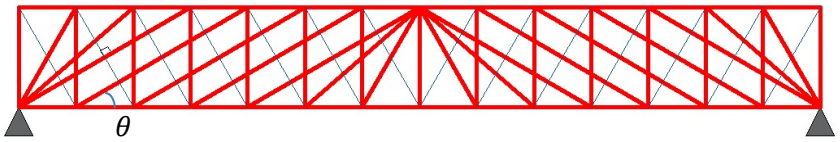
$N = 1$ $\theta = 26.5°$ $\cot\theta = 2$	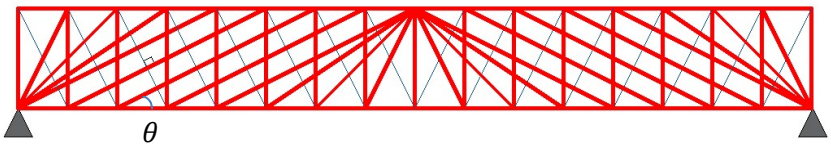
N *not integer* θ	$\left\lvert\frac{\varepsilon_1}{\varepsilon_2}\right\rvert = \left(\tan^2\theta + \frac{\left\lvert\frac{\varepsilon_1}{\varepsilon_{2i}}\right\rvert}{\cos^2\theta}\right)$